Northumbria University
NEWCASTLE

AN OBSERVATIONAL INVESTIGATION OF CORONAL RAIN IN THE QUIESCENT AND FLARING SOLAR CORONA

SERAY ŞAHİN

PhD

2023

AN OBSERVATIONAL INVESTIGATION OF CORONAL RAIN IN THE QUIESCENT AND FLARING SOLAR CORONA

SERAY ŞAHİN

A thesis submitted in partial fulfilment of the requirements of the University of Northumbria at Newcastle for the degree of Doctor of Philosophy

Faculty of Engineering and Environment in the Department of Maths, Physics, and Electrical Engineering

October 2023

"Sizi birer kıvılcım olarak gönderiyorum;
alevler olarak geri dönmelisiniz."

Mustafa Kemal ATATÜRK

Publications

Below is a list of peer-reviewed publications from the study presented in this thesis, including those in preparation, submitted, and published.

[1] **Şahin, S.** and Antolin, P. (submitted). *From Chromospheric Evaporation to Coronal Rain: An Investigation of the Mass and Energy Cycle of a Flare*. The Astrophysical Journal.

[2] **Şahin, S.** and Antolin, P. (submitted). *Comparison of Quiescent and Flare-driven Coronal Rain*. Astronomy & Geophysics.

[3] **Şahin, S.**, Antolin, P., Froment, C., Schad, T. A. (2023). *Spatial and Temporal Analysis of Quiescent Coronal Rain over an Active Region*. The Astrophysical Journal, 950(2), 171.

[4] **Şahin, S.** and Antolin, P. (2022). *Prevalence of Thermal Nonequilibrium over an Active Region*. The Astrophysical Journal Letters, 931(2), L2.

Abstract

The corona is the outer layer of the solar atmosphere and has a puzzling temperature hundreds of times higher than the underlying surface, which is a major unsolved astrophysics problem. The corona also contains a substantial quantity of cool material called coronal rain, hundreds of times colder and denser plasma grouped in showers, and is mainly observed in quiescent and flaring active regions (AR). The properties of rain are known to be deeply linked to the way the corona is heated, but its dynamics, origin, and morphology are yet poorly understood. In particular, the rain's spatial and temporal occurrence in an AR is unknown. Rain formation is driven by thermal instability (TI) in coronal loops that are in thermal non-equilibrium (TNE). In this thesis, using the IRIS and SDO instruments, I conducted the first high-resolution imaging statistical study of coronal rain (and showers) to investigate its origin, dynamics, morphology, energetics, and its link to coronal heating and solar flare mechanisms. In particular, I find that the volume under TNE-TI conditions can be over half the AR volume, indicating a prevalence of strongly stratified and high-frequency coronal heating. Overall, plasma downflows in the form of rain showers can be as energetic or more than the upward flare-driven chromospheric evaporation, placing coronal rain as a major player in the mass and energy circulation in the quiescent and flaring solar corona.

Acronyms

AC	Alternating Current
AIA	Atmospheric Imaging Assembly
AR	Active Region
BSS	Blind Source Separation
CCTR	Corona Condensation Transition Region
CME	Coronal Mass Ejection
CRIPS	Crisp Imaging Spectro-polarimeter
CRISPEX	CRIsp Spectral Explorer
DC	Direct Current
DEM	Differential Emission Measurement
DPFLs	Dark Post-Flara Loops
EIT	Extreme ultraviolet Imaging Telescope
EUV	Extreme Ultraviolet
EVE	Extreme ultraviolet Variability Experiment
FFT	Fast Fourier Transform
FUV	Far Ultraviolet
GOES	Geostationary Operational Environmental Satellite
GST	Goode Solar Telescope
Hi-C	High-Resolution Coronal Imager
HMI	Heliospheric and Magnetic Imager
H-R	Hertzsprung-Russell
HT	Hough Transform
HXR	Hard X-ray
IDL	Interactive Data Language
IRIS	Interface Region Imaging Spectrograph
JSOC	Joint Science Operations Center
KHI	Kelvin-Helmholtz Instability
LMSAL	Lockheed Martin Solar and Astrophysics Laboratory
LOS	line-of-sight

MHD	Magnetohydrodynamics
MK	Million Kelvin
TiO	Titanium-Oxide
TRACE	Transition Region and Coronal Explorer
NASA	National Aeronautics and Space Administration
NUV	Near Ultraviolet
PCTR	Prominence-Corona-Transition Region
PEA	Post-Eruption Arcade
PFLs	Post-Flare Loops
PIL	Polarity Inversion Line
PSD	Power Spectral Density
QS	Quiet Sun
RFit	Response Fit
RHT	Rolling Hough Transform
RTI	Rayleigh-Taylor Instability
SDO	Solar Dynamics Observatory
SG	Spectrograph
SJI	Slit-Jaw Images
SOHO	Solar and Heliospheric Observatory
SST	Swedish Solar Telescope
SUMER	Solar Ultraviolet Measurements of Emitted Radiation
SXR	Soft X-ray
TI	Thermal Instability
TNE	Thermal Non-Equilibrium
TR	Transition Region
UV	Ultraviolet

Contents

List of Figures

List of Tables

Acknowledgements

Despite the unprecedented challenges presented by the COVID-19 pandemic and a cyber-attack on the university, which wiped out my data, it has been a magnificent PhD journey! I would like to take this opportunity to express my deepest gratitude and appreciation to those who have supported and guided me throughout my PhD journey at Northumbria University. It has been an incredible experience, full of challenges and rewards, and I am honoured to have had the opportunity to pursue my research here with amazing Solar people!

A good supervisor is worth more than any wealth. Therefore, the first person I would like to express my appreciation to is my supervisor, Prof. Patrick Antolin. I did make the best choice for my research interest! This thesis would not have been possible without his support, patience, and invaluable advice. He introduced me to coronal rain, which became my baby after three and a half years. It has been a pleasure to be your first PhD student and to have you as my primary supervisor.

I would also like to extend my thanks to my second supervisor, Eamon Scullion, for being there to discuss science, life, and sports! I also would like to acknowledge my other collaborators and co-authors, Clara Froment and Tom Schad. I also would like to express my sincere gratitude to Prof. Vasyl Yurchyshyn for his help and guidance throughout my Ph.D. life!

They say a PhD is a lonely journey, but some friends make this journey enjoyable. I want to thank my friend Özlem, who shared the same journey with me in a different country. I will never forget our coffee time on Skype. My life in Newcastle wouldn't have been this fun without Hemanthi! Many thanks to Ramada, and my first friend Morgan, and Shannon, Dove, Jordan, and Vishal for the enjoyable place to study throughout my time here.

Thank you to my family for all your love and support throughout my studies.

Last but not least, my dear husband Oktay Solakci, you did something that not everyone can do! You encouraged me to apply for a PhD abroad, and then you became my biggest supporter by risking being separated for three and a half years. I am grateful for your constant support, patience (during my difficult time due to PhD) and encouragement. You are the co-owner of this success.

Declaration

I declare that the work contained in this thesis has not been submitted for any other award and that it is all my own work. I also confirm that this work fully acknowledges opinions, ideas and contributions from the work of others.

Any ethical clearance for the research presented in this thesis has been approved. Approval has been sought and granted by the Ethics Online system, submission reference 28838 on 03/02/2021.

I declare that the Word Count of this thesis is 37,395 words.

Name: Seray ŞAHİN

Date: 26 October 2023

Chapter 1

Introduction

The introduction section provides the background information necessary to comprehend the topics discussed in this dissertation. It begins with the fundamental structure of the Sun and gradually focuses on specific features, such as coronal heating, coronal loops, coronal rain, and showers. The chapter culminates in an overall outline of this dissertation, wherein the research problems are addressed.

1.1 Our Star: The Sun

The Sun is one of the hundred billion stars hosted by our home galaxy, the Milky Way, that provides all energy that fuels and nurtures life on the planet Earth. It is 149600000 kilometers (km) away from the Earth, and this distance is known as an Astronomical Unit. It is the only star whose surface can be directly observed from the Earth in great detail, and it hosts a variety of complex and dynamic physical processes that occur within its interior and atmosphere. The Sun is a middle-aged (4.6×10^9 yr) star of the G2V spectral class located at the main sequence of the Hertzsprung-Russell diagram (abbreviated as H-R) and rich in elements heavier than Helium. It primarily comprises Hydrogen (about 73% by mass), Helium (about 25% by mass), and a relatively small amount of other elements such as Oxygen, Carbon, and Neon. The Sun has a nearly spherical form, a solar mass ($M_\odot$) of 2×10^{30} kg, and a radius ($R_\odot$) of 6.957×10^8 m.

The Sun can be divided into two parts: its inner structure (see Figure 1.1), which we study via indirect observations and theoretical inferences (for instance, using Helioseismology), and the outer

atmosphere, which can be directly observed with various astrophysical instruments. A brief review of the solar interior and atmosphere is presented in the following subsections 1.2 and 1.3.

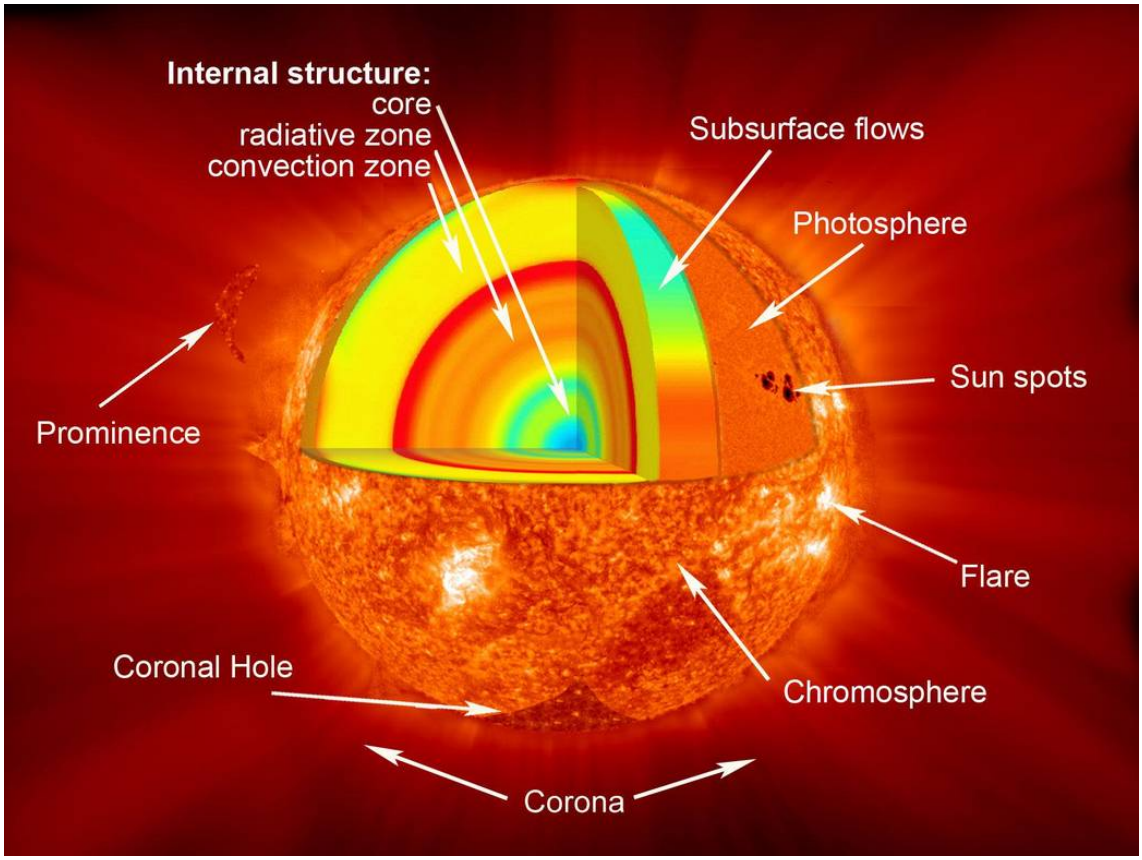

Figure 1.1: The Solar interior and outer atmosphere (Image Credit: NASA/Goddard)

1.2 Solar interior

The solar interior refers to the interior structure of the Sun, and it is bounded by the photosphere, a layer in the solar atmosphere from which all solar light is initially emitted. The interior is separated into four regions (Figure 1.1), namely, the core, the radiative zone, the interface layer (tachocline), and the convection zone. The core, which extends up to $0.25R_{\odot}$, is the central region of the Sun, and 99% of the Sun's energy is generated from the conversion of hydrogen into helium by means of nuclear reaction (e.g., Borexino Collaboration et al., 2018). The temperature and the density of the core are (1.5×10^7 K) and (150 g cm^{-3}), respectively. The energy generated in the core is carried out by photons through the radiative region situated above the outer edge of the core and extending up to 0.7 $R_{\odot}$. Here, in the radiative region, the temperature and density of the solar plasma drop from 20 g cm^{-3} to 0.2 g cm^{-3} and from 7×10^6 K to 2×10^6 K, respectively. Even

though photons travel at the speed of light, the numerous and complex interactions of the photons with particles within the radiative zone make it difficult for energy to propagate outward, and therefore, it takes millions of years for a photon to undergo a multitude of transformations. The outermost layer of the solar interior is known as the convection zone, where the main mechanism for energy transport to the outer layer is convection rather than radiation. This transition from radiation to convection is attributed to the decrease in temperature and the ionization degree of the plasma. Hence, the opacity of the plasma increases (absorption processes). So, radiation becomes progressively less efficient in transporting energy outwards. Eventually, at some point, convection becomes the more efficient energy transfer, taking over radiation as the primary mechanism for energy transportation up to the solar surface. The convection motions, with hot plasma rising and cool plasma sinking, produce cellular patterns of various spatial scales, and the smallest cells, known as solar granulation, represent the outer boundary of the solar interior that can be directly observed with telescopes. The temperature and density in the convective region are around 5800 K and 2×10^{-7}g cm^{-3}, respectively. The transition from a roughly static environment (the radiative zone) to an environment with bulk motions (convection) introduces a significant change in the solar environment. The dynamo mechanism involves the creation of strong toroidal magnetic fields through the interaction of velocity shear motions between these regions. These toroidal magnetic fields rise through the convection zone, driven by magnetic buoyancy and associated instabilities. These magnetic fields emerge at the Sun's visible surface, manifesting as bipolar magnetic regions. Due to the highly conductive nature of the plasma, this dynamic environment gives rise to a dynamo effect, hence giving birth to a region where magnetic fields are generated, the tachocline (Spiegel and Zahn, 1992; Charbonneau, 2020).

1.2.1 The Solar Magnetic Field and the Plasma-Beta Parameter

The Sun's magnetic field is responsible for most of the dynamic events in its atmosphere. As mentioned in the previous section, magnetic field generation occurs in the depths of the solar interior due to the dynamo mechanism. The kinetic energy in the Sun comes from the turbulent churning of ionized plasma within its interior and the dynamo mechanism can convert kinetic energy into electricity. These generate magnetic fields by transporting electrons in the form of electric currents. The magnetic fields produced by the Sun's dynamo undergo interactions that cause them to break, reconnect and rise through the Solar surface.

The formation of active regions involves the ascent of a flux tube in a Ω-shaped configuration from the base of the convection zone. As the flux tube rises, its apex intersects the photosphere, creating a bipolar region. Studies have demonstrated that magnetic buoyancy instability, or Parker instability, plays a crucial role in this process. This instability arises due to the accumulation of magnetic pressure at the boundary of the photosphere. The magnetic flux that reaches the photosphere undergoes dynamic expansion into the stably stratified solar atmosphere (Shibata et al., 1989).

The solar atmosphere, on the other hand, exhibits a complex plasma structure where the interplay between magnetic and plasma pressure often determines the dominant force at play. This dynamic balance is encapsulated by the plasma beta (β), representing the ratio of gas pressure to magnetic pressure, as defined in the following Equation (Equation 1.1):

$$\beta = \frac{P_{th}}{P_m} = \frac{n_e k_B T_e}{\frac{B^2}{2\mu_0}} \tag{1.1}$$

Here, P_{th} and P_m are the thermal (or gas) and magnetic pressure, respectively. n_e is the electron density, k_B the Boltzmann constant, T the gas temperature, B the magnetic field, and μ_0 the permeability of free space.

1.3 Solar Atmosphere

The long and gruelling travel of photons within the solar interior ends at the solar "surface", a thin (300 km), corrugated layer of solar plasma where photons can freely escape into space. That "surface" can therefore be directly observed with scientific instrumentation and is called the photosphere, the sphere of light. Above the photosphere is situated the solar atmosphere, which is a product of extremely complex interactions between plasma and magnetic fields (Priest, 2014). The solar atmosphere is usually divided into four distinct layers based on the physical properties of plasma, such as temperature and density. These regions are called the photosphere, chromosphere, Transition Region (TR), and corona (see Figures 1.1 and 1.2). Semi-empirical temperature and density profiles across these layers vary by several orders of magnitude within a relatively small height interval of 3,000 km. Of course, the observed profiles are much more complex and also vary strongly in time from one area to another, depending on the underlying magnetic fields.

These strong vertical and horizontal gradients combined with highly structured magnetic fields give rise to numerous complex and dynamic plasma structures that make the solar atmosphere mesmerizing to observe and often difficult to understand. While some of the structures can only be observed in the visible range of the solar spectrum, others emit light over the entire span of the spectrum, ranging from gamma rays to near Infra-Red radiation. The following subsections briefly review the properties of the solar atmosphere and the events it hosts.

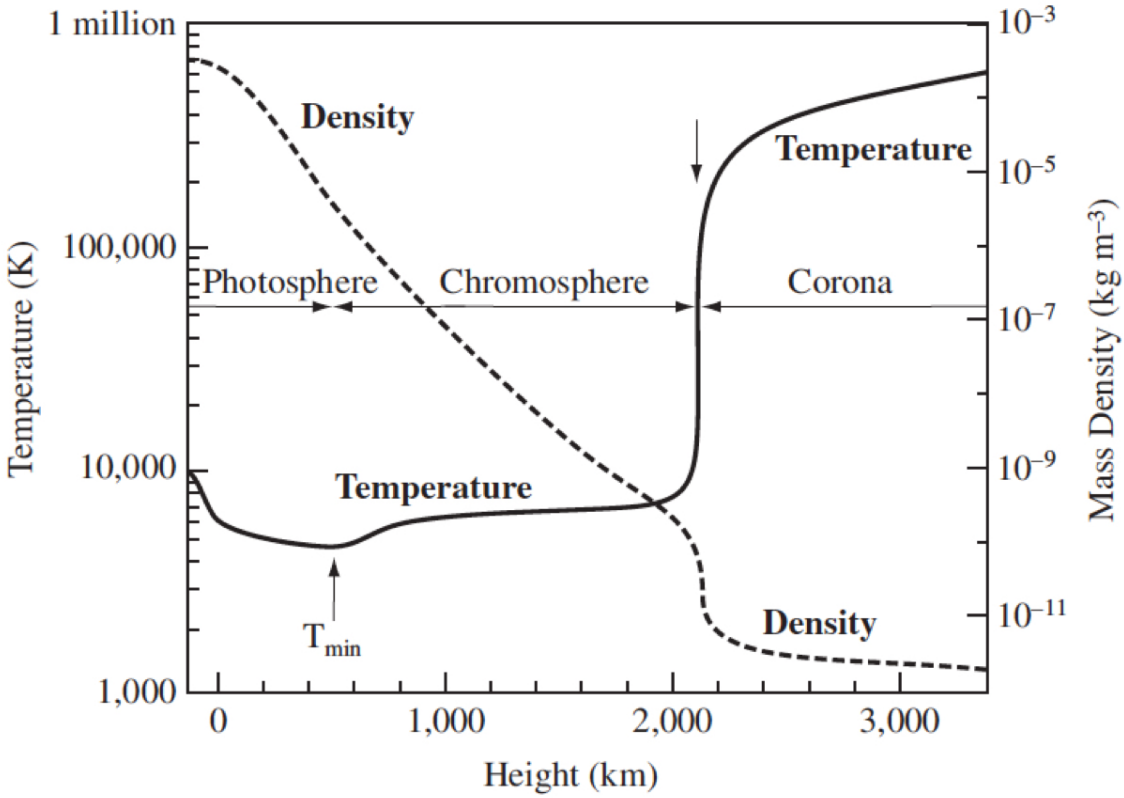

Figure 1.2: Temperature (solid) and density (dashed) profiles with height from the solar surface (Image Credit: Priest (2014))

1.3.1 Photosphere

The photosphere is the "sphere of light" that can be directly observed from space. It is the base of the Sun's atmosphere, and it represents an interface between the solar interior and its outer atmosphere. The thickness of the photosphere is approximately 500 km (i.e. less than 0.1% of solar radius), and within this layer, all observable solar energy is released. The temperature decreases with the height from about 10000 K at the bottom of the photosphere to about 4400 K at the so-called temperature minimum (T_{min}, Figure 1.2).

Optical depth describes absorption when light passes through an absorbing medium (such as a planetary atmosphere or interstellar dust cloud). If the optical depth at that wavelength is below unity, the probability of a photon escaping the solar atmosphere is very high. In the photosphere, the optical depth, τ, at 500 nm is unity (τ_{500} =1). The photosphere is very opaque (i.e., optically thick in all wavelengths) due to the presence of negative H^- ions that are abundant under the existing favourable plasma conditions (the temperature of ∼5800 K and the density of 2×10^{-4} kg m^{-3}) in this region. While the photospheric radiation covers the entire visible range of the solar spectrum, it is best observed using several narrow spectral ranges associated with molecular bands such as G-band at 430 nm and Titanium-Oxide (TiO) band at 705.7 nm, as well as in the blue continuum at 470 nm.

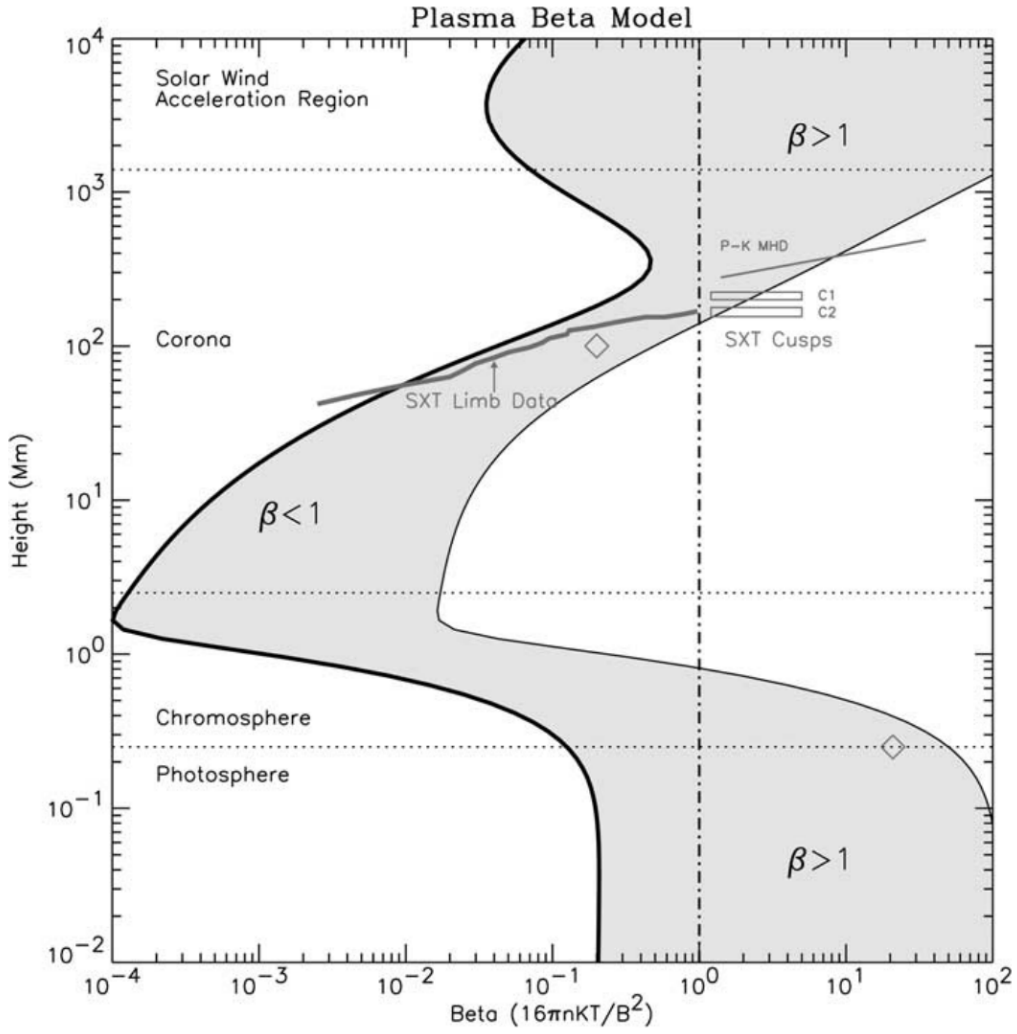

Figure 1.3: The plasma beta (β) model as a function of distance in the solar atmosphere above active regions, shaded for open and closed field lines originating between a sunspot of 2500 G and a plage region of 150 G. (Gary, 2001).

As shown in Figure 1.3, the gas pressure is significantly higher than the magnetic pressure in the photosphere ($\beta >> 1$). So, the flow of gas within the photosphere, specifically the granular flows, tends to push and displace the magnetic field lines. This displacement leads to the formation of an active network of magnetic flux along the intergranular lanes, which are commonly observed throughout the Sun (see review by van Driel-Gesztelyi and Green (2015)). This is primarily manifested as photospheric granulation (Figure 1.4). The granulation can generally be described as a dynamic field of convection cells where hot plasma arises from the convection zone in the centre of cells (granules), cools down and then sinks back at the edges of the cell, thus forming cooler (and darker) inter-granular lanes (network of dark lanes in Figure 1.4). Granules have a typical size of about 1.5 Mm (Nordlund et al., 2009), and the lifetime between 6 and 20 minutes (Bahng and Schwarzschild, 1961; Nordlund et al., 2009).

Sunspots are the visible outcome of the interaction between the concentrated solar magnetic fields and the solar plasma. Magnetic fields within the sunspot are strong enough to suppress the convective flow of plasma near the solar surface, reducing the heat flow to the region. The temperature of a sunspot ($\approx 4000\ K$) is lower than that of the surrounding photosphere ($\approx 5800\ K$). Therefore, they appear dark in the photosphere when toroidal flux ropes rise through the convective layer (see Section 1.2.1). A well-developed sunspot (see Figure 1.4) consists of two components. One is the darkest part of the sunspot, called the umbra, and the second one is the penumbra (the lighter part), which encircles the umbra. While the magnetic field is mostly vertical and strongest inside the umbra, it is weaker and nearly horizontal in the penumbral region. The magnetic field of a typical round sunspot may be roughly described as having a fan-like shape with its focal point positioned within the umbra. The other endpoints of the sunspot's magnetic field lines are usually rooted at both other sunspots and spotless areas of intense magnetic fields called faculae.

1.3.2 Chromosphere

The chromosphere is the next atmospheric layer which begins at the height of approximately 500 km, which corresponds to the "temperature minimum" layer (see Figure 1.2). The upper bound of the chromosphere represents a rugged surface formed by a multitude of spicules and jets shooting up into the corona. The temperature of the chromosphere increases with height from 4400 K to $\approx 10^4$ K over the height span of nearly 2000 km, while its density decreases from

10^{15} cm^{-3} to 10^{-11} cm^{-3}.

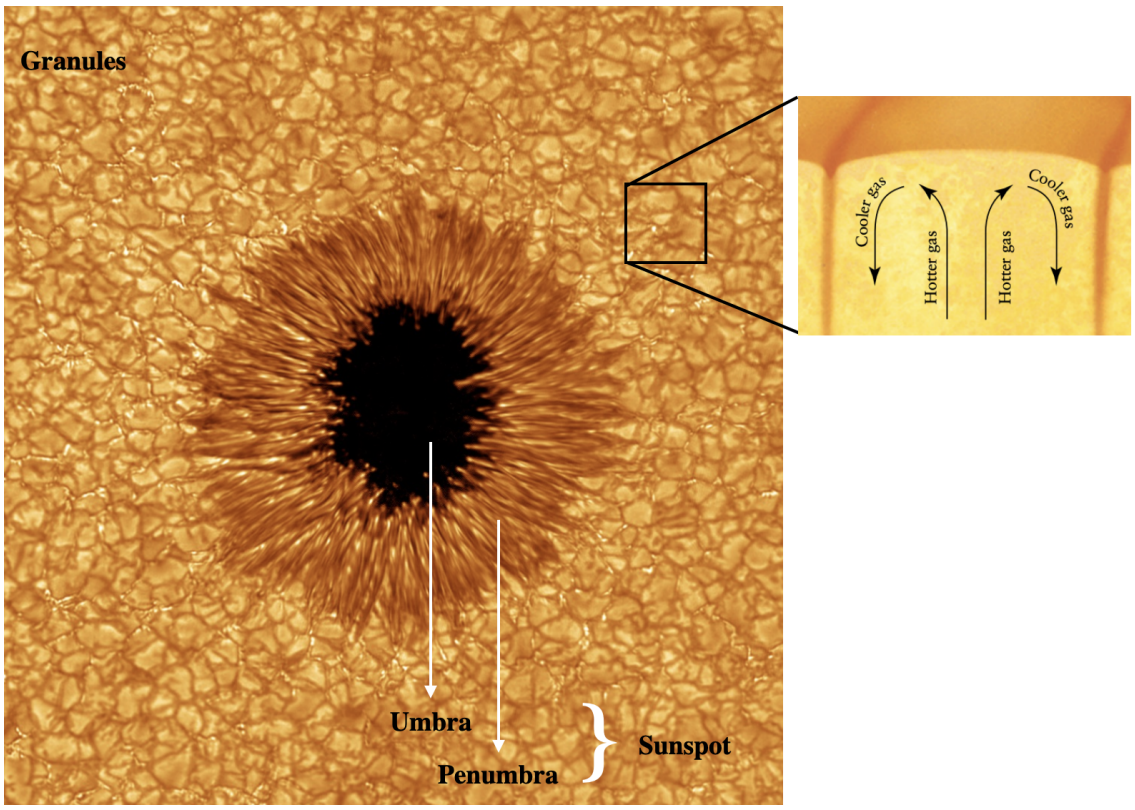

Figure 1.4: Left: Image of a well-developed sunspot of AR NOAA 1084 surrounded by the granulation field taken on July 2, 2010, with the Goode Solar Telescope using TiO (706 nm) broadband filter (Image Credit: Big Bear Solar Observatory). Right: Schematic representation of a photospheric granule Freedman and William III (2008)

As seen in Figure 1.3, plasma-β passes from being "$\beta >> 1$" (at the bottom) to being "$\beta << 1$" (at the top), which creates a distinct $\beta = 1$ region where important mode conversion processes occur. Additionally, high temperatures cause the chromosphere to be partially ionized and only partly transparent to radiation. Partial ionization introduces additional effects, such as ambipolar diffusion and the Stark effect, which modify the typical properties of waves and shocks observed in the plasma. Thus, the chromosphere is a somewhat difficult region to observe and study due to plasma-β variation, partial ionization, and radiative transfer effects, which significantly influence its physical characteristics and phenomena.

The off-disk chromosphere can be observed during a total solar eclipse (Figure 1.5), when the Moon blocks out the solar disk (up to the photosphere), revealing the reddish-pink glow of the chromosphere ("sphere of color"). Since hydrogen constitutes about a quarter of the Sun's mass, and is abundant in the chromosphere, the hydrogen Hα line at 656.3 nm, which is the first line of

the Balmer series, is one of the strongest absorption lines in the spectrum of the chromosphere. This wavelength corresponds to the red part of the spectrum, which explains the reddish-pink shade of the chromosphere seen during a total eclipse. While the chromosphere can be directly observed using a variety of spectral lines, the interpretation of data and modelling efforts face serious challenges due to the zoo of various dynamical events that the chromosphere hosts. Both gas pressure force and magnetic forces are important in the chromosphere, which makes it very rich in terms of physics.

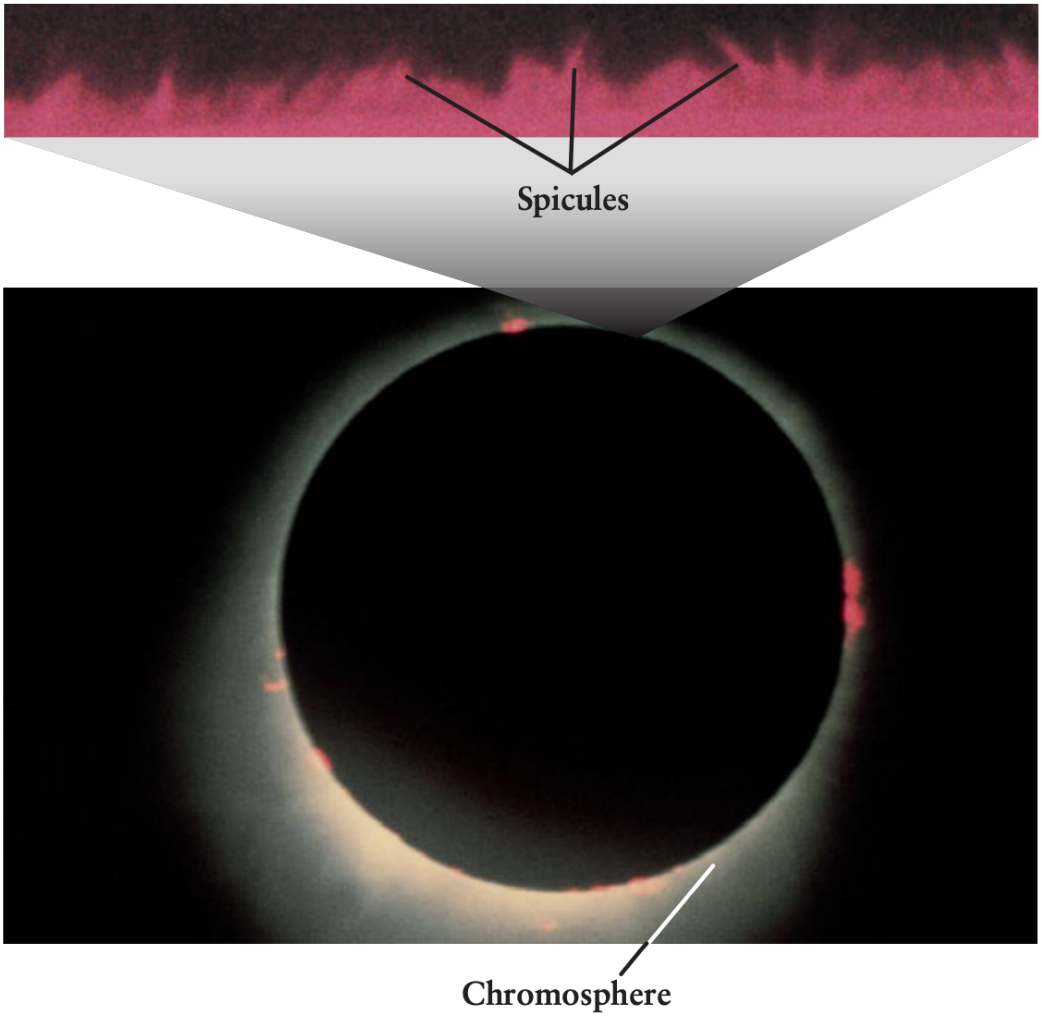

Figure 1.5: The Chromosphere during a total solar eclipse and the zoomed area above corresponds to the spicules (Image Credit: Freedman and William III (2008))

The temperature, density, and magnetic field strength of chromospheric plasma situated in a dynamic magnetic environment covers a wide range, which creates favourable conditions for various phenomena to occur, including spicules, jets, and solar flares. Spicules, seen in Figure 1.5, are

thin, elongated, short-lived, cold, and dense structures that are observed almost everywhere in the chromosphere extending up to 15 Mm into the solar corona (Beckers, 1972; De Pontieu et al., 2004). They are often seen as dark features against the bright background of the chromosphere and are typically several thousand kilometres in length.

1.3.3 Transition Region

The transition region (TR), as the name suggests, is a thin layer between the hot corona and the much cooler chromosphere. The temperature in this region dramatically increases from approximately $10^4 - 10^6$ K (Stix, 2002). The TR is also characterized by a high degree of ionization, with a significant portion of hydrogen and helium being in a state of ions due to the intense UV and X-ray emission and low plasma density. As the density decreases with height, heating events will have an easier time heating the plasma, so the heating per unit mass increases with height. This effect is particularly pronounced if the magnetic field strength does not decrease rapidly. Dissipative events (whose nature is still unclear) increase the heating, which strips more and more of the plasma of electrons until it becomes fully ionised, and any additional heating unavoidably increases its temperature. This interplay of diminishing electron density and increasing temperature explains the narrowness of the TR.

The TR is studied using spectroscopic and imaging data collected by space-based telescopes such as Solar Ultraviolet Measurements of Emitted Radiation (SUMER; Wilhelm et al., 1995; Lemaire et al., 1997) onboard the Solar and Heliospheric Observatory (SOHO) and the Interface Region Imaging Spectrograph (IRIS; De Pontieu et al., 2014) and the Solar Dynamics Observatory (SDO; Pesnell et al., 2012) (see Section 2.1 for more detail), which operate within the ultraviolet (UV) range. All these observations show that the TR is also dynamic and inhomogeneous, similar to the Chromosphere.

1.3.4 Corona

The corona is the outermost layer of the solar atmosphere composed of hot (10^6-10^7 K), tenuous (10^6-$10^9 \mathrm{cm}^{-3}$), and highly ionized plasma, where up to 15 electrons may be stripped off heavier atoms (Priest, 2014). The corona (as in the case of the chromosphere) is invisible to the naked eye since it is much fainter than the solar disk. It may, however, be observed during a total solar

eclipse when it reveals itself in all its complexity and beauty. Some of the most prominent coronal emission lines are located in the UV region of the solar spectrum and result from transitions of ionised elements and, in particular, metals.

Magnetic fields permeate the coronal plasma. Here the plasma-β is lower than unity ($\beta < 1$) (see Figure 1.3), indicating the magnetic pressure is greater than the thermal pressure of the plasma. Moreover, because of the high electrical conductivity, low plasma density and large spatial scales, coronal plasma is said to be "frozen" into the magnetic field, a condition that allows the plasma to move only along the field lines while the displacement of plasma across the field is prohibited on average. These effects result in the magnetic fields shaping coronal plasma and forming plasma structures, such as loops, coronal holes, X-ray bright points, prominences, and coronal rain. Since it is very difficult to directly measure coronal magnetic fields with a high spatial resolution (Tomczyk et al., 2008), the measurements of these magnetic fields can be studied by interpreting various plasma structures that magnetic fields generate. Recently, Landi et al. (2020) developed the technique known as the magnetically induced transitions (MIT) to measure coronal magnetic field using Hinode/EIS observations and found that the magnetic field strength evolves in non-flaring active regions over time, with values between a few tens to a few hundred of Gauss. They also produced, for the first time, two-dimensional magnetic maps for several active regions, including both on-disk and off-limb. The topology of the local magnetic field can vary, with some regions being magnetically closed, when the magnetic field lines originate and terminate at the solar surface (e.g., coronal loops) and other areas being magnetically open with magnetic field lines extending into the interplanetary space (e.g., coronal holes). It is thought that the energy for the hot corona is sourced from the convective motions of the solar photosphere, and the magnetic field plays an essential role in maintaining this extremely high temperature in the hot corona. However, how the energy is converted into heat, transported and dissipated is still not fully understood. So, this introduces the coronal heating problem. A detailed description of the coronal heating problem and its proposed mechanisms are given in the next section (Section 1.4).

Small-scale emerging flux regions have the potential to act as a contributing factor in what is known as the mass and energy cycle in the solar atmosphere (McIntosh et al., 2012). Since coronal plasma is not stationary, some plasma parcels are descending down toward the chromosphere, and they are being constantly replenished by new plasma injected from the lower layer of the solar

atmosphere. Coronal rain, representing patches of plasma falling down along magnetic field lines, is an example of such dynamic coronal flows. Since it allows us to trace the associated magnetic field, coronal rain studies offer yet another way to infer the coronal field structure and also the field strength through spectropolarimetry. See Section 1.5.4 for a comprehensive discussion about coronal rain and magnetic field.

Observations of the solar corona are mostly divided into two parts: quiet Sun regions (QSs) and active regions (ARs). These regions refer to regions of the Sun with different levels of magnetic activity. ARs are regions with high magnetic activity (containing structures and events such as sunspots, solar flares, coronal loops, and prominences) (see bright regions in Figure 1.6). QS (magnetic bright spots, coronal holes, etc.) are the regions which have a weak magnetic field (see remaining regions in Figure 1.6) (Gibson, 1973). On the other side, QS is also filled with loops, but they are much more diffuse, therefore, they cannot be distinguished against the background. Both active and quiet regions play important roles in the dynamics of the solar atmosphere and can impact the Earth and the rest of the Solar System through their effects on space weather.

1.4 Coronal Heating

The solar corona is multi-million degrees hotter than its underlying surface. However, the reason for that excess of temperature remains an unresolved problem known as the coronal heating problem. It has been a central problem in solar physics for decades (see e.g., Grotrian, 1934; Zirker, 1993; Klimchuk, 2006, and reference therein). While the solar community seems to agree that the energy to heat the corona is supplied by the magnetic field, it is debatable how the energy is released and transported. To fully understand the perplexity of the coronal heating problem, it is essential to have a good understanding of the second law of thermodynamics. According to this law, heat naturally flows from hotter regions to cooler regions, and this process can never be reversed entirely without the input of external energy. Therefore, energy cannot be transferred by conduction from the cooler photosphere ($\approx$5800 K) to the TR and the corona ($\approx$1-2 MK). This means that other mechanisms must be at work in order to heat and maintain the observed coronal temperatures.

There are two plausible mechanisms for coronal heating which can roughly be distinguished by the time scale of photospheric driving and Alfvén wave time (τ_A): alternating current (AC) and direct

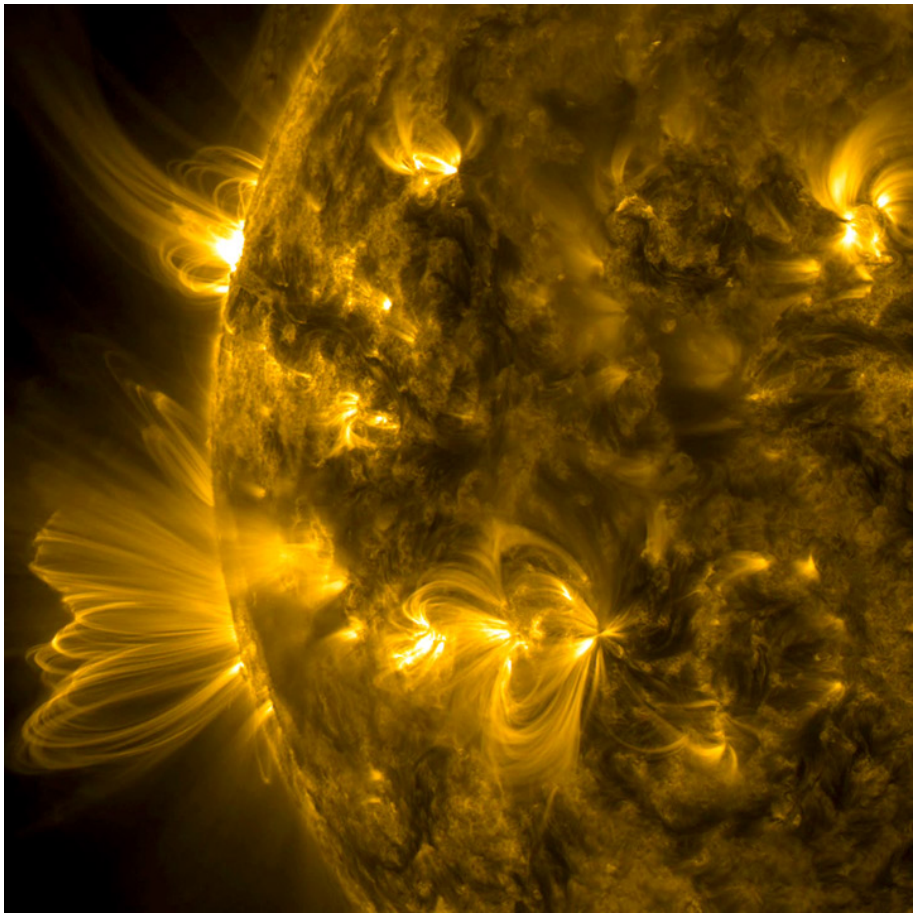

Figure 1.6: An image of the solar corona with coronal loop structures captured by the Atmospheric Imaging Assembly (AIA) at 171Å at the edge of the Sun on the 14th-15th October 2017 (Image Credit: Solar Dynamics Observatory/NASA)

current (DC), referring to waves and magnetic reconnection heating, respectively. The Alfvén time refers to the characteristic timescale associated with Alfvén waves. It represents the time it takes for an Alfvén wave to traverse a given distance or propagate through a medium. It is defined as follows, where L is a typical loop length and v_A is Alfvén speed:

$$\tau_A = \frac{L}{v_A} \tag{1.2}$$

The AC model suggests that the dynamics of the photospheric movements are characterized by timescales lower than the Alfvén time, and energy realises and propagates in the forms of MHD wave. Conversely, in the DC model, the timescale of photospheric movements is greater than the Alfvén time. These movements result in the braiding or twisting of the coronal magnetic field lines and bring in the hot plasma that could be released during magnetic reconnection.

According to the AC heating mechanism, in addition to Alfvén waves (Alfvén, 1947), there are two other types of waves that involve the magnetic field that can propagate in the solar atmosphere, which are known as fast and slow magnetosonic wave modes. The Alfvén waves are characterized by the perturbation of only magnetic field lines with magnetic tension as the only restoring force and propagate along the magnetic field lines. In contrast, the fast and slow magnetosonic wave modes correspond to the combination of sound waves and the magnetic field. Their restoring forces are a combination of magnetic and gas pressures and can propagate across the magnetic field lines. Magnetosonic wave modes exhibit wave speeds that are influenced by both the direction of propagation and the properties of the surrounding gas. However, due to significant pressure and density gradients in the region between the chromosphere and the corona, these waves undergo reflection when encountering the TR. Therefore, the ability of magnetosonic waves to transport energy from the photosphere to the corona is limited. In contrast, Alfvén waves possess greater resilience and are advantageous in that they can traverse the TR unhindered. However, this resilience poses a challenge in converting the wave energy into heat once it reaches the coronal region. In order to achieve efficient AC heating, it becomes necessary to enhance wave dissipation and promote the conversion of wave energy into thermal energy. Alfvénic turbulence, shear flow instabilities and generalised phase mixing are a few of the mechanisms proposed for wave dissipation in the corona. See review by Van Doorsselaere et al. (2020) for more detail on wave heating.

The DC heating mechanism, on the other hand, suggests the dissipation of magnetic energy by processes such as magnetic reconnection (Sturrock and Uchida, 1981) and viscous turbulence (van Ballegooijen, 1986). Most DC mechanisms rely on magnetic field braiding (Peter et al., 2004), in which the nearby magnetic field lines in the corona become intertwined and twisted due to displacement. It increases the free magnetic energy, which is then released through reconnection in the corona. The magnetic field in the solar corona is rooted in the photosphere, where the dominant convection processes exert a significant influence. So, the magnetic field lines at the surface are subject to displacement due to the stochastic motion of their footpoints. Consequently, gradients in the magnetic field are formed, generating electric currents (Galsgaard and Nordlund, 1996). When a critical shear is reached, the current sheets become thin, thus allowing the field lines to reconnect, releasing energy (an average of 10^{17} J or lower) (nano-flare) that effectively heats the corona (Parker, 1972, 1988). Moreover, Parker (1991) proposed a model in which 20%

of the energy released by reconnection events in the solar corona may be in the form of Alfvén waves.

1.5 Heating and Cooling in the Solar Corona

Solar corona has many unsolved questions, and the most important one is, as mentioned in the previous section, how it is heated. Coronal loops and solar flares are considered key elements in the transfer of energy and matter throughout the solar atmosphere. However, the corona hosts not only hot structures but also cool and dense structures. For instance, prominences have been known for hundreds of years (Secchi, 1875). Another example of cool and dense material in the solar corona is coronal rain, which has been observed since the 1970s (Kawaguchi, 1970; Leroy, 1972).

This section provides a detailed description of coronal heating and cooling events in the upper solar atmosphere, linking the properties of heating to cooling. By providing a comprehensive overview of the characteristics, dynamics, and formation mechanisms of these solar events, this section lays the groundwork for the remaining part of the thesis, which focuses on investigating coronal rain and its role in the heating and dynamics of the upper solar atmosphere.

1.5.1 Coronal Loops

Figure 1.6 shows the solar corona as captured by SDO. The bright EUV regions seen in the image are active regions (ARs) which can be defined as areas on the sun that include one or more sunspots. ARs host bright, arch-like structures known as coronal loops (Reale, 2014), thought to be hot and dense plasma confined by magnetic flux tubes anchored in regions with opposite magnetic polarity (such as sunspot pairs or plage regions). They are the building blocks of the inner solar corona and allow us to investigate coronal magnetism, dynamics, and the coronal heating mechanism. They are observed in extreme UV (EUV) and soft X-ray (SXR) spectral range (Peres et al., 2000). Plasma temperature in coronal loops ranges from 0.1 to 10 MK (Aschwanden and Boerner, 2011; Peter et al., 2013; Gupta et al., 2019) depending on the region in which they are rooted. Loops with temperatures below 1 MK are generally referred to as cool loops, which were first detected in UV lines by Foukal (1976). Temperatures of around 1-2 MK indicate warm loops that are well observed in EUV (Del Zanna, 2003), while hot loops display temperatures above 2

MK, and they comprise most of the structures visible in X-ray images (e.g., Nagata et al., 2003). It is important to note that this classification does not aim to distinguish between different structures but rather represents different stages in the evolution of the structures. For instance, a coronal loop can exhibit varying temperatures, ranging from hot to warm and cool, at different stages of its lifetime, depending on the frequency of the heating events. Typically, coronal loops can be seen simultaneously in several spectral lines, which allows us to study their multi-thermal structure. This critical data allows us, in turn, to make progress in understanding the underlying heating mechanism. Regarding the loops' morphology, their lengths and widths cover a vast range from a fraction of a few hundred km to several hundred Mm (Aschwanden and Boerner, 2011; Peter et al., 2013).

The high spatial resolution of the collected data plays a vital role in advancing our understanding of the solar corona. Observational studies using current solar instrumentation showed that some coronal loops (not all!) are composed of finer loops made of several individual strands. High-Resolution Coronal Imager (Hi-C, Rachmeler et al., 2019), data acquired with cadence ≈4 s and a pixel size of $0''.129$, has provided evidence of width of coronal strands being as thin as 200 km (Brooks et al., 2013; Williams et al., 2020). Observations of coronal rain obtained by CRisp Imaging SpectroPolarimeter (CRISP, Scharmer et al., 2008) with a very high spatial resolution (see Section 1.5.4 for details) also showed that the width of coronal strands is of a few hundred km (Antolin and Rouppe van der Voort, 2012).

The duration and characteristic timescales of the three distinct phases of the loop emission (rise, steady, and decay) are much longer than the cooling time (so-called radiative cooling time) for a loop. As shown in Figure 1.7, this suggests that the heating rate of the loop can increase gradually, reach a constant level, and then decrease gradually (López Fuentes et al., 2007). The radiative cooling time, τ_{rad}, can be estimated following Equation (Antiochos, 1980):

$$\tau_{rad} = \frac{(3/2)p}{n^2\Lambda} \approx 300(\frac{10^9}{n})(\frac{T}{10^6})s \tag{1.3}$$

Here, p represents the pressure. The number of electron density, n, is taken 10^9 cm^{-3} for the quiescent loops, and the optically thin loss function is approximated as $\Lambda = 10^{-21.31}$ for that temperature. For flaring loops ($n = 3\times10^{10}$ cm^{-3}), the radiative cooling time is then only 30 s.

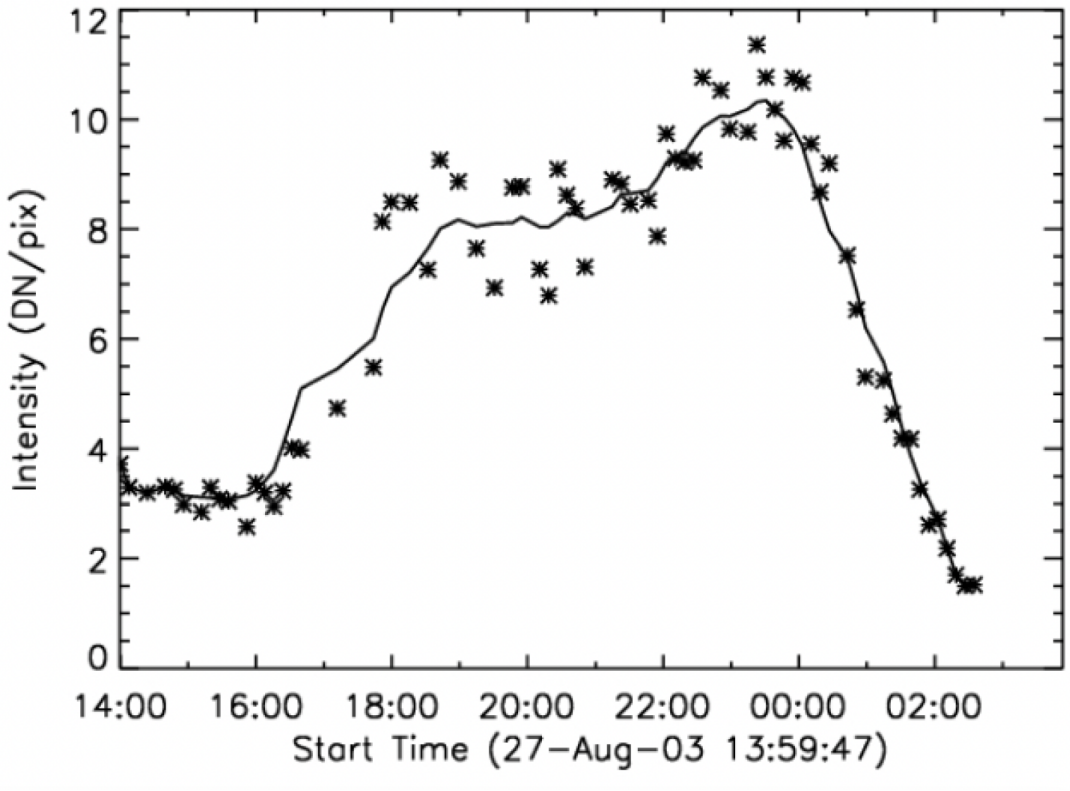

Figure 1.7: The SXI telescope on board GOES observed three phases of emission, which suggests that the lifetime of the coronal loop is significantly longer than the characteristic cooling times (Image Credit: Reale (2014)).

When a loop undergoes monolithic evolution, it experiences rapid heating followed by gradual cooling. A distinct characteristic of this process is the cooling that occurs through a specific passband. This passband corresponds to a narrow range of EUV wavelengths sensitive to the specific ion dominating the passband. Consequently, the loop only appears in the EUV passband for a brief period relative to its overall lifetime, which is determined by the time it spends around the temperature of maximum formation for that particular ion. This cooling through a passband phenomenon significantly influences the observed dynamics and temporal behaviour of coronal loops and can be incorrectly interpreted as heating.

There is also an ongoing debate about the apparent lack of expansion of loop structure as observed in soft Xray, EUV, and visible light wavelengths (Klimchuk, 2000; Watko and Klimchuk, 2000; López Fuentes et al., 2008; Klimchuk and DeForest, 2020, and reference therein). Due to the strong decrease of density with height, the magnetic field originating in the photosphere must diverge with height to fill the available volume in the force-free environment of the corona.

Since coronal loops are confined by the magnetic field lines, it is also expected that the majority of coronal loops should also diverge with height, where they appear wider at their apex than their footpoints. However, the observed loop structures give the impression that they have a uniform thickness throughout their length (Golub et al., 1990; Klimchuk, 2000). In the MHD simulation study by Peter et al. (2012), it was found that non-trivial density and temperature distribution throughout the cycle leads to the appearance of uniform thickness. It is difficult to clearly identify a coronal loop through observation due to the optically thin nature of the solar corona that leads to strong line-of-sight (LOS) superposition. There is also a possibility that the current understanding of coronal loops is not well defined due to ambiguous descriptions of what represents a coherent structure, particularly when considering its thermodynamic evolution and expected continuous changes in connectivity at chromospheric and photospheric levels, as suggested from numerical simulations (Gudiksen and Nordlund, 2005; Malanushenko et al., 2022). This is most clearly shown through 3D MHD simulations of the "coronal veil" concept introduced by Malanushenko et al. (2022). They proposed that some bundles of coronal loops are optical illusions in EUV passbands due to the overlap of the coronal emission along a given LOS, leading to a misleading loop-like structure. However, several phenomena indicate that loop structures defined as coherently evolving thermodynamic structures do exist. For example, the fact that transverse MHD waves are observed everywhere directly indicates that the structures that host the waves are coherent and not an artefact of LOS superposition. Also, the phenomenon of long-period intensity pulsations (explained in Section 1.5.2) observed within loops is proof of the coherent evolution of some coronal loops on a global scale.

1.5.2 Long-period EUV intensity pulsations

Periodic intensity variations have been extensively studied for several decades. These periodic variations occur everywhere in the corona, and their periods range from a few seconds (short-period) to several hours (long-period). Auchère et al. (2014) discovered the long-period EUV intensity pulsations, which are the periodic fluctuations in the intensity of the EUV radiation emitted by coronal loops. In that study, they used Extreme ultraviolet Imaging Telescope (EIT; Delaboudinière et al., 1995) observations on board the Solar and Heliospheric Observatory (SOHO; Domingo et al., 1995) throughout more than a solar cycle from January 1997 to July 2010. Later on, Froment et al. (2015) and Froment (2016) used six coronal EUV channels (94, 131, 171, 193,

211, and 335 Å) of SDO/AIA to confirm the existence of the widespread pulsations reported by Auchère et al. (2014) in the corona, as shown in Figure 1.8. In those studies, the periods of detected pulsations range from 2 to 16 hours, and 50% of them are associated with loop-like structures. Froment et al. (2020) also conducted a thermal analysis and found these pulsations in the corona can be attributed to repetitive heating and cooling cycles. They also observed a cooling trend from temperatures exceeding several million K to below 1 MK during the AIA channels. Significantly, their findings reveal that the temperature variations precede the density increase in each pulsation, typically by approximately 100 minutes. This aspect is also evident in the evolution of the DEM slope. Then, thermal non-equilibrium (TNE), which will be discussed in detail in Section 1.18, was first proposed by detecting long-period intensity pulsations (Auchère et al., 2014; Froment et al., 2015, 2020) in the EUV emission of specific coronal loops, where the quasi-steady heating (i.e. high-frequency repetition time of the heating events relative to the radiative cooling time) is localized close to its footpoints.

Auchère et al. (2016) critically assessed the discovery of these long-period EUV pulsations using Fourier and wavelets analysis, including a proper noise model, global confidence levels, and ensuring that no source of artefacts, such as prefiltering of the data, were present. The study demonstrated high confidence in the detection of these pulsations (see Section 2.2.5). They also showed that the Fourier spectrum does not correspond to the periodicity obtained by a wave phenomenon but by a pulsation (i.e. a mechanism that is repeating itself).

Moreover, the importance of coronal rain has also been emphasized in studies of long-term EUV intensity pulsations in coronal loops with a detailed analysis of the thermal structure of three events detected by AIA channels (Froment et al., 2015, 2017). Froment et al. (2015) used the method of Guennou et al. (2012, 2013) for the DEM analysis and the method of Viall and Klimchuk (2012) for the time delays between the AIA bands. They concluded that these events are caused by TNE. Then, Froment et al. (2017) performed 1D hydrodynamic simulations, and they show that the density profiles observed by AIA are well reproduced by TNE, thus strengthening the interpretation that the long-period density pulsations are the result of TNE.

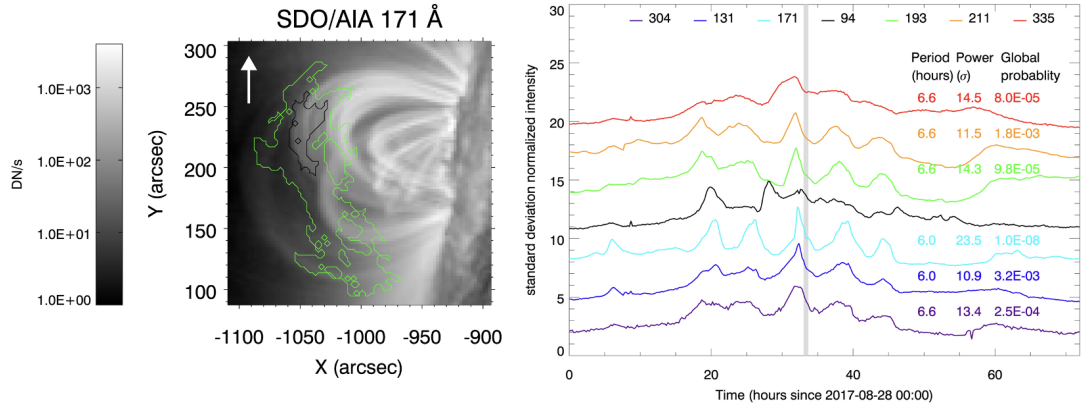

Figure 1.8: Left: The AIA 171 Å images on 29 August 2017, with the contour of detected long-period intensity pulsation regions. Different contour colours represent the regions with normalised power above 5σ (green) and 10σ (black). Right: The average intensity evolution over the black contour shown in the left panel over 3 days in seven AIA channels. Obtained period, Fourier power and the probability occurrence are given in the legend for each channel. (Adapted from Froment et al. (2020)).

1.5.3 Solar filaments and prominences

Solar filaments and prominences are magnetic arcade-like structures of cool and dense plasma that appear to be suspended at chromospheric and coronal heights in the hot and tenuous solar corona (see reviews by Labrosse et al., 2010; Mackay et al., 2010). These long dark slabs are called filaments when seen against the solar disk, and they are called prominences when observed near the edge of the sun as protruding features of various shapes and sizes. Temperature of solar prominences are around $10^3 - 10^4$ K and an electron density is $10^9 - 10^{11}$ cm^{-3} (Vial and Engvold, 2015). The plasma in the prominence is usually 100 times cooler and denser than the surrounding corona. They typically occur above polarity inversion lines (PIL) (Babcock and Babcock, 1955; McIntosh, 1972) within filament channels (Martin, 1998) where there is a strong shearing of the magnetic field (Antiochos and Klimchuk, 1991; Venkatakrishnan et al., 1989). They appear in the chromosphere as fibrils observed in the Hα line that aligns with the PIL (Tandberg-Hanssen, 1995; Martin, 1998) Prominences are typically divided into two types as shown in Figure 1.9a,b: quiescent and active (Zirin, 1988; Tang, 1987; Martin, 1998). Quiescent prominences are relatively stable features, mostly above the solar limb. Their lifetime varies from a few days to several months, equivalent to several solar rotations. They are approximately $10^4 - 10^5$ km in length and $10^3 - 10^4$ km in width, with a height range of $10^4 - 10^5$ km (Wang et al., 1998). Active

prominences are dynamic features that often appear near active regions and have a short lifetime. They are usually not as high up as quiescent prominences. In quiescent prominences, the plasma is much more turbulent and often oriented vertically. Magnetic bubbles, plumes and vortices are often observed, strongly suggesting Rayleigh–Taylor instability (RTI) and Kelvin–Helmholtz instability (KHI) processes (Berger et al., 2010, 2017). Active region prominences, on the other hand, exhibit much more field-aligned flows of plasma, so they are more filamentary, and the flows are much faster in general (reaching 200 km s^{-1}) (Arregui et al., 2018). These differences are explained by the difference in the plasma beta, being closer to 1 for the quiescent prominences (due to the lower field strengths) and much lower than 1 for active region prominences.

Prominence observations indicate that these structures are composed of dense, cool material from the chromosphere, which is immersed into the surrounding hot corona with a temperature of 1 MK. The region where these two environments meet is thought to be very thin and is referred to as the Prominence-Corona-Transition Region (PCTR).

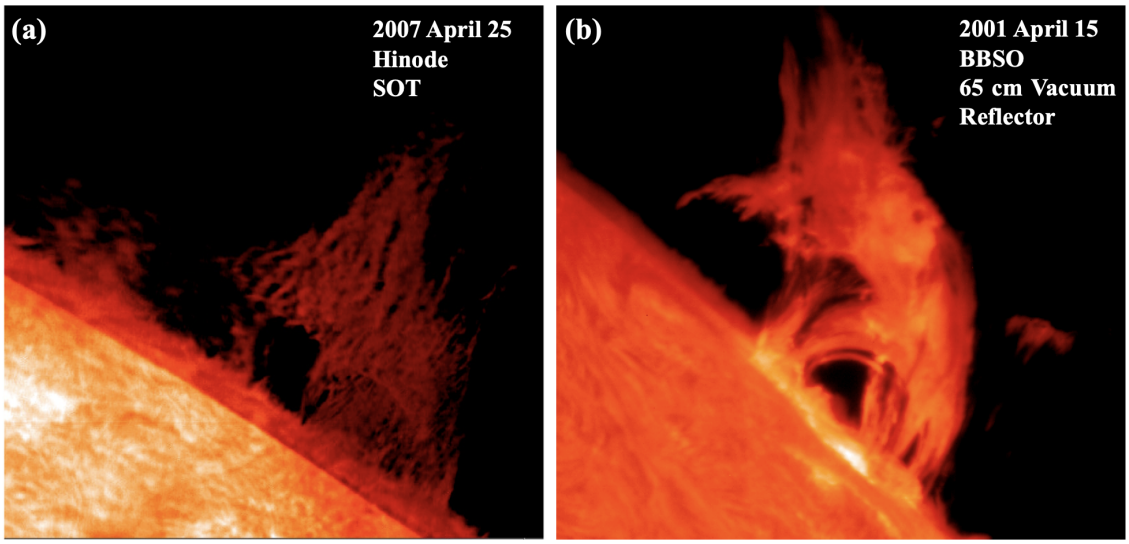

Figure 1.9: a)A quiescent solar prominence above the limb taken by Hinode Solar Optical Telescope (SOT) in NFI filter (Heinzel et al., 2008), b)An active solar prominence above the limb taken by BBSO 65 Vacuum Reflector in H-α (Image Credit: Big Bear Solar Observatory with private communication).

The prevailing understanding suggests that thermal instability (TI; see Section 1.18) plays a significant role in prominence formation, as proposed by Parker (1953). Furthermore, the presence of a favourable magnetic topology capable of supporting the plasma within the corona, such as long and predominantly horizontal magnetic fields or dipped fields, has been considered essential

for prominence formation, as highlighted by Vial and Engvold (2015). However, the discovery of TNE (see Section 1.18) (Karpen et al., 2001) has provided new insights into prominence formation. TNE, characterized by an evaporation-condensation cycle, has been proposed as a potential model for prominences, potentially aided by magnetic dips, and observational evidence exists supporting this type of prominence formation (Liu et al., 2012).

1.5.4 Coronal Rain

Coronal rain, the main subject of this dissertation, is a spectacular phenomenon observed in the solar atmosphere, where large amounts of cool (10^3 – 10^5 K) and dense ($\approx$ 10^{10} - 10^{12} cm^{-3}) material falls towards the solar surface along the magnetic field lines due to the solar gravity and other forces. The most optimal observation of coronal rain occurs at the solar limb (i.e. off-limb), displaying strong contrast against the dark background. This phenomenon becomes visible in chromospheric lines (Hα (Kawaguchi, 1970), Ca II K & H and He I 10830Å triplet (De Groof et al., 2004; Schad, 2018)), and also in transition region lines (Si IV 1402 Å or/and in He II 304 Å (Vashalomidze et al., 2015; Antolin et al., 2015)).

Coronal rain has been the subject of solar physics since the 1970s (Leroy, 1972; Kawaguchi, 1970); however, it has only been significantly studied in the last decade because it was considered to be simply downflows from prominence structures. Its significance is becoming apparent with the advent of high-resolution observations from Hinode, Solar Swedish Telescope (SST; Scharmer et al., 2003), and Interface Region Imaging Spectrograph (IRIS; De Pontieu et al., 2014). While the local formation process of prominences is related to coronal rain, they differ significantly in terms of morphology, kinematics, and magnetic field topology. These differences have led to the emergence of coronal rain as a significant research field in solar physics (Antolin and Rouppe van der Voort, 2012; Antolin, 2020).

Coronal rain forms relatively quickly, typically within minutes; however, it falls toward the solar surface over an order of magnitude longer timescales (Antolin and Rouppe van der Voort, 2012). Figure 1.10a shows a 3D sketch of a cross-section of a coronal loop with coronal rain clumps. The core of rain clumps is surrounded by thin, warmer TR temperatures, which are also surrounded by coronal plasma. This is called the Corona Condensation Transition Region (CCTR) (Antolin, 2020), similar to the PCTR for prominences. This unique arrangement highlights the clumpy

nature of coronal rain that is most noticeable in chromospheric wavelengths, as mentioned above. The loop intensity in the chromospheric and TR region along the LOS is given on panel b in the same figure.

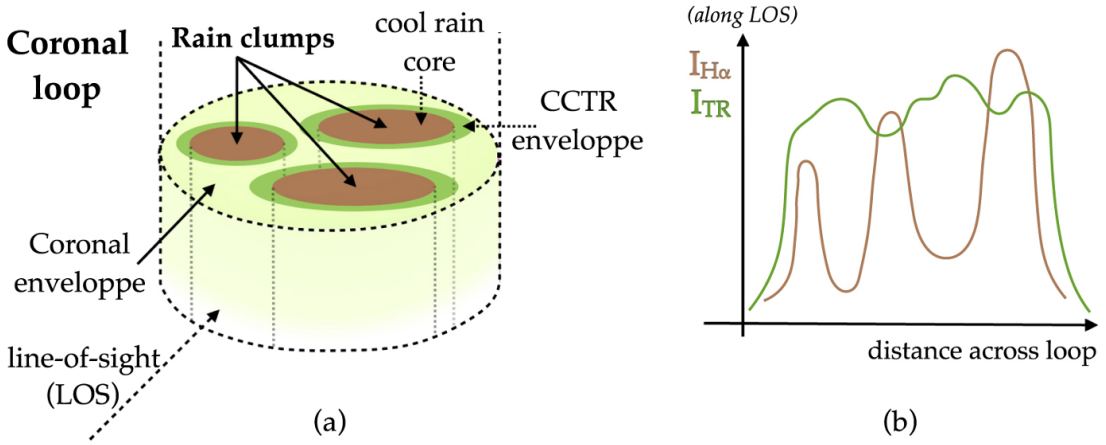

Figure 1.10: A cross-section of a coronal loop with rain clumps. Cool cores are surrounded by a relatively thinner but highly emissive transition region, referred to as the CCTR (Condensation-Corona Transition Region), which connects the chromospheric region to the outer coronal envelope that forms the loop. a) A line of sight (LOS) that is transverse to the loop under consideration. b) Estimated intensities of emerging radiation in a chromospheric and a transition region line (Antolin, 2020)

There are three distinct types of coronal rain observed within the solar atmosphere (Antolin and Froment, 2022). These are:

- quiescent coronal rain
- flare-driven coronal rain
- hybrid-prominence coronal rain

In Figure 1.11, these three coronal rain forms are presented. Quiescent coronal rain is the most common form of coronal rain associated with AR coronal loops. Flare-driven coronal rain is observed during the gradual phase of a solar flare (Bruzek, 1964; Foukal, 1978; Hara et al., 2006; Scullion et al., 2016). Hybrid prominence/coronal rain is observed in the magnetic configuration within the magnetic dips and magnetic null point topologies (Liu et al., 2016; Li et al., 2018; Chen et al., 2022). This type seems to be composed of two parts: an upper body that resembles quiescent prominences in terms of dynamics, morphology and duration and a lower arcade that hosts coronal rain-type downflows; therefore, they are called “hybrid prominence/coronal rain”

(Liu et al., 2016).

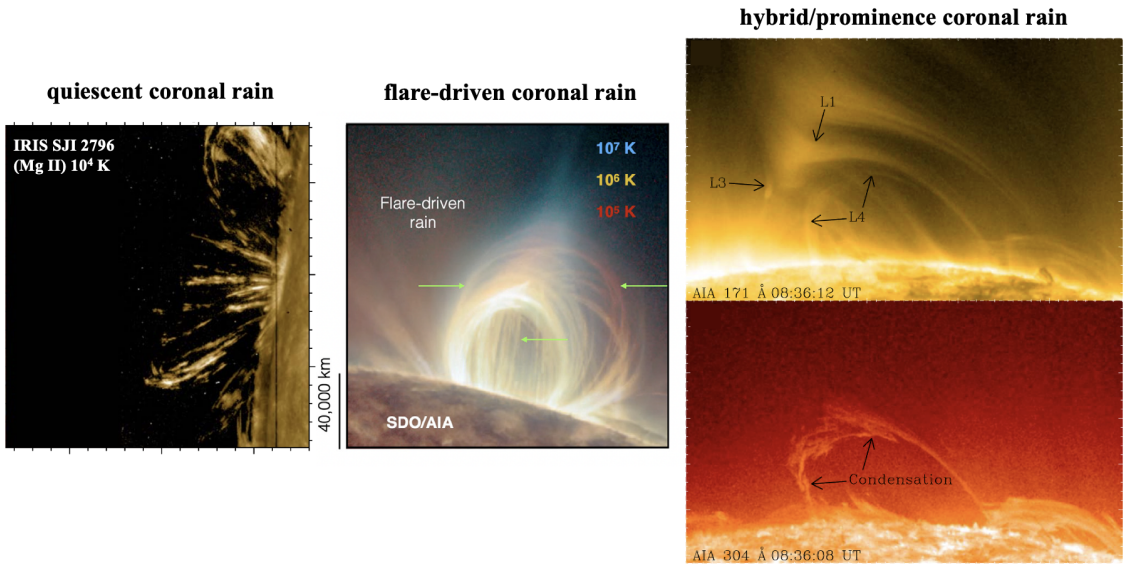

Figure 1.11: Three types of coronal rain: quiescent coronal rain (left), flare-driven coronal rain (middle), and hybrid-prominences coronal rain (right) (These figures are adapted from Antolin (2020), Antolin and Froment (2022), and Li et al. (2018), respectively,)

The observed properties of coronal rain mainly pertain to the quiescent coronal rain category. However, the exact differences between these types of coronal rain are unknown in terms of morphology and kinematics. Coronal rain quantity appears to have a significant association with the intensity and duration of flares (Mason et al., 2019). While there is not yet enough statistical data to fully understand flare-driven coronal rain, early research by Foukal (1978) and Tandberg-Hanssen (1995) suggests a strong connection between flare-driven coronal rain and flare evolution (see Section 1.5.5). Observations suggest that the morphology and dynamics of flare-driven rain are similar to the quiescent coronal rain observed in Hα, with clumpy, multi-stranded structures and downward velocities on the order of 100 km s^{-1} (Jing et al., 2016; Scullion et al., 2016; Kuridze et al., 2019). Another similarity is the multi-thermal nature of the rain. However, there are also important differences, such as the increased density of coronal rain during large flares, which is estimated to be in the range of 10^{12} to 10^{13} cm^{-3}, as determined from the white light continuum caused by Paschen and Brackett recombination (Jejčič et al., 2018) or Thomson scattering (Martínez Oliveros et al., 2014). This is also supported by non-LTE inversions of Ca II 8542 and Hβ lines (Koza et al., 2019).

A common proposed physical mechanism for the formation of coronal rain (and also for promi-

nences) is the thermal instability (TI) (Antiochos et al., 1999) within a coronal loop that undergoes TNE. It is known as the TNE-TI scenario, which is described in detail in Section 1.5.6, (Antolin, 2020; Antolin and Froment, 2022).

The formation mechanism of hybrid-prominence coronal rain, on the other hand, seems to involve the interaction of higher-lying open structures (or very long loops) and lower-lying closed loops. The curved higher-lying structures move down towards the surface and reconnect with the lower-lying closed loops (1.12a), forming a magnetic dip in the former (Li et al., 2018). The newly reconnected closed loops and open structures appear and retract from the reconnection region (see purple stars in Figure 1.12b,c). The coronal plasma surrounding the magnetic dip of higher-lying open structures converges into the dip, enhancing plasma density in the dip. Eventually, the material catastrophically cools down through TI, forming condensations that further push downwards and force reconnection (Srivastava et al., 2019). The cool material can then form a prominence in the magnetic dip (see 1.12c) and also slip through the null point and down into the coronal arcade as coronal rain. The cool material then facilitates the reconnection process.

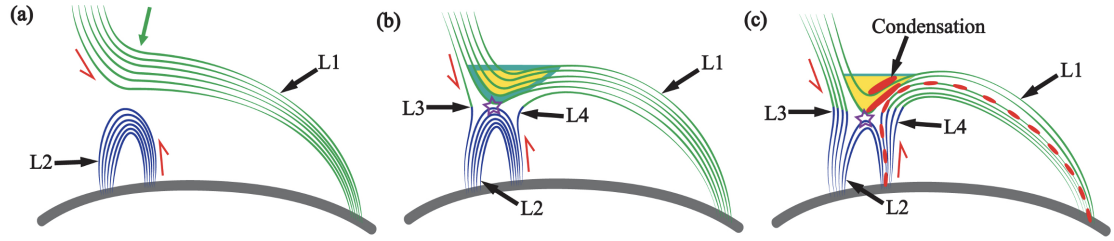

Figure 1.12: A sketch of the magnetic reconnection and coronal condensation. The thick grey curve indicates the solar limb. The magnetic field lines of loops L1, L2, L3, and L4 are represented by green, blue, and green-blue lines, with their directions indicated by red arrows. a) Green magnetic field lines (L1) create a dip where plasma accumulates and rapidly cools, leading to the formation of condensations. b,c) Magnetic reconnection (shown by purple stars) occurs between loops L1 and L2, allowing cooler material to fall down to L1 as coronal rain. Reconnection creates loops (L3 and L4) that may transport some condensed material. (This figure is adapted from Li et al. (2018))

1.5.4.1 Temperatures and Spectral Characteristics

Estimates of low temperatures have been derived from spectral line widths in Hα, Ca II H, and Ca II 8542 (Antolin and Rouppe van der Voort, 2012). These estimates indicate average temperatures ranging from 5000 K to 33000 K, with some minima reaching 2000 K or even lower (Antolin et al., 2015). Schrijver (2001) observed EUV variability, indicative of cooling associated

with coronal rain, using data from the Transition Region and Coronal Explorer (TRACE, Golub et al., 1999). The study reported time delays between the light curves of coronal channels and TR/chromospheric channels (see also the paper of Froment et al. (2020)). These findings provided compelling evidence of the cooling process occurring from coronal to chromospheric temperatures. However, coronal rain emits radiation in EUV, UV, and visible wavelengths despite the cooling, indicating the presence of multi-thermal and highly heterogeneous fine-scale structures. Continuous multi-thermal emission observed at high resolution indicates a more intricate structure surrounding individual coronal rain clumps. Specifically, each chromospheric clump is enveloped by CCTR (Antolin, 2020), as mentioned previously. This shell has a narrow width, as confirmed by the $0.''33$ resolution of IRIS, in agreement with 1D modelling by Xia et al. (2011). Moreover, the shell emitting in UV and EUV wavelengths is expected to exhibit a greater longitudinal extension (along the field) compared to the chromospheric emission, as supported by observational evidence (Ahn et al., 2014; Antolin et al., 2015; Vashalomidze et al., 2015). This is attributed to the pronounced compression exerted by the falling coronal rain downstream, particularly prior to its impact on the chromosphere, resulting in an increase in both density and temperature (Müller et al., 2003, 2004). The inhomogeneous nature of the rain results in the formation of highly localized high-density regions, as demonstrated in multi-dimensional simulations (Fang et al., 2015). As shown in Figure 1.13, the differential longitudinal velocity causes denser clumps to fall faster than lighter ones, giving rise to a distinctive V-shape structure in two dimensions, where the head of the clump is denser than the tail. Therefore, the UV and EUV emission is further extended along the path of the rain (Antolin, 2020).

Non-thermal broadening values reported averages between 6 and 12 km s^{-1}, with maximum values of 20 km s^{-1}. These values are crucial in studying coronal heating as they set limits for turbulence that could be dissipated into heat in thermally unstable coronal loops.

1.5.4.2 Morphology

Rain morphology is very dependent on wavelength and spatial resolution. For instance, observations in Hα with the SST instrument (with $\approx$ 100 km resolution) lead to an average width of 200-300 km (Antolin and Rouppe van der Voort, 2012; Froment et al., 2020). On the other hand, higher resolution observation of flare-driven rain with the GST (around 40 km) showed an average

width of 120 km, with a range of 70 to 250 km (Jing et al., 2016). Thus, the current structure may be a small portion of a larger distribution with more clumps visible at higher resolution (Scullion et al., 2014). This is also supported by 2.5D simulations conducted by Fang et al. (2013) and Li et al. (2022), in which the size of rain clumps is obtained between 50-100 km. Additional evidence can be seen in the observational study by Antolin et al. (2015) using the IRIS SJI 2796 passband at approximately 240 km resolution, dominated by the Mg II k line at similar formation temperatures to Hα. The width values in this observation show a significant increase, with 580 km on average, with minimum and maximum values of 300-900 km, respectively.

Lengths, on the other hand, distribute more widely, and their temperature dependence is unclear (Antolin and Rouppe van der Voort, 2012; Antolin et al., 2015). Although their average length is around 1000 and 3000 km, their tails can reach up to thousands of km (Antolin et al., 2015). This is due to factors like shear flows (Fang et al., 2015; Li et al., 2022) and regulated downward velocities (Oliver et al., 2014; Martínez-Gómez et al., 2020) that cause clumps to stretch out.

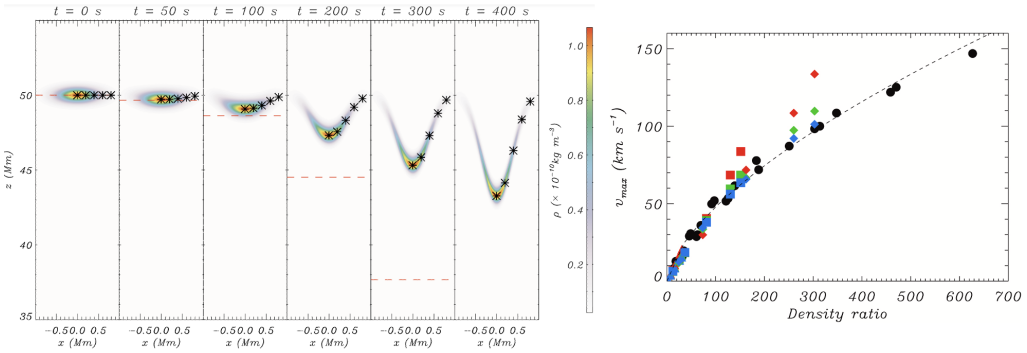

Figure 1.13: Left: Density variations over time as a clump falls due to gravity in a uniform atmosphere using a 2.5D MHD simulation. The dashed red line is the position corresponding to the free fall of rain. Right: The relationship between density ratio (blob density/reference density) and maximum falling speed of rain. Simulations with varying magnetic fields are indicated by different colours. (Image Credit: Martínez-Gómez et al. (2020).

1.5.4.3 Dynamics

Rain clumps velocities vary widely between $10 - 200$ km s^{-1} with 70 km s^{-1} on average (Schrijver, 2001; Müller et al., 2005; Antolin and Rouppe van der Voort, 2012). Additionally, the velocity distribution shows an extended tail, reaching higher speeds up to 200 km s^{-1} (Kleint et al., 2014; Schad et al., 2016).

Coronal rain does not fall towards the surface at the speed of free-fall or determined speed by

effective gravity, given the curved nature of coronal loops. TRACE and EIT have revealed that the downward accelerations are about a third of the solar gravity value (Schrijver, 2001; De Groof et al., 2004), and about half of what is expected based on the effective gravity along an elliptical loop (Antolin and Verwichte, 2011; Antolin and Rouppe van der Voort, 2012). On the other side, it is thought that gas pressure forces also play a major role, which leads to deceleration and even reversal of the direction of the rain (Antolin et al., 2015; Kohutova and Verwichte, 2017). Additionally, it is noted by Mackay and Galsgaard (2001) that the chromosphere operates as a piston that can effectively stop the downward motion of the rain, owing to downstream compression (Adrover-González et al., 2021). Oliver et al. (2014, 2016) have also conducted studies with a 1D simulation of fully and partially ionised plasma, and they found that the condensation formation produces a restructuring of the gas pressure downstream. This leads to constant downward velocities, in agreement with some observational studies (Antolin et al., 2010). It is important to mention that this gas pressure effect leads to a terminal speed dependence on density with an exponent of 0.64 (see Figure 1.13) for low beta environments (Martínez-Gómez et al., 2020). This relation is still not understood but may be the effect of drag or friction. The ponderomotive force generated by transverse MHD waves has been considered as another possible explanation. However, the observed wave amplitudes are typically insufficient to explain the dynamics of coronal rain Verwichte et al. (2017).

Furthermore, coronal rain observation shows that rain clumps not only move downward but also show upward motion and change in trajectories (Antolin et al., 2010). The numerical analysis, as demonstrated in the study by Li et al. (2022), supports the upward motion of coronal rain; however, no proper statistics on the upward motions existed prior to the work presented in this thesis.

1.5.4.4 Coronal Rain Shower

A notable feature of coronal rain is that it consists of clumps in groups. These rain clumps fall along a similar trajectory within the relatively large volume and at very similar times. For the first time, Antolin and Rouppe van der Voort (2012) (see Figure 1.14) introduced the notion of a rain shower to describe this attribute.

The shower behaviour has been partially explained by Fang et al. (2013, 2015) through their multi-dimensional simulations. The proposed underlying mechanism is known as “sympathetic cooling”

(see Figure 1.15). As shown in panel a in the same figure, coronal rain occurs first in a region consisting of magnetic field lines that are critically thermally stable. These lines are subjected to the same heating function but vary in length. Due to perturbations, TI will be triggered first in a given magnetic field line. In turn, this produces fast-mode perturbations that trigger TI in the neighbouring field lines. Those perturbations trigger TI in the neighbouring field lines, leading to continuous rain clumps forming. Clump formation is fastest in the transverse direction (panel d) and then grows longitudinally (panel g) to the field lines. This perpendicular growth happens in a minute or so.

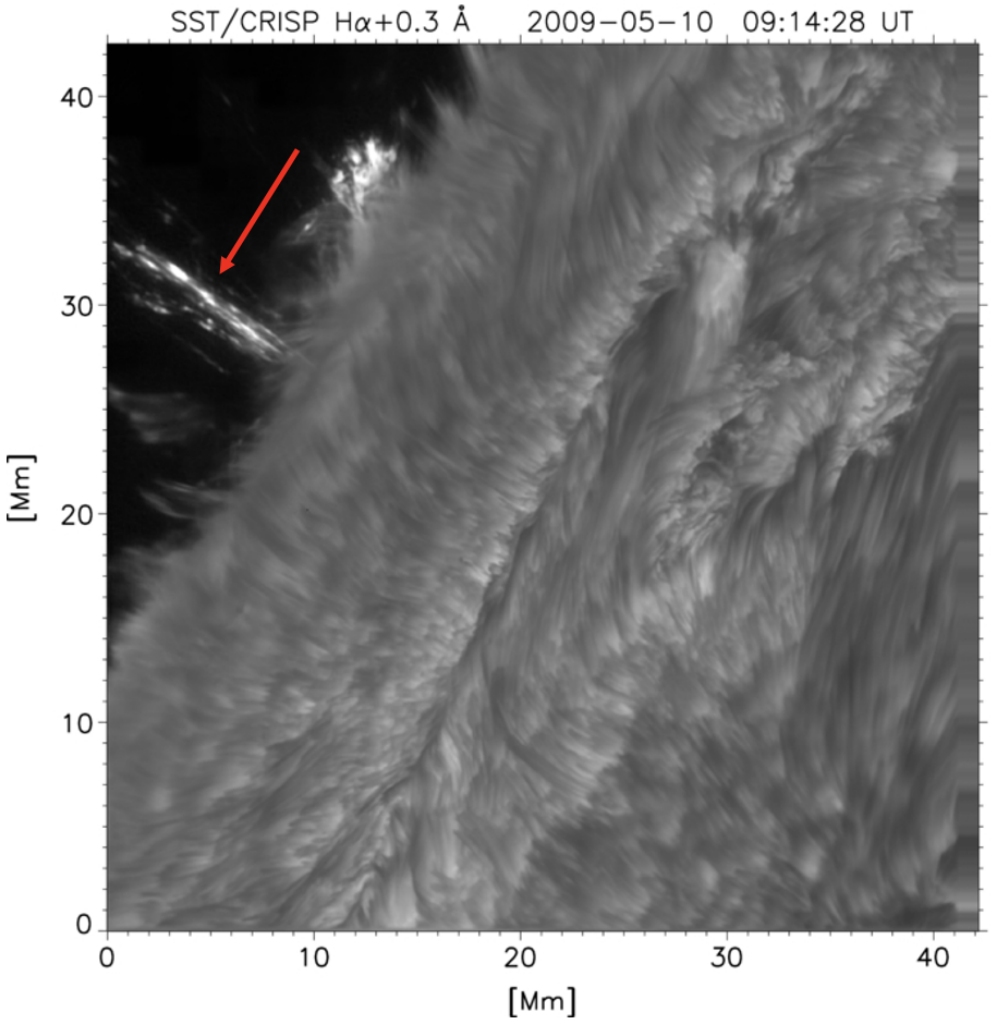

Figure 1.14: Observation of a group of coronal rain clumps (showers) falling down to the solar limb, indicated by the red arrow in H-α with the CRisp Imaging Spectro Polarimeter (CRISP; Scharmer et al., 2008) at the Solar Swedish Telescope (SST; Scharmer et al., 2003) on May 10, 2009, (Antolin and Rouppe van der Voort, 2012).

As will be shown later (Section 4), showers have large widths and lengths, producing EUV ab-

sorption characteristics (Antolin et al., 2015). An example of showers are the dark EUV flaring loops (or Dark Post-Flare Loops (DPFLs, Song et al., 2016)), as mentioned previously (Ruan et al., 2021).

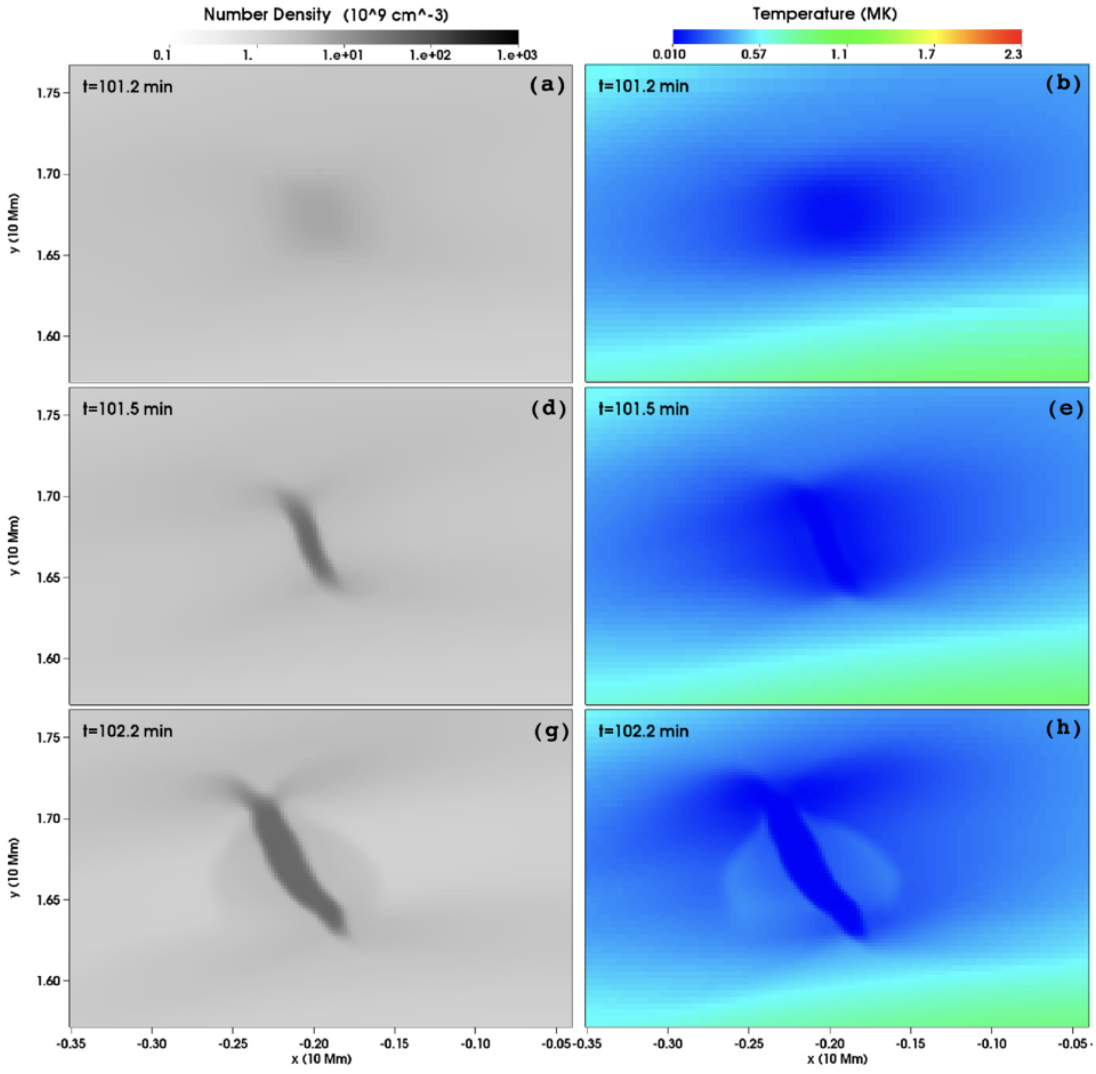

Figure 1.15: The formation process of 2.5D MHD modelling of coronal rain, which zoomed within a loop arcade (Fang et al., 2015)

Until now, no observational investigation adequately quantifies the rain shower properties, including the spatial and temporal scales within which the occurrence of sympathetic cooling. In this dissertation, for the first time, a statistical examination of rain showers is provided over an AR in Section 4.

1.5.5 Solar Flares

Solar flares are one of the most fascinating and, at the same time, the most energetic phenomena that can be resolved in time and space anywhere in the universe. These events involve the reconfiguration of the magnetic field, which is known as a magnetic reconnection (e.g., Sweet, 1958; Shibata and Magara, 2011). During this reconnection, a solar flare suddenly releases energy (10^{28}-10^{32} erg) stored in the magnetic field (Fletcher et al., 2011) within a typical timescale of tens of minutes. This released energy travels along newly reconnected magnetic field lines and is deposited in the chromosphere at the footpoints. Solar flares are observed in a wide range of the electromagnetic spectrum, from radio to gamma rays (Benz, 2008).

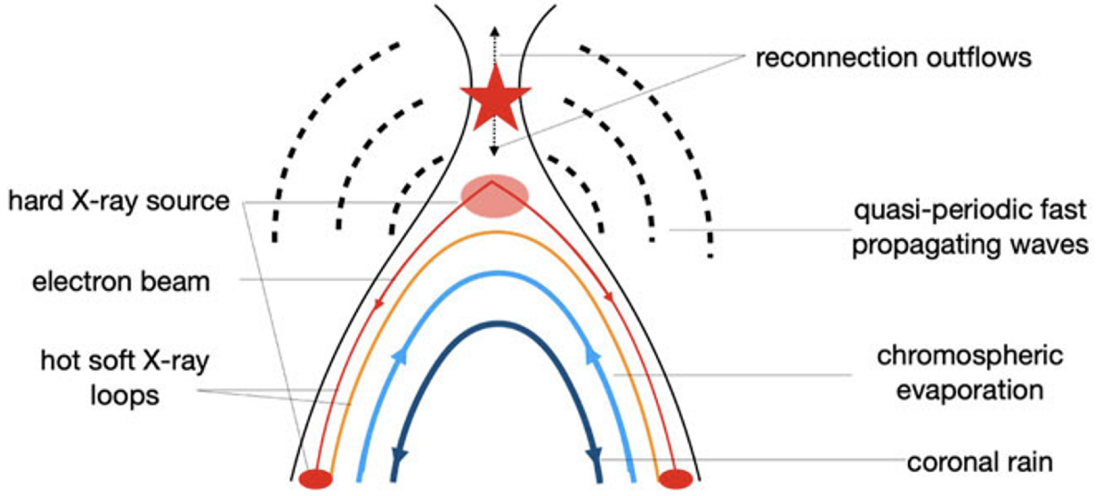

Figure 1.16: The Standard Solar flare model. The red star depicts the reconnection region in the corona. The sketch also includes some of the commonly observed processes during a flare. (Image Credit: (Antolin and Froment, 2022))

Figure 1.16 shows a so-called standard solar flare model of a twisted magnetic flux rope and overlying fields that stabilize the flux rope. When the system loses its stability (which may happen for various reasons), the flux rope expands upward and stretches the strapping fields. Magnetic reconnection takes place within the current sheet at the boundary between two oppositely directed field lines (red stars in Figure 1.16), releasing the free magnetic energy previously stored in the system. Energy is deposited in heating and accelerating the particles (electrons and ions), which escape the current sheet and propagate down along the magnetic field lines towards the chromosphere. Outflows driven by magnetic tension are produced perpendicular to the direction in which the initial field lines came together, leading to the contraction of the loops below the current sheet

towards the chromosphere and the expulsion of the closed field from above the current sheet. The newly formed hot loops are known as a Post-Eruption Arcade (PEA), while the escaping flux rope is further observed as a Coronal Mass Ejection (CME).

Solar flares have three distinct phases (Golub and Pasachoff, 2009) in their temporal evolution as follows:

- a pre-flare (precursor)
- a sudden impulsive phase
- a gradual or post-flare phase

In the pre-flare phase, small brightenings, called precursors, occur before the onset of a flare. The precursors are usually the first response to a flare trigger, which may be a new flux emergence, or filament activation, to name a few. The destabilized system causes magnetic fluxes (particularly reconnection) to interact, leading to the flare onset. The flare region is heated, and the coronal plasma becomes visible in soft X-ray and EUV lines. In the impulsive phase that follows, a large number of electron and ion beams are accelerated, and energy is suddenly released by the magnetic fields that rapidly transition to a lower energy state. It is easily seen in flare lightcurves derived from HXR, SXR, γ-rays, EUV, and, in some cases, white light emission (Fletcher et al., 2011). A significant fraction of this released energy is transported downward toward the lower atmosphere (TR and upper chromosphere) through radiation, thermal conduction, and high-energy particles (Priest and Forbes, 2002; Fletcher et al., 2011). This energy heats the local plasma at TR, chromospheric and even photospheric levels if the flare is strong enough to coronal temperatures and raises the plasma pressure, which leads to the upward motion of plasma known as chromospheric ablation or evaporation. Within the chromosphere and photosphere, flare ribbons are observed as elongated and concentrated regions of intensified brightness. These regions serve as the points of energy deposition where magnetic loops undergo reconnection during a flare event. It is the accelerated particle beams that produce the ribbons as they collide with the dense plasma of the chromosphere and photosphere. As a result, coronal loops, rooted at the heated locations, are filled with this hot ($\approx$ 10 MK) and dense ($\approx 10^{10}$ cm^{-3}) evaporated plasma, allowing it to an apparent expansion (e.g., Antiochos and Sturrock, 1978) due to the way reconnection progresses in time, with the oldest reconnected loops (and therefore cooler) at the bottom and the newest (and hottest)

at the top. This process may be observed as the appearance of a blueshifted component in ion emission when observing on-disk with a wide range of formation temperatures. The loops then cool all the way down to chromospheric temperatures. As the plasma cools, the gradual phase starts.

The gradual phase of a solar flare follows the impulsive phase and can last for several hours and up to a day or more. This phase is also characterized by cooling processes and a decrease in the intensity of X-ray and EUV emissions. The cooling process is also divided into three phases in itself, as shown in Figure 1.17 by the vertical dashed lines and highlighted regions of conductive cooling (phase III), radiative cooling (phase IV), and catastrophic cooling (phase V). The cooling process starts with thermal conduction (phase III) as the dominant loss mechanism due to high temperatures. In flaring conditions, conductive cooling may cause faster cooling (Doschek et al., 1982). According to the GOES light curve in Figure 1.17, the temperature peaks start in phase III at 15.4 MK and drop to 13.4 MK as phase III loses efficiency. Then, radiative cooling becomes more efficient as the radiative losses also increase when the temperature decreases, and the loop density increases (Antiochos and Sturrock, 1976; Cargill, 1994), which initiates phase IV. In this phase, the cooling is accelerated due to the shape of the optically thin loss function (Culhane et al., 1970), which eventually leads to a "catastrophic cooling" (or runaway cooling) event (phase V).

The chromospheric evaporation, as mentioned above, can result from both small localized heating events and large flares. While the former leads to the gradual heating of a few loop strands (Şahin et al., 2019), the latter may lead to the appearance of a large-scale system of very hot loops called post-flare loops (PFLs, Bruzek, 1964). These PFLs can be observed during their cooling stage as they progressively appear in X-ray and later in EUV and visible spectral lines. PFLs appear in Hα images when the hot plasma cools down to the chromospheric temperature, which results in coronal rain. These downflows (in PFLs) appear as dark loop-like features in EUV images due to the hydrogen and helium absorption in this cooling stage, and therefore, they are called DPFLs (Song et al., 2016). On the other hand, Reep et al. (2020) studied flaring loops using HYDRAD, focusing on the electron beam as the primary energy input and thermal conduction. They found that the electron beam heating alone cannot directly produce coronal rain since the electron beam heating localisation at the footpoint is too short. This short lifetime and its tendency to quickly

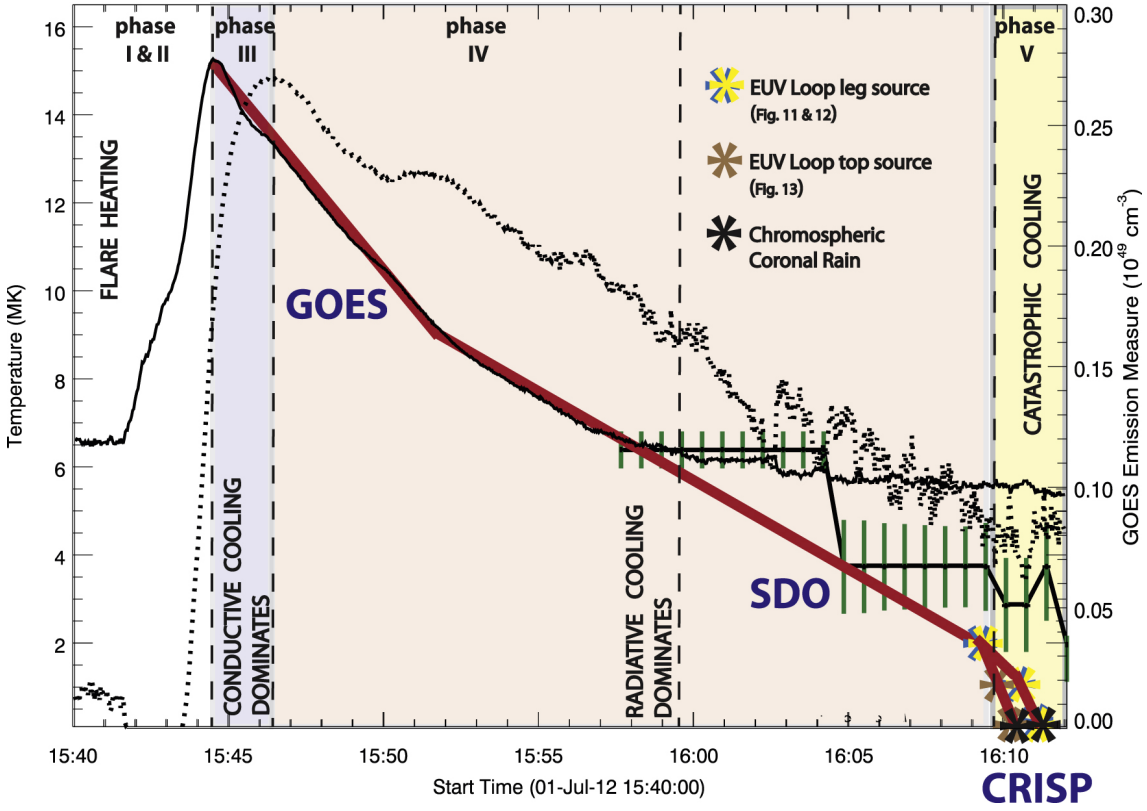

Figure 1.17: The cooling process of a flare with the temperature evolution from the impulsive phase until the catastrophic cooling time. The impulsive phase was observed in Geostationary Operational Environmental Satellites (GOES) (black solid curve) through EUV observations with AIA (black lines with green error bars). The catastrophic cooling time was observed with CRISP (star symbols). The solid red curve represents the cooling curve, starting from the cooling phase (phase III). The five phases (I-V) describe the evolution of cooling processes, with corresponding transitions indicated by vertical dashed black lines. The split branches of the red cooling curve during catastrophic cooling represent the temperature evolution of loop-top coronal rain (brown symbols) and loop-leg coronal rain (yellow symbols). The GOES EM is shown as a black dashed curve on the right-hand side. (Image Credit: Scullion et al. (2016))

shift from the base to the top, when long-lasting, ensure that the loops are uniformly heated as they cool down. In contrast, Ruan et al. (2021) achieved replication of post-flare rain using a 2.5D MHD simulation without the need for a beam. Their model effectively generates sufficient heating and condensation through magnetic energy conversion during flare reconnection. However, the exact mechanism leading to rain has not been identified yet.

Observations and analysis of upflows in solar flares have been the focus of many studies (Feldman et al., 1980; Veronig et al., 2010; Doschek et al., 2013, and reference therein), and they found that chromospheric evaporation can have very high speeds. In particular, Wuelser et al. (1994) observed 250 km s^{-1} upflows in the Ca XIX X-ray line measured with the YOHKOH spacecraft.

Using YOHKOH data Doschek et al. (1994) also observed upflows in the X-ray Ca XIX and Fe XXV lines, with velocities reaching as high as 800 km s^{-1}. Milligan and Dennis (2009) conducted a multiwavelength survey of Doppler shifted lines using HINODE/EIS data and reported that all ionization stages of iron above Fe XIII exhibited blueshifts, with the hottest ions indicating upflows in excess of 250 km s^{-1}. On the other hand, downflows have also been observed in the flaring atmosphere, and they are usually attributed to the so-called flare-driven coronal rain (Martínez Oliveros et al., 2014; Scullion et al., 2016), which is described in detail in the following sections.

1.5.6 Thermal non-equilibrium and Thermal Instability

One of the proposed mechanisms to explain the observed cooling of the solar corona (such as coronal rain and prominences) is TNE and TI. TNE is a fascinating and highly non-linear process that occurs in coronal structures, and it is important to understand the mass and energy exchange between the chromosphere and corona. In order to understand the TNE cycle well, first of all, it is necessary to understand the equilibrium and non-equilibrium states. According to theoretical models, spatially uniform coronal heating often leads to a state of equilibrium where the plasma remains unchanged. This equilibrium can be a static equilibrium or an equilibrium with steady end-to-end flow. In cases where there is a balance between the input energy, thermal conduction, and radiation, the plasma is at rest, resulting in a static equilibrium. However, most of the coronal loops are far from being equilibrium.

In addition to the solar corona, much larger scales in the universe also involve mass and energy cycles with heating and cooling processes linked to TI. These cycles encompass plasma existing at widely varying temperatures far more extreme than in the corona, ranging from a few K to 10^8 K, and are commonly referred to as multiphase environments. These different larger scales are interstellar, circumgalactic media, and intra-cluster media (White and Rees, 1978; Cavagnolo et al., 2008; Prasad et al., 2015), where plasma exhibit many similarities with coronal rain. These similarities arise from MHD processes that work regardless of scale; understanding them and the differences can help solve important problems in astrophysics. TI denotes the instability of the MHD thermal mode. This wave is also known as the entropy mode and has been shown to become unstable due to radiation by Field (1965) and Parker (1953). Numerical studies have shown how

TI leads to the formation of cool and dense condensations, through local pressure loss, with a filamentary structure that is often associated with the magnetic field structure (Sharma et al., 2010; Peng and Matsumoto, 2017; Ji et al., 2018).

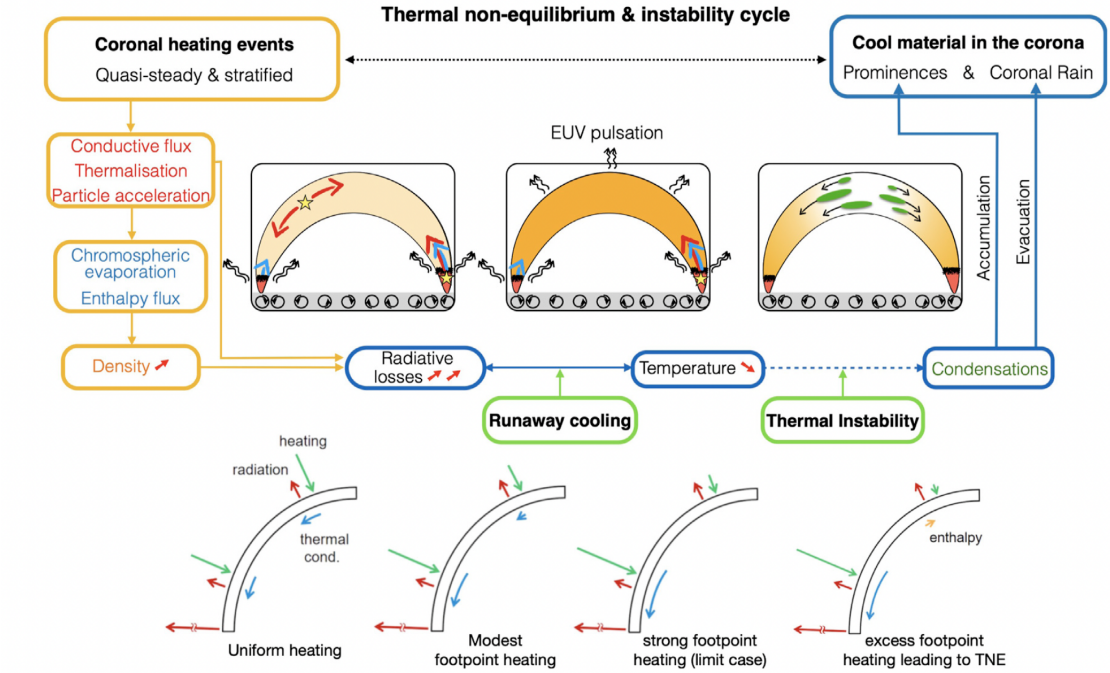

Figure 1.18: A sketch of the key physical processes involved in the TNE-TI cycle, with orange and blue boxes representing the heating and cooling phases, respectively. The three inset images depict different stages of the cycle, showcasing heating events (depicted as yellow stars) occurring either higher up or lower down in the atmosphere. Thermal conduction is represented by red arrows, illustrating the distribution of heat. Chromospheric evaporation is shown by blue arrows, resulting in the formation of dense loops, particularly in cases of footpoint heating. The loops become denser, as shown in the second loop image, and emit intense radiation. Radiative cooling is represented by wiggly black arrows, indicating the dominance of cooling over heating, resulting in successive peaks of emission in gradually cooler EUV passbands. During this stage, an EUV pulsation is observed. (Image Credit: Antolin and Froment (2022)).

A sketch of a TNE-TI cycle is shown in Figure 1.18. Here, a typical coronal loop, with the density of order 10^9 cm^{-3} and the temperature of order 10^6 K (Reale, 2014) in TNE undergoes a characteristic cyclical evolution. When the heating is concentrated at the footpoints (denoted by the yellow star in Figure 1.18), it is high frequency, meaning that repetition time is lower than radiative cooling time. A TNE-TI cycle is produced. TNE-TI cycle has two primary phases, which are called the evaporation (orange boxes) and condensation (blue boxes) phases (Antolin and Froment, 2022). Hot upward flows are produced due to chromospheric evaporation, and the coronal loop is filled by this evaporated plasma. The temperature and density increase as the

evaporated plasma reaches higher up in the corona. During this phase, the chromosphere operates as a mass reservoir. Then, the coronal loop becomes overdense, which causes stronger radiation (proportional to n_e^2) in the corona. The loop apex ends up with excessive radiative losses that cannot be compensated by the heating, eventually leading to thermal instability (TI). During the cooling, an EUV pulsation is produced (see Section 1.5.2). The loop begins to cool down gradually at first but then cools down rapidly by reason of the shape of the radiative loss function (see Figure 1.19) (Antiochos and Klimchuk, 1991; Antiochos et al., 1999). This rapid cooling is called catastrophic cooling or runaway cooling. TI produces high-density condensations at the loop apex. These condensations slide down to the solar surface along the loop's legs under the action of gravity, evacuating the coronal loop in a short time. This falling cool material is called coronal rain. If these condensations accumulate in the upper corona for many hours to several days hosted by magnetic dips (Adrover-González et al., 2021; Jenkins and Keppens, 2021), they can form prominences. If the heating is unchanged, the TNE-TI cycle is repeated (i.e., the evaporation phase takes over again). However, in some cases, the plasma undergoes reheating before its temperature drops to chromospheric temperatures, known as an incomplete condensation (Mikić et al., 2013). It is important to point out that TNE refers to the absence of thermal equilibrium, which differs from TI, where the system is disturbed from an equilibrium state.

The bottom panels in this figure (Figure 1.18) explain how TI is achieved in a coronal loop, as given with the schematic representation of the energy balance in three coronal loops. The first from the left represents the uniformly heated corona. In this case, thermal conduction (blue arrow) operates as a thermostat, regulating the energy flow. This excess energy is then transferred to the TR. The energy is subsequently released through radiation. This results in hydrostatic balance. Suppose the heating (or quasi-steady heating) is concentrated at low coronal heights. Thermal conduction becomes less effective, as shown in the second and third panels from the left in the same figure, due to the flat temperature profile in the corona. In that case, the heating decreases quickly with increasing distance from the footpoints, which means under specific conditions (see Equation 1.4 and Equation 1.7) discussed by Klimchuk and Luna (2019), it is impossible to achieve an equilibrium state in a loop due to high density and large radiative losses without an additional enthalpy flux energy. The specific requirements in order to trigger TNE is given by Klimchuk and Luna (2019) with two formulas as follows:

- The heating at the loop apex must be considerably less than the heating in the TR. It depends on the expansion factor, and it becomes less severe for greater expansion. To simplify, TNE is more likely to occur in loops that exhibit substantial expansion.

$$\frac{Q_{min}}{Q_\lambda} < (1 + \frac{c_1}{\Gamma_\lambda})^{-1} \tag{1.4}$$

where

$$\Gamma_\lambda \equiv \frac{A_\Lambda}{A_{tr}} \tag{1.5}$$

and

$$c_1 \equiv \frac{R_{tr}}{R_c} \tag{1.6}$$

Here, Q_{min} and Q_λ represent the volumetric heating rates at specific locations in the coronal loop: loop apex and one heating scale length above TR, respectively. λ denotes one heating scale length along the coronal loop from the top of the TR. A_Λ and A_{tr} refer to cross-sectional areas averaged along the first heating scale length and TR, respectively. R_{tr} and R_c represent the radiative losses per unit area, which are integrated along the coronal and TR sections.

- For TNE to occur, the loop should have small asymmetries in cross-sectional area and/or heating:

$$(\frac{Q_s}{Q_w})(\frac{\lambda_s}{\lambda_w})(\frac{\Gamma_s}{\Gamma_w}) < [1 - 4.3 \times 10^2 \frac{A}{A_w}(1 - \delta)\frac{L}{\lambda_s}]^{-7/2} \tag{1.7}$$

where

$$\delta = (1 + (\frac{c_1}{\Gamma_s})(\frac{Q_{min}}{Q_s}) \tag{1.8}$$

Here, L is the half-length of the coronal loop. The index S represents the strongly heated footpoint, while the index W represents the weakly heated footpoint. A and A_w represent the cross-sectional

areas at the location of minimum heating and one heating scale length above the TR on the weakly heated side. Typically, the area ratio falls between 1 and 2.2. A higher value of the right-hand side of Equation 1.7 corresponds to an increased likelihood of TNE occurrence. This value is greater when two factors are smaller: λ_s/L (a parameter related to the loop length) and Q_{min}/Q_s (ratios of heat inputs). Both of these factors support the occurrence of TNE in line with the principles outlined in Equation 1.4. The geometric asymmetry between the left and right footpoints should be smaller than 3 in order to facilitate the occurrence of TNE (Klimchuk and Luna, 2019). Otherwise, strong siphon flows can be set in, which effectively reduces the lifetime of the cooling plasma in the corona.

As shown in the bottom rightmost panel in Figure 1.18, the enthalpy flux is a consequence of the excessive heating at the loop footpoints, where the material is injected directly upwards (evaporation, see Section 1.5.5). If there are symmetric conditions from both footpoints, then enthalpy flux results in plasma accumulation at the loop apex. This is an unstable condition set by radiative cooling caused by a much faster increase in radiative losses with a density increase.

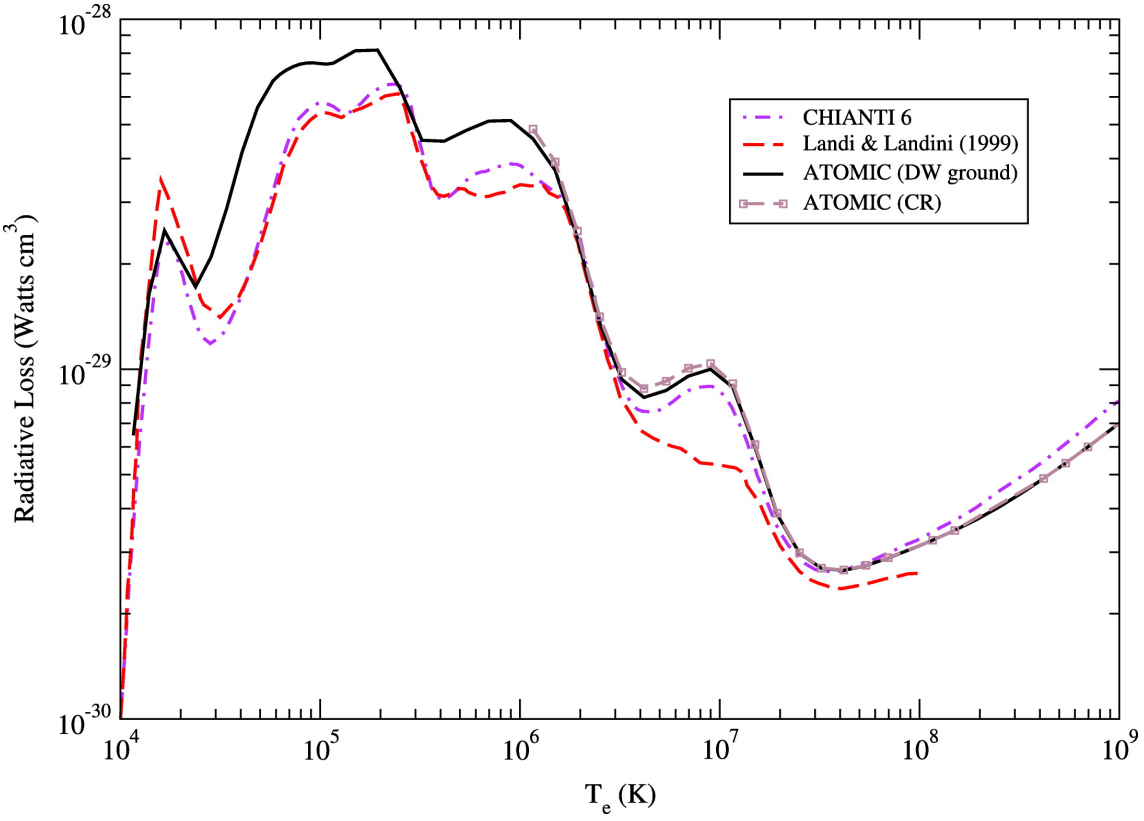

Figure 1.19: Radiative loss function for a plasma in the corona containing 15 elements. (Image Credit: Colgan et al. (2008)).

Observations at multi-wavelength (such as AIA, IRIS, or GST) have shown that coronal rain corresponds to the catastrophic cooling phenomenon in coronal loops (Ahn et al., 2014; Antolin et al., 2015; Kohutova and Verwichte, 2016). The precise role of TI remains a subject of discussion, as highlighted by Klimchuk (2019). However, the conditions for the onset of TNE are commonly observed in numerical simulations of strongly stratified and high-frequency heating of coronal loops (Antiochos et al., 1999). These simulations provide a means to explore the formation of coronal rain and parameter space of TNE-TI, enabling comparisons with observations and constraining the heating parameter space (Fang et al., 2013, 2015; Froment et al., 2018; Klimchuk and Luna, 2019; Johnston et al., 2019), as well as the heating mechanisms (Antolin et al., 2010). The specific requirements of spatio-temporal heating distributions necessary for coronal rain formation serve as valuable indicators of coronal heating properties. When the heating distribution in a coronal loop stays constant over the temporal and spatial domain, TNE causes the loop to go through cycles of heating and cooling because of the inability of the loop to reach thermal equilibrium, as shown by Kuin and Martens (1982).

Besides, some TNE cycles have minimal to no coronal rain, as demonstrated by Froment et al. (2015), while some, such as the "rain bow" in Auchère et al. (2018*a*), produce a significant amount of coronal rain. Moreover, compared to other periodic coronal rain events, the "rain bow" produces a higher amount of rain showers (Pelouze et al., 2022). Besides, observations indicate the possible formation of prominence. A recent study by Froment et al. (2018) conducted a parameter space investigation with varying heating functions of the form of Equation 1.9, to study the onset of TNE in a loop.

$$H(s) = H_0 + H_1(e^{g(s)/\lambda_1} + e^{-g(L-s)/\lambda_2}) \tag{1.9}$$

Here, the constant background volumetric heating rate is given by H_0, while the stratified volumetric heating rate is H_1. The λ_1 and λ_2 represent the scale heights of the stratified heating at both footpoints. $g(s) = max(s - \Lambda, 0)$ indicates a mechanism for introducing continuous heating in the chromosphere, extending up a distance of $\Lambda = 5$ Mm from both footpoints. In order to achieve stratified heating, H_1 should be greater than H_0, and both λ_1 and λ_2 should be smaller than the loop length (L). When using smaller heating scale height values or higher H_1/H_0 ratios,

a greater stratification is achieved. Increasing either λ_1 or λ_2 results in a higher energy deposition within the loop. When $\lambda_1 = \lambda_2$, symmetrical heating is achieved. Through an extensive study of the parameter space (Froment et al., 2018), TNE cycles exhibiting coronal rain, characterized by complete condensations, occur only in a relatively small portion of the parameter space. Thus, to observe coronal rain, highly specific heating and geometric conditions must be met. Pelouze et al. (2022) also explored the parameter space in the simulations of Froment et al. (2018) and found that the asymmetrical loops are unlikely to produce full condensations. These asymmetries give rise to siphon flows, which effectively curtail the duration over which cooling plasma persists in the corona. Consequently, the condensations encounter insufficient time to cool completely to temperatures characteristic of the chromosphere. Nonetheless, this outcome is contingent upon various factors, with the strength of heating, specifically the volumetric intensity of each heating event, playing a pivotal role. When heating is robust, leading to higher densities, asymmetries have a diminished impact due to the shorter timescale of radiative cooling. Therefore, instances of incomplete condensation are likely influenced by a combination of asymmetries and heating strength, with the latter emerging as a potentially more influential factor.

1.6 Importance of coronal rain to heating

Coronal rain is a distinct multithermal coronal plasma that exhibits simultaneous emission in various wavelengths at the same spatial location (Antolin et al., 2015). So, it serves as a valuable proxy for investigating the processes contributing to the coronal heating problem (Antolin et al., 2010). This contribution of coronal rain to coronal heating can be analysed first in terms of rain-hosting and non-rain-hosting loops. If the loops in the solar corona do not exhibit coronal rain, they are believed to be heated by mechanisms whose heating is spatially uniform along the loop. One such mechanism is the dissipation of nonlinear Alfvén waves through shocks (Moriyasu et al., 2004; Antolin et al., 2008). These waves, generated by photospheric motions, carry energy that can be converted into heat by nonlinearly mode converting into longitudinal modes, which then steepen into shocks in a spatially uniform way. In contrast, loops that do host coronal rain are thought to be heated through footpoint heating mechanisms (see TNE process in Section 1.5.6). This scenario is more likely to occur with ohmic heating, which results from slow magnetic stress caused by convective motions (Gudiksen and Nordlund, 2005; Lionello et al., 2013). Uniform

heating distributed over the loop fails to produce catastrophic cooling since the heating rate per unit mass must locally decrease over time within the corona to allow for the onset of thermal instability. Catastrophic cooling can happen without time dependency, even with a constant heating function. Simulations indicating footpoint-concentrated heating align with observational evidence from coronal loops above active regions, which are predominantly heated at their footpoints, as supported by Aschwanden (2001).

Studies mentioned in the above sections have established a correlation between coronal heating processes (such as loops and flares) and cooling phenomena (like coronal rain) by linking multiple scales, ranging from active region dimensions to rain clump size and spanning a broad spectrum of temperatures and energies. TNE occurrence and quiescent coronal rain provide additional support for the existence of highly stratified heating in active regions. Additionally, their presence can serve as an indicator of how coronal heating mechanisms are working rather than whether or not heating is occurring. As mentioned above, the nonlinear torsional Alfvén wave model, which may result in uniform heating, is unable to generate TNE cycles and coronal rain because the wave mode converts to longitudinal modes to dissipate their energy uniformly (Antolin et al., 2008, 2010). Investigating TNE-TI cycles, including coronal rain phenomena, not only provides valuable insights into coronal heating mechanisms but also offers a promising approach for estimating crucial in situ physical quantities in the solar corona. On the other hand, the detection of EUV long-period intensity pulsations (Auchère et al., 2014; Froment et al., 2017, 2020) provide significant insights into the prevalence of limit cycles involving heating and cooling, resulting from TNE-TI. These findings carry profound implications for the mass and energy dynamics of the solar atmosphere.

1.7 Motivation and Outline of the Thesis

Based on the literature review above, it is evident that studying the cooling of coronal loops, particularly coronal rain, through observations and numerical analysis can provide essential insights into the temporal and spatial properties of coronal heating. This PhD project aims to investigate observationally the relationship between coronal rain and the hot corona. The study also includes a comparative and detailed analysis of quiescent and flare-driven coronal rain. By comparing quiescent and flare-driven coronal rain in detail, we aim to gain unique insights into the temporal

and spatial properties of coronal heating. For this purpose, we employed state-of-the-art multi-wavelength, high-resolution space-based instruments such as the Interface Region Imaging Spectrograph (IRIS) and the Solar Dynamic Observatory (SDO) to investigate the connection between coronal rain and the hot corona. This thesis is structured as follows:

I begin by introducing the solar instruments in Chapter 2.1 and the methods in Chapter 2.2, which are used during this PhD research. I then present the analysis of detected quiescent coronal rain at chromospheric, TR, and coronal temperatures associated with intensity pulsations in Chapter 3 (Şahin et al., 2023). In Chapter 4 (Şahin and Antolin, 2022), I present the statistical study of rain showers over an AR, including their morphology and plasma's cooling behaviour, in order to explore the relationship with the TNE-TI scenario. I also give our results on the estimation of the TNE volume, which has never been done yet. In Chapter 5, we focus on a C2.1-class flare, especially its long gradual phases, where flare-driven coronal rain is seen. We present a comparative study of how flare-driven rain differs from its quiescent counterpart. We also investigate the temperature evolution throughout the flare, suggesting reconnection facilitated by the rain leads to significant energy release during the gradual phase. Additionally, we investigate the mass and energy circulation in the quiescent and flaring corona. Finally, in Chapter 6, I summarise the findings and discuss possible future work.

Chapter 2

Data and Method

2.1 Instruments

We analyse observations from the Interface Region Imaging Spectrograph (IRIS; De Pontieu et al., 2014) and Solar Dynamics Observatory (SDO; Pesnell et al., 2012) to investigate the connection between coronal rain and the hot corona. This study is largely based on analysing observational data from the aforementioned instruments. Therefore, this chapter provides an overview of those instruments and their characteristics, along with an explanation of the available data types.

2.1.1 Solar Dynamics Observatory

The Solar Dynamics Observatory (SDO; Pesnell et al., 2012) is one of the most preeminent solar instruments, and launched on 11th February 2010 at 15:23 UT in Brevard County, Florida, USA. It is a NASA mission designed to study the solar corona, the outer layer and hottest component of the solar atmosphere. SDO has been providing high-resolution observations of the full Sun continuously since then. It provides multi-wavelength views of the Sun, from the photosphere to the highly ionised corona. There are three instruments onboard SDO which are the Heliospheric and Magnetic Imager (HMI; Scherrer et al., 2012), Extreme ultraviolet Variability Experiment (EVE; Woods et al., 2012) and the Atmospheric Imaging Assembly (AIA; Lemen et al., 2012) (left panel in Figure 2.1). Each instrument provides a comprehensive and continuous view of the Sun's atmosphere, from the photosphere to the corona. The EVE instrument measures changes in the extreme ultraviolet (EUV) radiation of the Sun, which helps understand long-term solar

activity evolution. These data are mainly used to study Solar wind, and space weather. The HMI instrument measures the Solar magnetic field and the motions of its surface. The main focus is to study the solar internal structure and the origins of solar activity, such as sunspots and flares. The AIA instrument aims to study the Solar atmospheric variation, and it is covered in detail in the next subsection as it is the only SDO instrument used in this thesis.

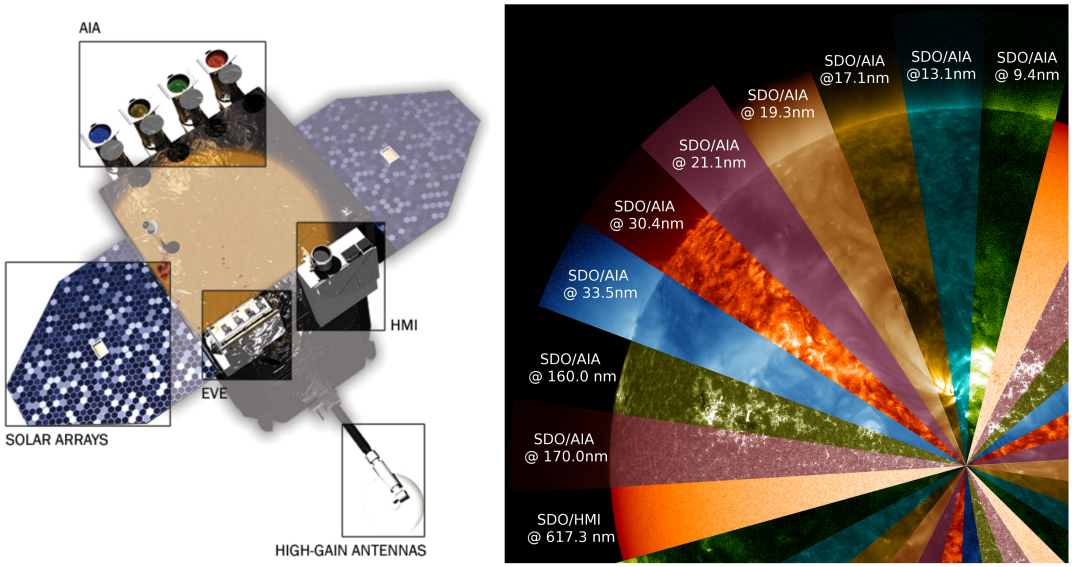

Figure 2.1: Left: A schematic diagram of Solar Dynamics Observatory (Pesnell et al., 2012). Right: Illustration of the AIA's different wavelengths filters. (Image Credit:SDO/NASA)

2.1.1.1 The Atmospheric Imaging Assembly

The AIA is an array of four telescopes, providing seven EUV wavelengths (94, 131, 171, 193, 211, 304 and 335Å), two UV (1600 and 1700Å), and one visible light (4500Å) (Pesnell et al., 2012). The right panel in Figure 2.1 shows these AIA channels with corresponding wavelengths. These images have $0.''6$ of spatial sampling rate per pixel, and the EUV wavelengths have 12 s cadence, while the UV ones have 24 s. AIA captures continuous 4096×4096 pixels full-disk high-resolution images, each corresponding to a range of temperatures emitted from plasma radiated along the LOS. Table 2.1 provides information about AIA channels and their main emitting ions and temperatures.

The AIA 94 Å channel is blended with three temperature emissions from Fe XV, Fe XIV, and

Fe XVIII. However, the main contribution comes from Fe XVIII 93.96 Å line emission with a peak at $\approx 10^{6.85}$ K. It is usually active in flaring conditions, which makes it important to study heating events (Testa and Reale, 2012; Ugarte-Urra and Warren, 2014).

The AIA 131 Å channel has contributions from two Fe VIII and Fe XXI lines at 130.94Å and 131.214Å, with a peak at $10^{5.6}$ and $10^{7.0}$ K, respectively, from the transition region and flaring corona.

Table 2.1: The primary ions observed by each AIA bandpass and their corresponding solar atmospheric region (Lemen et al., 2012).

Channel (Å)	Primary ion(s)	Region of Atmosphere	Char. log(T) [K]
4500	Continuum	photosphere	3.7
1700	Continuum	temperature min, photosphere	3.7
304	He II, Si XI	chromosphere, transition region	5.0
1600	C IV + cont.	transition region, upper photosphere	5.0
171	Fe IX	quiet corona, upper transition region	5.8
193	Fe XII,XXIV	corona and hot flare plasma	6.2, 7.3
211	Fe XIV	active-region corona	6.3
335	Fe XVI	active-region corona	6.4
94	Fe XVIII	flaring corona	6.8
131	Fe VIII,XXI	transition region, flaring corona	5.6, 7.0

The AIA 171 Å channel is dominated by the resonance transition from Fe IX at $10^{5.8}$ K.

The AIA 193 Å channel has two contributions formed at Fe XII at $10^{6.2}$ and Fe XXIV at $10^{7.3}$ K, which includes corona and hot flare plasma.

The AIA 211 Å is the least understood channel since it has many unidentified lines, which include cool and coronal (Del Zanna, 2009, 2012) lines. However, the main contribution comes from the Fe XIV 211.3 Å at $10^{6.3}$ K.

The AIA 304 Å has two contributions from He II 304 Å emission with a temperature response peak at 10^5 K and Si XI 303.32 Å at $10^{6.2}$ K. However, it is mainly dominated by He II 304 Å emission. In Section 2.2.6, we show how to separate these two emission components.

The AIA 335 Å is also multi-thermal. The main ion is centred in Fe XVI 335.4Å in the core of active regions (Liang et al., 2009).

The levels of data processing for AIA can be summarized in the following way:

- Level 0 data contains images from the raw telemetry stream.

- Level 1.0 data comprises images derived from Level 0, wherein processing involves tasks such as eliminating bad pixels, reducing spikes, and applying flat-field correction. All higher-level AIA data are based on this level of data.
- Level 1.5 data represents images modified to a common $0.''6$ plate scale. These images share uniform centres and rotation angles. Note that the exposure time is not corrected in this level of data.

2.1.2 Interface Region Imaging Spectrograph

The Interface Region Imaging Spectrograph (IRIS) (Figure 2.2) was launched on 27 June 2013 (De Pontieu et al., 2014) in a Sun-synchronous, low Earth orbit. The main focus of its mission is to understand the transport of energy and heat from the lower solar atmosphere to the corona through the chromosphere and transition region. IRIS provides high-resolution imaging and spectroscopic observation data from the photosphere to the corona.

Figure 2.2: The Interface Region Imaging Spectrograph (IRIS). Image Credit: IRIS Data notes (https://iris.lmsal.com/itn51/inst_overview.html)

IRIS uses a spectrograph (SG) and slit-jaw images (SJI) in various wavelengths, sensitive to the cool and hot plasma in the solar atmosphere. SG feeds light from three passbands, two in the far ultraviolet (FUV) and one in the near ultraviolet (NUV) (see Table 2.2), with $0.''166$ spatial pixel size and $175''$ spatial extent (long). SJI, on the other hand, captures images in four wide-range filters, two in the NUV and two in the FUV (see Table 2.3), with $0.''166$ spatial pixel size and $175'' \times 175''$ maximum FOV. IRIS also captures data at high temporal, spatial and spectral resolutions, providing information about the temperature, density, and velocity of the solar plasma,

as well as the structure of the magnetic fields.

Table 2.2: Overview of spectrograph (SG) channels of IRIS. This table is adapted from the IRIS data notes website (https://iris.lmsal.com/itn51/inst_overview.html)

Passband	Wavelength (Å)	Temperature log(T)
Far Ultraviolet (FUV1)	1331.7 - 1358.5	3.7 - 7.0
Far Ultraviolet (FUV2)	1389.0 - 1407.0	3.7 - 5.2
Near Ultraviolet (NUV)	2782.7 - 2851.1	3.7 - 4.2

The IRIS data are divided into six levels. Level-0 (L0) is the raw image from the Joint Science Operations Center (JSOC) at Stanford University and Lockheed Martin Solar and Astrophysics Laboratory (LMSAL). Then, the JSOC generates the Level-1 (L1) data by removing mirroring effects along various axes and adding informative headers (such as temperature, roll, and pointing data). Level-1.5 (L1.5) data are the lowest level of scientific data and are produced at LMSAL. These data are aligned and corrected for dark current, cosmic ray spikes, bad pixels, and flat fielding. Geometric and wavelength corrections are also applied to L1.5 data. Level-2 (L2) data (also the mainly used data type in this thesis) is generated at LMSAL using Level 1.5 data. L2 data have spectral rasters and SJI image time series (based on the observational identifier (OBS-ID)). Finally, the Level-3 (L3) data can be produced by the user using the "iris_make_fits_level3.pro" in the Interactive Data Language (IDL) SolarSoft (SSW). L3 data are mostly used in CRIsp SPectral EXplorer (CRISPEX; widget-based tools programmed in IDL) for spectral rasters. A detailed explanation can be found in (De Pontieu et al., 2014).

Table 2.3: Overview of slit-jaw images (SJI) channels of IRIS. This table is adapted from the IRIS data notes website (https://iris.lmsal.com/itn51/inst_overview.html)

Passband	Wavelength (Å)	Temperature log(T)
C II (FUV1)	1330	3.7 - 7.0
Si IV (FUV2)	1400	3.7 - 5.2
Mg II h/k (NUV)	2796	3.7 - 4.2
Mg II wing (NUV)	2832	3.7 - 3.8

In this thesis, the high temporal and spatial resolution images of IRIS and SDO helped us to investigate the highly dynamic solar coronal rain and its contribution to the coronal heating problem. Both SDO[1] and IRIS[2] data are available to the public on the websites, which allows anyone to access and study the sun's activity.

[1] http://jsoc.stanford.edu
[2] https://iris.lmsal.com/search/

2.2 Data Analysis Techniques

We mainly study the properties of the coronal rain with IRIS spectro-imaging observations and simultaneous observations from SDO/AIA.

This section will provide a fundamental description of the image processing and automatic detection techniques utilized in this study. The general methodology and a thorough explanation of the various parameters utilized throughout the analysis will be outlined. The following sections will present a comprehensive exposition of the specific algorithms and image processing techniques employed and the corresponding parameter values.

2.2.1 Co-alignment between SDO and IRIS

Co-alignment is aligning two or more images to have the same spatial registration. This process results in corresponding features in the images lining up with each other. In this thesis, the SDO/AIA and the IRIS/SJI are co-aligned to compare and analyze the observations. To achieve co-alignment between AIA and SJI data, it is necessary to account for differences in the spatial scale of the two instruments. The AIA and SJI instruments have different pixel scales (0.6 arcsecs pixel^{-1} and 0.3327 (or 0.166) arcsecs pixel^{-1}, respectively), which means that features in the images appear at different physical sizes.

Co-alignment is achieved by comparing the features observed on off-limb and on-disk in simultaneous images of SJI 2832 Å and AIA 1600 Å in quiescent coronal rain data (see Chapter 3). These two passbands are captured under similar conditions, ensuring accurate alignment between these two. For the flaring coronal rain data (see Chapter 5), the SJI 1330 Å and AIA 304 Å have been used since there is no SJI 2832 Å data. For the co-alignment, first, the shifts in the x-axis and y-axis are determined for different instances of time. Then, an interpolation process is conducted in order to estimate shifts for any other time. After that, these computed shifts are applied to all other channels accordingly.

2.2.2 Coronal Rain Detection: Rolling Hough Transform

The Hough transform (HT) is a robust image-processing technique for detecting linear and curvilinear structures. It was first introduced and patented by Paul V.C. Hough to detect complex lines in

bubble chamber photographs (Hough, 1962). Then, Clark et al. (2014) adapted the HT technique by introducing a rolling version (Rolling Hough Transform, or RHT) to detect linear structures in astronomical images. Later, Schad (2017) modified the concept of the RHT using error analysis in multidimensional data sets. In this thesis, the RHT technique developed by Schad (2017) has been used for the detection and quantification of the rain material and its apparent motion.

This section is divided into three subsections to describe the input parameters (2.2.2.1) of the RHT routine, how it works (2.2.2.2), and what the outputs are (2.2.2.3).

2.2.2.1 Input Parameters

The RHT routine contains some parameters (see below) that the user can define the values.

- **nlev** is a background noise level (σ_{noise}) for a single image.
- **rmean** (w_r) is the number of images to sum for running mean before the high pass filter. This parameter is used to make sure that the coronal rain clumps follow a trajectory for each specific time interval along the temporal axis. Subsequently, this path is employed to ascertain a direction of flow in the POS. The w_r value is chosen by considering the observed speed of rain clumps and the time needed for a visible change to appear in the image.
- **wlen** (D_w) represents the diameter of the circular RHT kernel width. It is centred on every image pixel that needs assessment at a given image time. It represents a minimum length of linear structures. Therefore, the value for this parameter is chosen based on the minimum length of the observed rain clump (see one example with three different values in Figure 2.3).
- **smr_xy** (D_k) is the highpass filter kernel size to enhance the large-scale components from the image (see Figure 2.4).
- **med_xy** is the median filter kernel size to remove some unwanted pixels from the image. Choosing a large number for this parameter may lead to the loss of some rain clumps pixels.
- **bidirectional difference filter step:** The RHT routine also uses a bidirectional difference filter along the temporal axis to help the segmentation of flow. Users can decide on the bidirectional step.

The bidirectional filter (bdf) with two-time steps is given as follows:

$$I_{bdf}(x,y)|_m = (I(x,y)|_m - I(x,y)|_{m-2} - (I(x,y)|_m - I(x,y)|_{m+2})) \tag{2.1}$$

Here, $I(x,y)|_m$ indicates the mth frame within the time series.

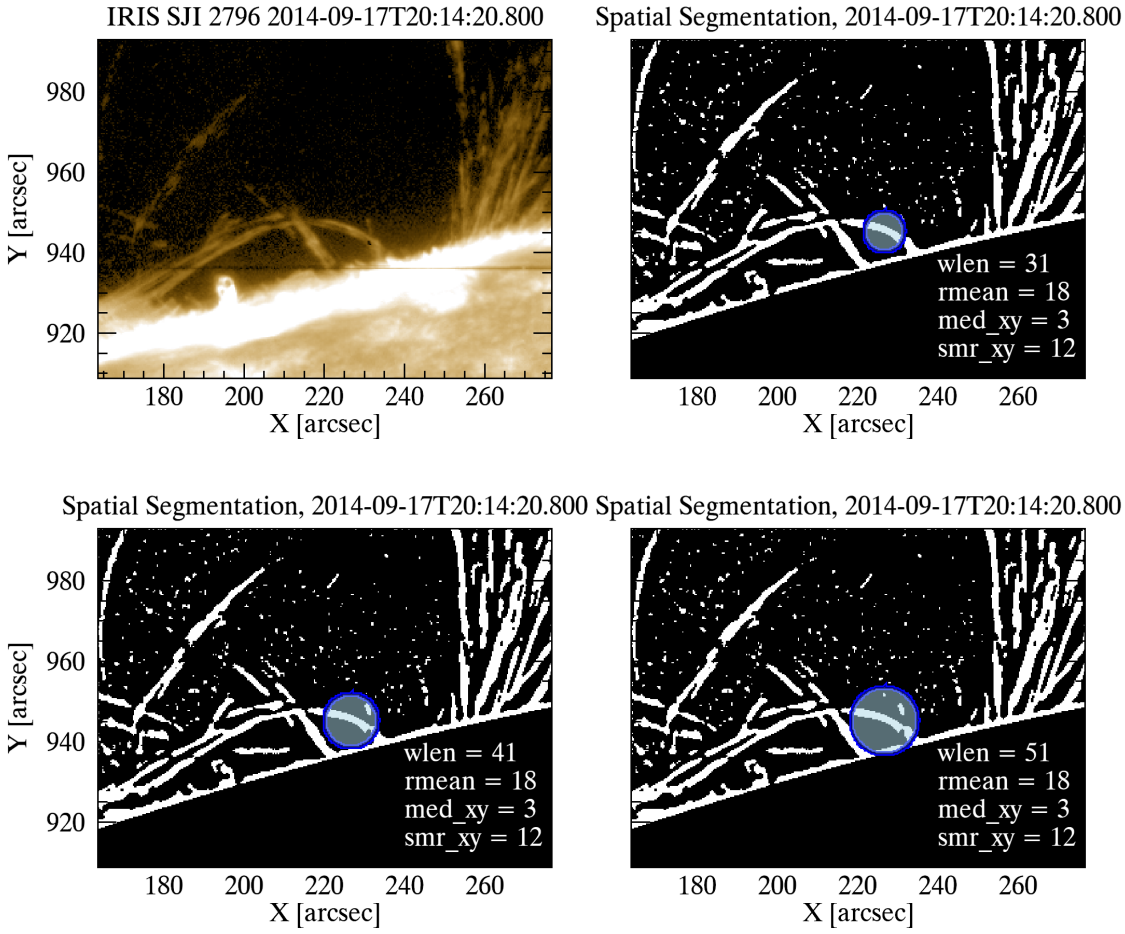

Figure 2.3: Top-left: Single IRIS SJI 2796 Å image from one of the analysed data in Sahin and Antolin (submitted). All other panels are the spatially segmented version of this IRIS SJI 2796 image resulting from the circular RHT kernel width (wlen; D_w).

2.2.2.2 How does the RHT work?

Figure 2.5 shows the demonstration of the RHT. The left image first illustrates a binary image, and its graphical representation is shown in the middle panel. In these plots, the light blue highlighted area (left) and green circle (right) denote the diameter of the circular kernel size (D_w). The sum of the illuminated pixels within the kernel size in the binary image is calculated. This calculation

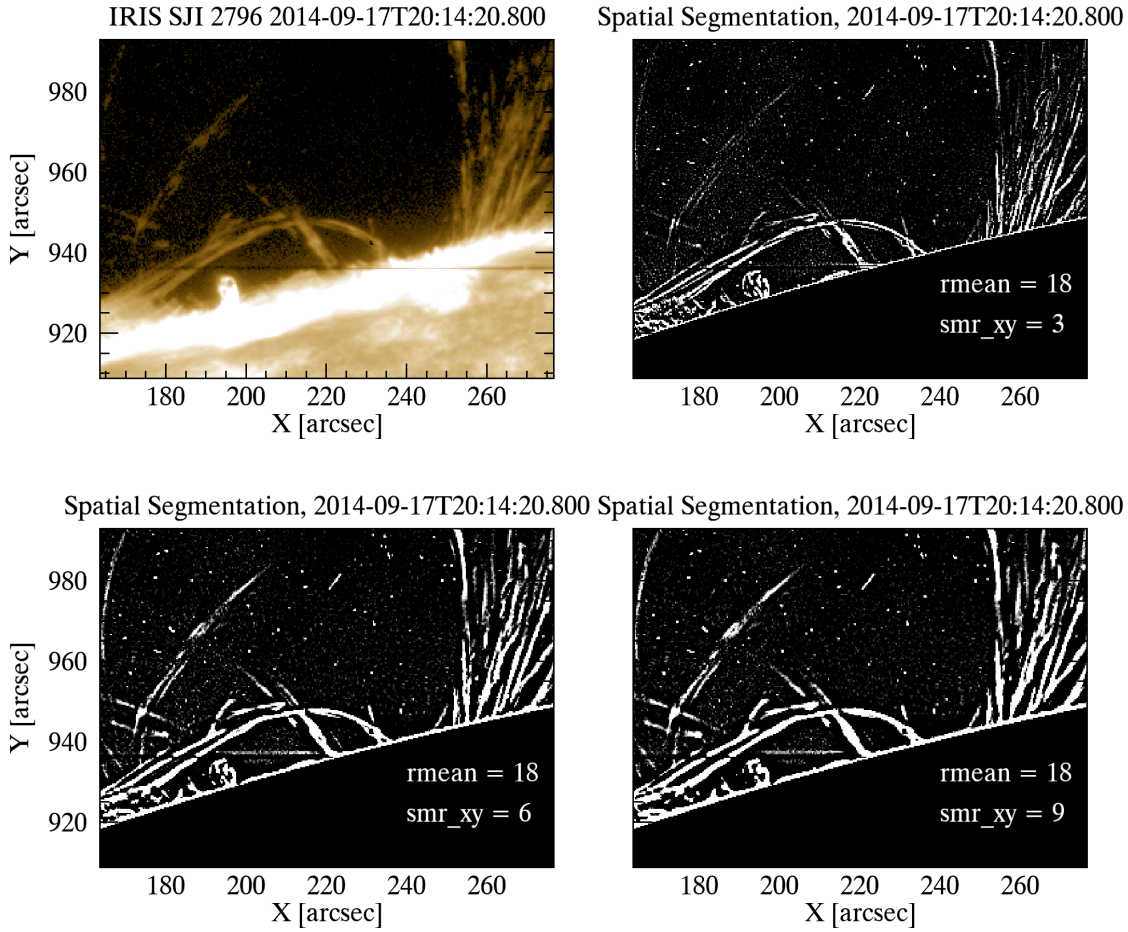

Figure 2.4: Top-left: Same IRIS SJI 2796 Å image shown in Figure 2.3. All other panels are the spatially segmented version of this IRIS SJI 2796 image resulting from the highpass filter kernel (smr_xy; D_k).

is done for all pixels in each axis direction (i.e. (θ)). Subsequently, it is normalized to the total number of pixels. In the polar plots (right panel), the RHT function $(H_{xy}(\theta))$ has been shown for both the noiseless and the noise-added cases. Here, $H_{xy}(\theta)$ varies from 0 to 1, and a value of 1 represents that all pixels in this direction are illuminated. In these panels, $H_{xy}(\theta)$ is peaked along the direction of the line in both noiseless and noise-added cases. An adaptive threshold (h_{xy}; see Equation 2.2) is defined in the routine to control the pixels that do not contribute to the mean direction. The reason behind this is simple. If random noise is present, non-isotropic noise groups will negatively influence the H_{xy}. So, with this adaptive threshold, the routine scales to pixels according to the peak of H_{xy} values. This means that values within some peak range are still counted as a measure of the peak's significance.

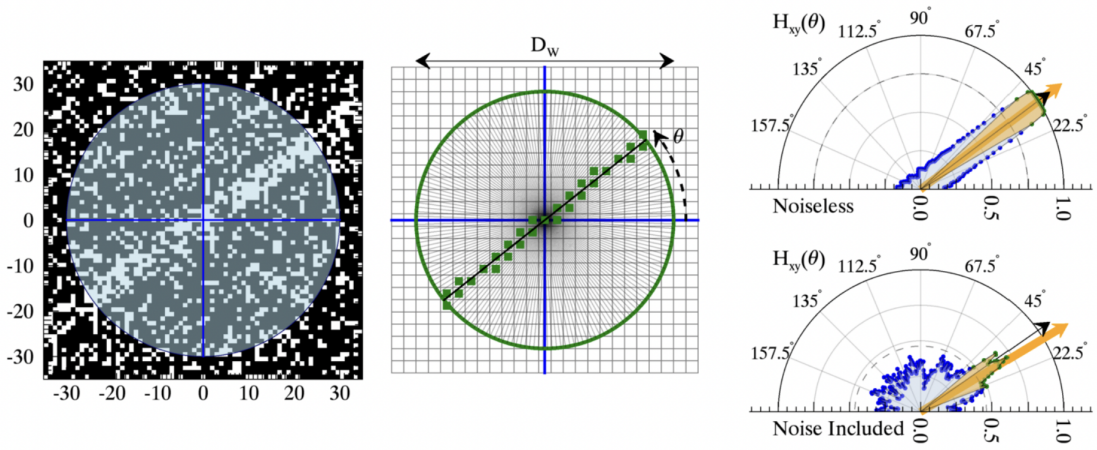

Figure 2.5: Demonstration of the RHT routine. Left: a binary image of a thick and straight line with added noise. The blue crosshair and its transparent overlay show the RHT is analyzing the pixel within the circular kernel. Middle: the RHT and the pixels that intersect the axis at angle θ. Right: the transformed function ($H_{xy}(\theta)$) without noise (top) and with noise (bottom). The black arrow indicates the line's orientation, while the orange arrow represents the orientation angle derived from the RHT. (Schad, 2017)

$$h_{xy}(\theta) = \begin{cases} H_{xy}(\theta), & \text{if } H_{xy}(\theta) \geq max[H_{xy}(\theta)] - f \\ 0, & \text{if } H_{xy}(\theta) < max[H_{xy}(\theta)] - f \end{cases} \tag{2.2}$$

Here, f defines a criterion for isolating peaks from the surrounding noise using adaptive thresholding ($h_{xy}(\theta)$). It means that a peak in the signal needs to have an amplitude that is f% greater than the surrounding noise in order to be effectively detected and separated from the noise by the adaptive threshold. During our analysis, we set f to 0.25 (same value as in Schad (2017)). It is ensured that the difference between the peak and the surrounding noise is substantial enough to identify the peak using the adaptive threshold method confidently. The RHT routine considers the direction axes within the D_w (for $\theta \geq 0$ and $\theta \leq \pi$) and defines the mean direction (θ) and its error. In the routine, the data are transformed into vectorial data because the orientations of 2° and 178° are not widely separated in the axial data. Then, using this vectorial statistics data, the mean direction is derived (see Equation 2.4).

$$\overline{C} = \frac{\sum_\theta h_{xy}(\theta)[\cos 2\theta]}{\sum_\theta h_{xy}(\theta)}, \; \overline{S} = \frac{\sum_\theta h_{xy}(\theta)[\sin 2\theta]}{\sum_\theta h_{xy}(\theta)} \tag{2.3}$$

Here, $\overline{C}$ and $\overline{S}$ are the weighted Cartesian coordinates of its vectorial counterpart.

$$(\overline{\theta}) = \begin{cases} 0.5 \arctan(\overline{S}/\overline{C}), & \text{if } \overline{C} \geq 0 \\ 0.5 \arctan(\overline{S}/\overline{C}) + \pi, & \text{if } \overline{C} < 0 \end{cases} \tag{2.4}$$

Then, the mean resultant length is defined (Mardia, 1999; Schad, 2017) as follows as a measure of the concentration:

$$\overline{R} = \sqrt{\overline{C}^2 + \overline{S}^2} \tag{2.5}$$

The resultant length helps quantify the concentration of the mean angles. In other words, it gives an idea of how concentrated (dispersed) angles are around the D_w. $\overline{R}$ is also related to the circular standard deviation (σ) (Mardia, 1999) as shown in the following Equation:

$$\sigma = \sqrt{-2 \ln \overline{R}} \tag{2.6}$$

Fisher and Lewis (1983) established an estimated confidence interval (with a confidence level of approximately 1-α) for the mean axial direction $\overline{\theta}$, without requiring assumptions about the underlying distribution shape. As the number of samples n becomes significantly large, the interval takes the following form (Schad, 2017):

$$\epsilon_\theta = sin^{-1}(u_\alpha \sqrt{\frac{(1-\alpha_2)}{2n\overline{R}^2}}) \tag{2.7}$$

Here, u_α represents the upper $\frac{1}{2}\alpha$ quartile of the standard normal distribution $N(0,1)$, while α_2 is associated with the distribution's variance and is calculated as:

$$\alpha_2 = \frac{\sum_\theta h_x y(\theta)[cos2(\theta - \overline{\theta})]}{\sum_\theta h_x y(\theta)} \tag{2.8}$$

RHT aims to detect structures with lengths greater than or equal to (D_w) and brightness greater than an intensity threshold Z. Choosing a wider D_k reduces the detection of rain clumps but also decreases background noise.

2.2.2.3 Outputs

There are four main outputs in the RHT algorithms. All these outputs are characterized by 3D dimensions, featuring positions x, y, and time t, and give spatial and temporal information for every input parameter. These outputs are itemized as follows:

Spatial Part

- resultant length ($\overline{R}_{xy}$)
- peak of the RHT function (max$[H_{xy}(\theta)]$)
- mean axial direction (θ_{xy})
- error in the mean axial direction (ϵ_{xy})

Temporal Part

- resultant length ($\overline{R}_{t}$)
- peak of the RHT function (max$[H_{t}(\theta)]$)
- mean axial direction (θ_{t})
- error in the mean axial direction (ϵ_{t})

The mean axial direction shows the spatial (θ_{xy}) and temporal (θ_t) direction of each detected pixel. The spatial mean angle is linked to rain inclination in the POS, while the temporal mean angle is associated with the dynamic variations along a given path. In the flare-driven (Section 5) case, a 0° spatial mean angle corresponds to the horizontal axis (x-axis), and increases in the anti-clockwise direction (vertical axis is then 90°). In the quiescent coronal rain case, a 90° spatial mean angle corresponds to the horizontal axis (x-axis), and increases in the anti-clockwise direction (vertical axis is then 0°). The reference direction for the temporal mean angle is aligned with the radially outward axis, and 0° corresponds to no motion and 90° (-90°) corresponds to maximum upward (downward) motion. The RHT function (both in spatial, $H_{xy}(\theta)$, and temporal, $H_t(\theta)$, parts) accumulates pixels in order to define mean directions accurately. To achieve this, an adaptive threshold (h_{xy}) is established using the RHT function peak (i.e., (max$[H_{xy}(\theta)]$)). Values lower than this threshold are excluded from the calculation of the mean direction. $\overline{R}$ indicates the dispersion of the length of the average vector in the mean axial direction, ranging from 0 to 1. A value around

0 indicates the presence of an ill-defined mean axial direction, while a value around 1 indicates a well-defined mean axial direction. ϵ is the final output generated by the RHT, which indicates the error in the mean axial direction. Please refer to the paper by Schad (2017) for a thorough description of these parameters.

2.2.3 Rain Shower Identification: Region Grow

The *region_grow* algorithm is used in image processing and computer vision to segment an image into distinct regions based on specific predefined criteria. The algorithm starts by selecting an initial seed point within the image and then expands the region by adding adjacent pixels that meet the predefined criteria. The process is repeated until the entire region is defined or until a stopping criterion is reached.

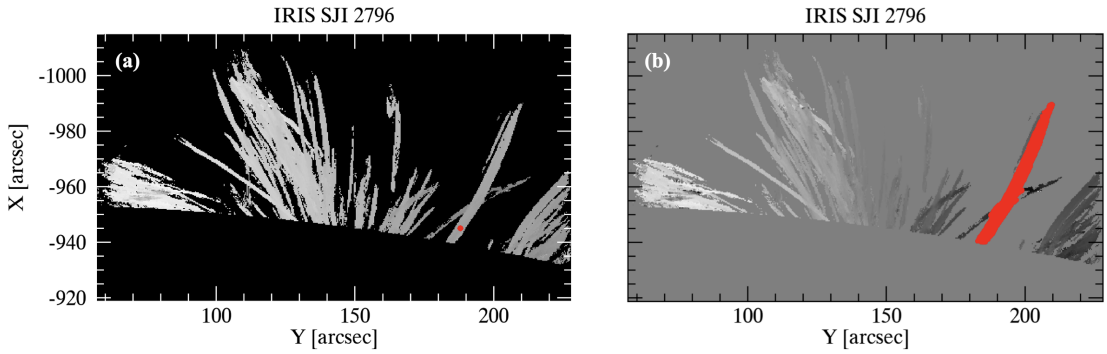

Figure 2.6: a) Single IRIS SJI 2796 Å image from one of the analysed data in Şahin and Antolin (2022), showing a selected region by the small red square. b) obtained segmented region using *region_grow*.

In this research, we used *region_grow* to identify rain showers. For this purpose, the information on spatial mean angle and time occurrence are initially extracted from the RHT routine for each pixel. Two shower events can have either similar paths but different occurrence times, or they can overlap but have different paths. Therefore, before applying the *region_grow* algorithm, we created a new array by multiplying time occurrence data with the spatial mean angle data. Then, the *region_grow* is applied to the newly obtained data to identify a shower. This pre-procedure effectively distinguishes between spatial and temporal overlap.

Figure 2.6 shows how the *region_grow* algorithm works. The red circle shows an initial seed point in Figure 2.6a. Then, adjacent pixels are checked according to the initial seed point. Suppose the neighbouring pixels meet the predefined rules (threshold or standard deviation). In that case, the

pixel is added to the region of the seed pixel and so on until no similarity remains (see Figure 2.6b).

2.2.4 Differential Emission Measurements

We have used the differential emission measure (DEM) to obtain information about the thermal structuring of the solar corona that hosts coronal rain. The DEM measurement provides a decomposition of the emission distribution of the plasma along the LOS according to its temperature.

Several routines have been developed to obtain DEM results from SDO/AIA images (Aschwanden and Boerner, 2011; Hannah and Kontar, 2012; Cheung et al., 2015; Plowman and Caspi, 2020). The algorithm developed by Hannah and Kontar (2012) struggles to remove negative emissions that are not realistic and may produce excessive high-temperature emissions in the results. Therefore, here, in this thesis, we have used two of them: the Basis Pursuit (bp) algorithm developed by Cheung et al. (2015) and a simple, robust algorithm ("simreg") by Plowman and Caspi (2020) to estimate the emission distribution of the coronal rain and its surroundings. The "basis pursuit" routine aims to identify the smallest set of non-zero basis coefficients necessary to accurately represent the data while accounting for reasonable uncertainties. To prevent undesirable negative outcomes, a positivity constraint is imposed on each of the non-zero coefficients that are determined. The DEM simple robust algorithm is a method designed to derive a differential emission measure distribution that is less sensitive to noise and uncertainties in the observed data. It focuses on minimizing the impact of measurement errors and outliers on the derived temperature distribution. This algorithm tends to provide a more reliable estimate of the true temperature distribution in the presence of noise and uncertainties.

Narrow-band EUV and broadband X-ray observations help understand the physical properties of the optically thin coronal plasma by integrating over temperature variations. The total intensity is given in Equation 2.9 for the EUV-UV optically thin lines.

$$I(\lambda) = \frac{1}{4\pi} \int_l \text{Ab}\, G(T_e, n_e) n_e n_H dl \tag{2.9}$$

Here, l denotes the LOS through the emitting plasma. The abundance of the element is given

by Ab with respect to hydrogen. $G(T_e, n_e)$ is the contribution function containing all the atomic physics parameters. n_e, T_e, and n_H are the electron number density, temperature, and hydrogen number density, respectively.

The distribution of the plasma emission measure (EM) with temperature along the LOS (l) is calculated in the following equation:

$$EM = \int_l n_e n_H dl \tag{2.10}$$

Then, the DEM is proportional to $n_e n_H$ in the temperature intervals dT_e, and it is obtained by the following equation:

$$DEM(T_e) = n_e n_H \frac{dl}{dT_e} \tag{2.11}$$

Here, $n_e(T)$ represents the electron number density of plasma at a certain temperature T. The emission measure (EM) is obtained by integrating DEM over a finite temperature range. The main aim is to use EUV imaging to deduce the EM distribution in the solar corona.

The effective temperature (DEM-weighted average) is obtained as follows:

$$T_{eff} = \frac{\int DEM(T) \times T dT}{\int DEM(T) dT} \tag{2.12}$$

Even though AIA has seven EUV channels, the DEM routine uses six (94, 131, 171, 193, 211, and 335 Å channels, i.e., m=6) of them to obtain EM measurements. The reason for this is emission in the AIA 304 is often optically thick, which cannot be accurately modelled with the CHIANTI database under the optically thin assumption. On the other hand, the DEM routine returns a series of EM maps calculated over a user-defined temperature range (denoted as N), which spans any $\log$T[K] value to another $\log$T[K] value at intervals of $\Delta \log$T[K] (for instance, 18 temperature bins (i.e., N=18) spanning $\log$T[K]=5.5-7.2 at intervals of $\Delta \log$T[K]=0.1).

This section provided a basic statement of the DEM, establishing the foundational understanding of this technique. Building upon this basis, the selection of the DEM version and temperature bins

with intervals will be presented for the purpose of each study.

2.2.5 Detection of the Long-period EUV Intensity Pulsations

In this thesis, I use an automatic long-period EUV intensity pulsations routine developed by Auchère et al. (2014) and Froment (2016). The automatic detection routine utilized for identifying the pulsations is briefly summarized in Figure 2.7. A detailed description can be found in Auchère et al. (2014) and Froment (2016).

First, the routine builds an AIA image cube in the specified spectral band (94 Å, 131 Å, 171 Å, 193 Å, 211 Å , and/or 335 Å) from a starting date and end. Using the *aia_prep* procedure of the IDL SSW, the AIA data are read and calibrated to L1.5. Then, we first normalised the intensity data to exposure times and applied 4x4 pixel binning to enhance the signal-to-noise ratio. Further details can be found in Froment et al. (2017, 2020). Second, Fourier analysis is performed independently on each cube pixel, in other words, on each time series independently. Each time series is resampled at a frequency twice greater than the data selection frequency chosen to build the cube to satisfy Shannon's theorem. To avoid aliasing, the time series are apodized with a sine on 5% of the signal at each foot. The power spectrum is calculated using a Fast Fourier Transform (FFT) algorithm. Each power spectrum (PSD: Power Spectral Density) is normalized to the variance of the signal (σ_0^2). To determine if a coherent signal exists at a particular frequency bin, each bin's value is compared to the average local power. The average local power is assumed to be representative of locally present white Gaussian noise (Torrence and Compo, 1998), which acts as the background power. If the value of a frequency bin in the PSD is significantly higher than the average local power, it indicates the potential presence of a coherent signal at that frequency. White noise is a type of random signal with a constant power spectral density (equal energy at all frequencies). Here, the main criterion is a detection threshold 10σ above (solid line in Figure 2.8) an estimate of the average local power (dashed line in Figure 2.8). The reason behind this is if the value of a frequency bin is greater than "m" (10σ, i.e. m=10) times the average local power, it suggests a higher probability that a coherent signal is present at that specific frequency (i.e. the signal is stronger than the local background noise).

The confidence level (so-called global probability) is calculated as follows:

$$Pg(m) = 1 - (1 - e^{-m})^{N/2} \tag{2.13}$$

Here, N is the number of data points in the time series (Auchère et al., 2016). This equation explains the probability that, among the N/2 frequency bins, there is at least one peak of power greater than mσ that occurs purely by random chance and not due to any underlying signal or pattern of interest.

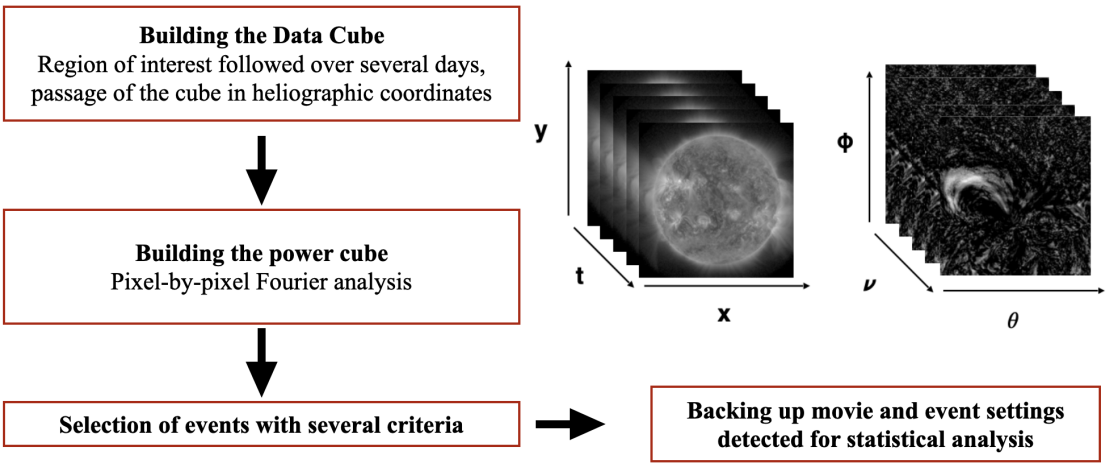

Figure 2.7: Representative diagram of the main steps followed in the long-period EUV intensity pulsations routine (With permission, this diagram is adapted from Froment (2016) thesis.)

It may be worth noting that in the detection routine, the images are actually converted to Carrington heliographic coordinates (see (Thompson, 2006)), and the differential rotation is corrected for on-disk data sets. However, in the thesis, we analyse off-limb data sets. We, therefore, do not compensate for the solar rotation, which led to slight shifts in the position of structures over the three-day observed period (see Section 3.2). However, it was observed that the pulsations corresponded to large areas in the POS, as shown in Figure 2.8 and also in Froment et al. (2015, 2020). As a result, small spatial shifts over time did not significantly reduce the Fourier power of all pixels, making the pulsations detectable. The off-limb application was also tested by Froment et al. (2020), and the three-day interval at the solar limb was a good compromise, as changes due to rotation did not significantly affect the height of the structures off-limb and allowed for reasonable frequency resolution.

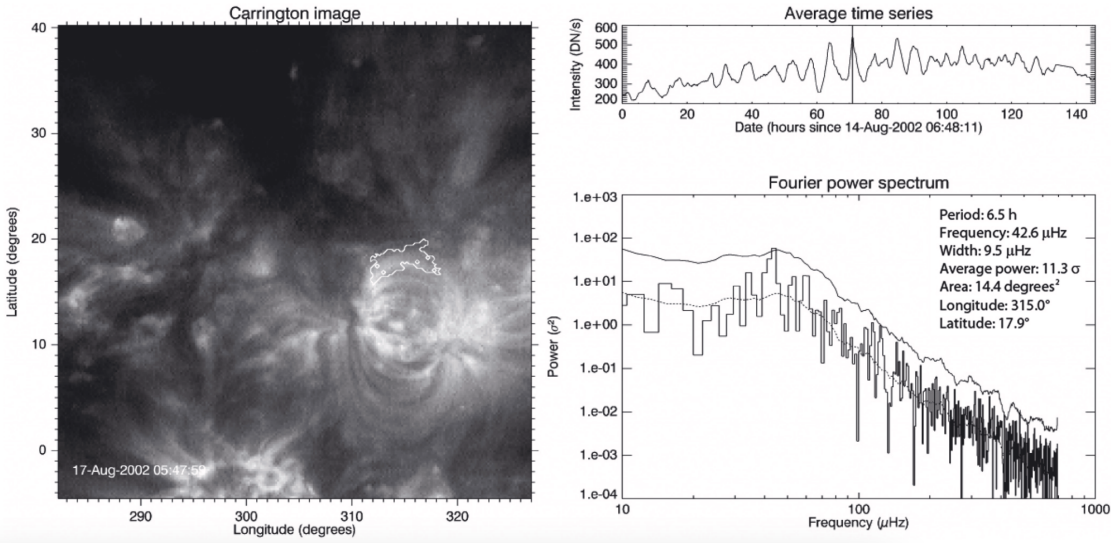

Figure 2.8: Left: the studied region by Auchère et al. (2014). The white contour shows the detected event from the long-period EUV intensity pulsation routine. Right: The average intensity variation over the white contour region (top) and obtained Fourier power spectrum (right). The average local power and detection threshold (10σ) is given by the dashed and solid lines.

2.2.6 Resolving AIA 304 channel emission

The AIA 304 passband exhibits two peaks (shown by red arrows in Figure 2.9) in temperature response functions. The first one is He II 303.8 Å emission at 10^5 K, and the second one is Si X 303.32 Å emission at $10^{6.2}$ K. Hereafter, these emissions are referred to as the cool and hot components, respectively. In the off-limb coronal rain observation, the hot component (i.e. Si X) originating from the surrounding diffuse hot corona has a greater extent along the LOS than the cool clumpy component (i.e. He II), which results in comparable intensity. In addition to temperature, there is a distinct difference in the appearance of plasma emissions. The hot emission is diffuse, while the cool emission appears clumpy. In this PhD thesis, two different approaches are used to separate hot and cool components. The first one is a morphology-based approach known as Blind Source Separation (BSS). The second one is the temperature-based approach called the Response Fitting (RFit).

2.2.6.1 Blind Source Separation (BSS)

The Blind Source Separation (BSS) routine developed by Dudok de Wit et al. (2013) based on the fixed-point fast Independent Component Analysis (FastICA) method (Hyvarinen, 1999) is used to separate the hot and cool components in the AIA 304 Å images. BSS decomposes images (or

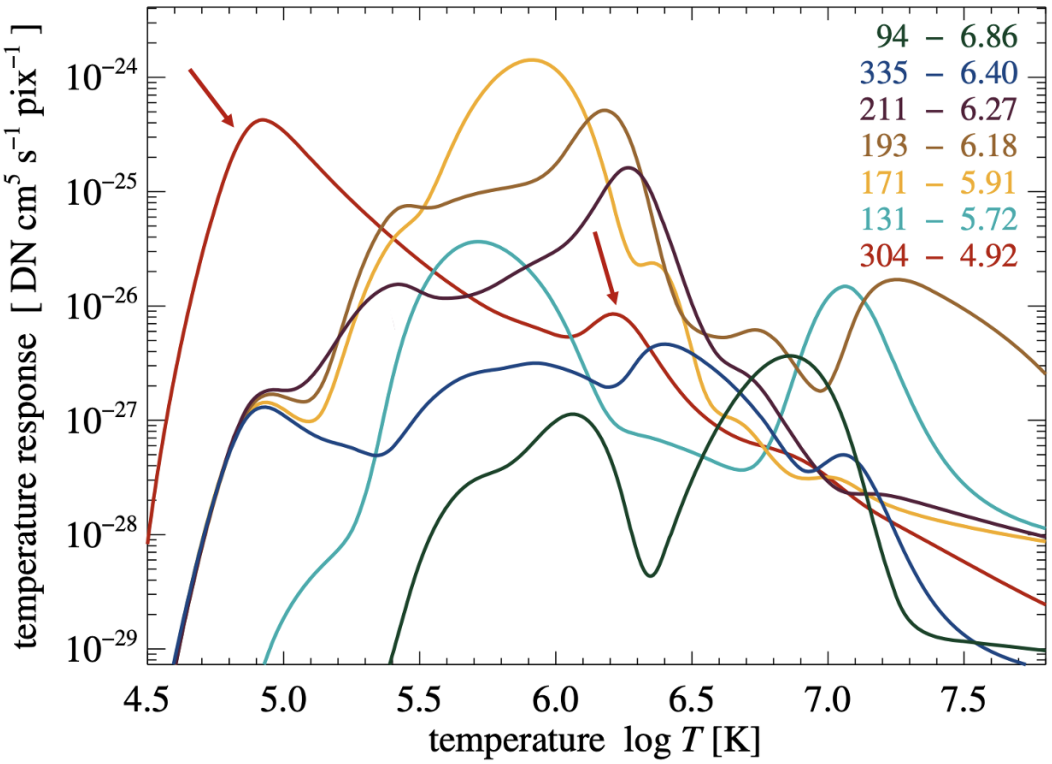

Figure 2.9: AIA temperature response functions (Adapted from Peter et al. (2012).)

signals) into sources that are independent of each other. The intensity of an AIA passband is given in the following equation:

$$I_\lambda = \sum_{k=1}^{N} V_{k,\lambda} S_k + B_\lambda \tag{2.14}$$

Here, S_k denotes the source components and $V_{k,\lambda}$ is the mixing coefficients. Instrumental noise and other errors are given with B_λ. First, a set of m equations is generated for each AIA passband, and then source terms and mixing coefficients are obtained by minimizing errors. N in Equation 2.14 refers to the number of sources and must be specified beforehand. It is important to identify a minimum number of N source images in each AIA passband from which most of the original image can be recovered. Since there was not much improvement for N>3 (Dudok de Wit et al., 2013), Antolin et al. (manuscript in preparation) took N=3 and tested different combinations of various AIA channels, obtaining the combination of four source AIA passbands (AIA 193, 211, 304, and 335 Å) as a good compromise. Each source function focuses on specific morphological structures and has a narrow temperature response with little overlap with other sources. This

essentially improves the sources as temperature gauges and Equation 2.14 turns into the following equation:

$$I_{304,c}^{BSS} = \sum_{k=1}^{3} V_{k,304} S_k \tag{2.15}$$

Here, $I_{304,c}^{BSS}$ represents the cool 304 components of a AIA 304 Å image; hereafter, we refer to it as cool AIA 304 Å. V_k and S_k indicate the mixing coefficients of cool emission and source terms, respectively. The hot component of the channel is obtained using the following equation:

$$I_{hot_j}^{BSS} = \sum_{k=1}^{3} V_{k,hot_j} S_k \tag{2.16}$$

where j=1,2

The original (left), cool (middle) and hot (right) AIA 304 Å images are shown in Figure 2.10. The cool AIA 304 Å data are used in Chapter 3.

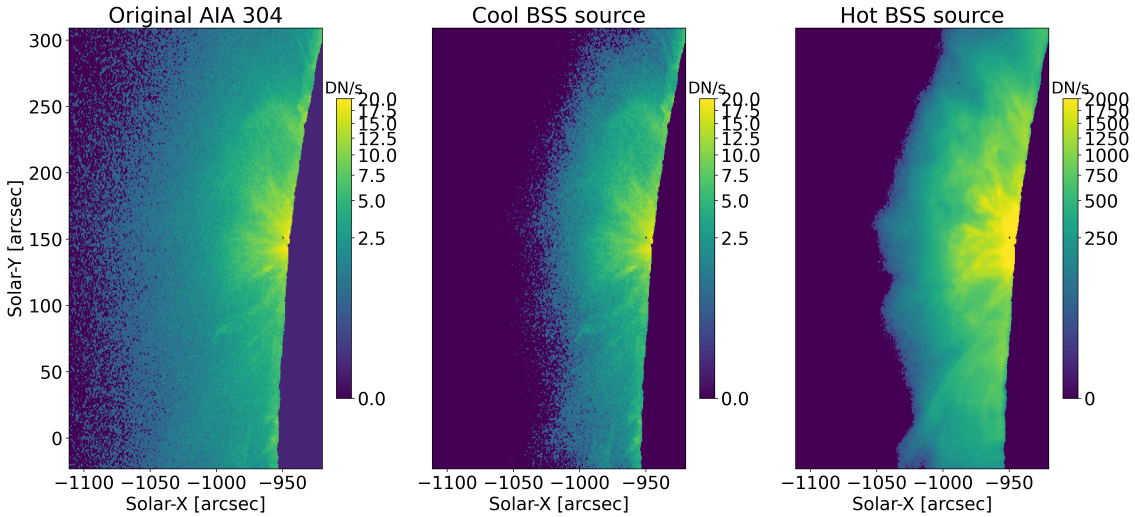

Figure 2.10: Comparison between original AIA 304 Å (left), cool AIA 304 Å (middle), and the hot AIA 304 Å (right) using the BSS approach. The solar disk is removed for better improvement.

2.2.6.2 AIA 304 response fit (RFit)

This method also aims to separate hot and cool components from the AIA 304 images. However, this method relies on understanding how the AIA 304 Å response function (see Figure 2.9) changes in relation to temperature. As can be seen in this figure, the first peak of the AIA 304 Å is isolated

on the left side, which corresponds to the cool temperature range. The second AIA 304 Å peak is located in the hot temperature region where there is a large overlap of EUV response functions. This indicates that a suitable decomposition of the hot part of the AIA 304 response function can always be found with all other EUV response functions.

In the RFit routine developed by Antolin et al. (manuscript in preparation), everything above logT=5.8 (in Figure 2.9) is defined as the hot temperature range in the AIA 304 emission. Then, everything below logT=5.5 is set to 0 and apodized with a cosine function between logT=5.5 and logT=5.8 to obtain the hot AIA 304 emission response function to fit ($R^a_{304,h}$). Apodisation minimizes the impact of lower temperature boundary fitting. The fit to $R^a_{304,h}$ with all other response functions is minimized using the least squares method (see Equation 2.17).

$$R^a_{304,h} = c_1 R_{94} + c_2 R_{131} + c_3 R_{171} + c_4 R_{193} + c_5 R_{211} + c_6 R_{335} \tag{2.17}$$

Here, $c_1 ... c_6$ represents the coefficients resulting from the fitting.

In the next step, the dot product is obtained between the coefficients ($c_1 ... c_6$) and the 6 AIA EUV images ($I_{6,EUV}$) that use response functions (in the same order) in the fitting procedure to obtain the hot component of the AIA 304 image, as given in Equation 2.18.

$$I^{RFit}_{304,h} = I_{6,EUV} \cdot \overline{c} \tag{2.18}$$

Here, the current 304 response fit method is given by "RFit". Finally, the hot component of the AIA 304 emission is subtracted from the original image (I_{304}) to obtain the cool AIA 304 Å emission (see Equation 2.19).

$$I^{RFit}_{304,c} = I_{304} - I^{RFit}_{304,h} \tag{2.19}$$

The original (left), cool (middle) and hot (right) AIA 304 Å images are shown in Figure 2.11. The cool AIA 304 Å data are used in Chapter 5.

Here, in this section, we presented two approaches to separating the hot and cool components

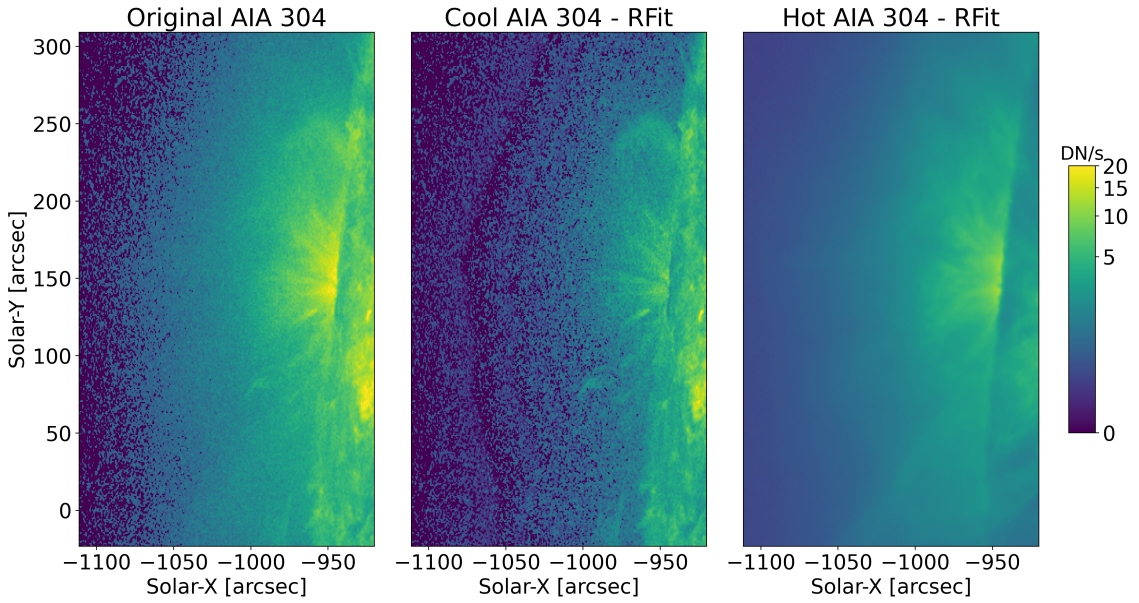

Figure 2.11: Comparison between original AIA 304 Å (left), cool AIA 304 Å (middle), and hot AIA 304 Å (right) using the RFit approach.

from AIA 304. In the RFit method, the intensities are expected to add up (as shown in Equation 2.19, i.e., Original image = cool + hot), meaning that we have one cool and one hot image from the original AIA 304 image. However, the BSS method differs from RFit in generating the cool and the hot emission. As mentioned in the previous section, in the BSS routine, we have as many images (N) as there are sources, and the user should identify a minimum number of N source images. Based on the result of Dudok de Wit et al. (2013), in our study, we have chosen 3 images (i.e. N=3), and we obtain one cool image, corresponding to the cool AIA 304 image, and two hot images, correlated with AIA 193 and AIA 94.

The ability of RFit to provide a hot AIA 304 image in addition to the cool AIA 304 image made it more useful in the flare-driven dataset (see Section 5) than the BSS routine. Indeed, the hot AIA 304 image allowed an additional view of the chromospheric evaporation dynamics. For the quiescent rain dataset (see Section 3), this was not required. However, the BSS method seems to perform better in noisy datasets, removing better the noise from the image, as can be seen comparing Figures 2.10 and 2.11. Hence, the BSS method was chosen over the RFit method for the quiescent rain dataset.

Chapter 3

Quiescent Coronal Rain Analysis

In this chapter, I build upon the findings and insights presented in my paper[3] titled "Spatial and Temporal Analysis of Quiescent Coronal Rain over an Active Region". The content covered here draws extensively from the information and results detailed in that paper, allowing for a deeper exploration and analysis within the context of my thesis.

3.1 A Brief Overview

Coronal rain is a remarkable phenomenon that is produced in the corona and is characterized by its significantly cooler and denser composition compared to its surroundings. Its morphology, origin, and dynamics remain poorly understood despite its connection to coronal heating. The TNE-TI scenario, which suggests that TI occurs in coronal loop structures experiencing TNE, is the leading theory for its origin.

This chapter presents the first high-resolution statistical investigation of quiescent coronal rain over an AR and long temporal scales of EUV intensity pulsation to provide valuable insights into the distribution, dynamics, and behaviour of coronal rain, using IRIS and SDO imaging data. It also contributes to advancing our knowledge of coronal rain and the occurrence of the underlying mechanisms.

Our findings reveal a pervasive presence of coronal rain throughout the observed AR, irrespective

[3] Şahin, S., Antolin, P., Froment, C. and Schad, T. (2023). Spatial and Temporal Analysis of Quiescent Coronal Rain over an Active Region. The Astrophysical Journal Letters, 950, 171.

of loop inclination, exhibiting minimal variation over a 5.45-hour observation period. The majority of the coronal rain follows a downward trajectory (87.5%), although upward motions (12.5%) are pervasive as well. The dynamics of rain exhibit a notable consistency across the range of temperatures observed, hinting at a co-localization of the TR and chromospheric emissions on average.

We also revealed the prevalence of long-period EUV intensity pulsations within the AR. Surprisingly, we detected a shorter periodicity (16 minutes) associated with the appearance of coronal rain and present challenges in explaining the short-term periodicity under the TNE-TI scenario.

3.2 Data and Method

3.2.1 Data

The studied AR was observed on June 2 2017, between 07:28:00 UT - 12:54:39 UT (5.45 hours) when it was close to the Solar East limb (see Figure 3.1). Level 2 SJI data from IRIS (De Pontieu et al., 2014) are used in this study, which combines both near-UV (NUV) and far-UV (FUV) passbands. One of them is centered on 1400 Å (dominated by the Si IV 1402.77 Å TR line forming at $10^{4.8}$ K) and other one is centered on 2796 Å (dominated by the Mg II 2796.35 Å chromospheric line forming at 10^4 K). IRIS spectrograph has a 64-step raster observation centred at [-970″,143″] with a maximum SJI FOV of 232″$\times$182″. The SJI data sets have a pixel scale of 0″.3327 pixels^{-1} and an exposure time of 15 s. The average cadence for the SJI 1400 and 2796 is 43.1 s and 32.3 s, respectively. We also analyzed this AR using the SDO/AIA observations with a cadence of 12 s. The exposure time for this dataset is around 2.9 seconds. We particularly analyzed the AIA 304 Å channel, which is dominated by the He II line and forms at approximately 10^5 K, to detect and study the rain. The AIA observations have seven passbands, but we specifically focused on the AIA 304 Å channel. The AIA pixel size is originally 0″.6 pixel^{-1}, but we have adjusted it by rebinning to align with the SJI plate scale. To differentiate between the data sets used in this study, we will assign specific names to each. The data set mentioned earlier will be called the "rain data set," and the data set presented below will be called the "pulsation data set." We analyze the long-term intensity pulsations in the AR over three days in all seven AIA EUV channels (94, 131, 171, 193, 211, 304, and 335 Å), starting from the 1st to 4th of June, using Level

1.5 datasets. The FOV for this channel is 332″ × 282″ (shown in Figure 3.1, right panel) with a centre at [-970″,142″]. The cadence for these data set is 5 minutes. The AIA data are processed using the routine "aia_prep" in IDL SSW to read and calibrate to Level 1.5. The intensities are normalized based on exposure times, and the signal-to-noise ratio is improved by applying a 4×4 pixel binning (see Section 2.2.5 and see Froment (2016)). We also investigate the presence of short-term periodicities (i.e., <1 hour) using the "rain data set" in the same AR, contrary to the previous works.

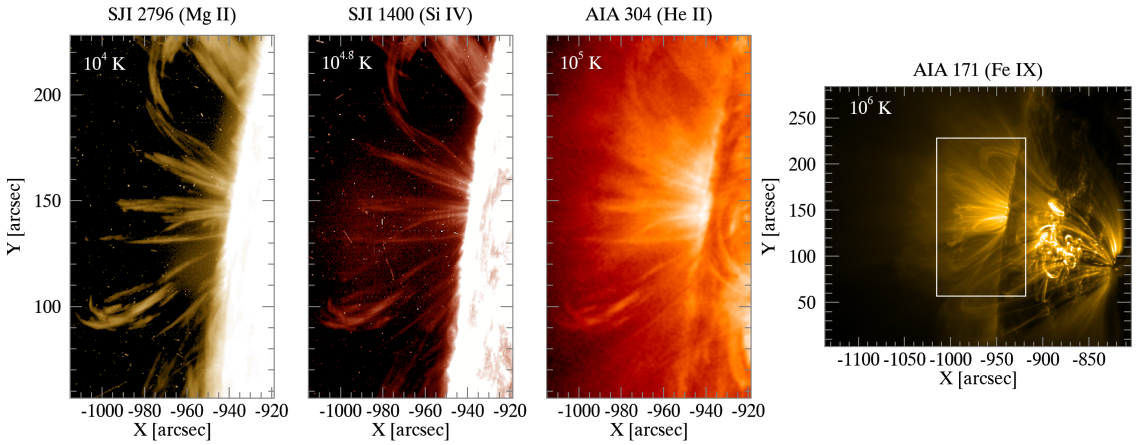

Figure 3.1: The studied AR of the Sun on 2 June 2017 taken by SJI 2796 Å, SJI 1400 Å, and AIA 304 Å, respectively, (from left to right). The most right panel displays a wider FOV with AIA 171 Å over the same AR. The white rectangle corresponds to the FOV shown on the left images. All SJI and AIA images were obtained by summing over ten images in the interval 07:28 - 07:34 UT. The movie of this figure is available in Şahin et al. (2023).

3.2.2 Data preparation

As explained in Section 2.2.1 and in Şahin et al. (2023), the AIA data are adjusted to align the SJI plate scale to ensure precise alignment between these channels. Co-alignment is achieved by comparing the features observed on off-limb and on-disk in the co-temporal images of SJI 2832 Å and AIA 1600 Å. The data in these two filters is captured under similar conditions, ensuring accurate alignment between these two channels. At various time intervals, x and y shifts are obtained, and then an interpolation process is performed to estimate shifts for any other time sequence. After that, these computed shifts are applied to all other channels accordingly.

IRIS channels exhibit a discernible influence of scattered light, which is pointing-dependent, as outlined in Wülser et al. (2018). This can be challenging to characterize off-limb observations.

As a consequence of this imperfect flat-fielding and scattered light in IRIS's raster mode, the resulting SJI images display a background contribution exhibiting apparent motion relative to the solar image. This phenomenon introduces a non-trivial time-dependent noise, leading to 17.2 min periodic intensity increases in the SJI 1400 Å and SJI 2796 Å images. This artificial periodic intensity is more noticeable in SJI 2796 Å closer to the limb, while it is comparatively more distinct in SJI 1400 Å relative to coronal rain intensity occurring at higher heights. To reduce this noise, the method involves computing the minimum intensity evolution over a grid in both SJI channels for each pixel. Then, these cubes are normalized by dividing each pixel and time step by its corresponding minimum intensity value.

As mentioned in Section 2.2.6, the AIA 304 Å passband exhibits two main peaks in the temperature response function, which have comparable intensities. To separate these cool and hot emissions in the AIA 304 Å emission, the BSS technique is employed (see Section 2.2.6). The subsequent analysis during this study utilizes the modified cool AIA 304 Å images to display the results from the cool emission.

3.2.3 Detection of coronal rain

Before running the semi-automatic technique for detecting coronal rain, the solar limb and its region were removed to prevent its large brightness contrast. Besides, to avoid most spicules and other low-lying, cool features, the spicular region above the solar limb was also removed. These features are commonly observed at altitudes between 4 and 10 Mm above the solar surface (Beckers, 1968); therefore, the minimum height for the spicular region was chosen as 6 Mm from the off-limb FOV. Then, the RHT algorithm (as described in detail in Section 2.2.2) was applied to detect and quantify the observable coronal rain motion.

For the running mean filters (w_r), 13-step(≈7 minutes), 10-step (≈7 minutes), and 17-step (≈3 minutes) were used for the SJI 2796 Å, SJI 1400 Å, and AIA 304 Å, respectively. For the bidirectional filter, a 5-step (≈3 minutes for the SJI 2796 Åand ≈4 minutes for SJI 1400 Å) bidirectional filter was used in the SJI channels and a 21-step (≈4 minutes) filter for the AIA 304 channel. The reason why the large step size is used in AIA 304 Å is to accommodate for the faster cadence. For instance, for ≈70 km s^{-1} flow, the number of SJI pixels the flow would cross would be ≈62 pixels. This is large enough to calculate the evolution of the flow accurately. However, the same

bidirectional filter step in AIA 304 Å results in ≈17 pixels, which is insufficient. Therefore, a 21-step bidirectional filter is used for the AIA 304 Å, and ≈73 pixels for the distance covered by the rain, matching the results with the SJI filter. RHT kernel width was chosen as 29 (i.e., $D_w = 29$) for all channels. The standard deviation (σ) for the background noise was chosen as 2 (for SJI 2796 Å), 2.1 (for SJI 1400 Å), and 0.008 (for AIA 304 Å). The reason behind the different noise values in AIA 304 Å is because of the preprocessing image technique (BSS), as explained above.

In total, 4×10^6, 2×10^6, and 3×10^6 rain pixels were detected in SJI 2796Å, SJI 1400Å, and AIA 304Å, respectively. Afterwards, we applied the following conditions. Pixels were included from all channels if they met the criteria: $\overline{R}_{xy} \geq 0.8$, $max[H_{xy}(\theta)] \geq 0.75$, $\overline{R}_t \geq 0.8$, $max[H_t(\theta)] \geq 0.75$. In addition to this, for the AIA 304 Å channel, the condition was set at $|\overline{\theta}_t| \leq 84^\circ$, while for both SJI channels, it was set to $|\overline{\theta}_t| \leq 88^\circ$ (see Figure 3.2), since the resulting velocity error is larger than the reasonable maximum cut-off for measurable projected velocity. The calculation of a reasonable maximum cutoff velocity is given in Schad (2017) as the following equation:

$$V_{cutoff} = \frac{\delta_x}{\delta_t} \tan(\pi/2 - \delta_\theta) \tag{3.1}$$

Here, δ_θ is the angular sampling of the RHT (i.e., $= 1/(D_w - 1)$, with Dw the kernel width). A reasonable maximum cutoff for measurable projected velocities for AIA 304 Å and SJI channels is 591 km s^{-1} and 215 km s^{-1}, respectively. Using the above condition, the results shown here are limited to ≈215 km s^{-1}.

The confidence interval is given in Equation 2.7 in Chapter 2.2.2.2, which is derived from the RHT angles. Therefore, it also gives the error estimation for the derived projected velocities as follows (Schad, 2017):

$$\delta v_{||} \approx (\frac{\delta_x}{\delta_t}) \frac{|tan(\overline{\theta}_t + \epsilon_\theta|_t) - tan(\overline{\theta}_t - \epsilon_\theta|_t)|}{2} \tag{3.2}$$

In Figure 3.2, the average 68% (green) and 95% (blue) confidence intervals are shown for the total projected coronal rain velocities for the SJI 2796 Å (a) and AIA 304 Å (b,c). For the $|\overline{\theta}_t| \leq 88^\circ$, AIA 304 Å shows large errors for high velocities, while for $|\overline{\theta}_t| \leq 84^\circ$, the errors are reasonable

(panel c).

After all these conditions, the remaining rain pixels are 7×10^5, 2×10^5, and 3×10^5 in the SJI 2796Å, SJI 1400Å, and AIA 304Å, respectively.

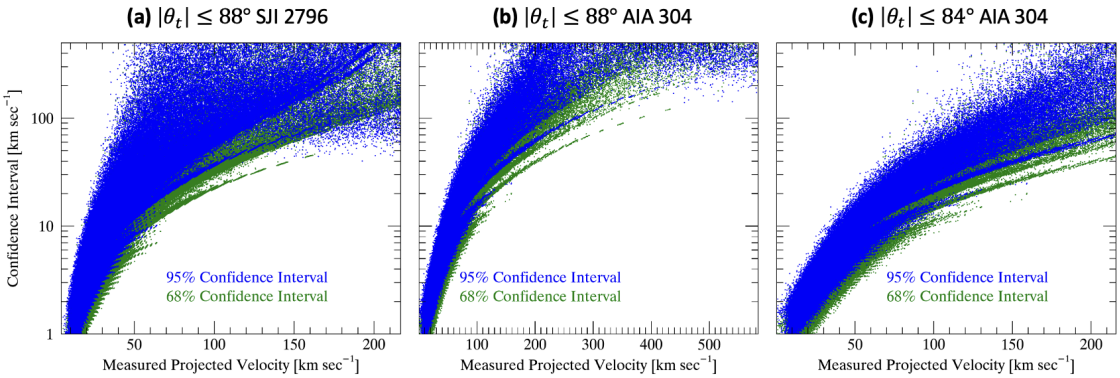

Figure 3.2: Confidence intervals for the projected velocity of the SJI 2796 Å (a) and Cool AIA 304 Å (b,c) with different conditions.

3.2.4 EUV Pulsation Detection

A study was conducted on 3-day data (i.e. "pulsation data set.") with a cadence of 5 minutes, spanning from 2017 June 1 at 05:00 UT to 2017 June 4 at 05:15 UT, for the long-period pulsation analysis. The study utilized AIA channels and implemented a modified version of the automatic detection algorithm (see Section 2.2.5) developed by Auchère et al. (2014) and by Froment (2016), specifically adapted for off-limb observations (Froment et al., 2020).

3.3 Results

3.3.1 Spatial and Temporal Mean Angle and Rain Occurrence

Figure 3.3 shows the average spatial ($\overline{\theta}_{xy}$; top panels) and temporal ($\overline{\theta}_t$; middle panels) mean angle maps over an entire observational time. Here, the spatial mean angle maps illustrate the rain inclination in the POS relative to the vertical direction, whereas temporal mean angle maps reveal the dynamic variations along a given path. All the coloured pixels in these maps represent coronal rain pixels, which occupy a large POS area over the AR. The FOV contains approximately ten times more rain pixels; however, not all are shown in these panels. This is due to the strict conditions mentioned above for detecting coronal rain pixels. In this way, the rain dynamics and

trajectories are accurately captured.

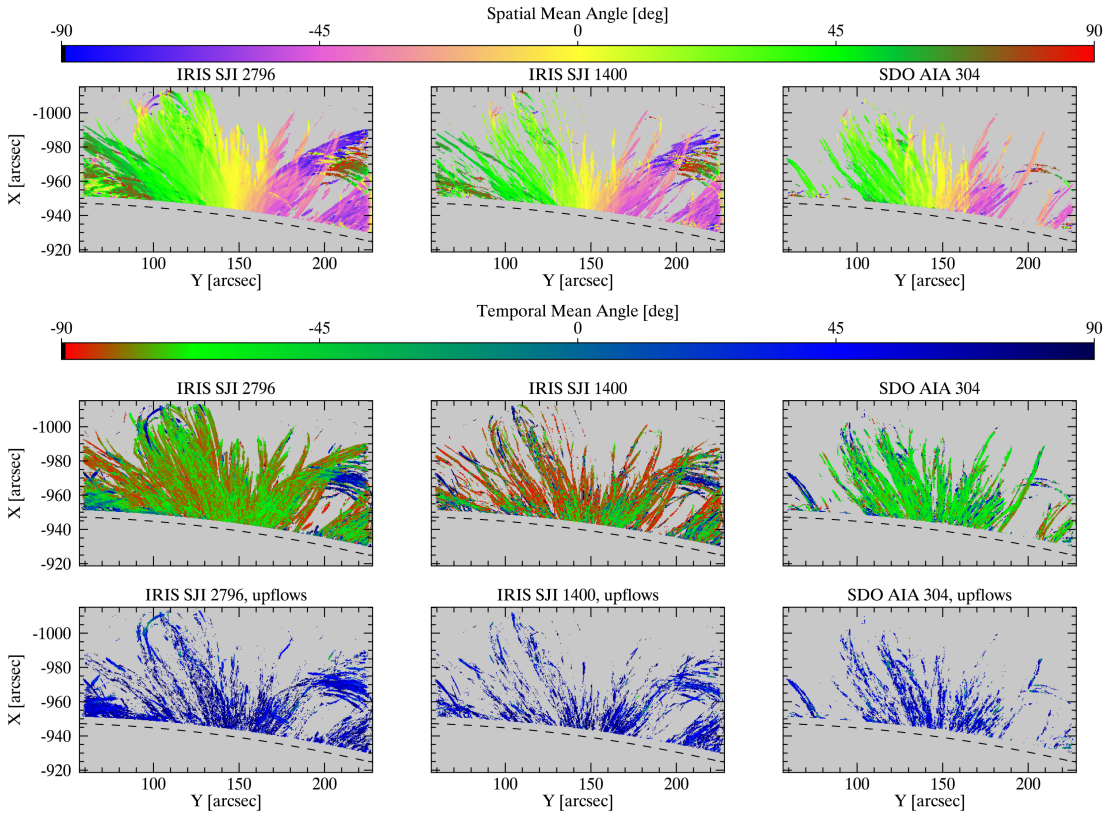

Figure 3.3: Average spatial (top) and temporal (middle and bottom) mean angles maps over the whole observational time. Average temporal mean angle maps show the upflow and downflow motions (middle), and upflow motions (bottom) only. The dashed black curves denote the solar limb.

The rain trajectories observed were consistent with the large-scale magnetic field topology of the active region, which was centred on the sunspot within the FOV. This study represents the first instance of achieving extensive, high-resolution tracking of coronal field lines using coronal rain on such a large scale. The green and red colours in the bottom panels of Figure 3.3 represent downward motion in the temporal mean angle maps. As seen on these panels, the downward motion is more dominant than the upward motion (shown by blue colours), as expected from the gravity effect on coronal rain. The total rain pixel numbers of downflow and upflow motions and their percentage are given in Table 3.1. As shown in the table and also seen on the bottom panels in Figure 3.3, the upward motions are also ubiquitous, particularly near the sunspot. This is unsurprising as gas pressure can impact coronal loops, as shown in previous research (Antolin et al., 2010) and confirmed by numerical simulations (Oliver et al., 2014; Li et al., 2022).

Table 3.1: The obtained rain pixel numbers of downflow and upflow motions and their percentage representation in all three channels.

Channel (Å)	$N_{downflow}$	$\%_{downflow}$	N_{upflow}	$\%_{upflow}$
2796	6×10^5	90	7×10^4	10
1400	2×10^5	83	3×10^4	16
304	29×10^5	89	3×10^4	11

Figure 3.4 shows the percentage difference in the occurrence of coronal rain (on the top panels) across the channels, along with scatter plots presenting the Pearson correlation coefficient of the spatial mean angle maps (on the bottom panels). In these panels, an equal number of time steps and the absolute spatial mean angle values were used across channels in order to obtain the difference maps in the occurrence of coronal rain. The SJI 1400 Å passband has the lowest cadence (43.1 s); therefore, it is used as a reference channel. Then, the closest times on SJI 2796 Å and AIA 304 Å are found according to it. The total number of rain pixels is calculated for each pair of cubes in this set of three. Then, the result is gathered in a new cube, based on their x and y positions over time, considering rain pixels as any spatial mean angle values that are nonzero. Finally, the difference between the two is computed, and this result is divided by the total number of images to yield the percentage difference in the occurrence of coronal rain.

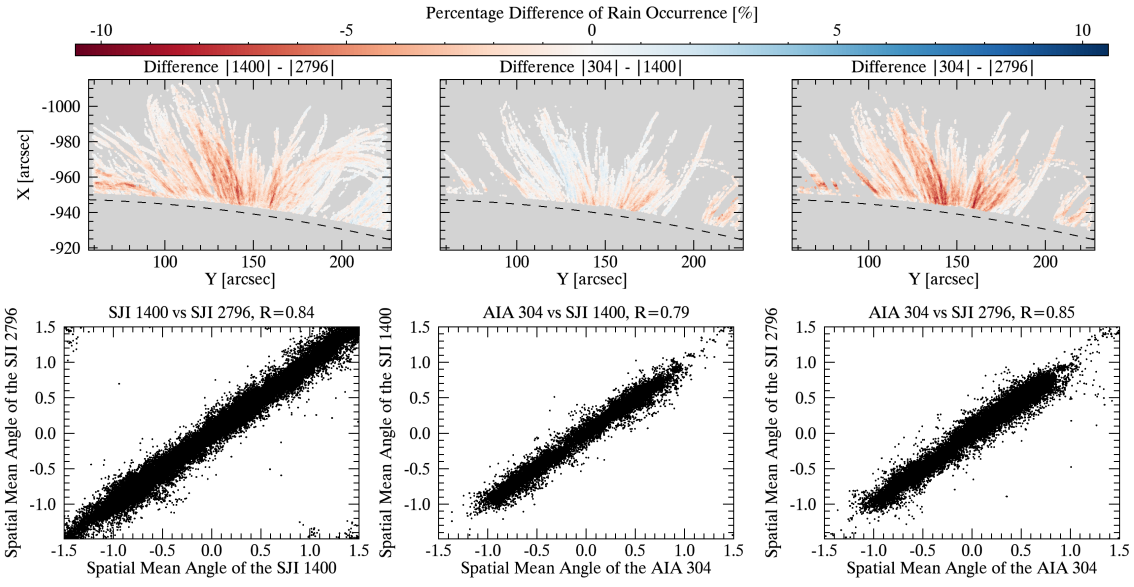

Figure 3.4: Top: Percentage difference panels in coronal rain occurrence. The solar limb is indicated by the dashed lines. Bottom: The scatter plots of the spatial mean angle maps. In the title of these scatter plots, the Pearson correlation coefficient (R) is given.

The scatter plots in the bottom panels in Figure 3.4 demonstrate a strong correlation (R=0.84 be-

tween SJI 1400 Å and SJI 2796 Å, 0.79 for AIA 304 Å and SJI 1400 Å, and 0.85 for AIA 304 Å and SJI 2796 Å) in coronal emission in all channels, which suggests that coronal rain is multithermal at a global level, where chromospheric emission is colocated on average with TR emission. However, strong localized differences are also seen in all channels in top panels in Figure 3.4. From the top right and left panels, more rain can be seen in SJI 2796 Å than in SJI 1400 Å and AIA 304 Å toward the footpoints. In the top middle panel, more rain emission in SJI 1400 Å is seen than in AIA 304 Å. These differences could also arise from line opacity (intensity), their contrast with the background, the instrumental spatial resolution and low instrumental sensitivity (particularly for AIA 304 Å).

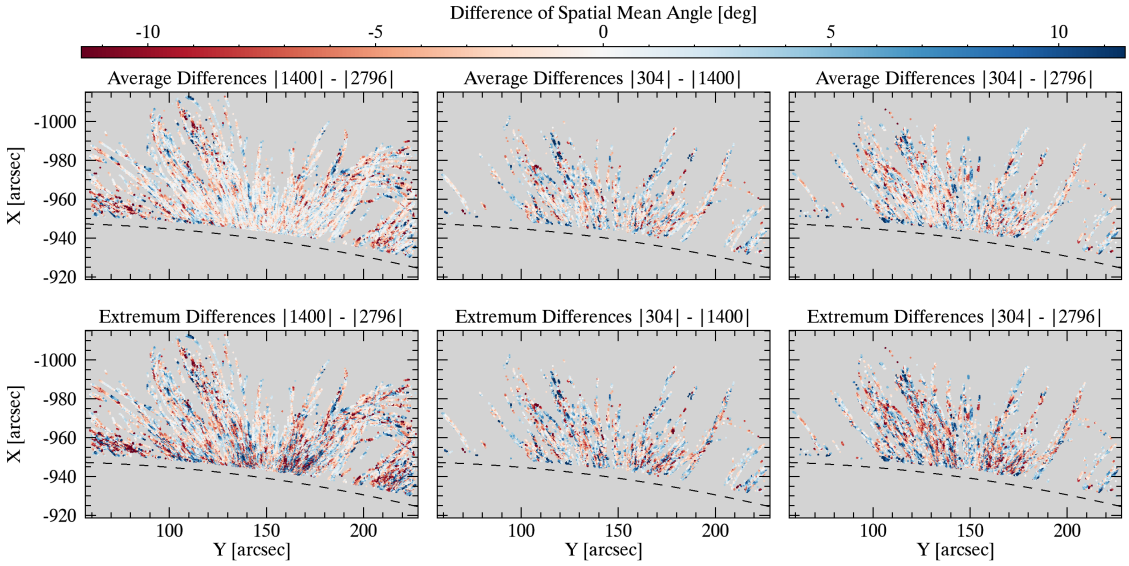

Figure 3.5: Average (top panels) and extremum (bottom panels) difference of absolute spatial mean angle as shown in Figure 3.3. To see the spatial variation better, we saturated these panels by 11°. The solar limb is indicated by the black dashed lines.

In Figure 3.5, we show the average and extremum difference maps of absolute spatial mean angle on the top and bottom panels, respectively, to examine the variations in trajectories across the temperature range. Similar to Figure 3.4, an equal number of images are used for the channels. First, common non-zero locations to both channels are found. Then, the difference between them is taken. Next, for a given time t, a time length around t is chosen to be equal to the running mean filter (see Section 2.2.2). This approach ensures that significant changes are locally seen within the selected time interval. The average and extremum of the differences between the two channel pairs over this time range (excluding zero instances) were computed, and these values were stored in two new cubes. This process was repeated for all spatial pixels. Finally, the average and extremum

of these two cubes over time were calculated over all non-zero time instances (see Figure 3.5 top and bottom panels, respectively). On average, the differences across channels are below 10°, while the extremum values cluster around 10°, with a few isolated instances reaching up to 20°. Here, the figure is saturated at 11° to see clear spatial trends). The panels for $|1400| - |2796|$ indicate that, on average, differences occur in regions with inclined structures or loop apexes. In addition to this, an increased variation can also be seen close to the solar surface or sunspot. Panel $|304| - |1400|$ and panel $|304| - |2796|$ exhibit more spatially uniform distributions of the differences. The differences observed in these panels are likely influenced by the accuracy of the RHT method near the apex of the loop because of the slower clumps' speeds in these regions. However, structures with higher speeds, such as those near sunspots and inclined structures, are more likely to have genuine differences observed. There are two possible scenarios to consider. First, they might be caused by overlapping loops in the LOS, particularly for SJI 1400 Å, since it is usually optically thin. Similarly, the rain's narrow width can cause a reduction of the optical thickness of SJI 2796 Å. Second, shear motions may be caused by multithermal plasma moving differently within the same pixel elements.

3.3.2 Morphology

Here, the statistical determination of the width and length of each detected rain clump is presented. To measure the width of the clumps, the following calculation step is applied:

1. For a clump pixel at a particular location and time, spatial mean angle information is obtained from the RHT.
2. A Gaussian is fitted to the intensity profile, which is interpolated over the perpendicular line to the trajectory (see the orange lines in Figure 3.6).
3. The Full Width at Half Maximum (FWHM) is obtained from the Gaussian fit, which is considered the width for the rain clump at that particular pixel.

In addition, a condition is set on the intensity of the profile to avoid background noise, and an intensity threshold is also set below which the intensity profiles are neglected. An area without any visible structure is chosen to determine the thresholds for each channel, and the average intensity throughout the observation sequence is calculated. As mentioned before, scattered light

and imperfect flat-fielding cause non-uniform noise levels during one raster and in the image. Although this non-uniform noise has been corrected in data calibration, it has not been completely eliminated. Therefore, a temporally and spatially non-uniform secondary noise threshold is taken into account, which is used to calculate the length.

In Figure 3.6, the depicted procedure establishes an intensity threshold known as the "intensity at half maximum" (indicated by filled circles aligned with the positions of the dotted lines in panel (d)). This threshold is utilized as the non-uniform intensity threshold for determining lengths (with intensity values corresponding to the positions of the dotted lines in panel (e)).

To calculate the length of the clumps, the steps below are followed:

1. Given a pixel location, we determine the centre point of the Gaussian fit used to calculate the width of clumps at that location.
2. Using the spatial mean angle (from RHT) at this centre point, a path along the same trajectory is drawn.
3. Along this path, the locations where the intensity of the clump falls below the non-uniform noise threshold are identified, as explained above.
4. These locations yield two points below and above the centre point, which define the extrema for the length calculation.
5. This process is performed for all pixels of a given clump, and length calculations are obtained for each.
6. Finally, the average of all the length calculations is obtained, which provides an accurate measurement of the length of clumps.

Panels a and b in Figure 3.7 show the width and length distribution of the detected coronal rain clumps in SJI 2796 Å (blue), SJI 1400 Å (red), and AIA 304 Å (green). The distributions for all channels are similarly shaped and slightly asymmetrical, with a small tail at higher values. The average widths and lengths found are summarised in Table 3.2. The widths between SJI 2796 Å ($\approx$0.8 Mm) and SJI 1400 Å ($\approx$0.7 Mm) are found similar, but the widths found in Cool AIA 304 Å ($\approx$1.2 Mm) are considerably larger. This could be due to the lower spatial resolution in AIA 304 Å and the narrow rain widths being slightly larger than the instrumental resolution ($\approx$0.5 Mm for the

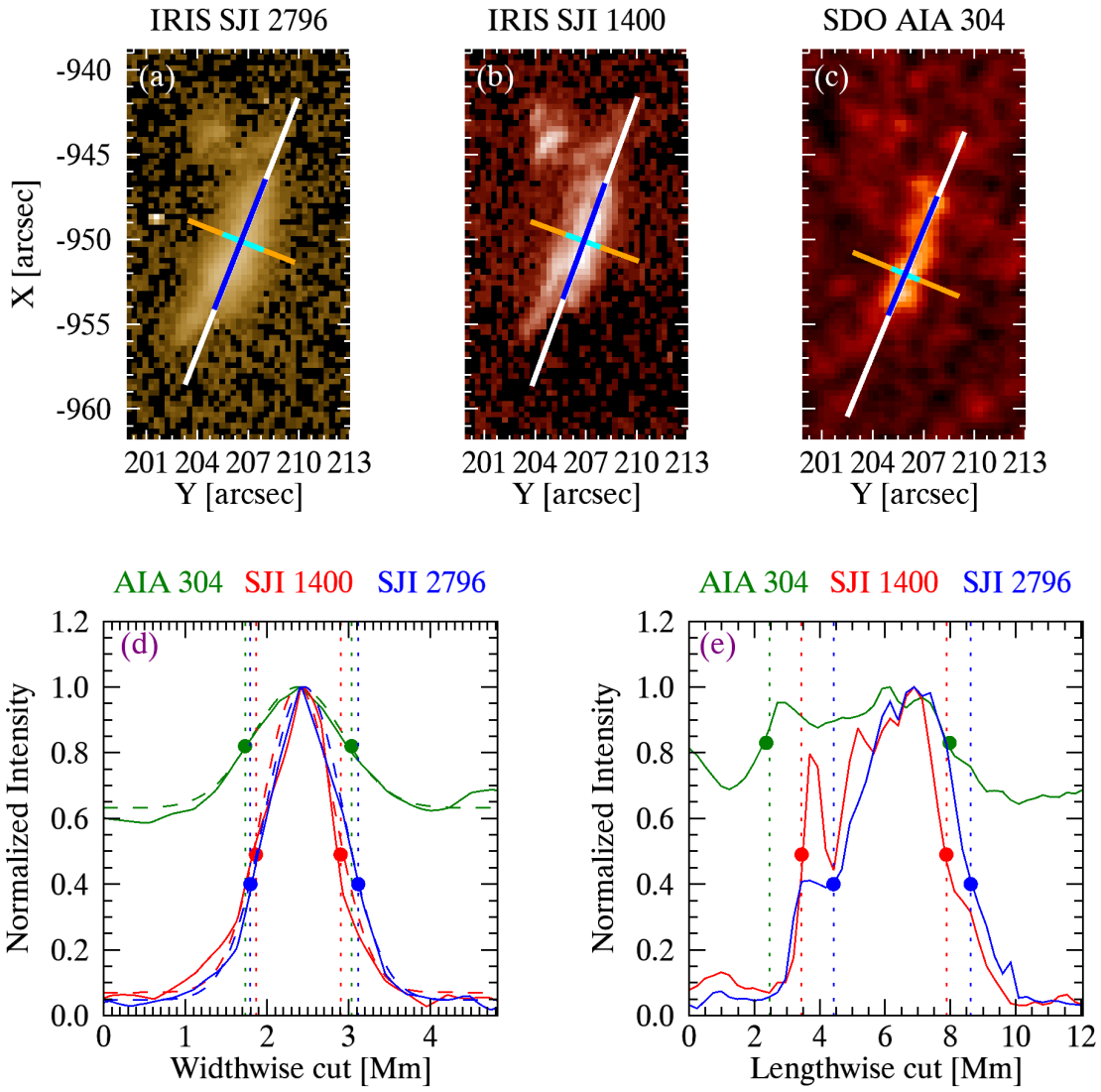

Figure 3.6: A method to determine the width (d) and length (e) of rain clumps in SJI 2796 Å (a), SJI 1400 Å (b), and AIA 304 Å (c). In these panels, the orange line represents a cut crossing the rain clump at a particular pixel perpendicular to the clump trajectory. This line is employed for calculating the clump width using a Gaussian fit to the intensity profile (i.e. FWHM, cyan line cut). The white lines indicate the cuts for the rain clump that determine its length (blue line). d,e) the intensity profiles of the clump along the orange and white cuts are shown in panels a,b, and c, together with the resulting extrema positions indicating the width and length (dashed lines in each panel with blue (SJI 2796 Å), red (SJI 1400 Å), and green (AIA 304 Å)). Filled circles in these plots indicate the positions of intensity at FWHM.

SJIs and ≈0.9 for the AIA). The lengths show a smaller degree of similarity compared to the widths, despite being ten times larger. On the other hand, the length and width variations with height above the surface of the Sun (z=0) are shown in panels c and d in the same figure. The widths remain constant as the rain clump falls, but the lengths vary considerably, where the rain

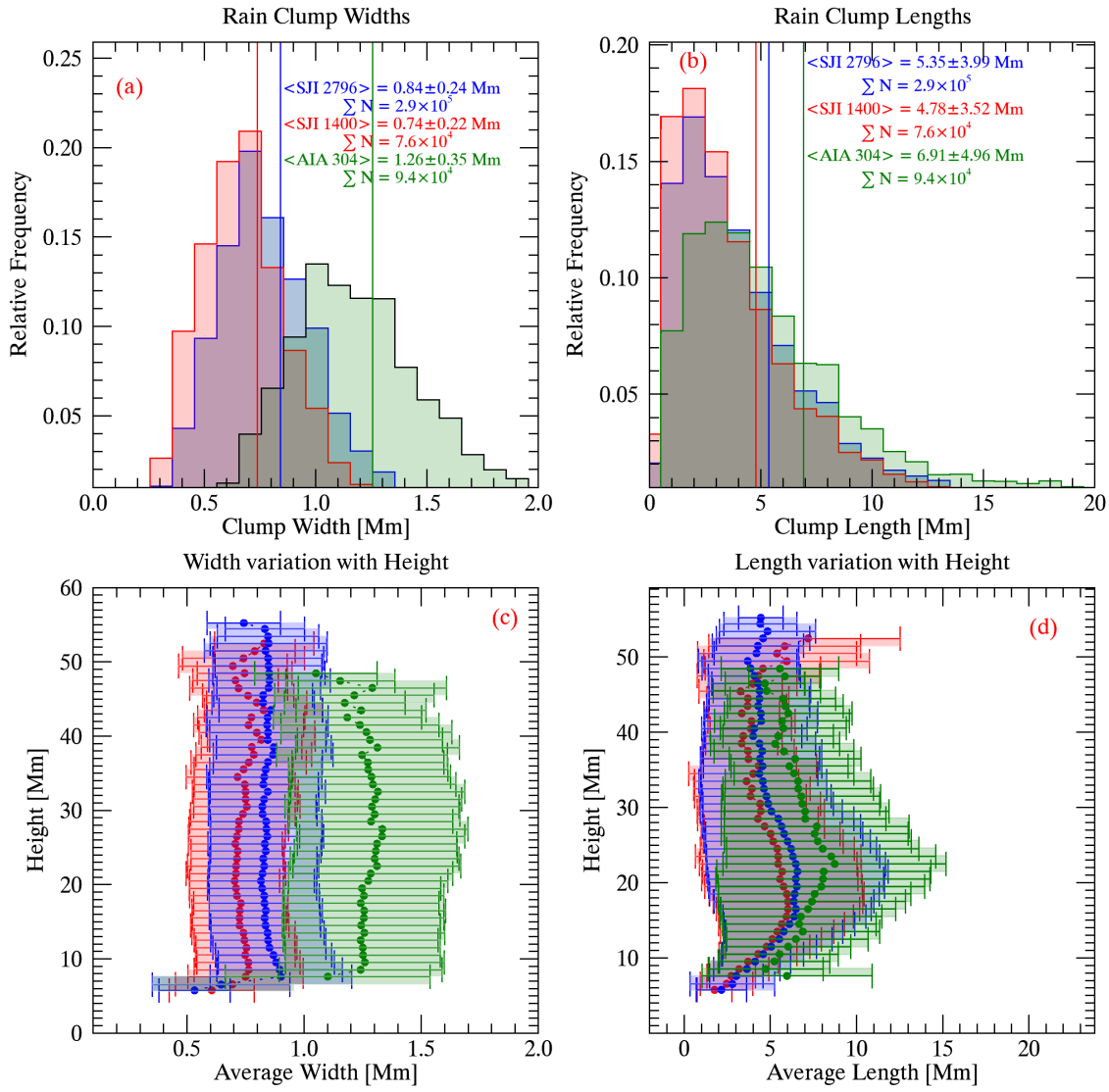

Figure 3.7: a,b) 1D histogram distribution of widths and lengths of rain clumps in SJI 2796 Å (blue), SJI 1400 Å (red), and AIA 304 Å (green). c,d) The width and length variation of rain clumps with height. Here, the filled circles and error bars indicate the average length and width and their average standard deviation at each height bin, respectively.

passes from ≈15 to 6 Mm. This shortening rain clump length is likely attributed to their crossing below the limb, making it challenging to track them any further.

Table 3.2: The average width and length values found in all three channels.

Channel (Å)	Average width (Mm)	Average length (Mm)
2796	0.8±0.2	5.3±3.9
1400	0.7±0.2	4.8±3.5
304	1.2±0.3	6.9±4.9

3.3.3 Dynamics

In this part, the dynamical results are presented. The top panels in Figure 3.8 show the projected velocity maps, including both downflow and upflow motions from the individual rain clumps measurements. The RHT temporal mean angle ($\overline{\theta}_t$) is used to determine the velocity on each curvilinear path, as shown in Equation 3.3 (Schad, 2017):

$$v_{||} = \tan \overline{\theta}_t (\frac{\delta x}{\delta t}). \tag{3.3}$$

Here δx corresponds to the spatial sampling on the date, which is 244.75 km for the AIA channel and 244.72 km for the SJI channels. The δt indicates the average cadence, which is 32.3 s, 43.1 s, and 12 s for the SJI 2796 Å, SJI 1400 Å, and AIA 304 Å, respectively.

The average velocity is also dependent on the spatial mean angle ($\overline{\theta}_{xy}$) through the vertical (Equation 3.5) and the horizontal (Equation 3.4) velocities:

$$v_x = v_{||} \cos \overline{\theta}_{xy} \tag{3.4}$$

$$v_y = v_{||} \sin \overline{\theta}_{xy} \tag{3.5}$$

The projected velocity can also be decomposed in terms of the radial and tangential components, as shown in Equation 3.7 and Equation 3.6, respectively.

$$v_{tan} = v_x(-\cos(\alpha)) + v_y(-\sin(\alpha)) \tag{3.6}$$

$$v_{rad} = v_x(-\sin(\alpha)) + v_y \cos(\alpha), \tag{3.7}$$

Here, α indicates the angle between the horizontal (parallel to the x-axis) and radial directions in radians. Then, the projected velocity is calculated as follows:

$$v_p = |v_{||}| = \sqrt{v_{tan}^2 + v_{rad}^2} \tag{3.8}$$

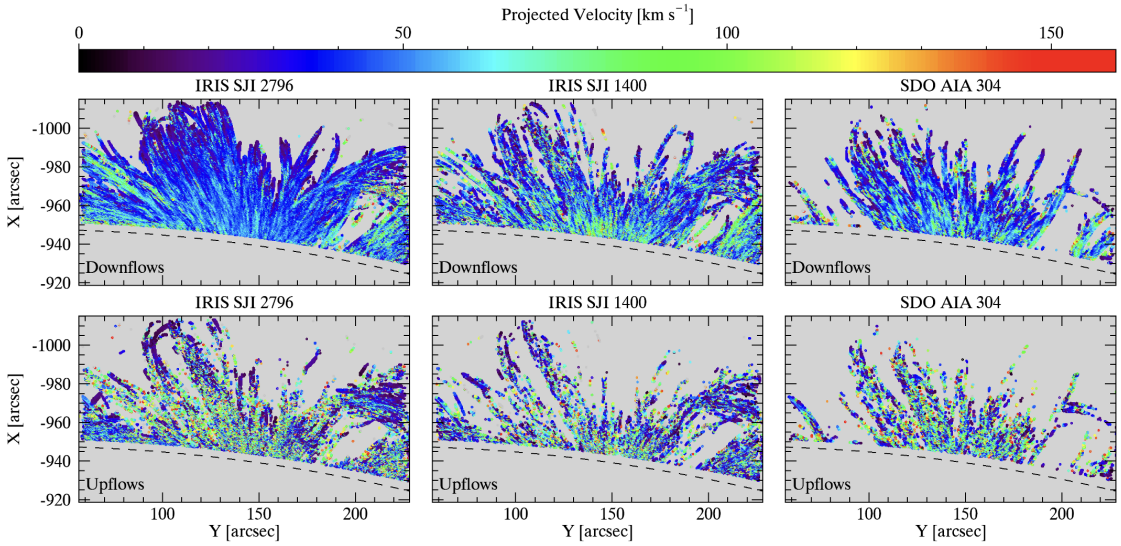

Figure 3.8: Average projected velocity maps with respect to downward (top) and upward (bottom) direction in the SJI 2796 Å, SJI 1400 Å, and AIA 304 Å. The dashed lines correspond to the solar limb.

The average projected velocity maps with respect to the downward and upward direction of the rain are shown in Figure 3.8. As shown in these maps, most of the rain clumps accelerate during their fall, and this can be clearly observed as higher velocities in the centre of the AR (or near the sunspot) in SJI and AIA channels in the top panels. Interestingly, this is also true for the upflow motions, indicating that gas pressure becomes more important at lower heights (See the discussion section for further details.)

Figure 3.9 shows the differences between projected velocities for each channel pair by following the same method as for Figure 3.5. In these maps, the highly localized red and blue values can be seen, indicating a salt-and-pepper distribution. This may happen when a rain pixel is detected in one passband but not the other passbands. However, there are notable differences on a large scale. For instance, the $|1400| - |2796|$ panel shows more blue pixels around the sunspot, indicating higher velocities (20 km s^{-1} higher) in the SJI 1400 Å compared to SJI 2796 Å. In the $|304| - |2796|$ panel, the larger loop patches are observed, and they exhibit consistency with a single colour. Higher velocity values seem to be found in the AIA 304 Å near the sunspot, supporting the previous finding. Finally, the $|304| - |1400|$ panel displays more red than blue, which suggests

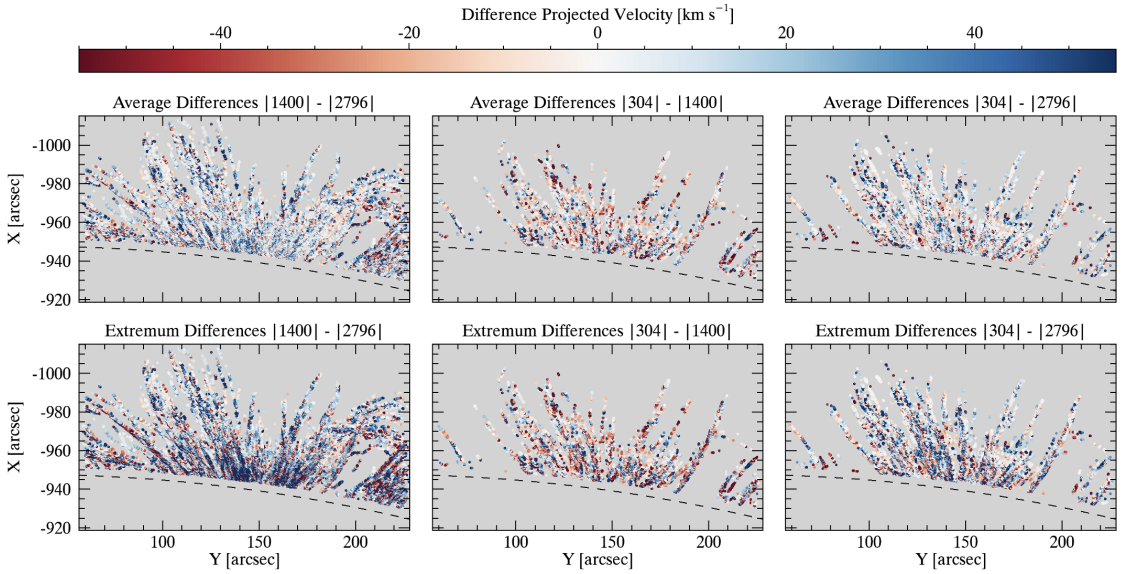

Figure 3.9: The average (top) and extremum (bottom) differences of the projected velocities. These panels are saturated by 55 km s^{-1}. The dashed lines correspond to the solar limb.

higher speeds in the SJI 1400 Å. This suggests the existence of shear flows that have multiple temperatures and/or speeds that are dependent on both temperature and density. However, the opposite result is predicted by the drag effect, which is dependent on density, indicating higher speeds for denser (and thus cooler) rain.

The SJI 2796 Å, SJI 1400 Å, and AIA 304 Å passbands have different numbers of snapshots (n_t) and exposure times (D_t). These differences influence the characteristics of the rain clumps, especially their length. Therefore, the rain area per second in each passband was calculated using the pixel size (dx, dy), number of snapshots (n_t), and exposure times (D_t) (see Equation 3.9).

$$\text{Rain area per second} = (N_{pixels}/n_t) \times (dxdy/D_t) \tag{3.9}$$

Here, N_{pixels} denotes the total number of pixels in the specific passband, and the units of this equation are arcsec s^{-1}.

The left panels in Figure 3.10 show a broad projected velocity distribution of downward (up) and upward (bottom) motions for the SJI 2796 Å (blue), SJI 1400 Å (red), and Cool AIA 304 Å (green). The peaks in these plots are below 50 km s^{-1} and long tails reaching up 160 km s^{-1}. The distributions have a similar shape across all the channels, and the median velocities are given in

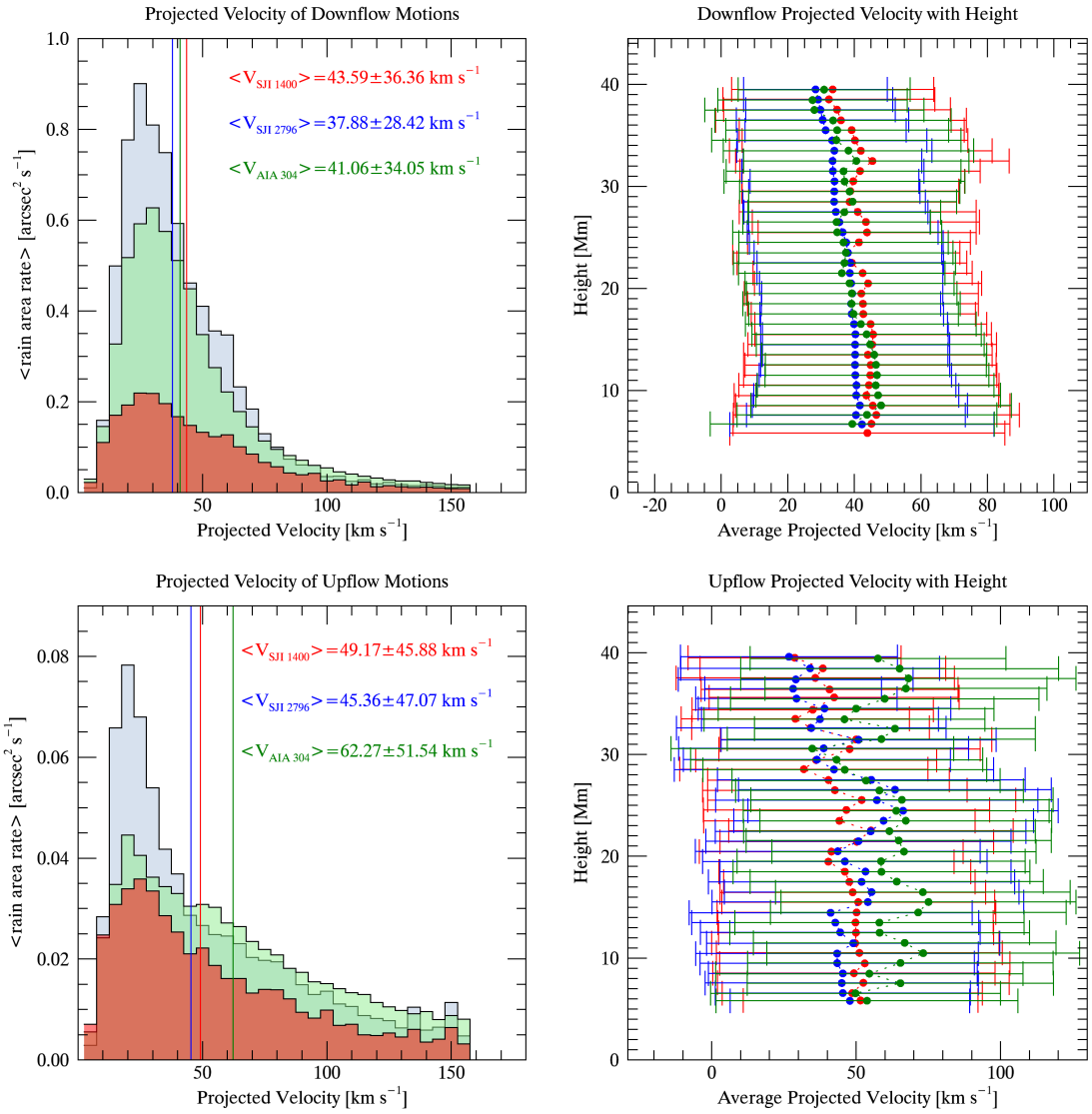

Figure 3.10: Top: The projected velocity histogram distribution and height distribution of downflows, separated by colour for the SJI 2796 Å (blue), SJI 1400 Å (red), and AIA 304 Å (green), along with their median and standard deviation. Bottom: Analogous to the upper panels, but focusing on upflow motion.

Table 3.3. The right panels in the same figure illustrate the median projected velocities variation for both downward (top) and upward (bottom) motions at different projected heights for each channel. In these plots, zero height indicates the solar limb, also shown in the previous figures with dashed lines. The downflow motions (top plot) display similar median projected velocities at all heights, especially when comparing the SJI 2796 Å (blue) and AIA 304 Å (green). However, SJI 1400 Å demonstrates relatively higher velocity values at higher heights ($\geq$18 Mm), supporting the results from Figure 3.8. Moreover, the plot demonstrates that the rain clump accelerates slightly at higher

heights (around the apexes of the loop) and then falls at an nearly constant speed. It could be due to the gas pressure force (Oliver et al., 2014). On the other hand, the projected velocities in the upward direction show much more variation with height, indicating significant changes in gas pressure related to the rain's fall. The high speeds shown in Figure 3.10, which corresponds to highly localized measurements, are likely caused by apparent effects or errors in the RHT routine rather than large-scale bulk flow due to gravity. A point to note here is that if the cool material does not move significantly during the time set by the running mean filter (rmean; see Section 2.2.2.1), then the RHT fails to detect it. This is the case if the LOS is roughly aligned with the POS and the rain occurs at the apex since the projected speed in the POS for this case is very small. In this study, many loops do appear to have their planes close to being aligned with the LOS, which is the reason why the RHT detects little rain at high altitudes.

Table 3.3: The median downflow and upflow projected velocities found in all three channels.

Channel (Å)	Downflow Velocity (km s^{-1})	Upflow Velocity (km s^{-1})
2796	38±28	45±47
1400	43±36	49±46
304	41±34	62±51

In Figure 3.11, the time-distance plots of spatial mean angles are obtained to investigate the time evolution of the rain clumps dynamics in SJI 1400 Å (top), SJI 2796 Å (middle), and AIA 304 Å (bottom). The positive and negative inclinations are given separately on the left and right panels by overlaying all time-distance plots for each radial axis. As can be clearly seen in these diagrams, rain clumps and showers are seen throughout the entire duration of the IRIS and AIA data. Despite many overlapping rain trajectories over time, the spatial mean angle changes with time and distance for individual trajectories. This suggests a change in the projected velocity of rain as it falls. This change appears to be an acceleration due to the small angle between the plane of the loop and the LOS, causing slower speeds for rain near the apex of the loop. On the other hand, Figure 3.10 demonstrates that as height decreases, velocity increases linearly, indicating a small constant acceleration. This could be due to the restructuring of gas pressure produced by the formation of the condensation (Oliver et al., 2014; Martínez-Gómez et al., 2020). The change in the slope may not indicate acceleration but could result from a shift in the angle between the LOS and flow tangent vector to the flow. The angle between the vector tangent to the flow and LOS will be almost zero at the loop apex if the LOS makes a small angle with the loop plane. This makes

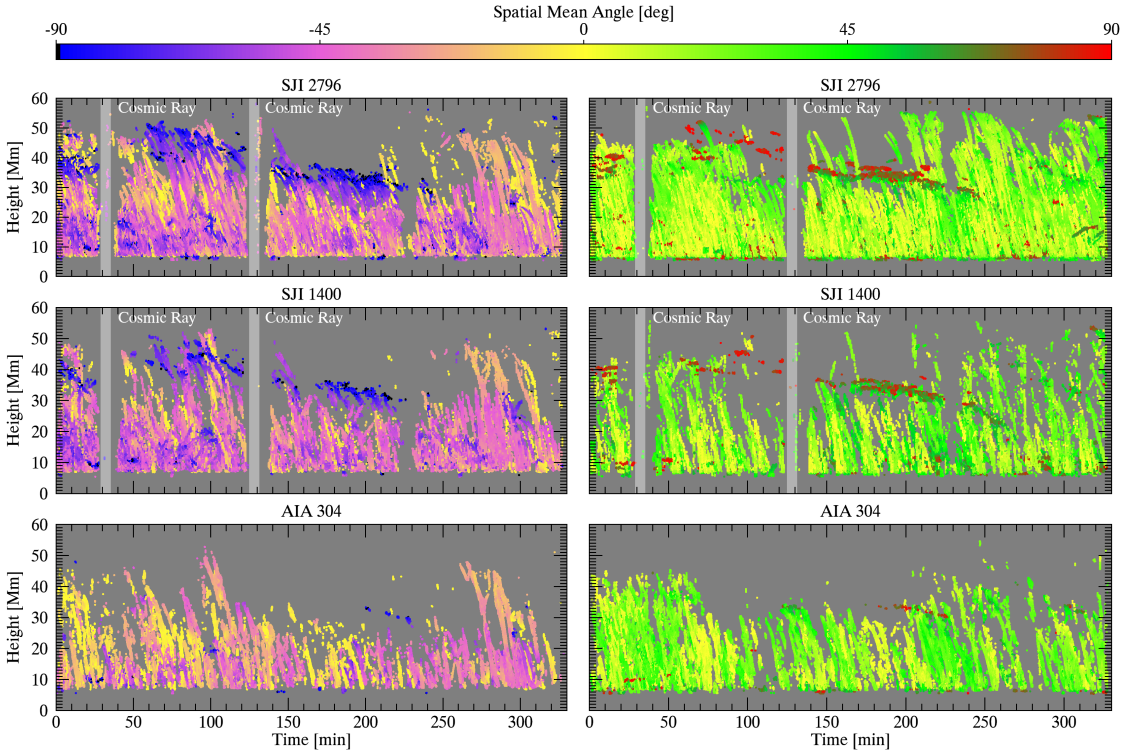

Figure 3.11: The time-distance diagram of negative (left) and positive (right) spatial mean angle inclinations for the SJI 2796 Å SJI 1400 Å and AIA 304 Å (from top to bottom panels). The grey-shaded areas in SJI plots indicate times when cosmic rays are present, causing a disruption in the detection of coronal rain.

the projected velocity very small. However, as the angle increases 90° towards the loop leg, the projected velocity approaches the total velocity.

Figure 3.12 shows the 2D probability distribution function (pdf) of the tangential (top), radial (middle) and downflow projected velocities (bottom) with height. As seen in Figure 3.3, rain clumps are distributed almost equally on both sides of the AR, resulting in a bimodal distribution in the tangential velocity maps in the top panels in Figure 3.12. In the middle and bottom panels in the same figure, the downward velocities are lower than the freefall speed limit (considering an average starting position from the rest of 45 Mm). These findings are in consistent with previous studies by Schrijver (2001), De Groof et al. (2004), and Antolin et al. (2015).

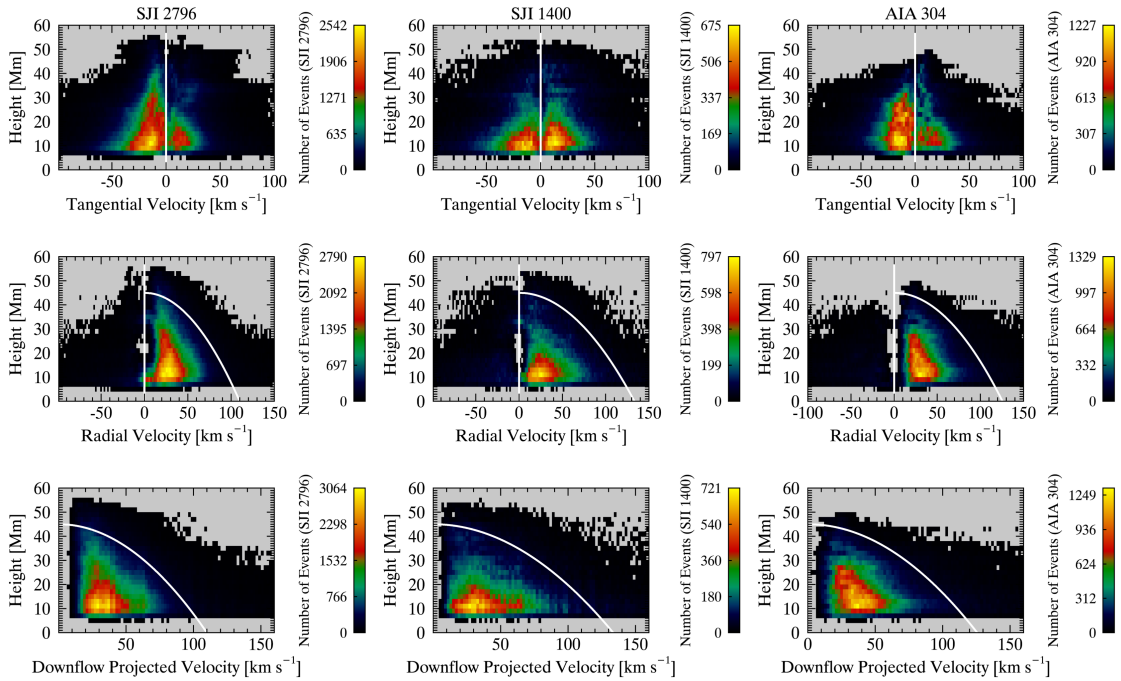

Figure 3.12: 2D PDFs of the tangential (top), radial (middle), and downflow projected (bottom) velocities for the SJI 2796 Å (left), SJI 1400 Å (middle), and AIA 303 Å (right). The white parabola indicates the change in freefall velocity with height, starting from the observed average height.

3.3.4 Long and short term periodicity

3.3.4.1 Long-term periodicity

In this section, the presence of long-period intensity pulsations is investigated using the "pulsation data set" (i.e., 3-day data set) between June 1, 2017, at 05:00 UT and June 4, 2017, at 5:15 UT. The cadence of this data set is 5 minutes.

Figure 3.13 shows some of the detected pulsations regions through contour lines, with AIA 171 Å (cyan) and AIA 193 Å (dark blue) over an AIA 171 Å image of the active region. Additionally, the SJI 2796 Å spatial mean angle (see Figure Figure 3.3) from the rain detection is also shown as an overlaid image. These contours represent the regions with normalized power exceeding 10σ (see Section 2.2.5). We find four pulsation regions that are predominantly at the coronal loop top or apex. This occurrence can be reasonably explained by a decrease in the superposition presence of bright coronal structures at higher altitudes. Smaller regions are manually selected within the contour regions (i.e. detected pulsations regions) to check the periodicity through Fourier power

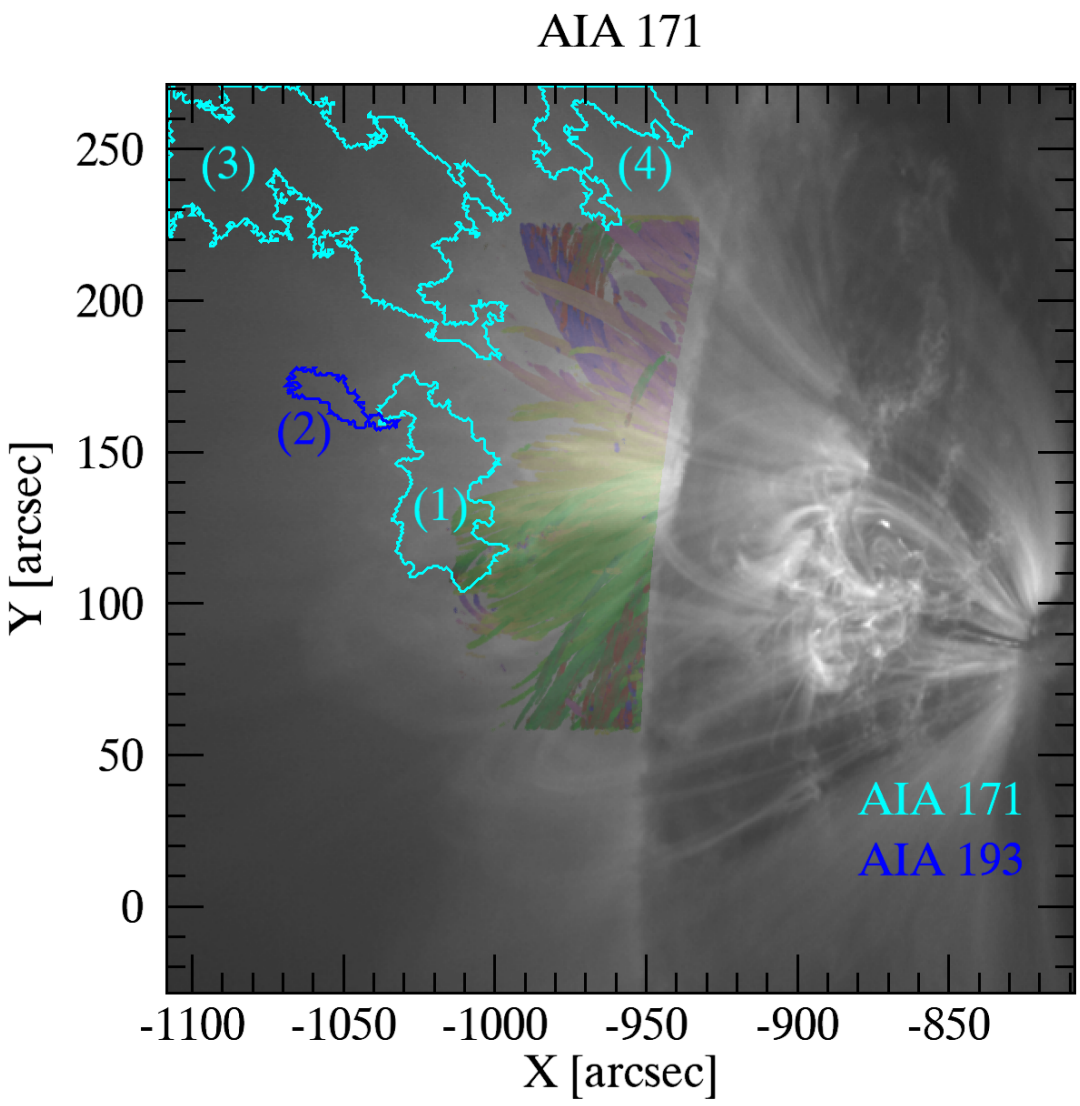

Figure 3.13: Detected long-period EUV intensity pulsation regions over AR in AIA 171 Å (cyan contours) and AIA 193 Å (dark blue contours) with normalised Fourier power above 10σ. Each contour is labelled with its dominant frequency: 75.97 μHz/3.65 hr (1), 65.28 μHz/4.25 hr (2), 38.40 μHz/7.23 hr (3), and 49.92 μHz/5.56 hr (4). The SJI 2796 Å spatial mean angle map is also overlayed.

calculation. The periods are found to be between 3 and 9 hours. Figure 3.14 shows one example of this analysis. In the top left figure, the selected subregion was shown with a pink square and analyzed in detail. On the right, the light curve of AIA 171 Å shows how the intensity varied over the 2.4-day period for the summed intensity variation within the pink square. The normalized power map (in a logarithmic scale) of the AIA 171 Å and the Fourier spectra are presented in the bottom left and right panels, respectively.

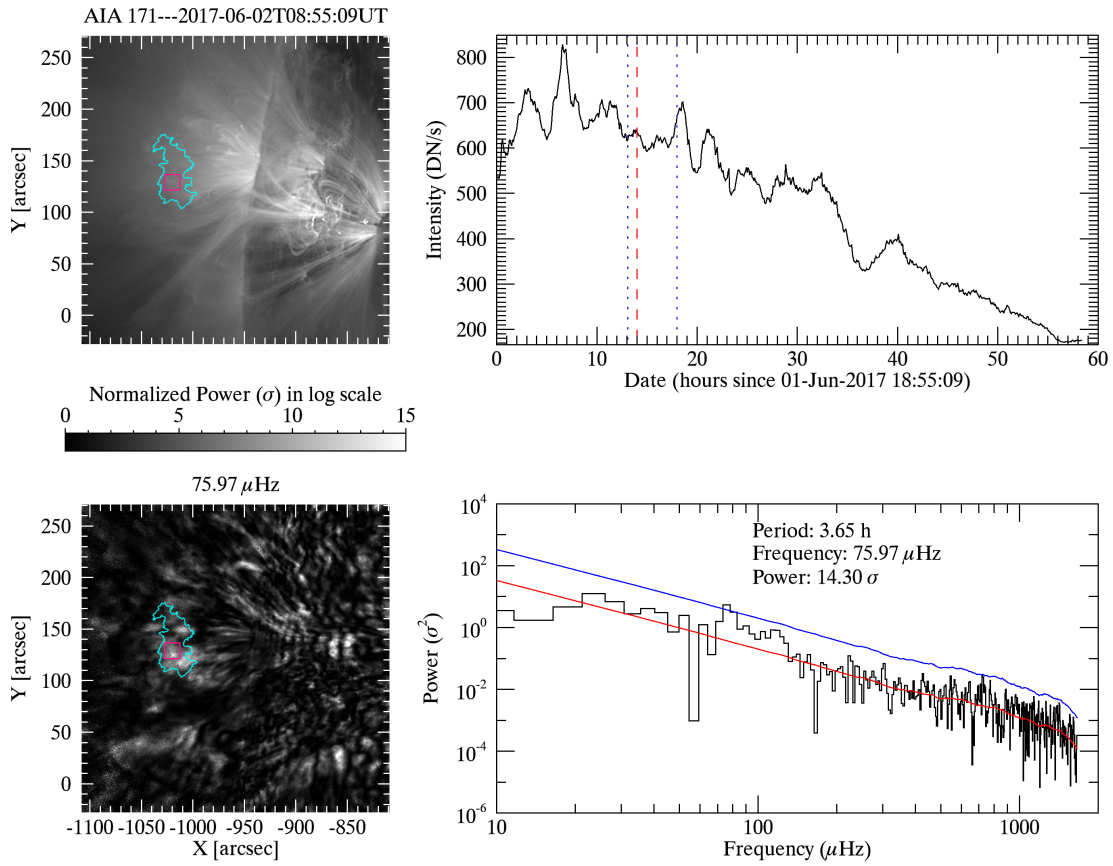

Figure 3.14: Top left: The AIA 171 Å map displaying one of the detected pulsation regions (cyan contour). The pink square denotes the selected sub-region for the detailed analysis. Top right: the temporal evolution of AIA 171 Å intensity throughout the observational period, summed over the pink subregion. The vertical dashed line marks the time corresponding to the right map, while the vertical blue dotted lines indicate the observation window of the IRIS instrument (i.e., 5.45 hours). Bottom left: a normalized power map of AIA 171 Å, presented on a logarithmic scale at a frequency of 75.97 μHz (3.65 hr). Bottom right: the Fourier power spectrum of the AIA 171 Å light curve. The solid red curve represents the estimation of the average local power, and the blue curve signifies the 10σ detection threshold. Animation of this Figure is available in Şahin et al. (2023).

In the bottom right panel, the Fourier spectra of the AIA 171 Å passband are shown. The highest power peak in this plot corresponds to the frequency of 75.97 μHz (3.65 hours). On the bottom left panel, the normalized power map of the AIA 171 Å at this frequency (75.97 μHz) of the highest power peak is presented in the logarithmic scale. Note that this figure has the same FOV as in the top left panel. The solid red curve in the Fourier spectrum represents the average local power, indicating the noise level. The blue curve represents the 10σ detection threshold. Power peaks at a frequency of 76.8 μHz are observed in the AIA 131 Å and AIA 193 Å channels, with normalized power values of 11.33σ and 8.77σ, respectively. There is no significant power for channels 94,

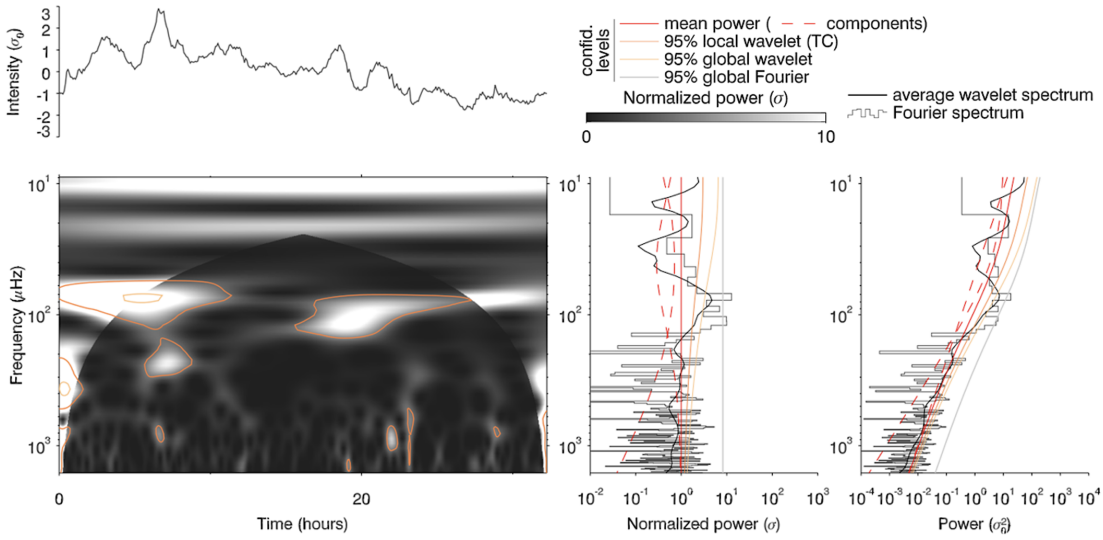

Figure 3.15: The average time series (top left) in the detected region is shown in Figure 3.14 with cyan colour and its time-averaged wavelet and Fourier power spectrum (grey histograms and black curves) (bottom).

211, and 335 Å. The 171 Å has the highest power at 14.30σ. This periodicity was also checked with a wavelet analysis as shown in Figure 3.15 and found that the power was clearly distributed in the time series, backing up the Fourier results. The result also shows a 95% confidence level for a significant power distribution (13.94 σ) for a time range between 18:55:09 and 3:15:09 UT.

3.3.4.2 Short-term periodicity

Figure 3.11 shows the presence of apparent quasi-periodic downflows in the time-distance series across the entire FOV. In this section, this phenomenon and the existence of short periodicity, in general, are investigated. For this purpose, specific data sets and time intervals were used wherein coronal rain is observable in both AIA and SJI channels (i.e. 5.45-hour data in SJI 2796 Å, SJI 1400 Å, and AIA 304 Å). Short periodicity was initially sought by establishing a constant height above the limb, where intensities were summed across the entire field of view and locally, with a constraint on the Y-axis range. Light curves are constructed at 8 Mm intervals, commencing from the solar limb and summing data over an 8 Mm height thickness. Subsequently, the corresponding Fourier spectrum is examined to identify prominent power peaks.

The red square at 15-23 Mm heights is presented in Figure 3.16 in the left panels for the SJI 2796 Å, SJI 1400 Å, AIA 304 Å, AIA 171 Å, and AIA 131 Å. The significant Fourier power spectra found

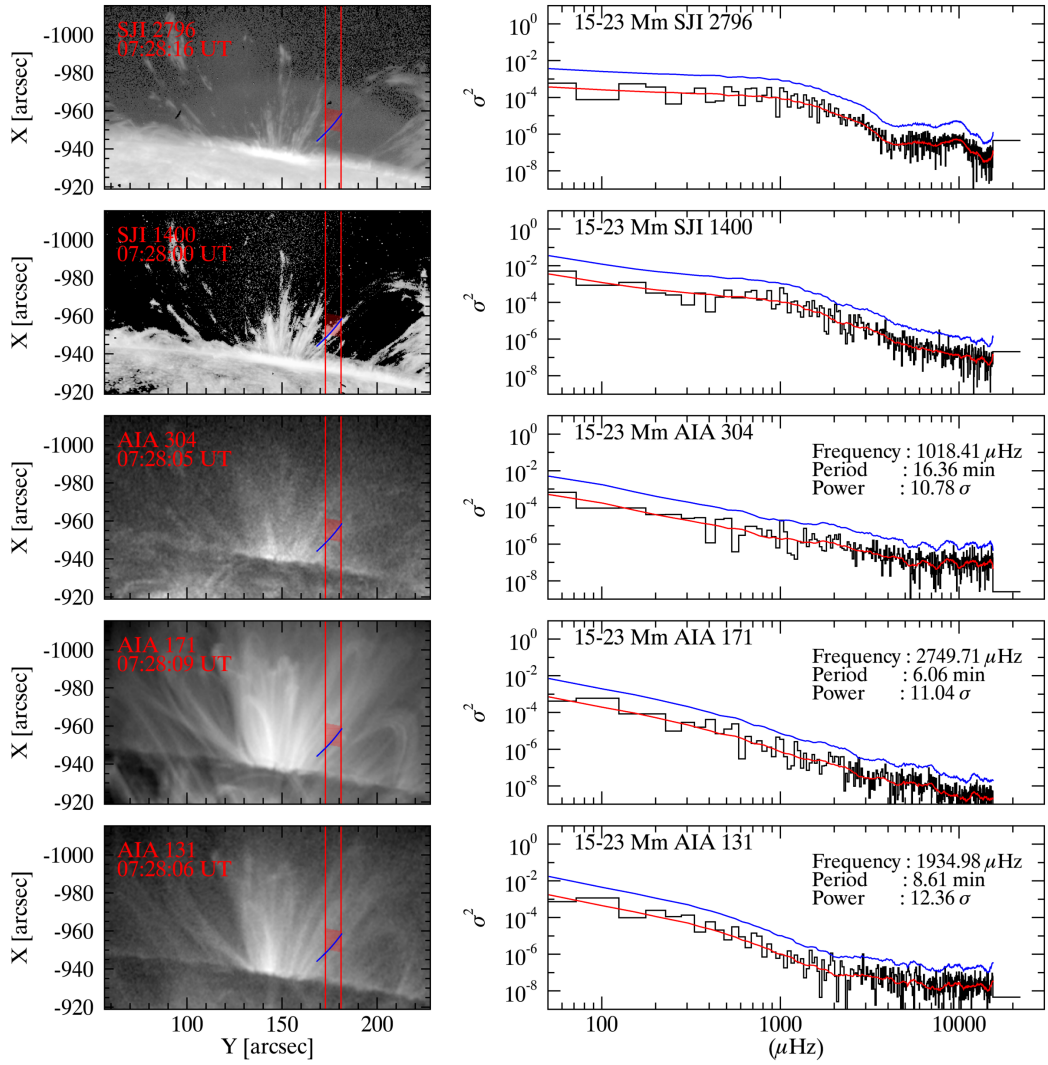

Figure 3.16: From top to bottom, the SJI 2796, SJI 1400, AIA 304, AIA 171, and AIA 131 Å images (left panels), and their Fourier power spectrum (right panels) for the light curves generated by summing over 15–23 Mm heights (indicated by red squares in the left images). The red and blue lines represent the average power and the power levels at 10σ, respectively.

are shown in the right panels. In these plots, AIA 171 Å has a peak of 11.04σ, dominating with 2749.71 μHz (6.06 min) frequency. Two peaks of 12.36σ and 13.84σ were found in the AIA 131 Å, with the frequency of 1934.98 μHz (8.61 min) and 2902.48μHz (5.74 min), respectively. We have not detected any peak at those frequencies in AIA 304 Å. However, we detected a peak of 10.78σ power at 1018.41 μHz frequency (16.36 min) in the AIA 304 Åchannel. The confidence levels and power at the same frequency are significantly lower for SJI 2796 Å and SJI 1400 Å, at 4.12σ and 6.26σ, respectively. The IRIS rastering mode, as mentioned in the previous chapter, causes a non-uniform background noise due to the apparent motion caused by

imperfect flat-fielding and light scattering. This effect causes a non-uniform increase in intensity across the AR, with the centre experiencing the most significant impact. The periodicity of this apparent motion is 17.2 minutes in the case of these SJI channels. Although the Fourier periodicity is not exactly this one, it is also possible that the power found in nearby frequencies is attributed to this apparent motion. To clear up this possibility, the time-distance maps over the blue path shown in Figure 3.16 are presented in Figure 3.17. These maps were produced using the CRISPEX tool (Vissers and Rouppe van der Voort, 2012).

To reduce the impact of the apparent motion effect, the IRIS raster is initially identified in both SJI 2796 Å and SJI 1400 Å with little to no coronal rain presence (depicted by the red rectangles in the figure). Subsequently, the intensity values within these identified rectangular areas are subtracted from all other IRIS rasters present in the time–distance maps (illustrated in the second and fourth panels). This process aids in enhancing the visibility and clarity of the coronal rain observations. As a result, the recurring short-timescale rain showers become readily discernible in both SJI 2796 Å and SJI 1400 Å channels. Furthermore, these repetitive downflows are also apparent in the time-distance maps of AIA 304 Å, AIA 171 Å, and AIA 131 Å. The consistent presence of these downflows across multiple wavelengths reinforces the reliability and validity of the observed phenomenon, supporting the notion of periodicity in the detected coronal rain events.

3.3.5 Discussion and Conclusion

This study is the first high-resolution work on quiescent coronal rain for a duration of 5.45 hours, covering an entire off-limb of an AR, in order to enhance our knowledge of its fine structure. This duration is long enough to examine the TNE cycles' cooling phase that lasts for hours (Froment et al., 2015).

We investigated rain dynamics and morphology, from its formation point high along coronal loops down to the chromospheric heights, as seen in a variety of channels that probe varying densities and temperatures. Previous observations of coronal rain have generally been limited to ground-based telescopes, which can only observe rain at the loops' base off-limb due to the limitations of adaptive optics. These observations have also focused on small-scale events rather than on the scale of active regions. Studying coronal rain is important for understanding coronal heating since

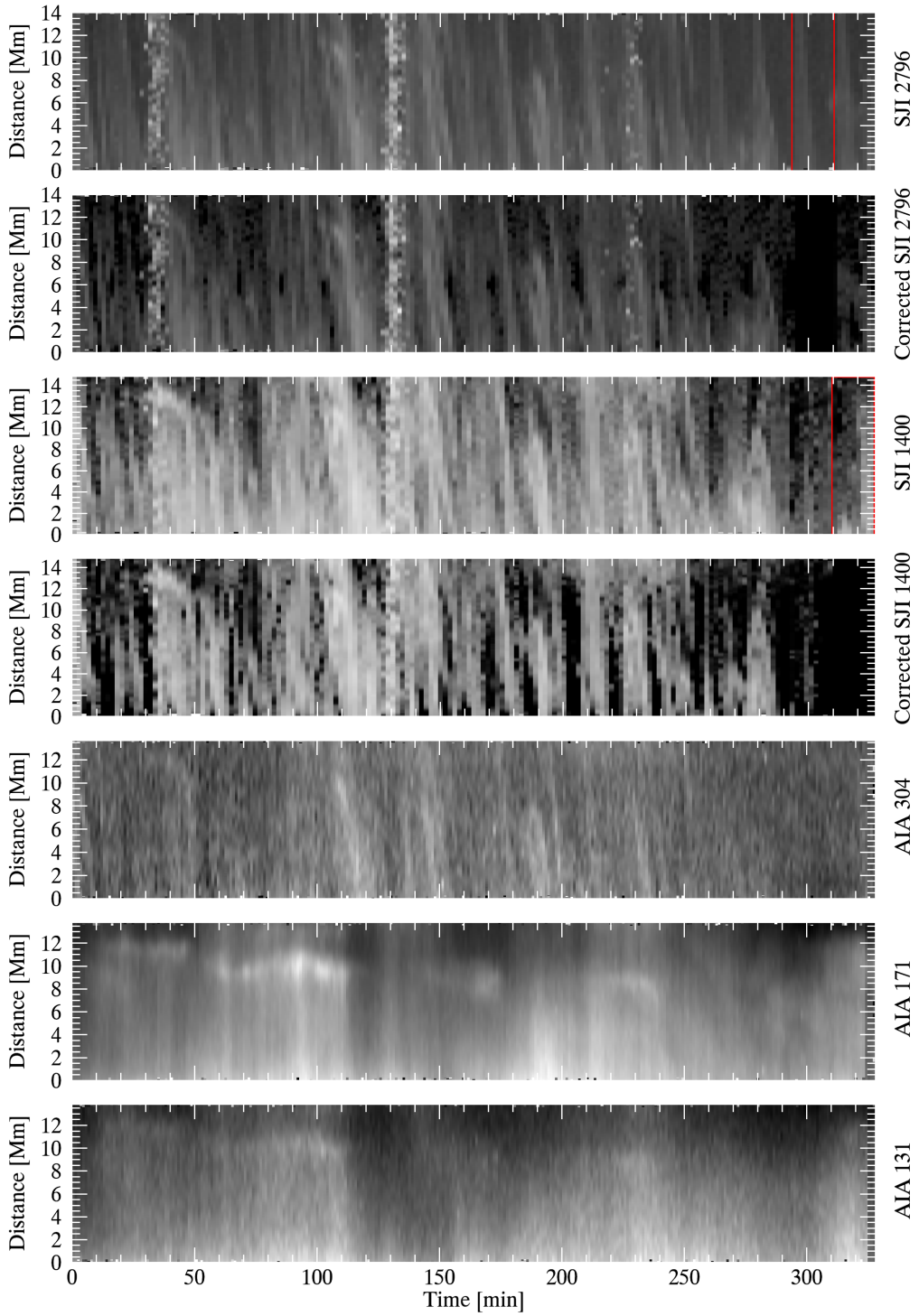

Figure 3.17: Time-distance maps for five channels along the blue paths in the left panels of Figure 3.16. The red rectangle area given in the first and third panels indicates the minimum solar activity region to quantify the apparent motion variation effect for each SJI channel. To minimize apparent motion effects, the intensity of this time-distance area is subtracted from all other rasters in the map. The first and third panels show the original time-distance maps, while the second and fourth panels display the corrected versions.

the properties of coronal rain can provide valuable information about the spatiotemporal properties of the heating mechanisms.

Our statistics indicate that rain clumps occur at chromospheric and TR temperatures, where Si IV and Mg II ions are formed. These clumps have widths ranging from 0.2 Mm to 2 Mm and lengths ranging from a few to 20 Mm. We found similar results for the rain widths to those found by Antolin et al. (2015), despite using a $2\times$ lower resolution dataset. On the other hand, these findings also agree with simulation results (Li et al., 2022). These widths are about 5.8 times wider than in Hα and 1.4 times wider in the same SJI channels of IRIS. This may be due to our data set having 6 times lower resolution than the SST (Antolin et al., 2015) and twice lower resolution than the IRIS data set used in their study. In addition to resolution, the wider widths in the Mg II and Si IV lines compared to Hα studies may be caused by their larger opacities. Moreover, the degradation of the SJI channels could also play a substantial role in increasing the rain widths. However, the length measurements obtained are notably longer. This difference is attributed to the analysis of larger spatial scales and the impact of longitudinal effects along loops, for instance, gravity and gas pressure. This is confirmed by the similarity between the length measurements in AIA 304 Å and those found in Antolin et al. (2015) using the same passband. The findings indicate that factors determining the width of coronal rain act quickly upon formation and remain constant as they fall along the loop length. The width of a coronal rain clump may be influenced by both the fundamental nature of coronal heating (Antolin et al., 2015, 2022) and the granular scales and currents that may be associated with it (Martínez-Sykora et al., 2018). Another explanation is that the rain's width is determined by the cooling mechanism (i.e., TI). This can occur through the wavelength of the unstable mode, as discussed in van der Linden and Goossens (1991). The data set has good resolution for scales above 800 km, but may not effectively capture structures below 500-600 km. Using the Gaussian fitting, we can identify consistent variations in width $\approx$800 km with height. We also recognize that our limit to detect a discernible pattern, if it exists, might be constrained by factors such as low resolution and the impact of degradation. In any case, this finding suggests that the width of the clumps does not change due to heating or cooling as they fall. Rain clumps exhibit a wide range of velocities, from a few to over 100 km s^{-1}, which is in agreement with numerical simulations (Fang et al., 2015; Li et al., 2022) and observational studies (De Groof et al., 2005; Müller et al., 2005; Antolin and Rouppe van der

Voort, 2012). We analyzed how rain dynamics change with height and found small downward accelerations at heights of between 30-40 Mm. Nevertheless, rain clumps exhibit nearly constant speeds during most of the fall, with a minor average linear increment. This increment in velocity at lower heights could be due to a combination of gravity and pressure changes (Antolin et al., 2010; Oliver et al., 2014; Martínez-Gómez et al., 2020). We have not observed any higher speeds in the chromospheric SJI 2796 Å channel, which is normally expected because of higher densities than SJI 1400 Å. This could be due to the rain's strong multi-thermal nature, as discussed further below.

In addition to moving downwards, coronal rain can also exhibit upward motion and undergo complex trajectory changes. The upward motion of coronal rain has not been thoroughly studied. However, Antolin et al. (2010) have observed changes in the trajectory of rain clumps, including upflows. Our study determined the amount of downflow to upflow motions in the observed clumps over time, with an average ratio of 7 and widespread spatial incidence. The upward rain motions have also been observed in a study by Li et al. (2022) using a 2.5D MHD simulation. Our findings indicate that the upward and downward speeds of coronal rain are similar, with upward speeds being slightly higher on average. One explanation could be that the upward motions are caused by a perceived change in opacity during the fall. For sure, rain experiences cooling as it falls (Antolin et al., 2015), leading to increased opacity during its fall. This appearance can occur suddenly, resulting in an apparent fast upward motion. Conversely, these dynamics may be real and indicate a substantial impact from gas pressure. Indeed, Mackay and Galsgaard (2001) state that the chromosphere can stop the rain by acting as a piston and compressing the downstream. Adrover-González et al. (2021) studied a loop system caused by line-tying conditions in the lower atmosphere. These conditions result in oscillations and therefore upflows as well. The gas pressure gradients adequately eliminate the acceleration of downflow motions as shown by Oliver et al. (2014). Therefore, changes in gas pressure can lead to both upflows and downflows at similar speeds.

As the rain falls, we notice that the upward speeds increase while the height decreases. This matches the greater gas pressure difference caused by compression. Most of the observed downward motions move toward the sunspot, with only a small number falling into nearby regions where the other loop footpoints are anticipated. This indicates that the sunspot's lower gas pres-

sure, caused by the strong magnetic field, creates siphon-like conditions that are thermally unstable under the TNE-TI scenario. Other sunspot observations have consistently shown that rain tends to fall more heavily in either the penumbra or umbra (Ahn et al., 2014; Kleint et al., 2014; Antolin et al., 2015; Schad et al., 2016; Froment et al., 2020). The rain's impact is expected to cause strong pressure changes, creating upflows and modifying the dynamics of the trailing rain clumps.

During the 5.45-hour observation, we observed coronal rain spread uniformly in the POS above the AR (on both sides of the sunspot). This indicates that many loops, regardless of their geometry and footpoint location, experienced coronal rain at some point. As shown in the next chapter and in Şahin and Antolin (2022), we estimated the volume by quantifying the rain showers over the spatial and temporal extent. This helped identify coronal loops against the LOS superposition because of the optically thin coronal radiation. We found up to 150 showers with a TNE volume estimated to be at least half (50%) of the active region volume. This indicates the prevalence of TNE over the active region. However, this statement contradicts the findings of Mikić et al. (2013) and Froment et al. (2017), which indicate that the geometry and heating asymmetries between loop footpoints are significant factors in the formation of coronal rain, and even slight changes in these conditions can prevent TNE. However, Froment et al. (2018) and Pelouze et al. (2022) discovered that stringent conditions are relaxed with stronger footpoint heating, resulting in TNE becoming prevalent in the parameter space. Therefore, This implies that the loops we observe in this study experience relatively strong, stratified, and high-frequency heating.

Furthermore, we also showed a strong correlation between chromospheric emission in SJI 2796 Å and TR emission in SJI 1400 Å and AIA 304 Å from coronal rain. This indicates a multi-thermal character, as previously indicated by isolated rain events (Antolin et al., 2015) and supported by 2.5D radiative MHD simulations (Antolin et al., 2022). This suggests that catastrophic cooling driven by TI is very rapid, happening much faster than the plasma's freefall time. As a result, the AR experiences "complete" condensations rather than "incomplete" or "aborted" ones (Mikić et al., 2013). Although in some isolated cases, an extended tail at TR temperatures may result in longer coronal rain lengths in lines like Si IV λ1402 or He II λ304, but not in general, as suggested by the numerical results (Antolin et al., 2022). The simulation results show that chromospheric emission is limited to the rain's head, contrary to our results where SJI 2796 Å emission is, in general, co-located with SJI 1400 Å. This could indicate that TI is extended along the loops we

observe and that Joule heating is excessive in the simulations.

We detected several long-period EUV pulsations that were associated with the coronal rain. These pulsations occurred at the loop apex with periods ranging from 3 to 9 hours. Our findings support the conclusion of Froment et al. (2020) that the coronal rain and EUV pulsations are two sides of the same coin, connected through the TNE-TI scenario. We are only detecting the strongest pulsations using the Fourier method, indicating there may be more pulsations that we are not currently detecting. We may be only observing some of the coronal rain connected to longer pulsations (around 9 hours) due to the limits of our data set. As mentioned in the next chapter and in Şahin and Antolin (2022), observed coronal rain and associated TNE-TI volume above the AR are lower limits. We observe them near the apexes of the coronal loop because there is less superposition along the LOS, which has been noted in previous studies (Auchère et al., 2018*b*; Froment et al., 2020).

The TNE cycles typically last for a few hours, which is determined by how long it takes for a coronal loop to cool through radiation. However, we observed faster timescales (5-20 minutes) in this study, posing a challenge to explain using the TNE-TI scenario. This behaviour may be attributed to a partially sustained TNE cycle where only one loop leg is impacted by the TNE while the other is consistently supported by a siphon flow. In this scenario, the loop remains partially dense, and temperatures consistently stay at the warm upper transition region level. Under these circumstances, the radiative cooling timescale is short and could lead to TI in a cyclic manner. To investigate this possibility, future models need to investigate TNE parameter space.

Chapter 4

Rain Shower Analysis

In this chapter, I build upon the findings and insights presented in my paper[4] titled "Prevalence of thermal non-equilibrium (TNE) over an Active Region". The content covered here draws extensively from the information and results detailed in that paper, allowing for deeper exploration and analysis within the context of my thesis.

4.1 A Brief Overview

Coronal rain is frequently observed to occur simultaneously over a large area in comparison to the width of the clump. This widespread occurrence is typically defined as a "shower" with a cross-field length scale of a few Mm and is observed in both simulations (Fang et al., 2013) and observations (Antolin and Rouppe van der Voort, 2012). The present chapter focuses on the thermodynamic and morphological multi-wavelength study of rain showers. The main objective of this study is to quantify the properties of showers within the temporal and spatial scales where sympathetic cooling takes place. To achieve this objective, rain showers have been studied using the off-limb data taken with SDO and IRIS instruments, spanning chromospheric to TR and coronal temperatures. The rain showers are found to be widespread across the AR over 5.45-hour observing time. These showers exhibit an average width, length, and duration of 2 ± 0.7Mm, 27 ± 12 Mm, and 35 ± 20 minutes, respectively. A good correspondence was found between the cooling coronal loops (subject to catastrophic cooling) and rain showers. This is consistent with

[4] Şahin, S., & Antolin, P. (2022). Prevalence of Thermal Nonequilibrium over an Active Region. The Astrophysical Journal Letters, 931(2), L27.

the TNE-TI scenario, thereby identifying coronal loops in the "coronal veil", including the strong cross-section expansion at low altitudes and a roughly zero expansion in the solar corona. This finding is consistent with previous studies, which suggest that specific cross-field temperature distribution is the reason for the observed zero expansion in the EUV. When the temperature across the entire loop bundle varies significantly, it indicates that the loop is not evolving coherently and, instead, is subjected to catastrophic cooling. Hence, a particular EUV passband will likely see part of the loop, but this part of the loop is also the loop that catastrophically cools down and shows rain. Consequently, we do not observe an expanding shower or loops in the EUV images because expansion implies thermodynamic changes across the field. These changes manifest as longer loop lengths, variations in the heating from the apex to the footpoint of the loop, and different conductive fluxes. All of these factors can influence the way a loop evolves. On the other hand, the total number of showers was estimated to be 155 ± 40, which led to a TNE volume of $4.56\pm[3.71]\times10^{28}\mathrm{cm}^3$, indicating that the TNE volume was on the same order of magnitude as the volume of the AR under study. Our finding indicates the prevalence of TNE over the AR, which also suggests an average of strongly stratified and high-frequency heating.

The following subsections will comprehensively explain data and methodology in Section 4.2 and Section 4.3, respectively. Subsequently, the findings and a detailed discussion will be presented in Section 4.4 and Section 4.5, respectively.

4.2 Observations

The data presented in this chapter (shown in Figure 4.1(a)) is an observational sequence obtained on 2017 June 2 between 07:28:00 UT and 12:54:39 UT at the east limb by IRIS/SJI on 1400 Å and 2796 Å. This is the same data used in the previous Chapter and in Şahin et al. (2023). The IRIS/SJI was focused on the active region NOAA 12661, and FOV for this AR is $232'' \times 182''$. We also used observations of this AR in seven passbands (94, 131, 171, 193, 211, 304, 335 Å) by SDO/AIA.

4.3 Methodology

4.3.1 co-alignment

As mentioned in Section 2.2.1, to achieve co-alignment between the AIA and the SJI channels, we aligned the solar limb (off-limb) and on-disk features at similar times for both SJI 2832 Å and AIA 1600 Å. These two channels have similar chromospheric conditions. This method is explained in detail in Section 2.2.1.

4.3.2 RHT and region grow

The automatic detection algorithm RHT (Schad, 2017), as mentioned in Section 2.2.2, was applied to detect coronal rain. The RHT provides the time occurrence of detected rain pixels and spatial mean angle (i.e., inclination of rain pixels) in the FOV.

On the one hand, a pair of showers may appear simultaneously and follow similar trajectories. On the other hand, they may also overlap and fall in different directions. To identify these showers, we employed a semi-automatic method that considers the time occurrence and spatial mean angle of the showers. This method creates a new array by considering the time occurrence, spatial mean angle data, and the shower's trajectory-time domain values. This procedure can help distinguish between temporal and spatial overlaps mentioned above.

As described in Section 2.2.3, the 'region_grow' routine has been applied to this new trajectory time array to identify a shower. This routine is an algorithm for filling spaces that allows the selection of pixels within a specified range of values defined in a domain along with a standard deviation. The routine starts with an initial pixel that serves as a seed to identify all the pixels that belong to a shower. The algorithm then looks for all the pixels that belong to the shower within a specified range of values in the trajectory-time domain, which is determined by a standard deviation. The standard deviation is carefully chosen by visually determining time range values and possible trajectory. To ensure accuracy, this process was repeated for 50 showers by choosing 50 starting positions over the FOV and across the time sequence, with a preference given to isolated events to minimize errors due to overlaps. Most of the rain clumps are visible through all channels, so most (if not all) of the showers can be seen through each channel. Considering this, 50 shower events were manually chosen to analyse their properties in each channel for the rest of this

chapter.

4.3.3 Differential Emission Measurement

The Differential Emission Measure (DEM) algorithm based on the bp (see Section 2.2.4) method (Cheung et al., 2015) was also used to estimate the temperature variation of the coronal loops hosting the shower events. Data taken from six EUV channels of SDO/AIA (94 Å, 131 Å, 171 Å, 193 Å, 211 Å, and 335 Å) were used to derive the emission measure (EM) distribution for every pixel.

4.4 Results

The results are organized into three subsections: morphology, thermal evolution, and TNE Volume estimation. In the first subsection, the morphological properties of the showers are presented. This is followed by a discussion of our results related to the thermal properties of the showers in the second subsection. Finally, in the third subsection, the estimation of TNE volume is presented.

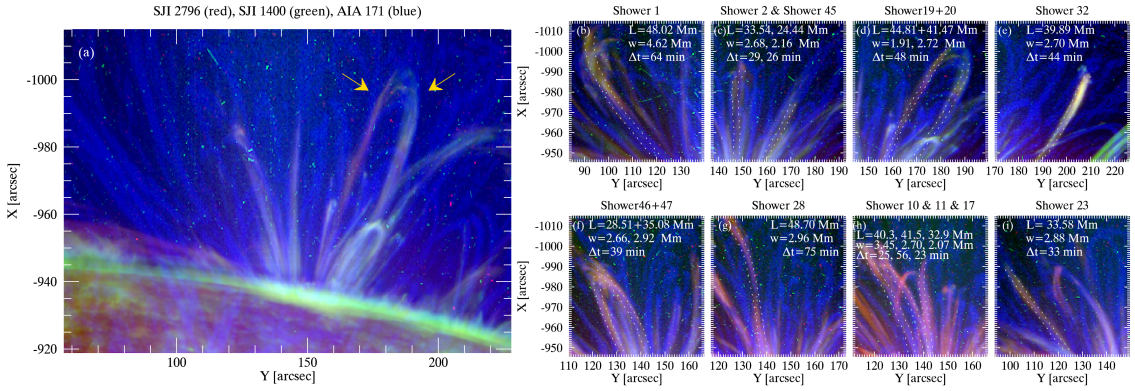

Figure 4.1: (a) Composite image of a studied AR on June 2, 2017. It is observed by SJI 2796 Å (red, dominated by the Mg II k line), SJI 1400 Å (green, dominated by the Si IV 1402.77 Å line), and AIA 171 Å (blue, dominated by the Fe IX 171.073 Å line). The image shows the variation of 30 images taken between 08:59:54 UT and 09:16:05 UT for each channel. We enhanced the coronal structures in AIA 171 Å using multi-scale Gaussian normalization technique (Morgan and Druckmüller, 2014). The depicted yellow arrows denote two legs (19 and 20, referred to as Shower 19+20) of a traced shower event, which we focus its thermal evolution in Section 4.4.2. Panels (b) to (i) are the composite images of some detected showers. The dotted curves denote the shower contours based on the SJI 2796 Å.

.

4.4.1 Morphology

Initially, the focus of the investigation was on the morphological properties of the showers. Several parameters, including their width, length, and duration, were analyzed.

Figure 4.1a shows the studied AR, combining the SJI 2796 Å (red), SJI 1400 Å (green), and AIA 171 Å (blue). Panels b to i in the same figure show eight shower events with their corresponding length (L), width (w), and time duration (Δt) in the inner caption. To determine these parameters, we used the methods summarised in Section 4.3. These shower events have been chosen based on their clean coronal emission (in blue) and their relative isolation. Here, the dotted lines correspond to the SJI 2796 Å contours. As can be seen, these contours match the coronal structure well, suggesting that the widths of coronal loops and showers are very similar. Furthermore, most of these shower events occur in one of the two loop legs, while only some of the shower events cover the entire loop structure, including the loop apex. The average of both in the respective measured quantity (width (W), length (L) and duration (Δt)) was taken for the few cases where shower events occurred along both loop legs. Shower events are estimated to occupy one-third of the loop length based on visual inspection.

Figure 4.2 displays all the traced 50 shower events in SJI 2796 Å (a), SJI 1400 Å (b), and Cool AIA 304 Å (c) (top panels). The colours in these panels correspond to the time occurrence of shower events. Slight differences are observable among the channels, arising from variations in intensity (line opacity) and contrast against the background, amount of noise (instrument sensitivity), spatial resolution of the instrument, and differences in height occurrences. In any case, the shower events can be distinguished and appear ubiquitous over AR. Panel (d) and panel (e) in the same figure (Figure 4.2) show 1D histogram distributions of the lengths (L_{shower}) and widths (W_{shower}) of shower events, respectively. A very similar average L_{shower} and W_{shower} were found across the channels. Namely, average L_{shower} of 28$\pm$12 Mm for the SJI 2796 Å, 27$\pm$11 Mm for the SJI 1400 Å, and 26$\pm$13 Mm for the AIA 304 Å, and average W_{shower} of $\approx$ 2$\pm$0.7 Mm, for all channels. The L_{shower} and W_{shower} appear slightly shorter in SJI 1400 Å and AIA 304 Å due to the higher noise, lower sensitivity and opacity, compared to SJI 2796 Å. A detailed explanation of these differences between the channels is given in the previous chapter in Figure 3.6.

As shown in panel (f), shower events are relatively long-lived. Their time durations across chan-

nels are similar (35±19 min for the SJI 2796 Å, 35±22 min for the SJI 1400 Å, and 36±19 min for the AIA 304 Å) and lasting up to 80 minutes. Panel g in the same figure shows the average width variations with height. Here, the zero indicates the solar limb. We found almost no expansion in the upper corona up to 40 Mm height, while the very strong expansion can also be seen below 12 Mm. The RHT routine does not accurately track the rain at the loop apex because of the low velocities, especially when the angle between the LOS and loop planes is minimal. This causes significant variations in the measured widths observed above 40 Mm in Figure 4.2.

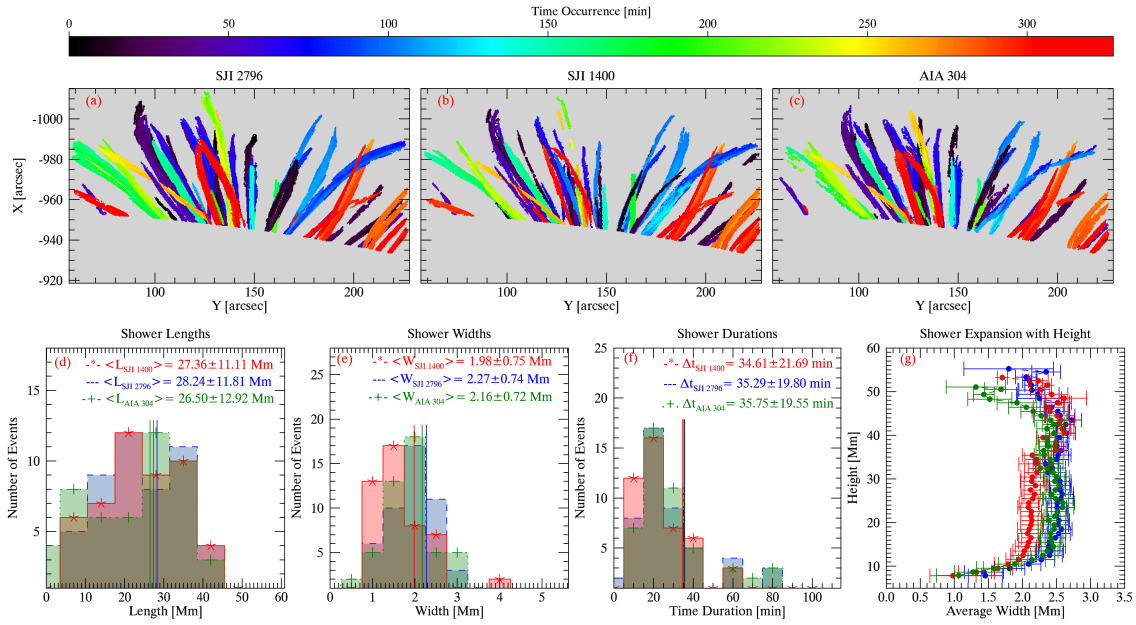

Figure 4.2: Top: Time occurrence panels of traced 50 shower events in SJI 2796 Å (a), SJI 1400 Å (b), and AIA 304 Å (c). Bottom: 1D Histogram distribution of shower lengths (d), widths (e), and durations (f) (from left to right, respectively) and their corresponding mean and standard deviation in the inner caption. The average width of the shower and its standard deviation with height (g).

4.4.2 Thermal Evolution

The apex of loop structures where showers occur often appears bright in the EUV, prior to or during the appearance of coronal rain and catastrophic cooling. An example of this is displayed in Figure 4.3, where Shower 19+20 is shown (see also panel (d) and panel (e) in Figure 4.1). In order to investigate the thermodynamic evolution in more detail, we focus on relatively isolated two shower events (Shower 19+20 and Shower 32 in Figure 4.1 on panels d and e, respectively), thus minimising loop overlapping.

Figure 4.4 (and the corresponding animation in Şahin and Antolin (2022)) shows the DEM results

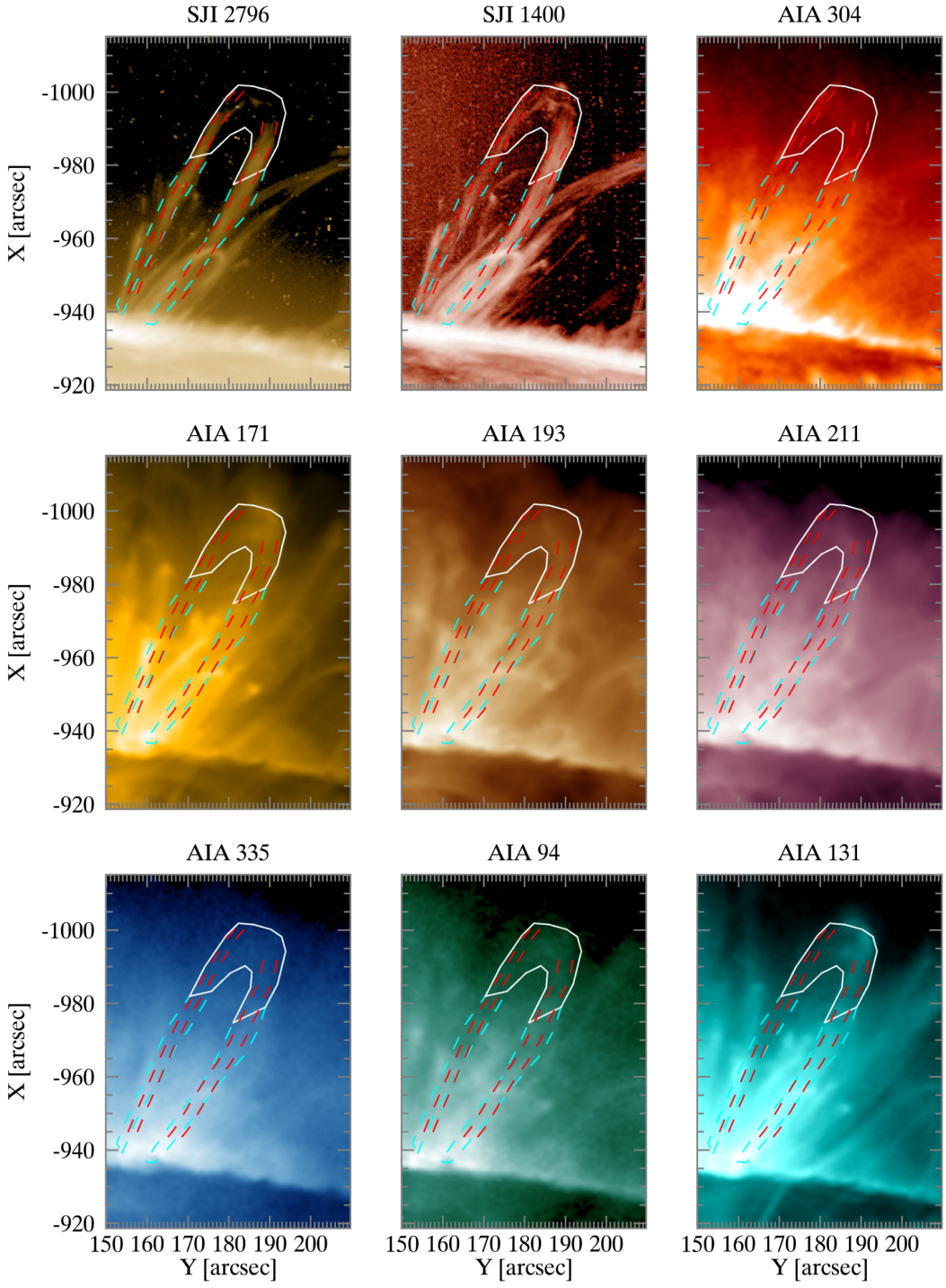

Figure 4.3: SJI and AIA channels of Shower 19+20. Each image represents an average of an 11-minute time period. The loop apex is indicated by the solid white contour. The cyan contour shows the loop legs derived from AIA 171 Å, while the red contour corresponds to the shower captured by the "region_grow" algorithm. The AIA 304 Å correspond to the original AIA 304 (i.e. without removal of the diffuse component). The accompanying animation (between 7:55 and 09:45 UT) is available in Şahin and Antolin (2022).

for various temperature bins corresponding to Shower 19+20 (shown by arrows in Figure 4.1). The loop apex hosting this shower event can be identified in almost all EM maps inside the solid-white contour lines. This shower event started at 08:54:29 UT and lasted 48 minutes. However, the DEM was examined one hour before the start of the shower event. The cooling is particularly clear in this loop despite being observed coronal temperature throughout the FOV. The DEM increases in the cooler temperature bins within the solid-white contour lines (loop apex), indicating evidence of loop cooling.

We display the scaled total DEM over the loop apex (solid white-contour line in Figures 4.3 and 4.4) in Figure 4.5 with respect to time in order to see the cooling trend more clearly. We compare the emission evolution at hot temperatures with that at cool temperatures, seen in the histograms corresponding to coronal rain pixels for these shower events at the loop apex and along the legs.

4.4.3 TNE Volume

In this part of the study, the aim is to estimate the volume affected by TNE over the AR. Given the very good match found between the widths of the shower and coronal loop, as well as the significant loop portion occupied by showers, for the TNE volume calculation, the properties of the rain clumps and showers were used. This calculation is divided into the following steps, which are performed for each channel. Since coronal rain is dynamic and falls on average, two successive snapshots may overlap rain pixels in the FOV area, depending on the clump length (l_{clump}), width (w_{clump}), velocity (v_{clump}) and cadence of the instrument. The length and area of this overlap are:

$$< length\_overlap > \;=\; < l_{clump} > - cadence \times < v_{clump} > \tag{4.1}$$

$$< area\_overlap > \;=\; < length\_overlap > \times < w_{clump} >, \tag{4.2}$$

The area in the FOV occupied by a single rain clump as:

$$< area\_clump > = < l_{clump} > \times < w_{clump} > \tag{4.3}$$

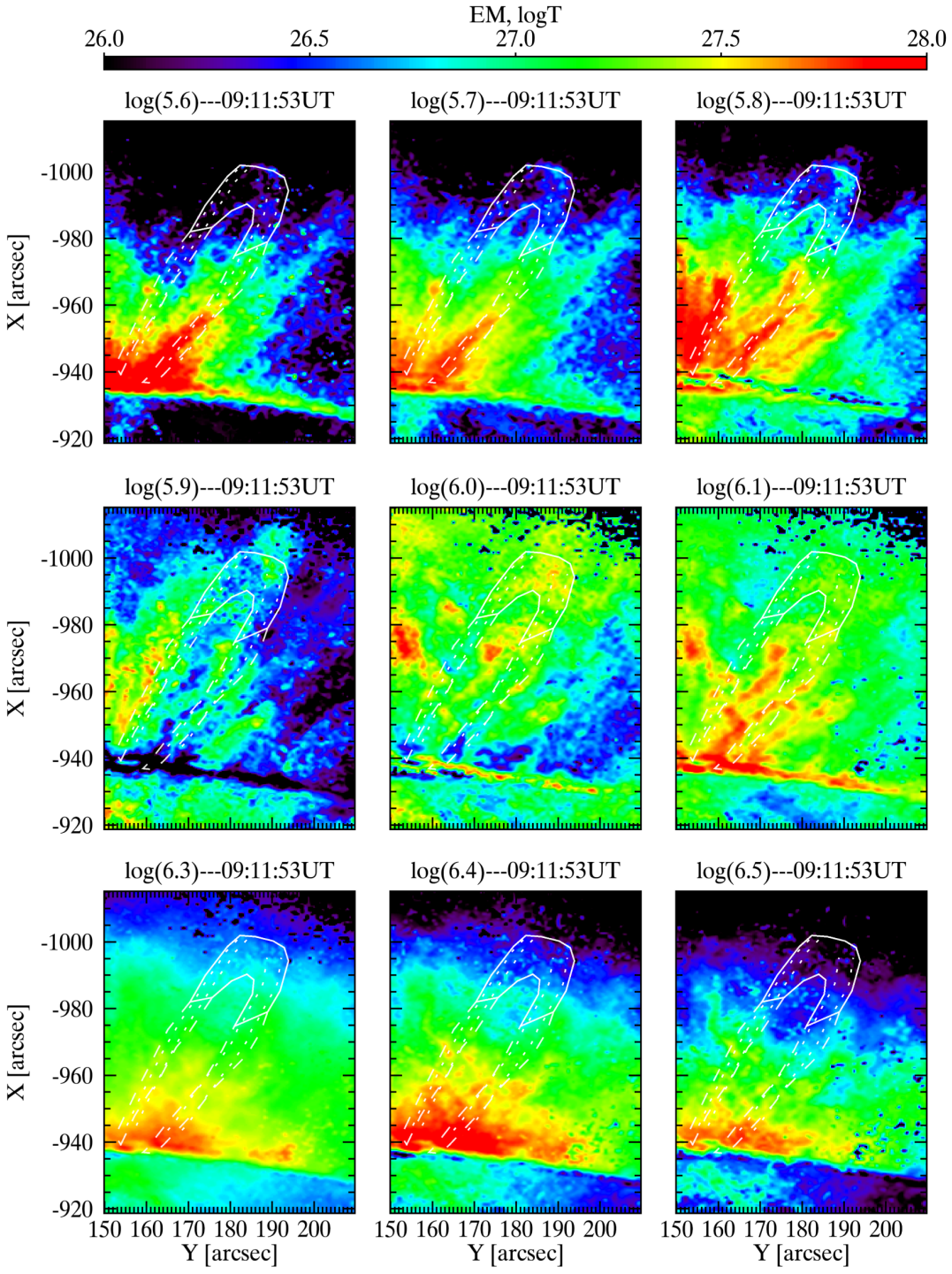

Figure 4.4: EM maps of Shower 19+20. The loop apex is indicated by the solid white contour. The dashed contour indicates the loop legs derived from AIA 171 Å, while the dotted contour corresponds to the shower captured by the "region_grow" algorithm. The accompanying animation (between 7:55 and 09:45 UT) is available in Şahin and Antolin (2022).

Then, the fraction of rain clump overlapping between 2 consecutive images is:

$$< fraction >= \frac{< area\_overlap >}{< area\_clump >} \tag{4.4}$$

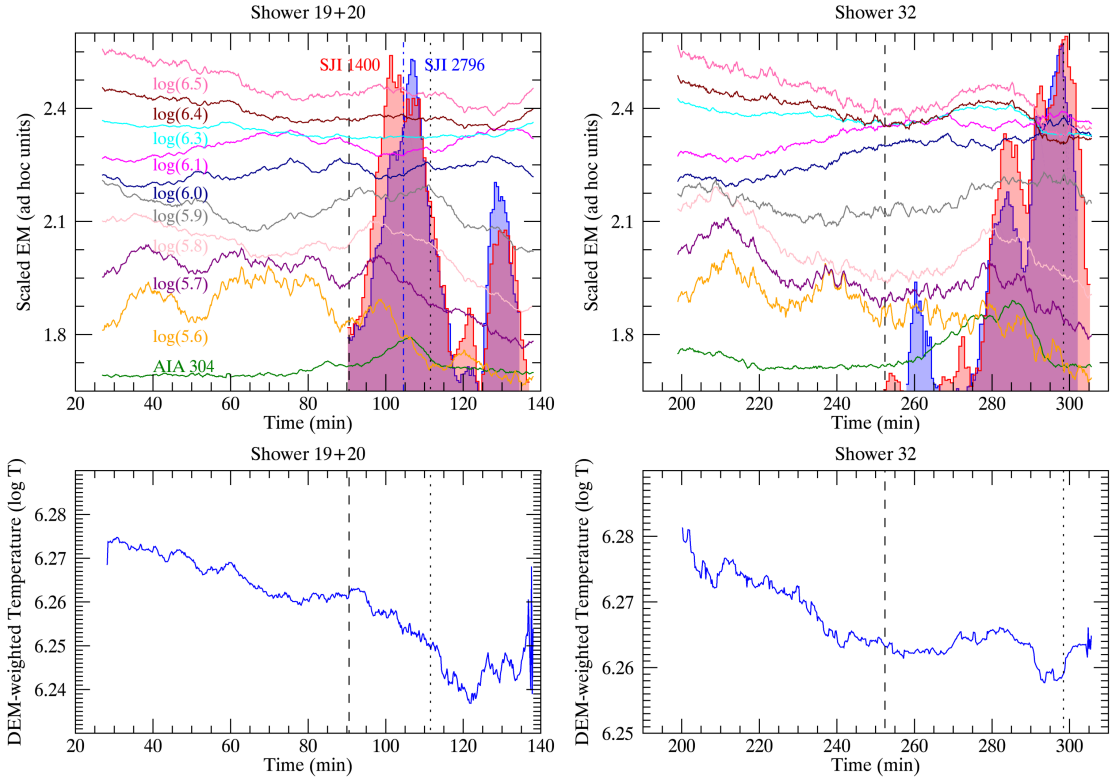

Figure 4.5: Top: Scaled EM plots for showers 19+20 (left) and 32 (right) over the white-solid contour shown in Figures 4.3 and 4.4. The histograms indicate the rain pixels (including both legs of shower 19+20), which are detected with RHT and "region_grow" routines in SJI 2796 Å (blue) and SJI 1400 Å (red). The legend for each curve is shown in the top left plot and it is the same order and colours for Shower 32. The blue dashed-dotted vertical line on Shower 19+20 plot indicates to the time of Figures 4.3 and 4.4. Bottom: DEM-weighted temperature plots for showers 19+20 (left) and 32 (right). The vertical black dashed lines depict the beginning of the shower events, while the black dotted line shows the time when the shower is not observed anymore at the loop apex.

The number of pixels in the non-overlapping area is then given by:

$$N_{no\_overlap} = N_{\theta_{xy}} \times (1 - < fraction >), \tag{4.5}$$

where $N_{\theta_{xy}}$ is the number of coronal rain pixels detected with the RHT routine. The number of expected shower events is given by:

$$N_{exp\_shower} = \frac{N_{no\_overlap} \times N_{shower}}{N_{shower\_pixels}}, \tag{4.6}$$

where $N_{shower} = 50$ corresponds to the manually identified showers, and N_{shower_pixels} is the total number of pixels for these 50 showers.

The TNE volume is estimated as:

$$V_{TNE} = \pi \frac{1}{f} N_{exp\_shower} \times < l_{shower} > \left(\frac{< w_{shower} >}{2} \right)^2, \tag{4.7}$$

where f shows the average fraction of the loop occupied by a shower (we take $f = 1/3$), and we approximate a shower as a cylinder.

In order to estimate the number of showers (in Equation 4.6), we used the average $< w_{clumps} >$ (1.2±0.3, 0.7±0.2, and 0.8±0.2 Mm for the AIA 304 Å, SJI 1400 Å, and SJI 2796 Å, respectively) and $< l_{clumps} >$ (11±7, 7±5, and 9±6 Mm for the AIA 304 Å, SJI 1400 Å, and SJI 2796 Å, respectively). We found $185 \pm 39, 208 \pm 77$, and 71 ± 4 expected shower events in the SJI 2796 Å, SJI 1400 Å, and AIA 304 Å, respectively. Then, the TNE volume is found to be $6.34 \pm 4.91 \times 10^{28}$ cm^3 for SJI 2796 Å, $5.26 \pm 4.52 \times 10^{28}$ cm^3 for SJI 1400 Å, and $2.07 \pm 1.71 \times 10^{28}$ cm^3 for AIA 304 Å. The estimated TNE volume is expected to be higher since the rain detection conditions used for the RHT routine are strict to avoid any influence from noise, since the rain intensity can sometimes be in the same order as the noise (see Schad, 2017, for detailed information).

4.5 Conclusion and Discussion

In this study, one of the first big questions we focus on is whether a proper definition or identification aid for what is loosely and observationally attributed as a coronal loop can be derived from the coronal volume occupied by a shower. This question is important because the coronal magnetic field cannot be observed directly. The optically thin coronal emission can create a loop-like structure that may be misleading, which is demonstrated by the concept of "coronal veil" introduced by Malanushenko et al. (2022). Furthermore, there is a debate on whether coronal loops have a clear definition, as global MHD simulations indicate that there are continuous magnetic connectivity changes and fuzzy boundaries among various magnetic field structures (Gudiksen and Nordlund, 2005). As shown in Antolin (2020), on the other hand, a coronal rain shower occurrence indicates a TNE-TI scenario and, consequently, a coherent thermodynamic evolution over a bundle of magnetic field lines. Showers of high coronal rain densities and an abundance of rain clumps can cause notable optical thickness in chromospheric and TR lines. This reduces the projection effect.

During a 5.45-hour observation of an AR at the east limb, we observed a widespread presence of

showers. We detected 50 shower events and measured their average length and width, which were approximately 27±11.95 Mm and 2±0.74 Mm, respectively. There was a small variation in these measurements across the temperature range we examined. The widths found closely match the initial estimates made in Antolin and Rouppe van der Voort (2012) and Antolin et al. (2015) for individual events. The observed coronal loops in the EUV bands are compared with the shower in terms of morphology and a good agreement is found. The widths we found match previous 3D MHD simulations (Peter and Bingert, 2012) and X-ray and EUV observations (Aschwanden and Boerner, 2011; Peter et al., 2013). Showers within coronal loops can reliably identify loop structures in observations, particularly those in a TNE state, due to their ubiquity and estimated length of one-third of the entire loop length. Our analysis of the shower morphology is consistent with the literary study of loops and provides insight into the mystery of their constant cross-section. In agreement with EUV observations (Aschwanden and Nightingale, 2005; López Fuentes et al., 2008), little average expansion of the shower cross-section with height was found, further supporting that this effect is not apparent (López Fuentes et al., 2008). Only a part of the flux tube is affected by TNE, specifically a 2 Mm width where the temperature is evenly spread, even if the cross-section expands in volume. This agrees with Peter and Bingert (2012) that a particular thermodynamic distribution perpendicular to the magnetic field is responsible for this effect. However, we see significant growth in lower coronal altitudes. Above the solar surface (at a height of 8 to 12 Mm), the width expands from 1 to 2.4 Mm resulting in an area expansion of 5.7, which is consistent with earlier findings by Antolin et al. (2015).

We further examined the thermal evolution of a few coronal structures that hosted showers. These structures were chosen based on their relative isolation in the FOV. According to the DEM results, cooling patterns are consistent with prior studies (Viall and Klimchuk, 2012). These cooling patterns were most noticeable in the coronal structures. An hour before the shower events, consistent heating and cooling were observed in the hot (logT 6.3-6.5) and cool coronal temperatures (logT 6-6.1), respectively. This matches the expected time it takes for loops to cool through radiation at the start of the TNE cycle, with an average temperature of 3×10^6 K and density of 10^9 cm^{-3} (see Equation 18 in Antolin and Froment (2022)). Stronger variation was observed during TR temperatures ($\log T$ = 5.6-5.9) and shower events throughout this time period. This type of increased activity is often observed in AR (Ugarte-Urra et al., 2009; Reale, 2014) and corresponds to the

radiation-dominated evolution of coronal loops, followed by catastrophic cooling at the end of the TNE-TI cycles (Antolin et al., 2022).

We have finally determined the amount of coronal volume in an AR that is in a state of TNE. Coronal volume determination is important because TNE is associated with highly stratified and high-frequency heating (Klimchuk and Luna, 2019), which limits potential heating mechanisms. Therefore, in this study, we estimated the total number of showers and found an average of 155 ± 40 across all channels. We estimated the average TNE volume of $4.56\pm3.71\times10^{28}$ cm^3 by assuming that a shower takes up 1/3 of a coronal loop. Assuming the same length along the LOS as the width of the IRIS FOV, we estimate the total AR volume to be roughly 8.7×10^{28} cm^3. This approach relies on an approximation where the AR is modelled as a trapezoidal shape that encompasses the observed coronal loops. Our estimated volume for TNE is approximately 50% of the volume for AR. However, it is important to note that this estimation is very likely a lower estimate since we are not able to detect certain TNE cycles through IRIS that do not experience catastrophic cooling and therefore do not reach TR temperatures or lower. Likewise, the probability of detecting loops with TNE cycle periods longer than our observation sequence decreases with the period. Studies by Auchère et al. (2014) and Froment (2016) show that these cycles occur at a similar rate between 6 and 16 hours in AR. Moreover, we applied strict conditions to detect coronal rain, disregarding rain with low emissivity. These findings indicate that TNE is prevalent in this AR with strong stratification and high-frequency heating on average.

Chapter 5

Flare-driven Coronal Rain Analysis

Parts of this chapter form the basis of the content of a paper[5] entitled "From Chromospheric Evaporation to Coronal Rain: An Investigation of the Mass and Energy Cycle of a Flare" that has been submitted to the Astrophysical Journal. We also submitted a short review entitled "Comparison of Quiescent and Flare-driven Coronal Rain" to A&G journal.

5.1 A Brief Overview

Solar flares often display very puzzlingly long gradual phases, which has led to conjectures about their sub-structure and the existence of additional heating mechanisms besides the coronal magnetic reconnection above the loop tops (Fang et al., 2015; Reep and Toriumi, 2017). Similarly, little is known about the coronal rain often seen during the gradual phase (Scullion et al., 2016; Song et al., 2016; Jing et al., 2016), how it differs from its quiescent counterpart and, in particular, its formation mechanism. 1D radiative MHD simulations clearly show that electron beams alone are not enough to generate it (Reep et al., 2020), and it is not clear whether additional long-duration heating mechanisms exist and/or whether multi-dimensional effects are necessary. In this Chapter, we investigate a C2.1-class flare with IRIS and SDO imaging data spanning chromospheric to coronal temperatures and pay particular attention to the flare-driven rain. We analyse its evolution, dynamics, and morphology and compare it to quiescent rain in the same dataset. In response to the large energy release, compared to the pre-flare state, the amount of coronal rain increases.

[5] Şahin, S., & Antolin. From Chromospheric Evaporation to Coronal Rain: An Investigation of the Mass and Energy Cycle of a Flare.

The average widths and lengths of the clumps exhibit similarity across the examined temperature range. We estimate the total mass transported upwards due to chromospheric evaporation and downwards in shower events. Our findings reveal a noteworthy interplay: the mass draining from the shower matches with mass sourced from chromospheric evaporation. This mass correlation indicates that most of the loop undergoes catastrophic cooling and suggests an essential role of coronal rain in the mass and energy cycle of a flare. We also investigated the impact of the flare on neighbouring quiescent coronal rain. Interestingly, we observed a velocity increase of 10%-20% during the transition from pre-flare to gradual phases, indicating a discernible impact of the flare on the thermal properties and dynamics of neighbouring loops. Finally, using the DEM method, we also investigate the temperature evolution throughout the flare. The chromospheric evaporation is directly observed (also in the Fe XVIII line) with an average of 138 km s^{-1} for episodes lasting almost an hour. We observe a Kelvin-Helmholtz vortex pattern emerging in the corona as a consequence of the evaporation process. Additionally, there is a distinct and pronounced similarity in shape between the chromospheric evaporation and the subsequent occurrence of a rain shower. Notably, during this rain event, we observed a secondary increase in temperature to 7 MK highly co-localised with a rain shower, alongside nanojet-like features, which indicates a reconnection process in the post-flare loop. To our knowledge, this is the first observation of such extreme multi-thermal behaviour at the small coronal rain scales. This observation points toward the possibility that reconnection continues in the post-flare loops, probably facilitated by the partial ionisation state of the rain, and may explain the long duration of the gradual phase.

5.2 Data and Method

5.2.1 Data

We studied the AR of NOAA 12158 observed by IRIS and AIA on 2014 September 17, between 18:18:34 and 22:02:51 UT. It is located at the west limb, which is shown in Figure 5.1. During the observed period, a C2.1-class solar flare occurred in 19:29:11-20:24:26 UT time range. We use IRIS level 2 slit-jaw imager (SJI) 2796 Å and 1330 Å data which are retrieved from the instrument website[4]. The SJI 1330 passband is dominated by the C II 1335.5 Å in the upper chro-

[4]https://www.lmsal.com/hek/hcr?cmd=view-event&event-id=ivo%3A%2F%2Fsot.lmsal.com%2FVOEvent%23VOEvent_IRIS_20140917_181834_3860107353_2014-09-17T18%3A18%3A342014-09-17T18%3A18%3A34.xml

mosphere/lower transition region forming at $10^{4.3}$ K, but emission from the Fe XXI 1354.08 Å chromospheric line forming at 10^7 K can also be observed during flares. The SJI 2796 passband is dominated by the 2796 Å emission from Mg II 2796.35 Å chromospheric line forming at 10^4 K. The IRIS SJI obtained 10.36 s cadence images in the 1330Å and 2796Å over an area of $120'' \times 119''$with an image scale of $0''.3327$ pixel^{-1}.

The SDO/AIA data also analyzed in this study are level 2 downloaded through the same instrument website as IRIS with a 12 s cadence. The AIA observations contain seven broad passbands (94 Å, 131 Å, 171 Å, 193 Å, 211 Å, 304 Å, and 335 Å). However, we focused on the AIA 304 Å channel dominated by He II 303.8 Å line (forming at $\approx 10^5$ K) for the rain detection and its analysis. The pixel size of AIA is $0''.6$ pixel^{-1}; however, for the purpose of co-alignment, we have rebinned the AIA data to match the SJI plate scale.

Based on the C-class solar flare, we have divided our analysis into three parts: the pre-flare, impulsive and gradual phases. In the result section, we present the analysis of each phase. We also provide the observational time range for the pre-flare and gradual phases in Table 5.1 for each instrument.

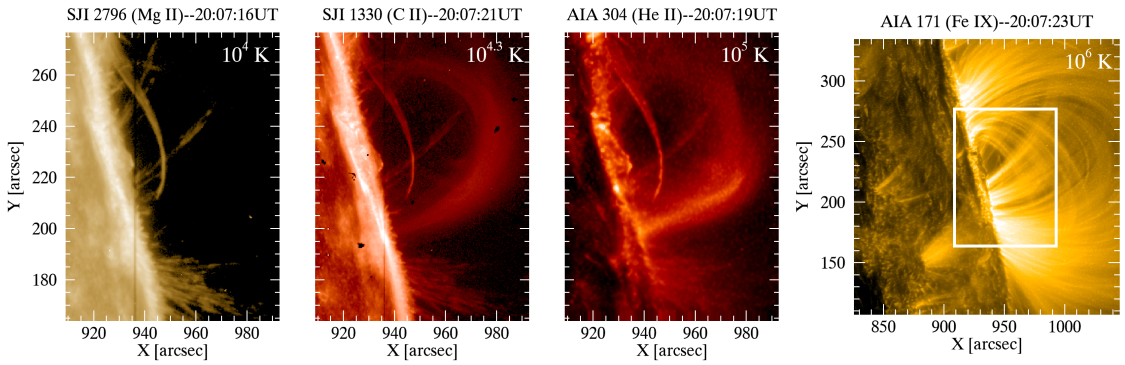

Figure 5.1: The studied region (AR NOAA 12158) at the West limb of the Sun on 17 September 2014, observed by IRIS/SJI 2796 Å (left), 1330 Å (second from left), and SDO/AIA 304 Å (third from left). The separated panel on the right shows a wider FOV with SDO/AIA 171 Å over the same AR, with a white rectangle outlining the FOV shown on the left panels.

5.2.2 Data preparation

We first resample the AIA images to match the IRIS SJIs and co-align them by matching the solar limb and using several characteristic features (such as bright points and filament patterns) on the disc and off-limb. We computed spatial shifts (x and y) at various time instances using the images

of AIA 304 Å and SJI 1330 Å. These shifts were then applied to all other AIA channels to align images with respect to the SJI images.

As mentioned in Section 2.2.6, the AIA 304 Å channel exhibits a temperature response peak at $\approx 10^5$ K, resulting from He II 304 Å emission. However, the bandpass also includes an additional secondary peak at $\approx 10^{6.2}$ K, which can be attributed to ion Si XI 303.32 Å. To remove the hot emission from the AIA 304 passband, we first fit the response function of AIA 304 over the hot temperature range with the other EUV passbands of AIA (which offer good coverage over that specific temperature range), as shown in Equation 2.18 and Equation 2.19.

The convolution of the new response function with the EUV passbands, therefore, provides the hot AIA 304 emission. The cool AIA 304 emission is then obtained by subtracting this hot component from the original AIA 304 intensity. Further details on this procedure can be found in Antolin et al. (manuscript in preparation).

Similarly to the AIA 304 Å channel, the AIA 94 Å channel is blended with three temperature emissions from Fe XV, Fe XIV, and Fe XVIII. Here, in this study, we separated the hot Fe XVIII 93.96 Å line emission with a peak at $\approx 10^{6.85}$ K from the warm component in the AIA 94 Å channel since it is particularly important to study heating events (Testa and Reale, 2012; Ugarte-Urra and Warren, 2014). For this, we use the empirical method by Del Zanna (2013) to compute the hot contribution from a weighted combination of emissions from the AIA 94 Å, AIA 211 Å and AIA 171 Å channels (see Equation 5.1).

$$I_{FeXVIII} = I_{94} - \frac{I_{211}}{120} - \frac{I_{171}}{450} \tag{5.1}$$

From now on, we will refer to those images as Fe XVIII, as opposed to the original AIA 94 Å.

5.2.3 Detection of coronal rain

Before running the semi-automatic technique for detecting coronal rain, the solar limb and its region were removed to prevent its large brightness contrast, as we did the same in Chapter 3. We have chosen a 6 Mm minimum height above the solar surface to avoid most spicules and other low-lying, cool features. Then, the automatic detection routine called the RHT (as described in detail in Section 2.2.2) was applied to detect and quantify the apparent motion of the coronal rain

Table 5.1: Observational time range with total average detected rain pixel per image for the SJI 2796, SJI 1330, and Cool AIA 304 for the pre-flare and gradual phases

Instruments	pre-flare phase	N_{pixel}/N_{image}	gradual phase	N_{pixel}/N_{image}
SJI 2796	18:18:40-19:29:06	955	20:24:42-22:02:56	2180
SJI 1330	18:18:34-19:29:01	460	20:24:37-22:02:51	1548
Cool AIA 304	18:18:31-19:28:55	718	20:24:43-22:02:55	2003

material.

For the running mean filters (w_r), we used 18-step (≈3 minutes) for the SJI 2796 Åand SJI 1330 Å, and we used 16-step(≈3 minutes) for the AIA 304 Å. For the bidirectional filter, an 18-step bidirectional filter was used in three channels. For the circular RHT kernel width (D_w), the value was chosen as 31 (i.e., $D_w = 31$) for all channels. The standard deviation (σ) for the background noise was chosen as 1.1 DN for the SJI 2796 Å and SJI 1330 Å, and 1.4 DN for the AIA 304Å.

As shown in Table 5.1, in total, we detected 955, 460, and 718 coronal rain pixels per image in the SJI 2796 Å, SJI 1330 Å, and AIA 304 Å, respectively, during the pre-flare phase. These numbers are 2180, 1548, and 2003, in the same order for the gradual phase. The following set of conditions has also been applied considering the maximum cut-off for measurable projected velocity. Only the pixels for which $\overline{R}_{xy} \geq 0.8$, $\max[H_{xy}(\theta)] \geq 0.75$, $\overline{R}_t \geq 0.8$, $\max[H_t(\theta)] \geq 0.75$ were included for all channels, and $|\overline{\theta}_t| \leq 85^\circ$ for the AIA 304 Å and $|\overline{\theta}_t| \leq 84^\circ$ for both SJI channels (see Figure 3.2), in order to make the velocity error smaller than the reasonable maximum cut-off for measurable projected velocity (see Equation 3.1). A reasonable maximum cutoff for measurable projected velocities for AIA 304 Å and SJI channels is 576 km s^{-1} and 670 km s^{-1}, respectively. Using the above condition, the results shown here are limited to ≈226 km s^{-1}.

5.3 Results

In the following subsections, I present a comprehensive analysis of the outcomes obtained from our investigation into chromospheric evaporation, flare-driven coronal rain, and neighbouring quiescent coronal rain topics. This exploration delves into the detailed aspects of morphology, dynamics, and thermodynamics.

5.3.1 Chromospheric Evaporation

Flare ribbons in chromospheric lines such as Hα, which are a direct signature of the impact of electron beams in the chromosphere, set the onset of chromospheric evaporation (CE). Here, we study the impulsive phase of the solar flare, where we see the flare ribbons and CE (i.e. hot regions). CE occurs between 19:29 and 20:24 UT time range. In Figure 5.1, the characteristics of the diffuse emission signature of CE can be clearly seen in the SJI 1330 Å and AIA 304 Å. The SJI 2796 Å, on the other hand, presents an absence of this evaporation while showcasing the intricate clumpy morphology of quiescent coronal rain. We applied the RHT routine to SJIs and AIA data during the impulsive phase and found that RHT was also able to detect the CE dynamics. In Figure 5.2, we show the spatial (top) and the temporal (bottom) mean angles of the observed active region. Here, in the SJI 1330 Å (bottom-middle) map, the region filled with pink-purple colours corresponds to pixels within the CE. As can be clearly seen, the other two channels (SJI 2796 Å and Cool AIA 304 Å) do not have any signature of this chromospheric evaporation.

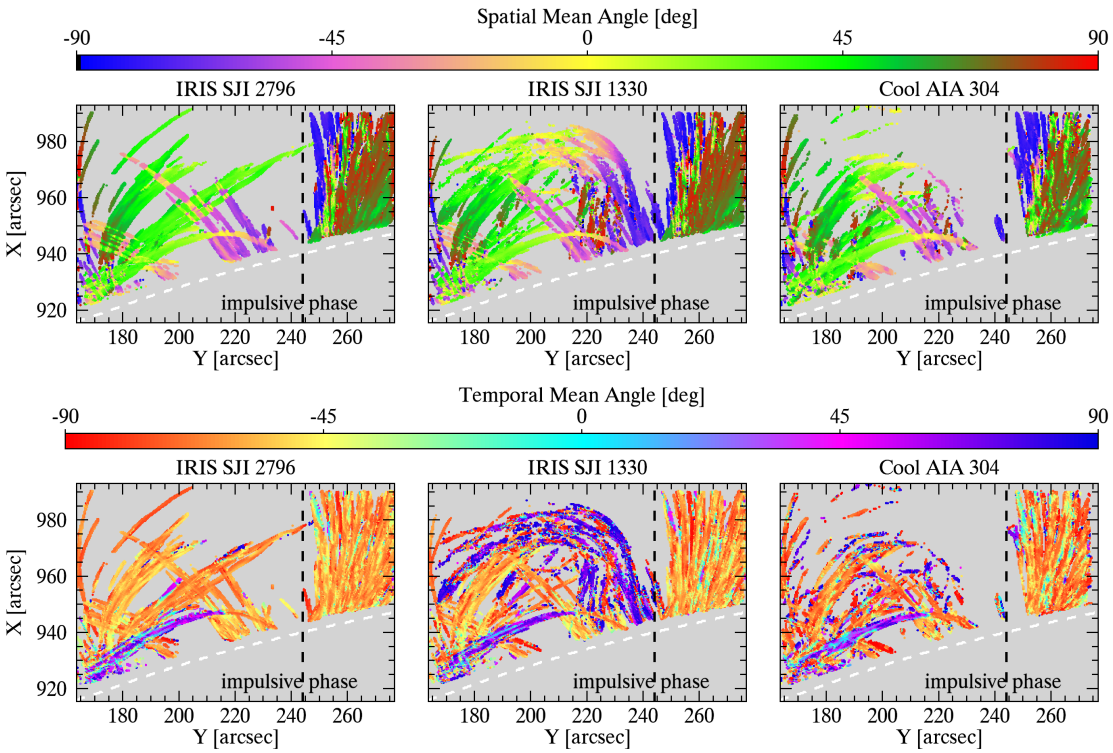

Figure 5.2: Average spatial mean angle (top) and temporal mean angle (bottom) map over the entire time sequence of the impulsive phase as derived using the RHT

In the following subsections, we focus only on the upward direction originating from CE.

5.3.1.1 Dynamics

Using this ability of RHT, we eliminate the coronal rain pixel and focus only on the region where CE occurs (see the left panel in Figure 5.3) in the SJI 1330 Å. Note that, in this plot, we relaxed the conditions we used after the RHT routine to capture more material in the CE. We only include pixels for which $|\overline{\theta}_t| \leq 87°$ instead of $|\overline{\theta}_t| \leq 84°$. The left panel in Figure 5.3) shows the projected velocity (saturated by 200 km s^{-1}) in the SJI 1330 Å, which is obtained using the above conditions. The right panel in the same figure shows a 1D velocity distribution which is derived from the left-side plot. The maximum velocity is up to ≈400 km s^{-1}. We found that the average speed of CE is 139±83 km s^{-1}.

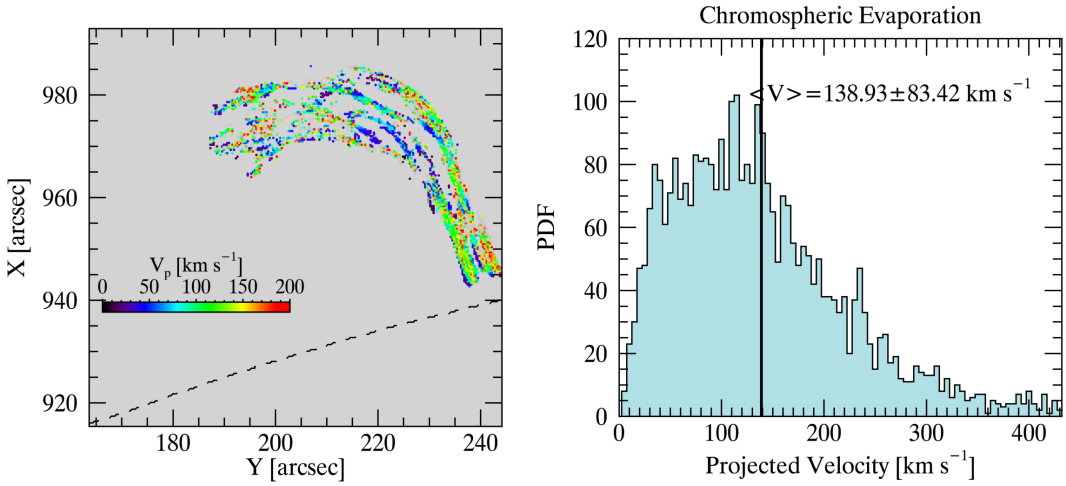

Figure 5.3: Average upflow projected velocities of chromospheric evaporation in SJI 1330 Å and its 1D velocity histogram distribution.

We have also tracked the CE along the loop with the help of the CRisp SPectral EXplorer (CRISPEX) and Timeslice ANAlysis Tool (TANAT), two widget-based tools programmed in the Interactive Data Language (IDL). These tools provide easy browsing of the image or spectral data, the determination of loop trajectory, extraction, and further analysis of time-distance diagrams. The white dashed line on the left top panel in Figure 5.4 shows the tracked path along the CE loop over the SJI 1330 Å image. Its time-distance map from TANAT is shown on the bottom panel in the same figure. The region between the two solid vertical lines on this diagram shows the region of interest (i.e. observation time range of CE), where we derived the velocity information from the

observed slopes. The velocity of the CE varies along their paths. Therefore, we made multiple velocity measurements at different heights. A 1D histogram plot of these measurements is given on the top-right panel in the same figure. A broad distribution of velocity between 50 km s^{-1} and 100 km s^{-1} with an average 136±32 km s^{-1} is obtained. Notably, this result is in agreement with the velocity from the RHT finding. In the existing literature, the velocities associated with CE display a range of values. For instance, Li et al. (2022) reported an observed velocity of 126-210 km s^{-1} with the C6.7-class solar flare. We also observed a vortex, as shown in Figure 5.5, produced by the CE flow, closely resembling the results of Fang et al. (2016) in the 2.5D MHD model. Therefore, it is likely that this is a Kelvin-Helmholtz vortex produced by shear flow. In the numerical model, the shear flow is produced due to asymmetric heating at both footpoints, leading to asymmetric CE between both footpoints.

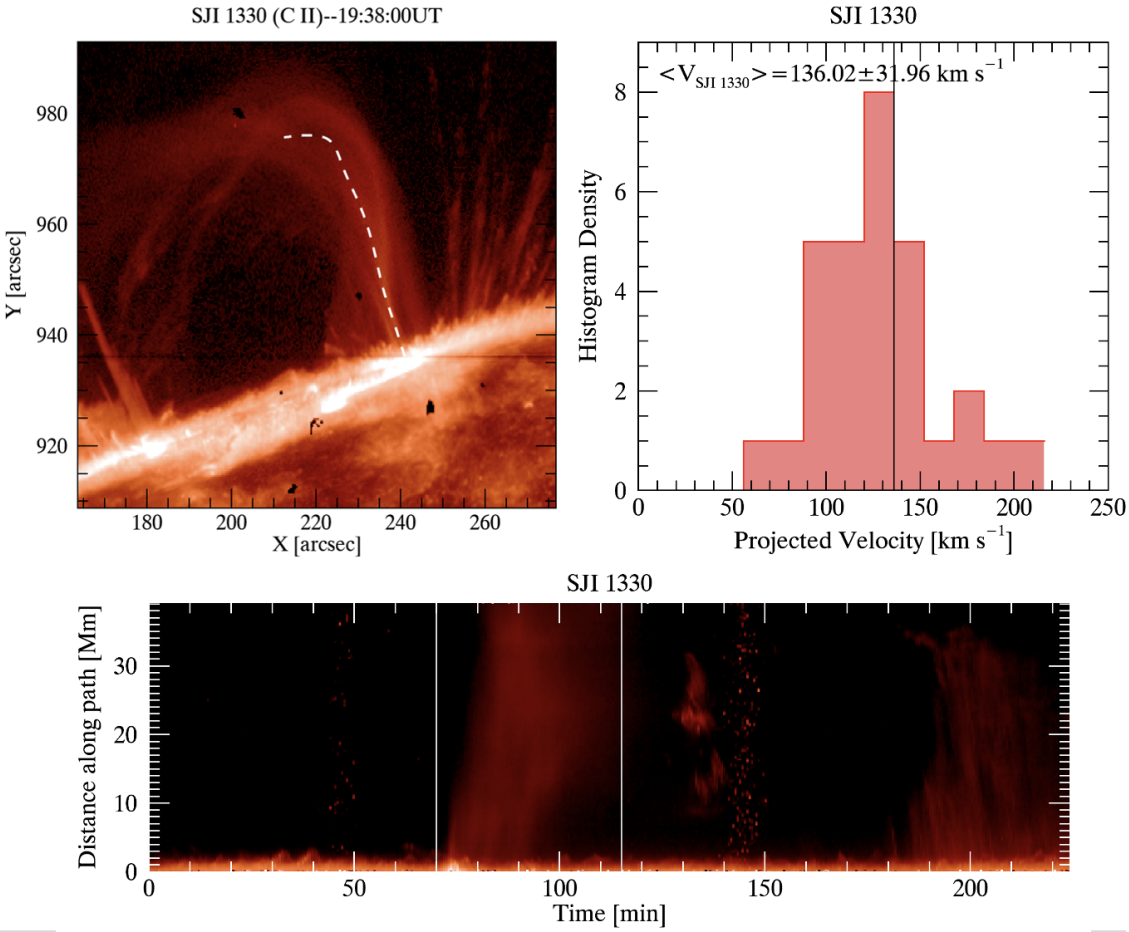

Figure 5.4: Top-left: IRIS observation in the SJI 1330 Å at 19:38:00 UT. The white dashed line denotes the paths of the tracked chromospheric evaporation. Top-right: Measured speed distribution of chromospheric evaporation. Bottom: time-distance map of the traced paths.

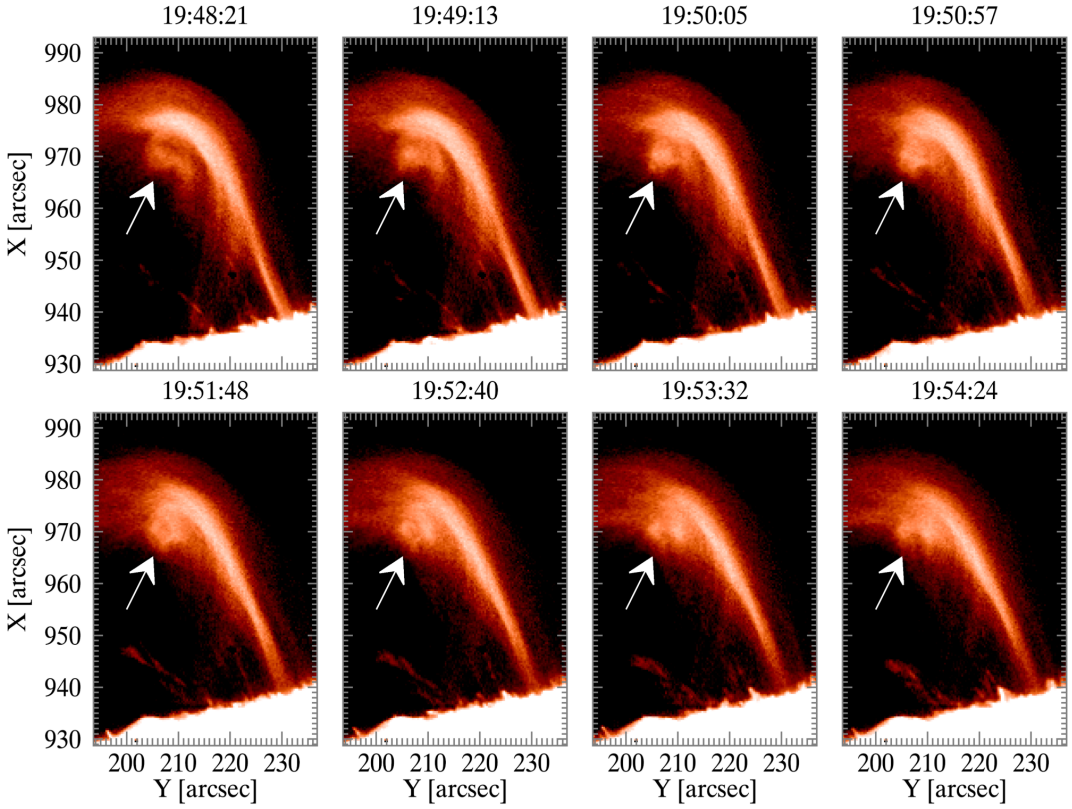

Figure 5.5: The evolution of Kelvin-Helmholtz (KH) type vortex (shown by white arrow) in response to the shear flow in the SJI 1330 Å.

5.3.1.2 Morphology

We compare CE and flare-driven coronal rain to determine if the regions where we observe the rain showers align with those of CE. Figure 5.6 presents a composite image showing impulsive and gradual phases together. Here, the red and blue corresponds to the SJI 1330 Å and AIA 94 Å images, respectively, taken during the impulsive phase (19:30 - 20:25 UT), while the green is only taken from the SJI 2796 Å images in the time corresponding to the gradual phase (20:25 - 20:37 (left) and 21:45 - 21:57 (right) UT). Contours drawn in different colours correspond to regions obtained using the SJI 1330 Å with different threshold values in the impulsive phase. Here, the region with the highest intensity value is given with the innermost contour (brightest red), and the intensity decreases as you go further out (darkest red).

We select two main shower events that correspond to two main CE regions. These shower events are also shown in Figure 5.6 with the black arrows; hereafter, shower 1 (or SH1; left panel) and shower 2 (or SH2; right panel). Similarly, CE events are hereafter named CE1 and CE2. In

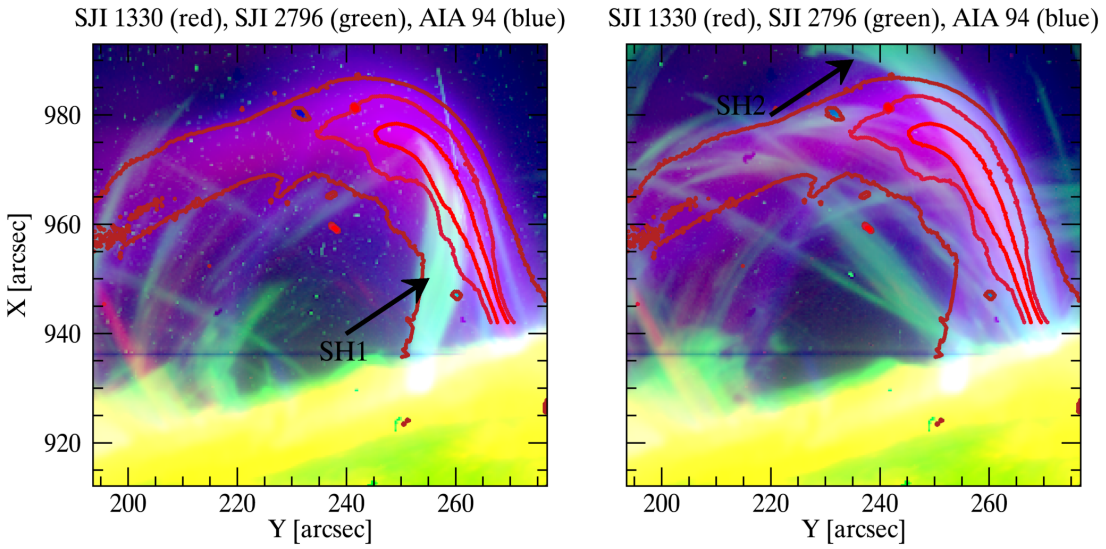

Figure 5.6: Composite image of the SJI 1330 Å (red), SJI 2796 Å (green), and AIA 94 Å (blue) taken by different observational time range. The SJI 1330 Å and AIA 94 Å were obtained by summing the images in the interval 19:30 - 20:25. The SJI 2796Å results from images summed during the 20:25 - 20:37 UT (left panel) and 21:45 - 21:57 UT (right panel) interval. The contour lines are derived from the SJI 1330 Å, emphasizing chromospheric evaporation region based on the different intensity thresholds. The black arrows show the two shower events (SH1 (left) and SH2 (right)).

Figure 5.7, we show the CE1 (left) and SH1 (right) observed during the impulsive and gradual phases, respectively. The rainbow colours show the cut along the shower and CE events at the same locations. In other words, the cuts on panel a1 have the same locations as the cuts on panel b1. The bottom panels in the same figure provide the intensity over the distance of these coloured cuts. The black line on these plots corresponds to the average intensity of these cuts. Similarly, in Figure 5.8, we show the other CE and SH events; CE2 and SH2. We have obtained the width measurement from FWHM. However, we have only taken into account the measurements where the CE/shower does not cross other CE/shower events. The average substructure width (w_{strand}) is 838 km and 1339 km for the SH1 and CE1, respectively, while it is 973 km and 1535 km for the SH2 and CE2, respectively. For the larger structure, the average width is 4965 km and 5586 km for the SH1 and CE1, respectively. It is 6369 km and 6184 km for the SH2 and CE2, respectively. These results suggest that there is a strong correspondence between CE and shower in morphology. The narrow Gaussian distribution indicates the substructure (≈1535 km) in the CE (as can also be seen in Figure 5.6 with the shades of red contours).

Note that we have also checked CE and shower events in the other channels (including AIA 304,

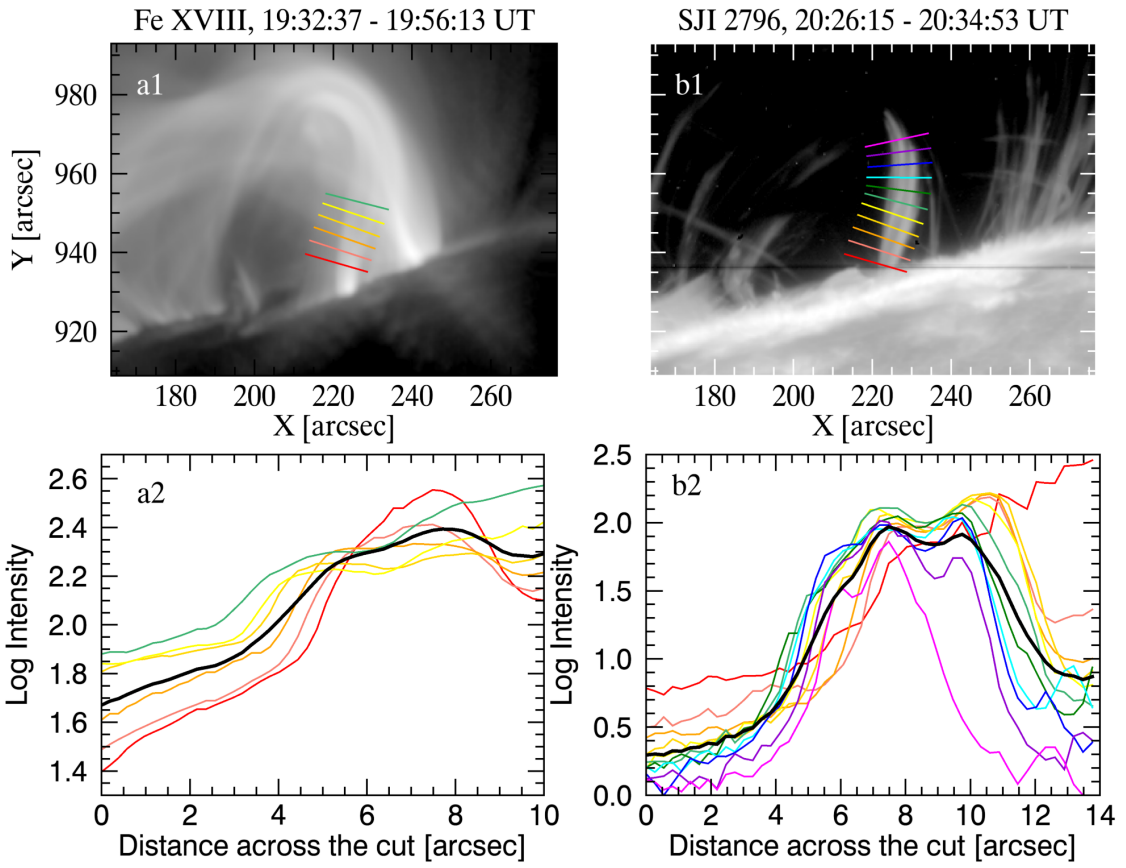

Figure 5.7: Top: The observed chromospheric evaporation (CE1, a1) and shower (SH1, b1) events during the impulsive phase in Fe XVIII (a1) and the gradual phase in SJI 2796 Å (b1). The rainbow colours indicate the perpendicular cuts to the loop trajectory. Bottom: The intensity variation over the distance of these perpendicular cuts.

131, 171, 193, 211, 335 Å), where we present these maps and their intensity plots in Figures A.5 to A.4 in the Appendix. The average width measurements for these channels are given in Table 5.2 for each CE and SH event. As can be seen in this table, CE and SH events are observed in the SJI 1330 Å. As mentioned in the data preparation section mentioned, this channel has two components: a hot emission at $\approx 10^7$ K, and a cool emission at $10^{4.3}$ K. Therefore, it is possible to observe both cool structures (SH events) and hot components (CE) in this filter.

5.3.1.3 Energetics and Thermodynamics

We also examined the mass and energy cycles during the CE time (i.e. impulsive phase). As mentioned in the previous section, there are two CEs (CE1 and CE2) at different times. We first applied the DEM method based on the "simreg" technique (see Section 2.2.4; Plowman and Caspi, 2020) and obtained the emission measure (EM) for each temperature bin (from logT 5.5 to 7.2)

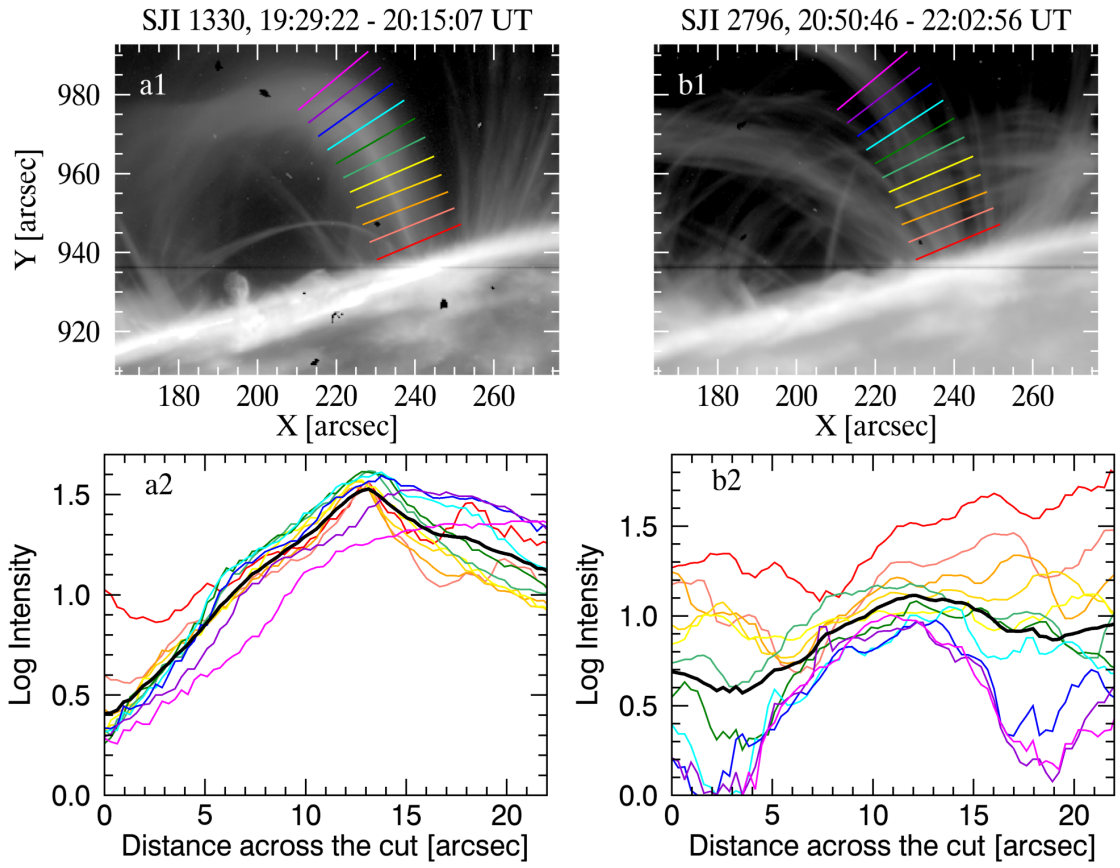

Figure 5.8: Top: The observed chromospheric evaporation (CE2, a1) and shower (SH2, b1) events during the impulsive phase in SJI 1330 Å (a1) and the gradual phase in SJI 2796 Å (b1). The rainbow colours indicate the perpendicular cuts to the loop trajectory. Bottom: The intensity variation over the distance of these perpendicular cuts.

for each CE event.

In Figure 5.9, we show two EM maps for the logT = 6.9 - 7.0 (left) and logT = 7.1 - 7.2 (right) temperature bins, which are the only bins in which the CE is observed. We defined subregions (denoted by white rectangles) for each CE (CE1 and CE2). We start our analysis by obtaining the average EM variations for the two temperature bins and each CE event over individual observed times. The logT = 6.9 - 7.0 bin starts at 19:40:07 and ends at 20:13:07, while the logT = 7.1 - 7.2 bin starts at 19:33:07 and ends at 19:50:55 (see Figure 5.11 for the CE1. For the CE2, logT = 6.9 - 7.0 bin starts at 19:29:07 and ends at 20:12:43, while the logT = 7.1 - 7.2 bin starts at 19:29:19 and ends at 19:55:31.) The average DEM-weighted temperature (See Equation 5.2) is found to be 9.4×10^6 K and 8.6×10^6 K for the CE1 and CE2, respectively.

Table 5.2: Obtained width measurements for the CE and SH events across the channels

	CE1 [km]	CE2 [km]	SH1 [km]	SH2 [km]
SJI 2796	-	-	5339±90	6350±187
SJI 1330	-	4322±253	4916±101	5460±177
AIA 304	-	-	4818±89	8588±211
AIA 171	-	-	5626±128	5221±146
AIA 193	-	-	5394±129	5973±101
AIA 211	-	-	6089±173	5798±83
AIA 335	6872±280	8761±146	-	-
AIA 94	3986±57	6331±250	-	-
AIA 131	3995±44	5752±174	-	-

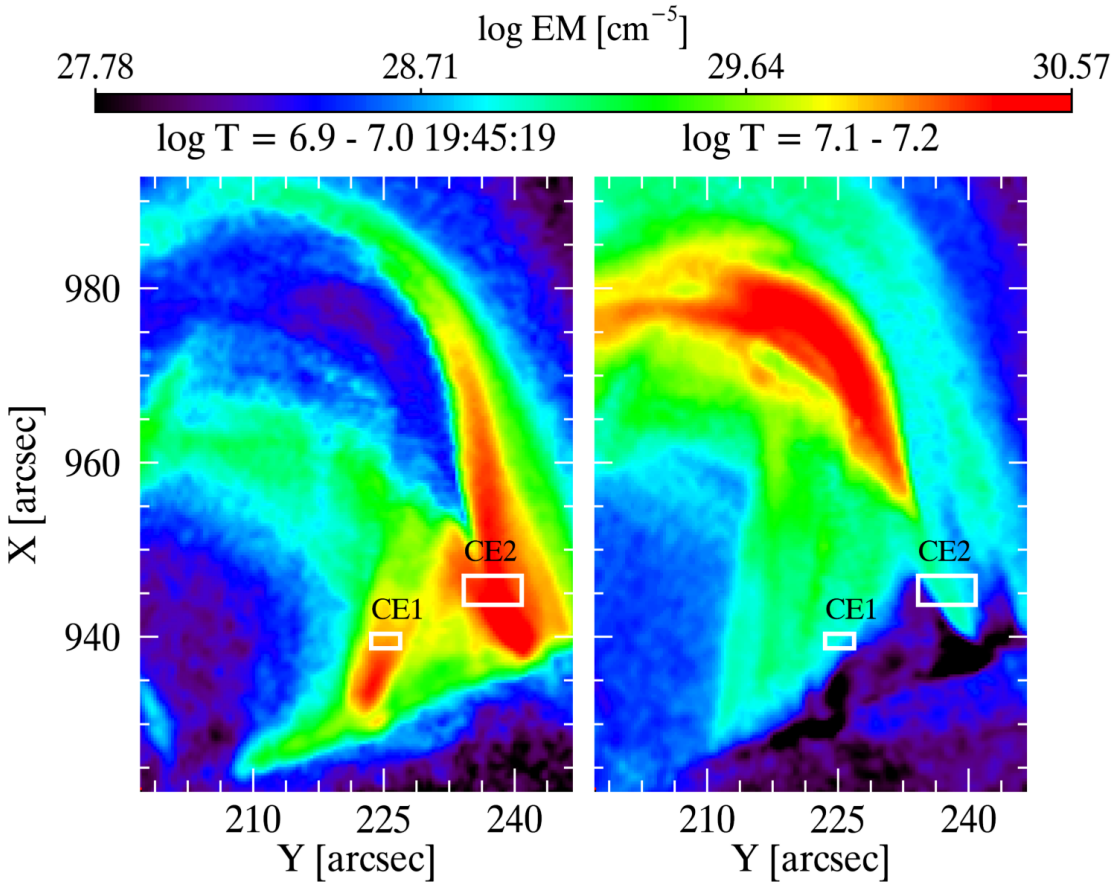

Figure 5.9: Emission Measurement (EM) for the logT = 6.9 - 7.0 (left) and logT = 7.1 - 7.2 (right). The white rectangle areas show the focused region within the CE1 and CE2 for the detailed mass-flux analysis.

$$\overline{T}_{DEM} = \frac{\int DEM(T) \times T dT}{\int DEM(T) dT} \tag{5.2}$$

We first calculated the average EM for these temperature bins using the total EM equation:

$$EM = \int DEM(T)dT. \tag{5.3}$$

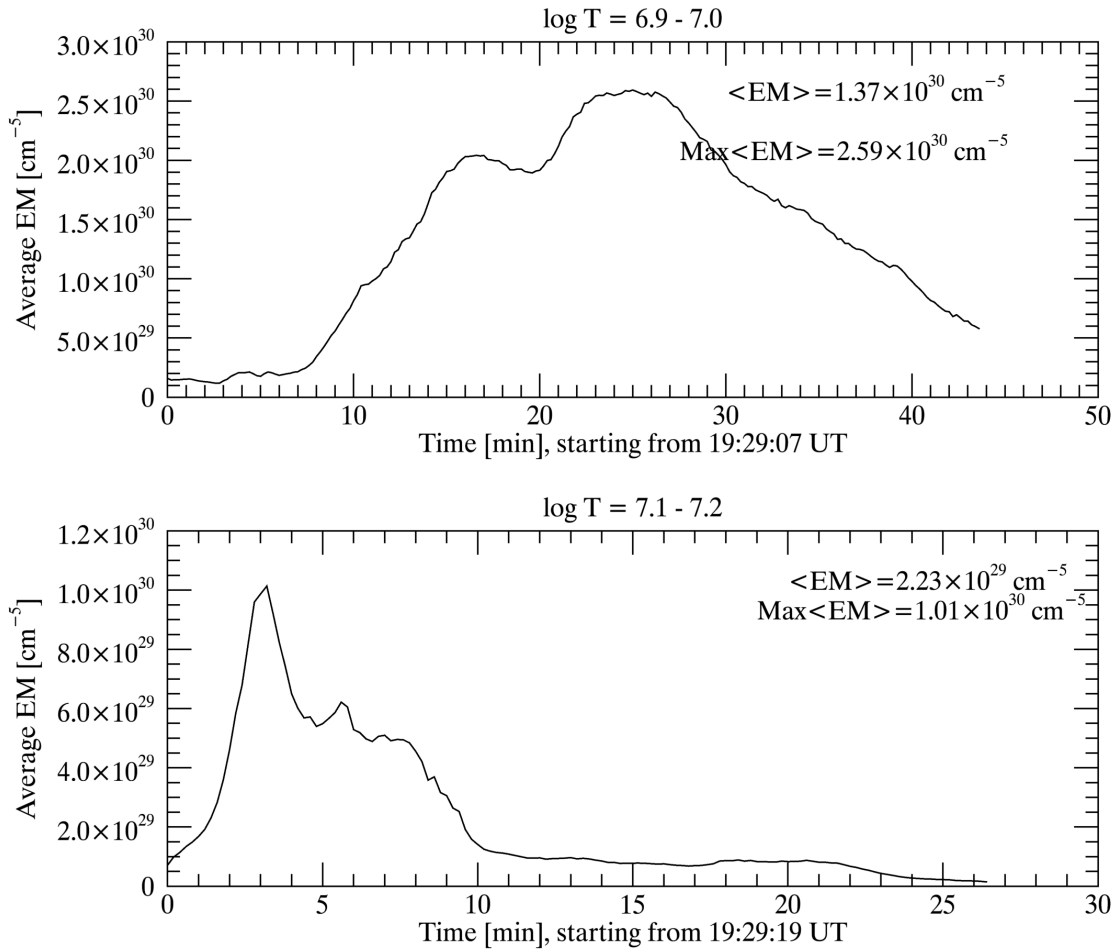

Figure 5.10: The EM variation over the observed time for individual temperature bin for the CE1, with mean and maximum values.

We found the average EM is 4.02×10^{29} cm^{-5} and 9.35×10^{29} cm^{-5} for the CE1 and CE2, respectively. Using this, we calculated the number density as follows:

$$n = \sqrt{\frac{EM}{1.2 \times w_{strand}}} \tag{5.4}$$

Here, 1.2 is a constant that comes from under a 10% Helium abundance and a fully ionised plasma assumption. We are also assuming that the strand width (w_{strand}) is representative of the smallest sub-structure present in the loop that undergoes CE. Hence, we consider that the loop can be composed of a certain number of strands whose summed intensities along the LOS result in the

observed overall CE image. The smallest sub-structure, as mentioned previously, is found to be 1339 km and 1535 km for the CE1 and CE2, respectively. We found the number density of the strand is 4.77×10^{10} cm^{-3} and 7.13×10^{10} cm^{-3}. We then calculated the mass density (ρ) by multiplying the number density by the proton mass (1.67×10^{-24} g). Then, we calculated the mass flux (F_{mass}) and mass rate (R_{mass}) as follows:

$$\begin{aligned} F_{mass} &= \rho v_{ce} \\ R_{mass} &= \rho A_{ce} v_{ce} \end{aligned} \tag{5.5}$$

where, v_{ce} and A_{ce} indicate, respectively, the velocity and area (πr^2, assuming a cylinder) of the CE events. The calculated velocity is taken as 115 km s^{-1} based on the previous section for the CE1 and is taken as 136 km s^{-1} for the CE2. For the thinnest CE strand observed, the mass flux (F_{mass}/strand) and mass rate (R_{mass}/strand) are found to be 9.17×10^{-7} g cm^{-2} s^{-1} and 1.29×10^{10} g s^{-1}, respectively, for the CE1. For the CE2, the mass flux (F_{mass}/strand) and mass rate (R_{mass}/strand) are 1.62×10^{-6} g cm^{-2} s^{-1} and 2.99×10^{10} g s^{-1}, respectively. Given the 33 and 18 minutes time range for the $\log$T = 6.9 - 7.0 and $\log$T = 7.1 - 7.2, respectively, for the CE1, the total mass (Mass$_{strand}$ = $R_{mass}\times$time) is 1.97×10^{13} g. It is found to be 6.29×10^{13} g for the CE2 for the time range of 44 and 26 minutes. To calculate the respective quantities for the entire CE, we calculated the minimum number of strands needed to cover the CE width (which is almost 5586 km for the CE1 and 6184 km for the CE2) and found the number of loop strands should be 4 for both CE1 and CE2, respectively. Then, we found that the total mass rate (Total R_{mass}) is 5.39×10^{10} g s^{-1} for the CE1 and 1.21×10^{11} g s^{-1} for the CE2. We found that 8.22×10^{13} g and 2.53×10^{14} g of total mass going up in the CE1 and CE2, respectively. Finally, we obtained kinetic energy using the following equation:

$$\begin{aligned} E_k &= \frac{1}{2}\rho v^2 \mathrm{V} \\ \mathrm{V} &= \pi r^2 v t \end{aligned} \tag{5.6}$$

where v and V indicate, respectively, the velocity and volume of the CE events. t is the duration

over which we see the upflow. We found that the kinetic energy is 5.22×10^{27} erg for the CE1 and 2.33×10^{28} erg for the CE2. A summary of all these calculations is given in Table 5.3.

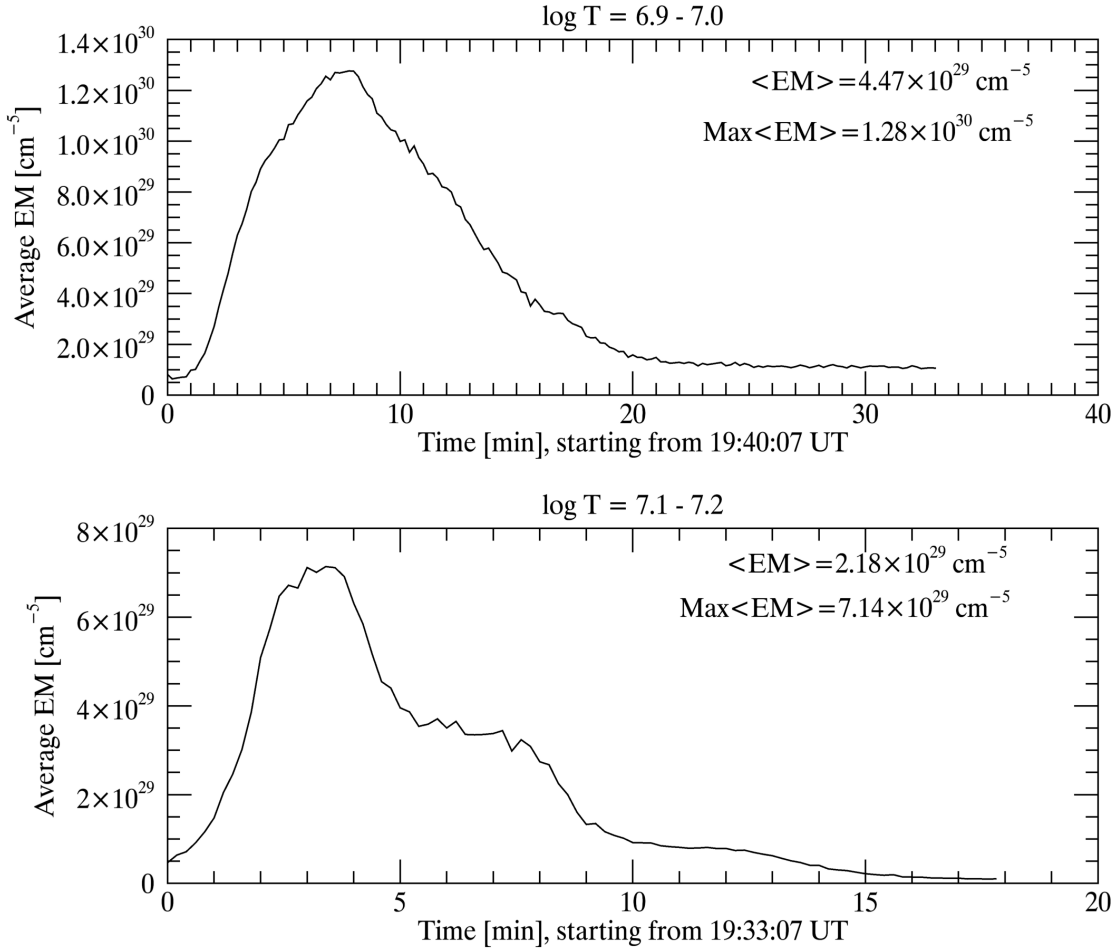

Figure 5.11: The EM variation over the observed time for individual temperature bin for the CE2, with mean and maximum values.

5.3.2 Flare-driven Coronal Rain

Now, we turn to the gradual phase of the solar flare, where we see coronal rain (i.e. flare-driven coronal rain). The gradual phase happens between 20:24:42 and 22:02:56 UT time range. As in the chromospheric evaporation part, in this Section, we will focus on flare-driven coronal rain in terms of morphology, dynamics and thermodynamics. Additionally, we will also present a comparison between flare-driven coronal rain and its quiescent coronal rain counterpart observed in the same FOV.

We first investigate the pre-flare and gradual phases, where we observe the quiescent and flare-

Table 5.3: Obtained measurements for the mass-energy cycle for the CE events

	CE1	CE2
Δt [min]	33 & 18	44 & 26
v [km s^{-1}]	115	136
w_{strand} [km]	1339	1535
$< EM >$ [cm^{-5}]	3.66$\times$10^{29}	9.36$\times$10^{29}
T$_{DEM}$ [K]	9.5$\times$10^{6}	8.6$\times$10^{6}
n [cm^{-3}]	4.77$\times$10^{10}	7.13$\times$10^{10}
ρ_{strand} [g cm^{-3}]	7.97$\times$10^{-14}	1.19$\times$10^{-13}
R$_{mass}$/strand [g s^{-1}]	1.29$\times$10^{10}	2.99$\times$10^{10}
F$_{mass}$/strand [g cm^{-2} s^{-1}]	9.17$\times$10^{-7}	1.62$\times$10^{-6}
Total R$_{mass}$ [g s^{-1}]	5.39$\times$10^{10}	1.21$\times$10^{11}
Mass$_{strand}$ [g]	1.97$\times$10^{13}	6.29$\times$10^{13}
Total mass [g]	8.22$\times$10^{13}	2.53$\times$10^{14}
Kinetic Energy [erg]	5.22$\times$10^{27}	2.33$\times$10^{28}

driven coronal rain, respectively. For this purpose, we use SJI 2796 Å, SJI 1330 Å, and AIA 304 Å channels. In Figures 5.12 and 5.13, we present the average spatial (top) and temporal (bottom) mean angle maps over the pre-flare and gradual phases from the RHT analysis, respectively.

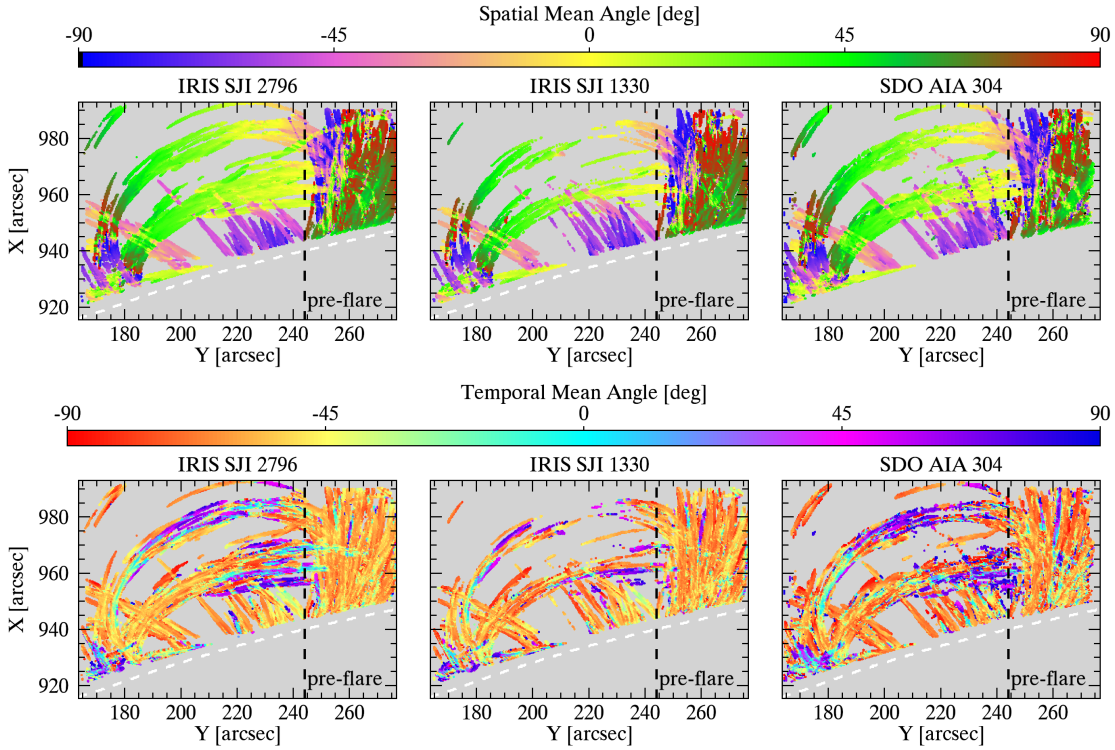

Figure 5.12: Average spatial mean angle (top) and temporal mean angle (bottom) maps over the entire time sequence of the pre-flare phase as derived using the RHT. The dashed white lines indicate the solar limb. The right side of the vertical black dashed line represents the (neighbouring) quiescent coronal rain that is observed at all times.

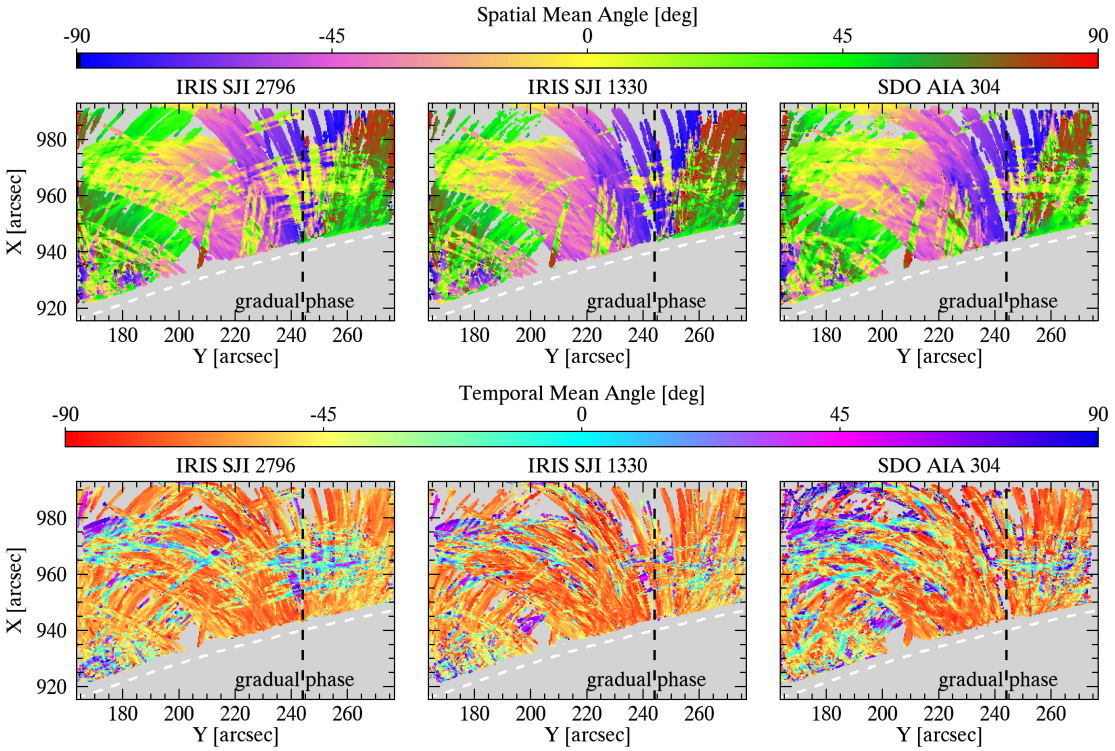

Figure 5.13: The same maps as shown in Figure 5.12 but for the gradual phase.

The spatial mean angle is associated with the inclination of the coronal rain observed in the plane of the sky (POS), whereas the temporal mean angle indicates the dynamic variations occurring along the trajectory of the coronal rain. The coloured pixels on these maps represent coronal rain, and the negative values in the temporal mean angle maps (bottom panels in Figure 5.12 and Figure 5.13) indicate the downward motion of coronal rain. As can be seen in these maps, downward motions are dominant, as expected. In these figures, the dashed white lines indicate the solar limb. We also divide these maps into two regions with the vertical dashed black line. The region to the right is observed during the entire observation time (i.e. from pre-flare to the gradual phases), and we refer to it as neighbouring coronal rain, which deserves to be analysed under a separate heading in this Chapter.

As shown in Table 5.1, the average number of detected rain pixels per image is 463, 176, and 410 for the pre-flare phase in the SJI 2796 Å, SJI 1330 Å and AIA 304 Å, respectively, while it is 1003, 646 and 1041 for the gradual phase. We would like to highlight that these average numbers are based on the left side of the vertical dashed black line shown in Figure 5.12 and Figure 5.13. Notably, the SJI 1330 Å exhibits the smallest numbers compared to the other two channels. It

Table 5.4: Increase in intensity and quantity from pre-flare to gradual phases for the SJI 2796, SJI 1330, and AIA 304

	SJI 2796	SJI 1330	Cool AIA 304
%Intensity	172	130	252
%Quantity	128	236	179

might be because of the surrounding hot material. Although coronal rain occupies a large POS area on the AR in both phases (see Figure 5.12 and Figure 5.13), it is clear that the rain quantity increases by 128%, 236% and 179% from pre-flare to the gradual phases for the SJI 2796 Å, SJI 1330 Å and AIA 304 Å, respectively.

We also investigate the relationship between the intensity of coronal rain over the solar limb and the detected rain pixel number. The top panels in Figure 5.14 show the detected rain pixels at one particular time for the SJI 2796 Å, SJI 1330 Å, and Cool AIA 304 Å, with spatial mean angle. The bottom panels in the same figure provide information on the quantity of these detected rain pixels (bottom left) and the average intensity variation above the limb (roughly 8 Mm to avoid eruption occurring in the limb) and above the threshold given in the RHT conditions over the observation time. Similarly to the rain quantity, the average intensity above the limb also increases by 172%, 130%, and 252% from pre-flare to the gradual phases for the SJI 2796 Å, SJI 1330 Å, and Cool AIA 304 Å, respectively. All these calculations are given in Table 5.4. The increase in intensity shows a similar trend as the increase in quantity.

5.3.2.1 Morphology

We perform a statistical analysis of the width and length of individual rain clumps during the pre-flare and gradual phases. The width and length are calculated in the same way as we described in the previous Chapter (see Section 3.3.2) and in Şahin et al. (2023). The histogram plots in Figure 5.15 show the distribution of the rain clump width in all three channels during the pre-flare (left) and gradual (right) phases. In each phase, these distributions are similar in shape across all channels. The average widths are found to be 0.8±0.2 Mm for SJI 2796 Å, 0.7±0.2 Mm for SJI 1330 Å, and 1.2±0.4 Mm for the AIA 304 Å in the pre-flare phase. These findings are consistent with those presented in Section 3 and in Şahin et al. (2023) where we also investigated the widths of quiescent coronal rain. In this study, widths increased by 10%, 4%, and 2% in the gradual phase and were found to be 0.8±0.3 Mm, 0.8±0.2 Mm, 1.2±0.4 Mm for the SJI 2796 Å,

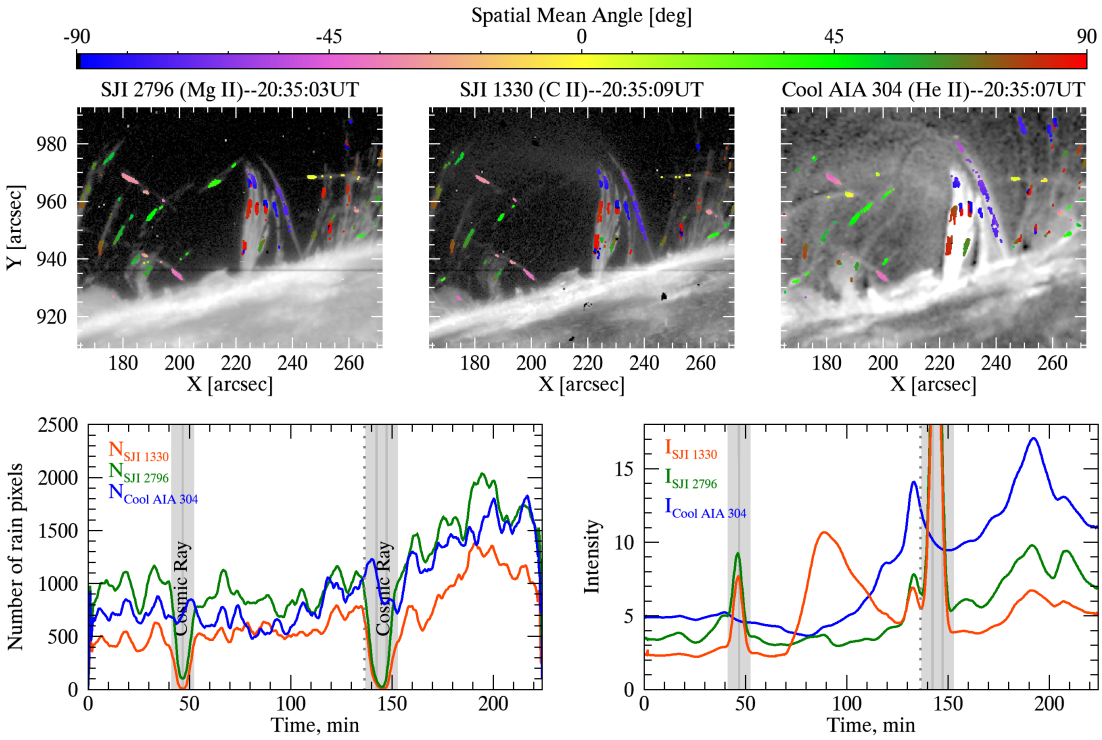

Figure 5.14: Top: An example of detected rain pixels at 20:35 UT in SJI 2796 Å, SJI 1330 Å, and Cool AIA 304 Å. Bottom: Number of rain pixels (left) and intensity (right) variation over time for the SJI 1330 Å (red), SJI 2796 Å (green), and Cool AIA 304 Å (blue). The grey-shaded areas show where the cosmic ray happens in the SJI channels. The vertical dotted lines show the time of the top panels.

SJI 1330 Å, and AIA 304 Å, respectively. However, these increments are within the standard deviation (though SJI 2796 seems more relevant), so they may not be statistically significant. The bottom plots in the same figure show the width variation with height above the solar surface, where z = 0 indicates the solar limb. In both phases (pre-flare (left) and gradual (right)), the widths remain roughly constant as the rain falls.

In Figure 5.16, we show the distribution of the rain clump lengths during the pre-flare (left) and gradual (right) phases. The average lengths are found to be 5±3 Mm, 4±3 Mm, and 7±6 Mm for the SJI 2796 Å, SJI 1330 Å, and AIA 304 Å, respectively. These lengths increased by 50%, 55%, and 13% in the gradual phase and were found to be 8±6 Mm, 7±5 Mm, 8±7 Mm for the SJI 2796 Å, SJI 1330 Å, and AIA 304 Å, respectively. Contrary to the width variation with height, the lengths of the clumps show considerable variation, becoming shorter as the rain falls. This reduction in length might be attributed to the clumps passing below the solar limb, making it difficult to continue tracking them. As given on top panels in these figures (Figure 5.15 and

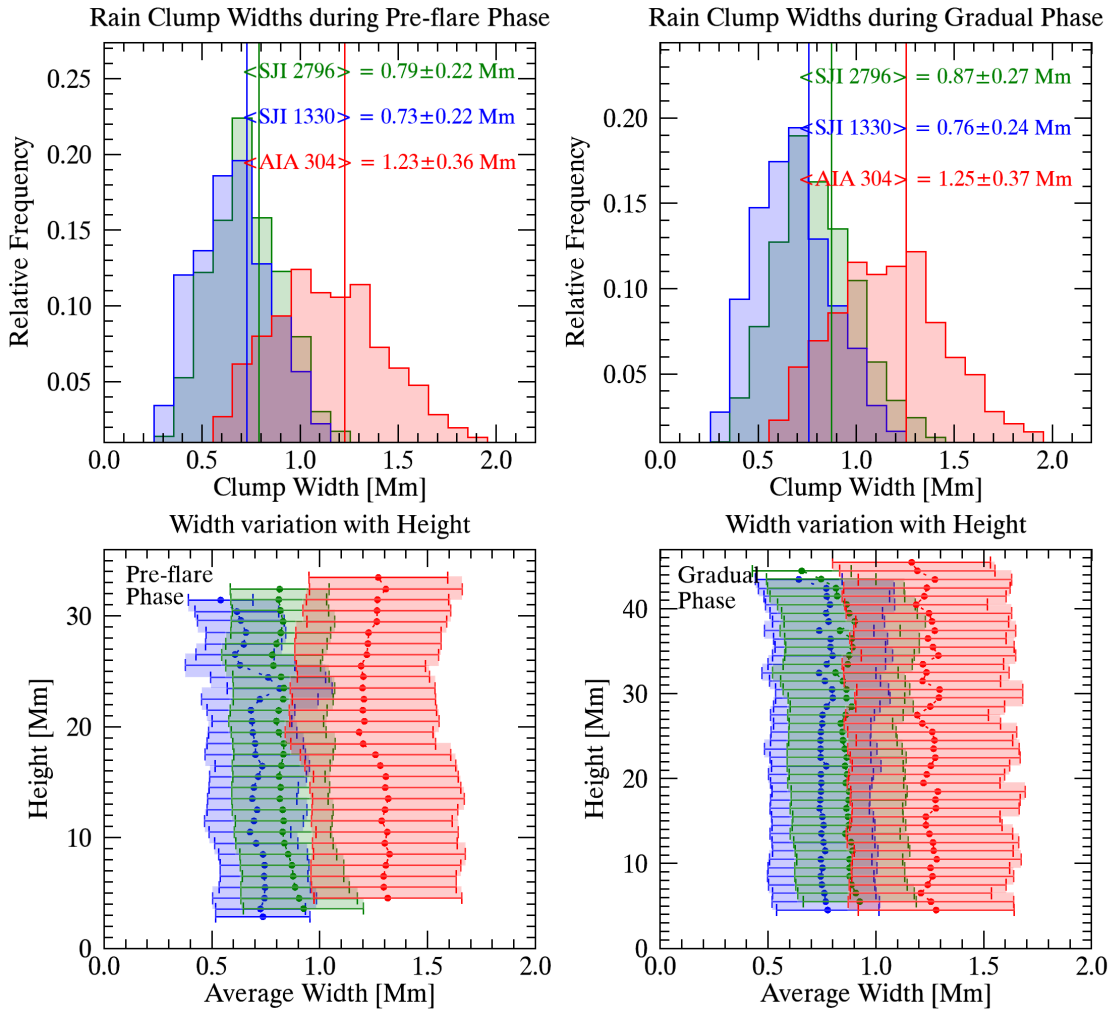

Figure 5.15: Top: Histograms of rain clump widths during the pre-flare (left) and gradual (right) phases. Green, blue and red denote SJI 2796 Å, SJI 1330 Å, and AIA 304 Å, respectively (see legend). Bottom: The width variation with projected height during the pre-flare (left) and gradual (right) phases. Here, the circles and error bars correspond to the median width and their standard deviation at each height bin.

Figure 5.16), the average width and length between the SJI 2796 Å and SJI 1330 Å are similar, in AIA 304 Å they are found significantly larger. A similar result but a bit higher degree is seen for the gradual phase for the average widths and lengths. In the pre-flare phase, rain lengths are quite different across the channels. The width discrepancy between the SJI and 304 channels may simply be due to the lower spatial resolution, which is close to the resolution limit. However, lengths are significantly longer, so it is likely that other factors are at play, such as higher opacity in 304 Å. However, during the gradual phase, they all become very similar. This may simply be due to the large increase in rain quantity, with rain lengths becoming roughly 20% of half the loop length.

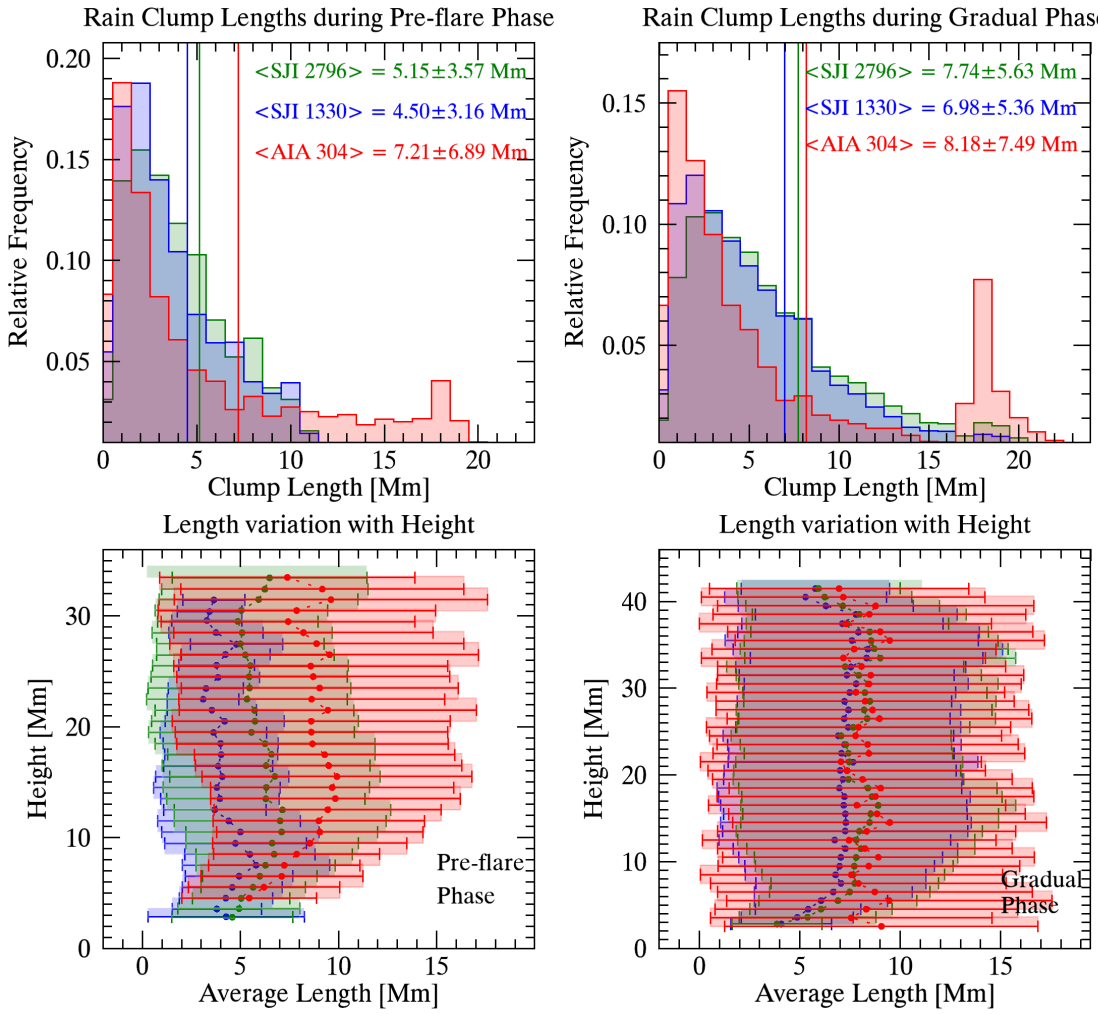

Figure 5.16: The same plots as shown in Figure 5.15 but for the length of rain clumps.

5.3.2.2 Dynamics

We now turn to the dynamics of coronal rain clumps. Figure 5.17 and Figure 5.18 provide the projected velocity of each rain clump obtained from the RHT analysis over the pre-flare and gradual phases, respectively. The velocity on each curved path is obtained using the RHT temporal mean angle as shown in Equation 3.3 in Chapter 3:

$$v_{||} = \tan \overline{\theta}_t (\frac{\delta x}{\delta t}). \tag{5.7}$$

Here, δ_x and δ_t represent the spatial sampling on the given date and the average cadence, respectively. δ_x is 242.51 km for the SJI channels and 242.45 for the AIA channel. δ_x, on the other hand, is 10.36 s and 12 s for the SJI and AIA channels, respectively. Then, the horizontal and vertical

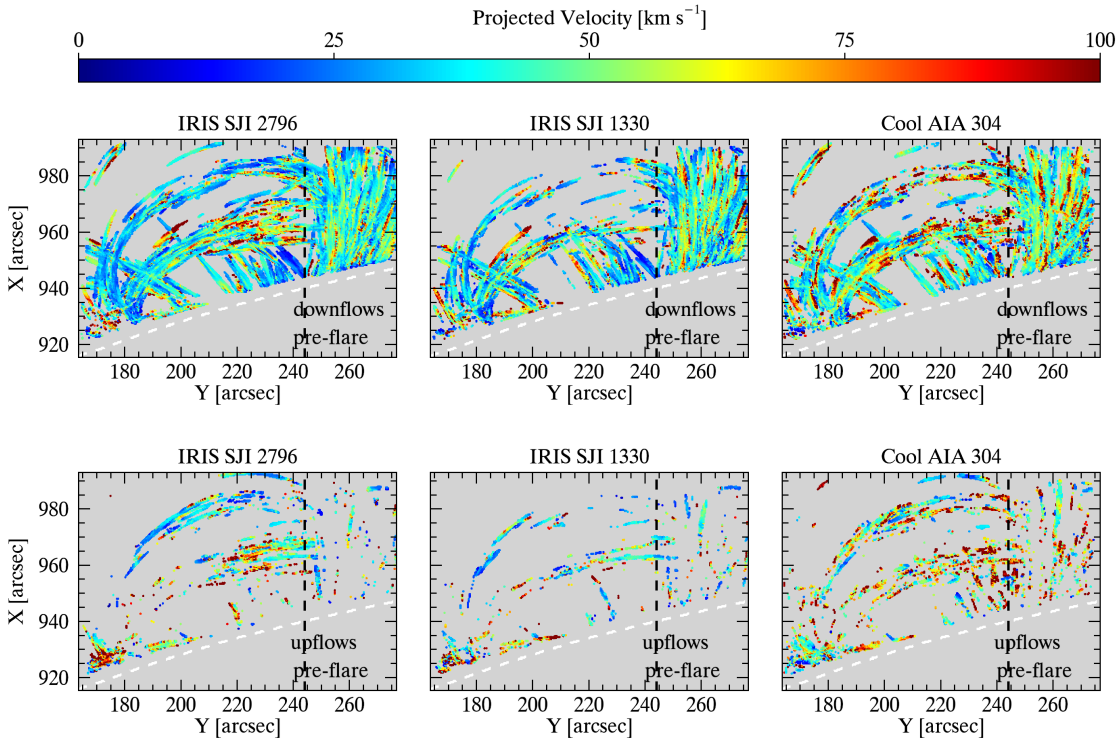

Figure 5.17: Average downflow (top panels) and upflow (bottom panels) projected velocities in SJI 2796 Å (left), SJI 1330 Å (middle), and Cool AIA 304 Å (right) over the pre-flare phase. The dashed white lines over the plots indicate the solar limb. The right side of the vertical black dashed lines represents the quiescent coronal rain that is observed at all times.

velocities are calculated using Equation 3.4 and Equation 3.5 given in Chapter 3, respectively, through the RHT spatial mean angle. Using these equations, tangential and radial velocity components are derived, which in turn provide the projected velocity as given in Equation 3.8.

Figure 5.17 and Figure 5.18 show the average projected velocity of SJI 2796 Å, SJI 1330 Å, and Cool AIA 304 Å obtained from the above-mentioned Equations with respect to downflow and upflow motions. Again, we focus on the left side of the vertical dashed lines for further analysis of rain dynamics. Most coronal rain clumps have higher downflow velocities at lower heights, indicating acceleration during the fall. This is especially clear during the gradual phase.

In order to see the velocity distribution for each rain clump, we present 1D projected velocity histograms in Figure 5.19 for downflows (left) and upflows (right) for the pre-flare (top) and the gradual phases (bottom) based on the left side of the vertical dashed lines. It is apparent from these plots that downflow and upflow projected velocities have a broad distribution, up to 200 km s^{-1}. The overall shape of the downflow velocity is very similar across the channels for each phase. The

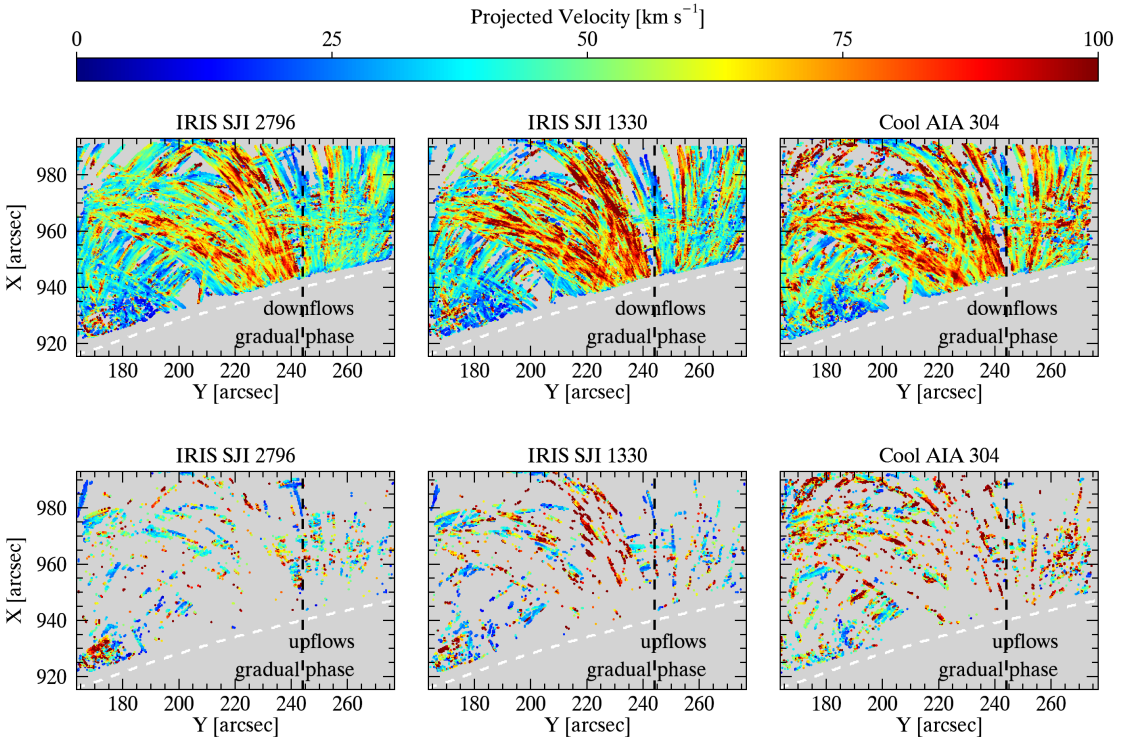

Figure 5.18: The same plots as shown in Figure 5.17 but for the gradual phase.

median downflow velocities are found 34±28 km s^{-1}, 35±28 km s^{-1}, and 38±27 km s^{-1} during the pre-flare phase and 47±35 km s^{-1}, 52±40 km s^{-1}, and 51±38 km s^{-1} for the gradual phase in SJI 2796 Å (green), SJI 1330 Å (blue), and AIA 304 Å (red), respectively. On the other hand, these median velocities are 38±41 km s^{-1}, 38±42 km s^{-1}, and 48±46 km s^{-1} for the upflow projected velocity during the pre-flare phase and 38±44 km s^{-1}, 48±53 km s^{-1}, and 50± 48 km s^{-1} for the gradual phase in the SJI 2796 Å (green), SJI 1330 Å (blue), and AIA 304 Å (red), respectively. The downflow velocity results indicate a 38%, 51%, and 33% increase in velocity from the pre-flare to the gradual phases for the SJI 2796 Å, SJI 1330 Å, and AIA 304 Å, respectively. The same results are also found in the upflow projected velocity. The percentage increases by 1%, 25%, and 5% in upflow from the pre-flare phase to the gradual phase, but this increase is much lower than in the case of downflow motions. These results represent very small increments that may not be statistically significant, except SJI 1330 Å. This might be explained by the change in opacity of coronal rain, which undergoes cooling as it falls and results in an increase in opacity. Therefore, some upflow motions correspond to an apparent effect due to this opacity changes during the fall and leads to apparent fast upward motion.

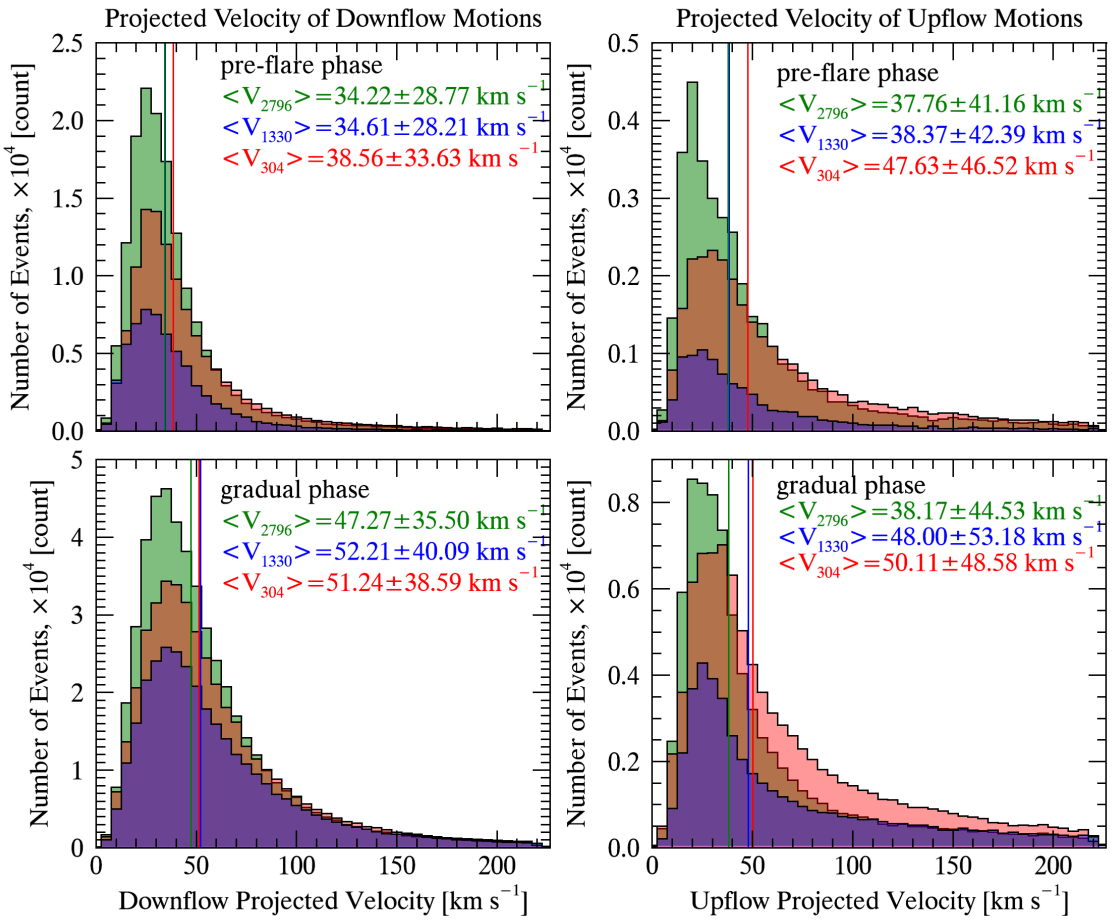

Figure 5.19: Top: 1D histogram distribution of the projected velocities during the pre-flare phase for the downflow (left) and upflow (right) motions in SJI 2796Å (green), SJI 1330Å (blue), and AIA 304Å (red), with the corresponding median and standard deviation in the inner caption. Bottom: Same as the top panels, but for the gradual phase.

We also present the average projected velocities for both downflow and upflow motions with projected height during the gradual phase in Figure 5.20. Here, zero height indicates the solar limb. The average projected velocities for the downflow motions are quite similar at all heights. It is clear that rain clumps have small acceleration at higher heights (between approximately 35 - 43 Mm). Then, they fall roughly at a constant velocity, which is expected from the gas pressure (Oliver et al., 2014). Relative to the downward motion, the upflow projected velocities exhibit more chaotic behaviour. This can be clearly seen in Figure 5.21. Here, we only focus on one particular shower event. As can be seen, downward motions (positive values) are bulk motions, while upflow motions (negative values) are more localised and sporadic in time.

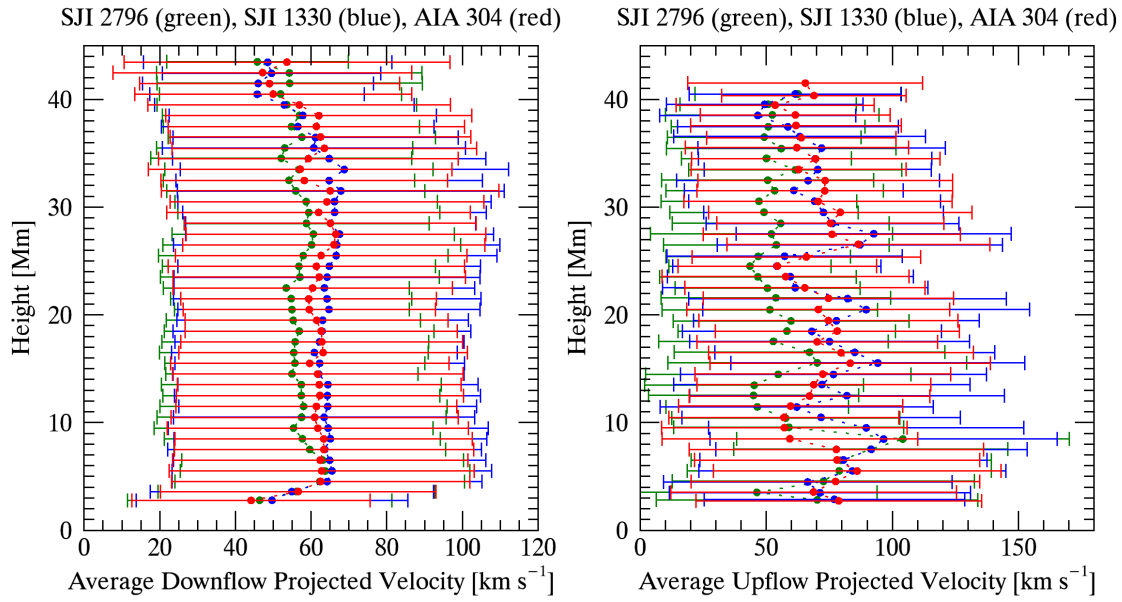

Figure 5.20: The variation of the downflow (left) and upflow (right) motions and their standard deviation at each height bin during the gradual phases. Green, blue and red colours denote SJI 2796 Å, SJI 1400 Å, and AIA 304 Å, respectively.

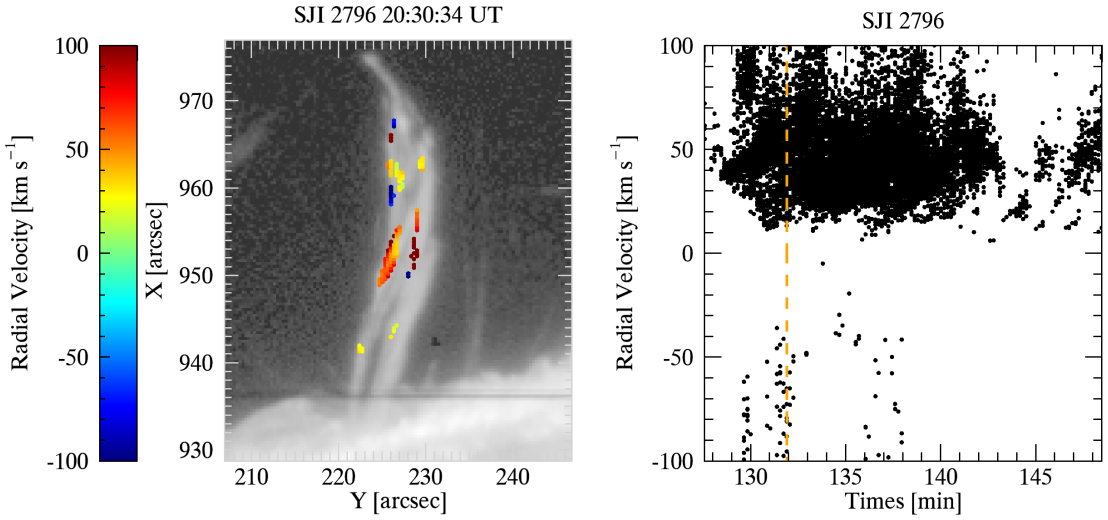

Figure 5.21: Left: One of the shower events observed in SJI 2796 Å during the gradual phase. The coloured detected pixels show the radial velocity obtained from RHT results. Right: The variation of radial velocity with the observational time. The orange dashed line indicates the time.

5.3.2.3 Energetics and Thermodynamics

Similar to CE, we investigated the mass and energy cycles during two shower events: SH1 and SH2, which correspond to the same location but at different times as CE1 and CE2, respectively. Figures 5.22 and 5.23 show obtained EM maps for each temperature bin and each SH case. In

these maps, we remove the EM trend value at t=0 since the difference will then give us a more precise EM of the shower without the background. In the CE case, this was not necessary since the background was dark in the hot temperature bins before the start of the CE.

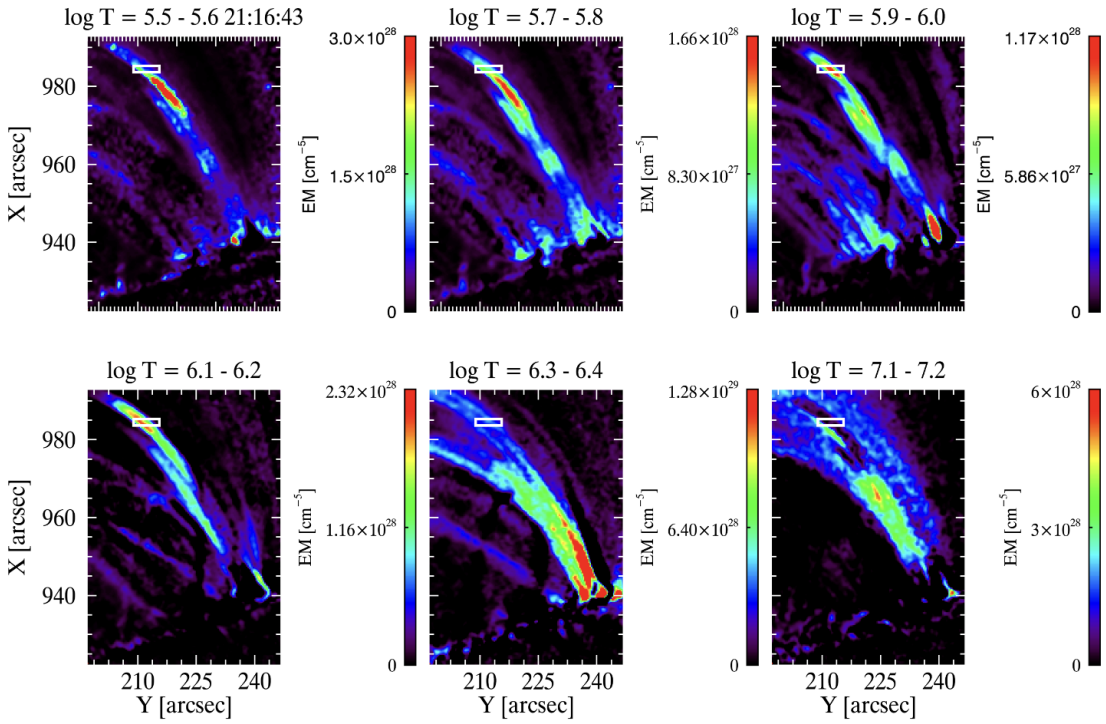

Figure 5.22: EM maps for some temperature bins indicated in the title. The white rectangle areas show the focused region within the SH1 for the detailed mass-flux analysis.

SH1 events start at 20:26:31 UT and end at 20:35:31 UT, while the SH2 is between 21:18:31 and 21:46:43 UT for each temperature bin. The DEM-weighted temperature (see Equation 5.2) is found to be 4.26×10^6 K and 5.84×10^6 K for SH1 and SH2, respectively. The average EM (see Equation 5.3) is 2.07×10^{28} cm $^{-5}$ for the SH1 and 9.11×10^{27} cm $^{-5}$ for the SH2.

Using the same equation (Equation 5.4) as in the CE case, we find the density of the optically thin plasma surrounding the rain, as given by ρ_{DEM} in Table 5.5. As previously mentioned, the thinnest strand width (w_{strand}) is 838 km and 973 km for the SH1 and SH2, respectively, and we found that the number of loop strands should be 6 for both shower events. To calculate rain density, we assume that the rain is in pressure balance with its environment and use the surrounding density, integrated temperature and rain temperature as given in the following equation:

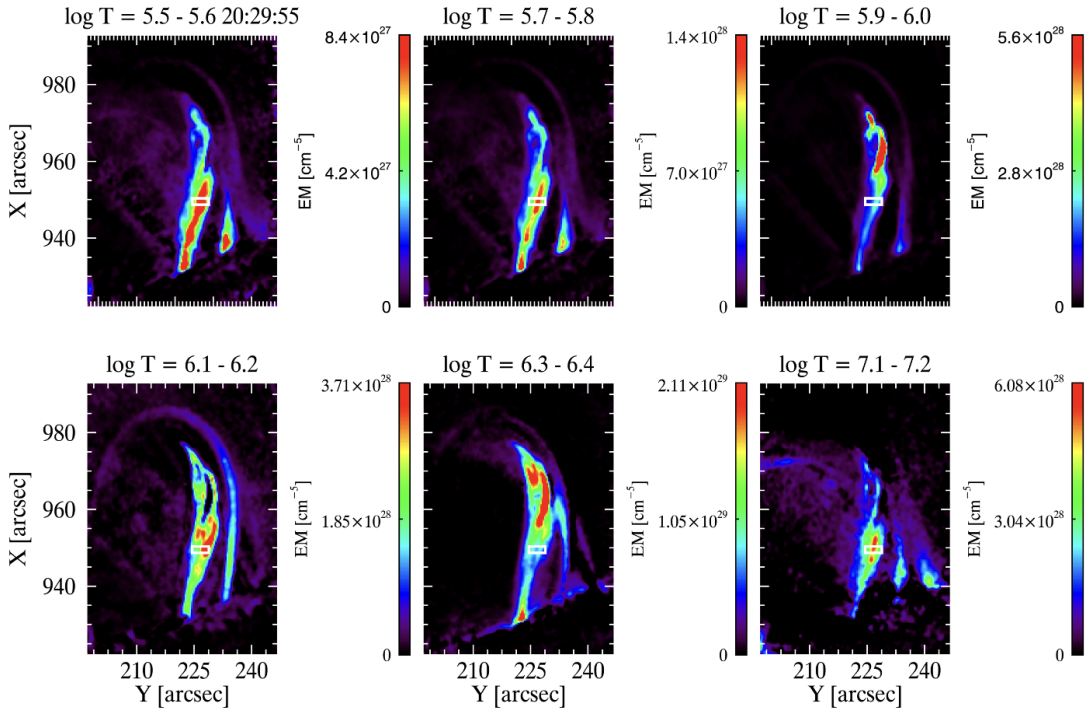

Figure 5.23: Same EM maps as in Figure 5.22 but for the SH2.

$$\rho_{rain} = \frac{\rho_{DEM} T_{DEM}}{T_{rain}} \tag{5.8}$$

Here, T_{rain} is the temperature of rain, and we took the temperature value of the SJI 2796 Mg II line (10^4 K). The mass density (ρ_{rain}) of coronal rain is found to be 1.01×10^{-11} g cm^{-3} and 8.55×10^{-12} g cm^{-3} for the SH1 and SH2, respectively. The calculated average velocity is taken as 61 km s^{-1} and 76 km s^{-1}. For the thinnest CE strand observed (w_{strand}), the mass flux (F_{mass}/strand) and mass rate (R_{mass}/strand) are found to be 6.11×10^{-5} g cm^{-2} s^{-1} and 3.37×10^{11} g s^{-1}, respectively, for the SH1. These are 6.55×10^{-5} g cm^{-2} s^{-1} and 4.87×10^{11} g s^{-1} for the SH2, respectively. Given the 9 and 28 minutes time range for the SH1 and SH2, respectively, for all temperature bins from logT=5.5-5.6 to logT=7.1-7.2, the total mass ($Mass_{strand}$ = $R_{mass}\times$time) is found to be 1.82×10^{14} g for the SH1 and 8.24×10^{14} g for the SH2. To calculate the respective quantities for the entire SH, we calculated the minimum number of strands (see previous paragraph) needed to cover the SH width (4965 km and 6369 km for the SH1 and SH2, respectively.) Then, we found that the total mass rate (Total R_{mass}) is 2.36×10^{12} g s^{-1} for the SH1 and 2.43×10^{12} g s^{-1} for the SH2. We found that 1.24×10^{15} g and 4.12×10^{15} g of total mass

going down in SH1 and SH2, respectively. We found that the kinetic energy (see Equation 5.6) is 1.34×10^{28} erg for the SH1 and 9.65×10^{28} erg for the SH2. A summary of all these calculations is given in Table 5.5. In the case of CE, we found that the number of loop strands is 4 for both CE1 and CE2, while here, for SH1 and SH2, it is 6. These numbers are comparable between the two cases.

Table 5.5: Obtained measurements for the mass-energy cycle for the SH events

	SH1	SH2
Δt [min]	9	28
v [km s^{-1}]	61	76
l_{strand} [km]	838	973
$< EM >$ [cm^{-5}]	2.07×10^{28}	9.11×10^{27}
T$_{DEM}$ [K]	4.2×10^{6}	5.8×10^{6}
n_{DEM} [cm^{-3}]	1.43×10^{10}	8.83×10^{9}
ρ_{rain} [g cm^{-3}]	1.01×10^{-11}	8.55×10^{-12}
R$_{mass}$/strand [g s^{-1}]	3.37×10^{11}	4.87×10^{11}
F$_{mass}$/strand [g cm^{-2} s^{-1}]	6.11×10^{-5}	6.55×10^{-5}
Total R$_{mass}$ [g s^{-1}]	2.36×10^{12}	2.43×10^{12}
Mass$_{strand}$ [g]	1.82×10^{14}	8.24×10^{14}
Total mass [g]	1.24×10^{15}	4.12×10^{15}
Kinetic energy [erg]	1.34×10^{28}	9.65×10^{28}

5.3.3 Quiescent Neighbouring Coronal Rain

In this section, we analyze the quiescent coronal rain that was there during the entire observation time, as shown on the right side of the vertical black dashed line in Figure 5.12. We refer to that as neighbouring quiescent coronal rain. Here, we investigate these neighbouring quiescent coronal rain during the pre-flare and gradual phases to see whether the solar flare had an impact on it.

In Figure 5.24, we first present the downflow projected velocity maps of the quiescent coronal rain during the pre-flare and gradual phases. Here, the reason for the gaps between the pixels in these maps, especially in the gradual phase, is that we disregard the pixels having temporal mean angle values ranging from -90 to -45 degrees, as they pertain to the loop emanating from the left side of the vertical black line. Their 1D histogram distribution is presented in Figure 5.25. For the pre-flare phase, the median velocity was found to be 43$\pm$16 km s^{-1}, 47$\pm$20 km s^{-1}, and 50$\pm$22 km s^{-1} for the SJI 2796 Å (green), SJI 1330 Å (blue), and AIA 304 Å (red), respectively. These velocities were notably higher in the gradual phase, with a median of 47$\pm$17 km s^{-1},

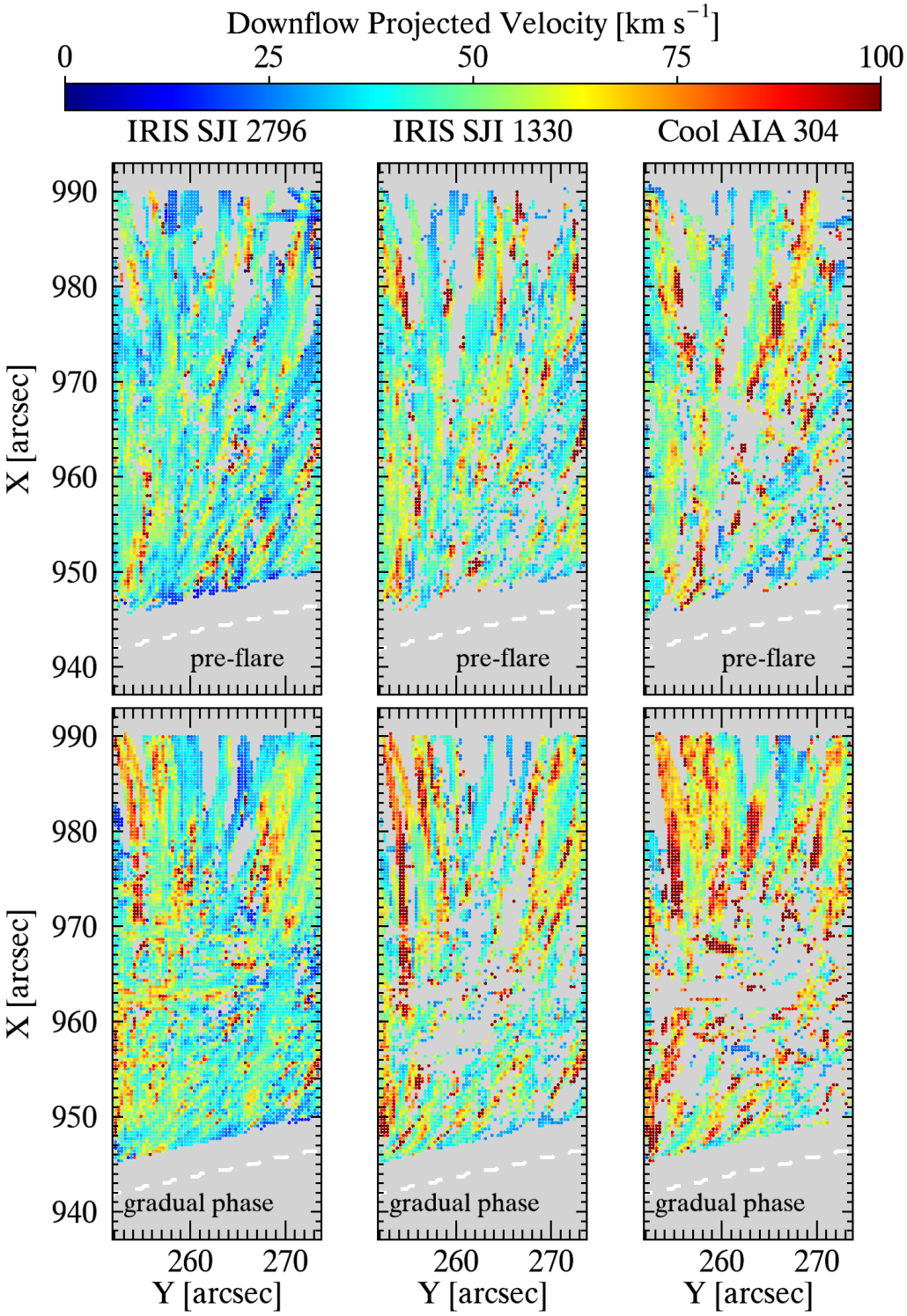

Figure 5.24: Average downflow projected velocities of the quiescent coronal rain that is observed at all times in the right side of the vertical dashed black line in Figure 5.12 in SJI 2796 Å (left), SJI 1330 Å (middle), and AIA 304 Å (right) during the pre-flare (top) and gradual (bottom) phases. Here, we exclude pixels with temporal mean angle values falling within the range of -90 to -45 degrees as they correspond to loops originating from the left side.

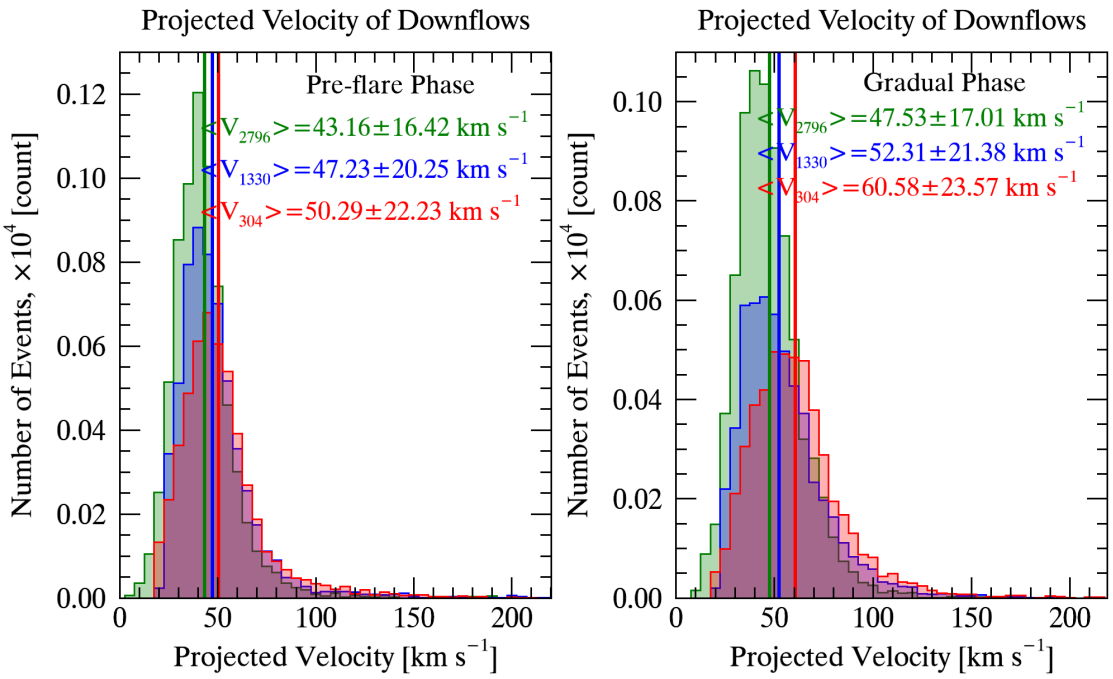

Figure 5.25: Histogram showing the distribution of projected downflow velocities as shown in Figure 5.24 during pre-flare (left) and gradual (right) phases.

52±21 km s^{-1}, and 60±23 km s^{-1} for the SJI 2796 Å (green), SJI 1330 Å (blue), and AIA 304 Å (red), respectively. This increased velocity is clearly shown in the velocity maps (see Figure 5.24), highlighting the similarities and differences between these two phases. The percentage increase in downflow projected velocities from pre-flare to gradual phases are 10%, 11%, and 20% for the SJI 2796 Å, SJI 1330 Å, and AIA 304 Å, respectively.

We have also checked the rain quantity from pre-flare to the gradual phases. We found that rain quantity increased by 3% for the SJI 2796 Å; however, it decreased by -9% and -1% for the SJI 1330 Å and AIA 304 Å, respectively. The increase in SJI 2796 Å and the decrease in AIA 304 Å are not statistically significant; however, the decrease in SJI 1330 Å is a bit higher than the AIA 304 Å. This may be due to the surrounding diffuse material in the gradual phase.

5.3.4 Secondary Heating

Our attention is once again directed toward SH1 since the analysis of SH1 yields intriguing and noteworthy outcomes. In Figure 5.26, we show the EM maps panels with the white contour of SH1 based on the SJI 2796 Å. On the bottom plot, we show the time evolution of EM within the pink contour for each temperature bin (colours indicated on the right-hand side) over the entire

observational time, including pre-flare, impulsive and gradual phases. The yellow highlighted region shows the observational time of SH1. The right-hand side plots show the time evolution of EM based on the contour of Cool AIA 304 (top) and SJI 2796 (bottom).

The first peak of each temperature bin corresponds to the chromospheric evaporation time, starting at around 90 min, which is followed by the rain shower (SH1) 30 min later. We observe a Kelvin-Helmholtz (KH) type vortex in the corona in response to the evaporation and a strong morphological correspondence between the evaporation and the (later occurring) rain shower. During the shower and co-located with it, we observe nanojets-like features (bright, thin structures that travel perpendicular to the magnetic structures discovered by Antolin et al. (2021)) and a secondary increase in temperature to 7 MK. To our knowledge, this is the first time such a highly localised and strongly multi-thermal behaviour has been observed and suggests that reconnection facilitated by the rain leads to significant energy release during the gradual phase. One question raised by these findings is what causes the braiding that leads to small-angle magnetic reconnection. We speculate that dynamic instabilities at the top of the flare loop, such as Rayleigh-Taylor or Kelvin-Helmholtz, could be the cause of this. Our discovery of the KH vortex supports this hypothesis.

This part is an ongoing study that is planned to be submitted in the near future.

5.3.5 Discussion and Conclusion

In this Chapter, we present the first high-resolution statistical study comparing quiescent and flare-driven coronal rain, which is observed by SDO and IRIS with a high cadence over an AR off-limb. Flare-driven coronal rain is draining in C2.1-class solar flare. Our observational results are summarized and discussed as follows:

Flare-driven coronal rain increases in quantity at roughly 128%, 236%, and 179% for the SJI 2796 Å, SJI 1330 Å, and AIA 304 Å, respectively. Similarly, the intensity also increases from pre-flare to gradual phases, at around 172%, 130%, and 252% for the SJI 2796 Å, SJI 1330 Å, and AIA 304 Å, respectively. This is expected because the flare-driven coronal rain has a higher intensity in the low TR (Foukal, 1976; Lacatus et al., 2017).

Coronal rain clumps exhibit a wide range of velocities, spanning from a few km s^{-1} to 200 km s^{-1}.

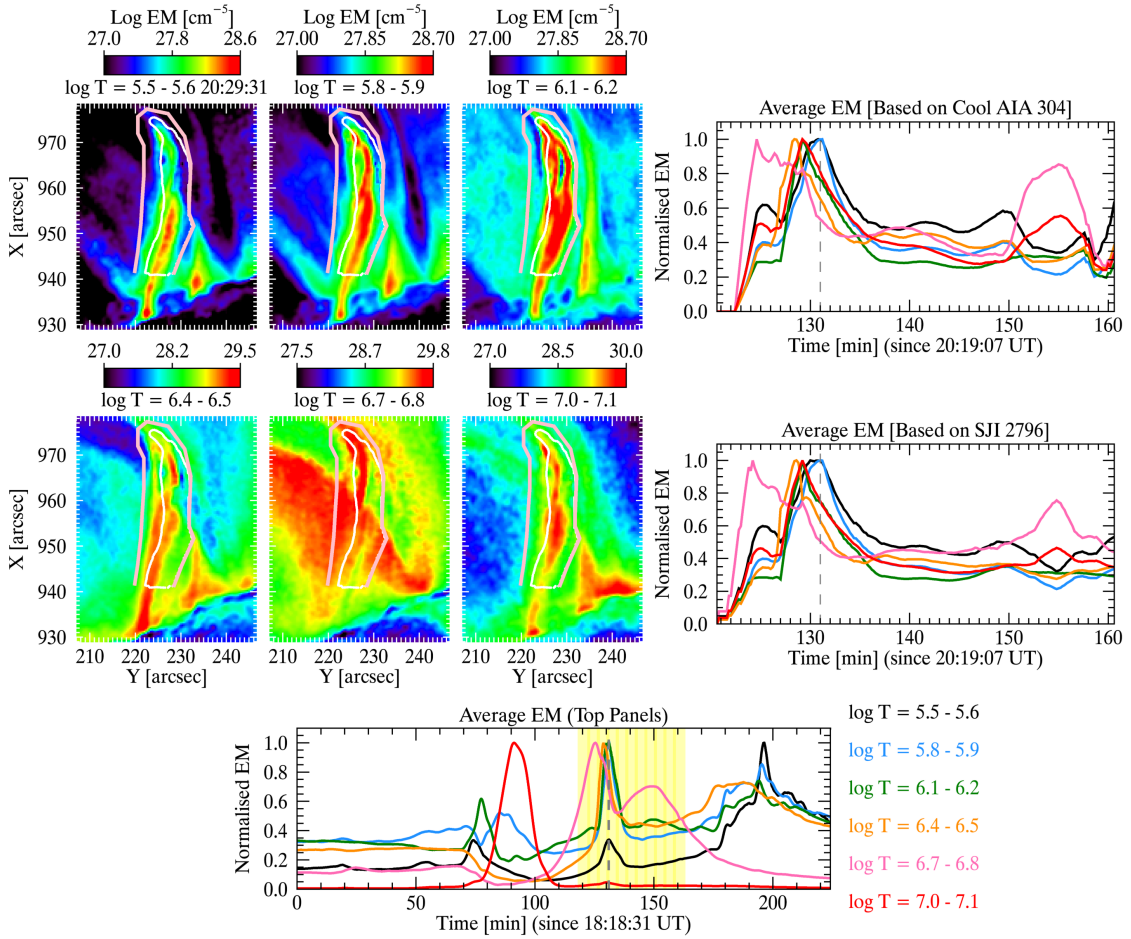

Figure 5.26: EM maps of SH1 for each temperature bin with the white contour of SH1 based on the SJI 2796 Å. The bottom plot shows the time evolution of EM from pre-flare to the gradual phases within the pink contour area. The right-hand side plots show the average EM based on the Cool AIA 304 (top) and SJI 2796 (bottom).

These results are in agreement with the previous findings with both empirical observations (Müller et al., 2005; Antolin and Rouppe van der Voort, 2012; Froment et al., 2020; Şahin et al., 2023) and simulated data (Fang et al., 2015; Li et al., 2022). Coronal rain not only moves downward but also upward and in varying trajectories. The upward motion of coronal rain dynamics has not been extensively studied in existing literature. The change in the trajectory of coronal rain, including the occurrence of upward motion, was first noted by Antolin et al. (2010). Recent observational and simulation studies have shown that upward motions are also ubiquitous (Li et al., 2022; Şahin et al., 2023). In a study conducted by Şahin et al. (2023) on only quiescent coronal rain, it was found that upflow velocities have higher velocities than downward velocities. However, upward motions are more stochastic and more sporadic, corresponding to localised events and not bulk flows, contrary to the downward motion. Here, in this study, we considered not only the quiescent coronal rain but

also flare-driven coronal rain, and we found that the downflow and upflow velocities are increased by roughly 38%, 50%, and 33% and roughly 1%, 25%, and 5% from pre-flare to gradual phase for the SJI 2796 Å, SJI 1330 Å, and AIA 304 Å. A possible cause of this increased downflow and upflow speeds may be an effect due to the way the rain appears. Indeed, as it falls, it undergoes cooling, which results in an increase in opacity, leading to fast apparent upward and downward motions. Another possibility is that gas pressure may play a significant role in these upward and downward dynamics. In the study of Mackay and Galsgaard (2001), the chromosphere acts as a piston that effectively stops the downward movement of rain by compressing it downstream. Adrover-González et al. (2021) conducted an analytical investigation of critical points along a loop, studied as a dynamical system resulting from line-tying conditions in the lower atmosphere. This analysis revealed that these line-tying conditions induce oscillations, leading to upward flows in the system.

We have also checked the average projected velocity in terms of downflow and upflow motions with height. Downward accelerations are found at higher heights in both pre-flare and gradual phases. However, the rain has a consistently steady speed during their fall, which could be due to a combination of the effective gravity and pressure changes (Antolin et al., 2010; Oliver et al., 2014; Martínez-Gómez et al., 2020). We found a higher velocity in the SJI 1330 Å and AIA 304 Å during the gradual phase, which would be expected due to the higher densities compared to the SJI 2796 Å. Relative to the downward motion, we found a more chaotic behaviour in the upward motion in projected velocity variation with height. The fact that we observe an increase in upward speeds for lower heights supports this possibility since compression increases as the rain falls. However, it is unclear whether this effect can explain the sporadic character of the upflows. Another possibility is the presence of sporadic small heating events at the footpoints of the loop, whose localised character may affect single clumps but not the bulk flow.

According to our observational results, the width of coronal rain clumps varies from 0.3 Mm up to 2 Mm in both phases. These results are consistent with the previous finding (Antolin et al., 2015; Li et al., 2022; Şahin et al., 2023), which considers the quiescent coronal rain. Here, we have also investigated the flare-driven coronal rain morphology, and we found that the average width in flare-driven rain is 10%, 4%, and 2% times larger than in quiescent coronal rain. These increments might not be statistically significant. However, it points to the fact that rain widths

are more fundamental and invariable regarding the amount of rain during flaring conditions. This consistent relationship suggests a connection between rain widths and the interaction between the magnetic field and thermal instability. For instance, the numerical simulations conducted by Antolin et al. (2022) elucidate the emergence of a fundamental magnetic field strand produced from TI due to gas pressure loss and flux freezing. Another study by van der Linden and Goossens (1991) showed that the widths could be set by the eigenfunction of the thermally unstable mode. This framework explains our findings and invites future investigation into how magnetic fields and TI define coronal rain widths. Similarly, the length of coronal rain clumps changes from a few to 22 Mm, and flare-driven coronal rain is 50%, 55%, and 13% times larger than quiescent coronal rain. This may result from more material being generated at higher heights in the gradual phase, known from the TNE-TI scenario (Antolin, 2020; Antolin and Froment, 2022).

In both phases, the width of coronal rain is relatively consistent along the lengths of the loops as it falls. It implies that the factor affecting the width of coronal rain becomes apparent immediately after it forms. On the other hand, the lengths are longer at higher heights, and they become short as the rain falls.

We also focused on the impulsive phase during our observational data. We found that the RHT routine is also able to capture chromospheric evaporation (CE) dynamics in the impulsive phase. The CE events displayed an average upward speed of 115 km s^{-1} and 136 km s^{-1}. We also compare this CE with two different flare-driven coronal rain showers (SH). Even though CE has diffuse emission, substructures suggest strands with a minimum width (w_{strand}) of 1339 km and 1535 km. On the other hand, the observed minimum sub-structure for the SH1 (838 km) and SH2 (973 km) are found to be comparable with those CE substructures. The average widths of the entire structure (or whole envelope, in contrast with the sub-structure) are comparable, which are 4965 km and 5586 km for the SH1 and CE1, respectively and are 6369 km and 6184 km for the SH2 and CE2, respectively. These findings suggest a strong association between CE and SH in morphology. The coronal rain widths, as measured in the highest resolution, match the widths of coronal strands seen by advanced observations such as Hi-C 2.0 (Williams et al., 2020). Although simultaneous observations in EUV and X-ray wavelengths are yet to be realized, if there were a direct correspondence between rain and coronal strand widths, it would suggest that we are indeed capturing the genuine spatial scales of energy transport within thermally unstable coronal

loops. This idea is supported by Jing et al. (2016). Their findings showed that the widths of flare ribbons are similar widths with those with the flare-driven rain observations, suggesting a fundamental scale of mass and energy transport. A recent study by Antolin et al. (2023) with Solar Orbiter/HRI$_{EUV}$ in the 174 channel, with the highest resolution ever achieved in the EUV of the solar corona, also showed that the observed rain widths are similar to those of EUV strands. However, they also observed that these EUV strands predominantly manifest just prior to rain appearance. This suggests that the widths may be defined by the cooling mechanism (TI) and not the heating length scales. That means both heating length scales and TI produce comparable widths.

We investigated the mass and energy cycle through the CE during the impulsive phase and SH during the gradual phase. We estimated the mass pushed upward to be 8.22×10^{13} g and 2.53×10^{14} g for the CE1 and CE2. The estimated total mass going down is found to be 1.24×10^{15} gr and 4.12×10^{15} gr for the SH1 and SH2, respectively. The mass going down is over 1 order of magnitude larger than the mass going up. This discrepancy could be due to the fact that the CE is more diffuse, so there may be a larger number of strands (our assumptions are lower estimates). Also, it is very likely that we have CE on the other loop footpoint (that cannot be seen in the IRIS FOV) but that most of the rain falls on the observed footpoint due to pressure imbalance (which is the reason why we observe a KH vortex since the pressure imbalance leads to shear flows). In any case, this large mass coming down suggests that most of the loop plasma undergoes TI and becomes coronal rain. These numbers indicate that coronal rain plays a significant role in the mass and energy cycle between the chromosphere and corona.

Furthermore, we studied neighbouring quiescent coronal rain that was observed at all times during the entire observation time. These quiescent neighbouring rains have roughly 10%-20% higher velocity in the pre-flare than in the gradual phase, suggesting that the solar flare had an effect on the rain dynamics. Solar flare produces very strong perturbations, such as quasi-periodic fast waves. These waves are produced near the reconnection sites, as proposed by the "tuning fork" model (Takasao and Shibata, 2016). These rapid oscillations, characterized by their quasi-periodic nature, play a significant role in influencing the dynamics of the neighbouring environment. These fast waves have the potential to trigger TI within adjacent critically stable loops.

Finally, we focused on the SH1 and found evidence of secondary heating 30 min after the first

peak of solar flare observed at logT 7.1-7.2. This finding suggests that it is possible that such heating happens during the gradual phase of a flare, which could be the reason for both the long duration of flares and the formation of flare-driven coronal rain.

Chapter 6

Conclusion and Future Work

Recent studies have shown that the corona contains a large amount of cool material called coronal rain, which is formed by TI within a coronal loop in a state of TNE. In this thesis, we report the first high-resolution statistical study of the quiescent and flare-driven coronal rain over an active region off-limb. Over the course of this thesis, we have been wholly focused on the study of this fascinating phenomenon. Our investigation has encompassed a thorough analysis of its morphology, dynamic behaviours, and thermal attributes, resulting in a comprehensive understanding of its fundamental nature.

In Chapter 3, we aimed to investigate the dynamic behaviours and structural characteristics of quiescent coronal rain as observed in different wavelengths. We examined coronal rain, which spans from the formation point high along the loops and extends downward to the chromosphere. It is noteworthy that the majority of the previous observations of coronal rain have been conducted either utilizing ground-based telescopes, limiting the off-limb observations to the loop base due to constraints in adaptive optics capabilities off the limb, or have been confined to examining localized instances. We found that rain clumps exhibit widths spanning from 0.2 Mm to 2 Mm, with lengths extending an order of magnitude larger, ranging from a few to 20 Mm. On the dynamic side, these clumps have a broad velocity distribution and show small downward accelerations at higher heights. However, during most of the fall, the rain shows almost constant velocities, with only a small linear increase on average. We also found that coronal rain was evenly distributed in the POS above the AR. This indicates that many loops experience coronal rain at some point

regardless of their geometry and footpoint location. We found that coronal rain in SJI 2796 Å is highly correlated with transition region emission in SJI 1400 Å and AIA 304 Å indicating a strongly multithermal character. The catastrophic cooling driven by TI is very fast, occurring on timescales much faster than the freefall time of the plasma. We found multiple long-period EUV pulsations associated with the observed coronal rain, and it is likely that we are only observing part of the rain associated with the pulsations that have periods longer than the duration of our data set. Lastly, we observed TNE cycles that were much faster than the radiative cooling time of a coronal loop. This behaviour may partially correspond to a TNE cycle in which the loop is continuously sustained by a siphon flow.

In Chapter 4, we focused on groups of coronal rain clumps, which are called "showers". This study is also the first observational study on rain showers that properly quantifies their properties on the spatial and temporal scale over which sympathetic cooling occurs. The quantification of showers holds significance due to its capacity to offer an assessment of the estimation of the coronal volume. We found coronal rain showers to be ubiquitous over an active region. The average lengths, widths, and duration of the showers are found to be 27 Mm, 2 Mm, and 35 min. The morphological compatibility of our shower analysis with the studied loops in the literature sheds light on another puzzle about loops linked to the observed constant cross-section along their lengths. As mentioned before, it is expected that magnetic field lines should expand with height (wider at the apex than the footpoints) to maintain the pressure balance between the internal and external plasma of the loop, which arises due to gravitational stratification and decreasing strength of the magnetic field. However, the observed coronal loops give the impression that they have a constant cross-section with height. This aligns with the findings of (Peter and Bingert, 2012), indicating that a specific thermodynamic distribution perpendicular to the magnetic field is responsible for this effect. The expansion factor of 5.7 observed in this study between 8 and 12 Mm above the surface is in agreement with previous individual results. We found global-averaged cooling, which is particularly evident in the coronal structures hosting the showers. Stronger variation, particularly at transition region temperatures, was found throughout this time and also during the shower events. This is in agreement with the large EUV variability associated with coronal rain found by Solar Orbiter/EUI (Antolin et al., 2023). Finally, we have addressed how much of the coronal volume in an active region is in a state of TNE. We estimated the total number

of showers in the active region and obtained an estimate for the average TNE volume of 4.56×10^{28} cm^3. This is a lower estimate than the actual TNE volume because we are not able to detect loops with TNE cycles without catastrophic cooling.

In Chapter 5, we focused on a C2.1-class flare and paid particular attention to the flare-driven rain. This is the first study that directly compares the morphologies, dynamics and energetics between quiescent and flare-driven coronal rain. We presented the first high-resolution statistical study comparing these two types of coronal rain over a flaring active region. We found that rain quantity increased at around 116%, 268%, and 154% from pre-flare to gradual phases in the SJI 2796 Å, SJI 1330 Å, and AIA 304 Å, respectively. We found that the observed flare-driven rain displays almost the same average widths as the quiescent coronal rain, suggesting an underlying fundamental relationship unaffected by rain amount during flares, potentially linked to the magnetic field and TI interactions. Coronal rain clumps can vary in length from a few to 22 Mm. Flare-driven coronal rain is significantly larger than quiescent coronal rain, with a 50%, 55%, and 13% increase. This is likely due to the very high densities in the flaring loop, which lead to enhanced TI. We found that the downflow and upflow velocities also increased by roughly 38%, 50%, and 33% and roughly 1%, 25%, and 5% from pre-flare to gradual phase for the SJI 2796 Å, SJI 1330 Å, and AIA 304 Å, respectively. The higher speeds during the gradual phase may simply be due to the larger densities. However, this would also point to larger speeds in SJI 2796 Å, which are not found. This suggests that other mechanisms are at play (such as opacity effects). On the other hand, we also found that the upflow motions are more sporadic during the gradual phase. This may be because the compression increases as the rain falls or the presence of sporadic small heating events at the loop footpoints, where the localised character may affect single clumps but not the bulk flow. Furthermore, we also study chromospheric evaporation and compare its mass and energy flux to that obtained from the rain. The average upward speed of the CE events was 115 km s^{-1} and 136 km s^{-1}. In the literature, CE speeds exhibit variation from tens of km s^{-1} to hundreds of km s^{-1} (Tomczak, 1997; Liu et al., 2006; Huang et al., 2020, and references therein). For example, the speeds of 126–210 km s^{-1} observed by Li et al. (2022) for a C6.7 class solar flare, which aligns with our findings. We also found a strong morphological association between CE and SH. We found a mass drain from the shower ($\approx10^{15}$ g) comparable with the mass supply from CE ($\approx10^{14}$ g), indicating that most of the loop undergoes TI. The mass going down is 1

order of magnitude larger than the mass pushed up, probably due to the diffuse CE, potentially resulting in a larger number of strands. We would like to highlight that our assumptions are the lower estimation. Also, we have only analysed one footpoint of the CE since the other footpoint is out of the IRIS FOV. However, most of the rain falls on the observed footpoint. This may be due to the pressure imbalance produced by the asymmetric heating that leads to the KH vortex. Finally, we observed a secondary increase in temperature to 7 MK roughly 30 min after the flare peak. This is the first observation of such localized and multi-thermal behaviour, indicating significant energy release during the gradual phase as a result of rain-facilitated reconnection.

Advances in observational techniques, such as those provided by the Solar Orbiter and/or DKIST mission, are expected to provide new insights into coronal rain. Using these new observations, we can refine the models of coronal rain and gain a better understanding of the formation mechanisms. The mechanism behind the rain widths is still unclear. Why does the rain have clumpy and filamentary morphology? It may be related to both the cooling through TI and the heating mechanism (as found in our flaring case). On the other hand, we found that the TNE volume over an active region could be in the same order as the coronal volume. However, this is a lower estimation and it may vary from region to region. Therefore, the following questions, as mentioned in Antolin and Froment (2022), are still open: What is the fraction of the coronal volume that is controlled by TNE and that is subject to thermal instability? How pervasive is coronal rain? How do these volume fractions vary across the solar cycle? Another open question is how flare-driven rain is produced and how common it is. We conducted a comprehensive study on flare-driven coronal rain, and showed evidence of secondary heating. Hence, it is possible that such heating happens during the gradual phase, which would explain why the gradual phase of flares can be so long. In addition, the additional heating observed may happen throughout the gradual phase and may be concentrated towards the footpoints, that is, the kind that leads to TI. This secondary heating may, therefore, also explain the formation of coronal rain. We found nanojet-like features at the location of the rain, indicating that small-angle magnetic reconnection is on-going in the post-flare loops. One question that results from these findings is what generates the braiding that leads to small-angle magnetic reconnection. We conjecture that this may be caused by dynamic instabilities at the flare loop top, such as Rayleigh-Taylor or Kelvin-Helmholtz. The KH vortex we found provides support for this theory. However, we need more studies to understand their formation

mechanism. Here, we found a lower estimation for the mass and energy of the flare-driven rain and showed that they are comparable to the chromospheric evaporation and, therefore, the entire flare energy. This shows that the rain plays a major role in the mass and energy circulation in a flare. However, rain is often neglected in flare energy budget estimates. Thus, we need to continue examining the rain and flare types to understand the correlation between them. This will bridge a major gap in the standard flare model.

Appendix A

Flare-driven Coronal Rain Analysis

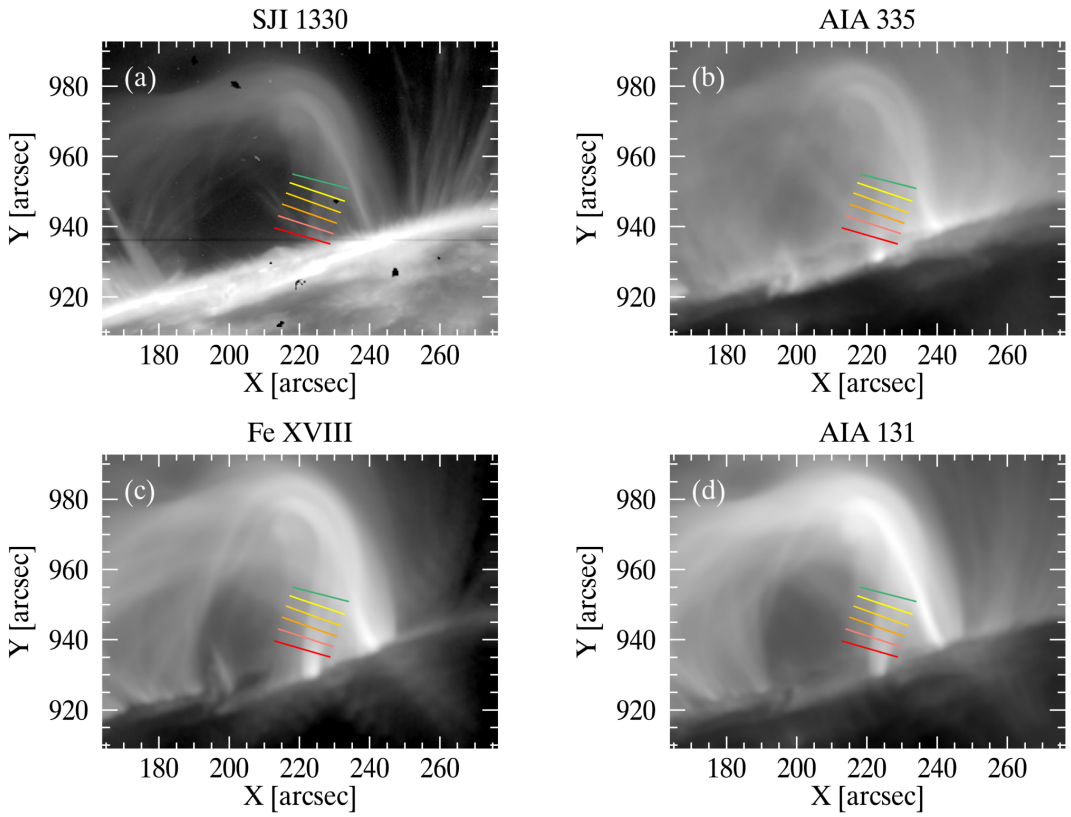

Figure A.1: The observed CE1 event shows a summed image over 19:29 and 20:15 time intervals during the impulsive phase. The rainbow colours indicate the perpendicular cuts to the loop trajectory.

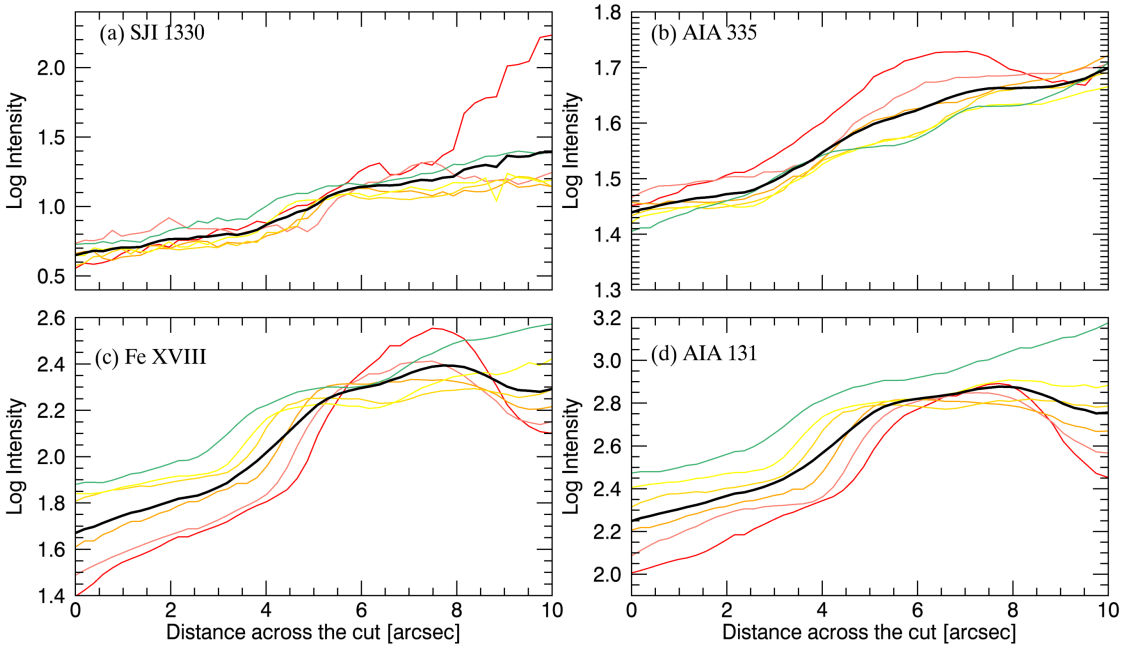

Figure A.2: The intensity variation over the distance of the perpendicular cuts shown in Figure A.1

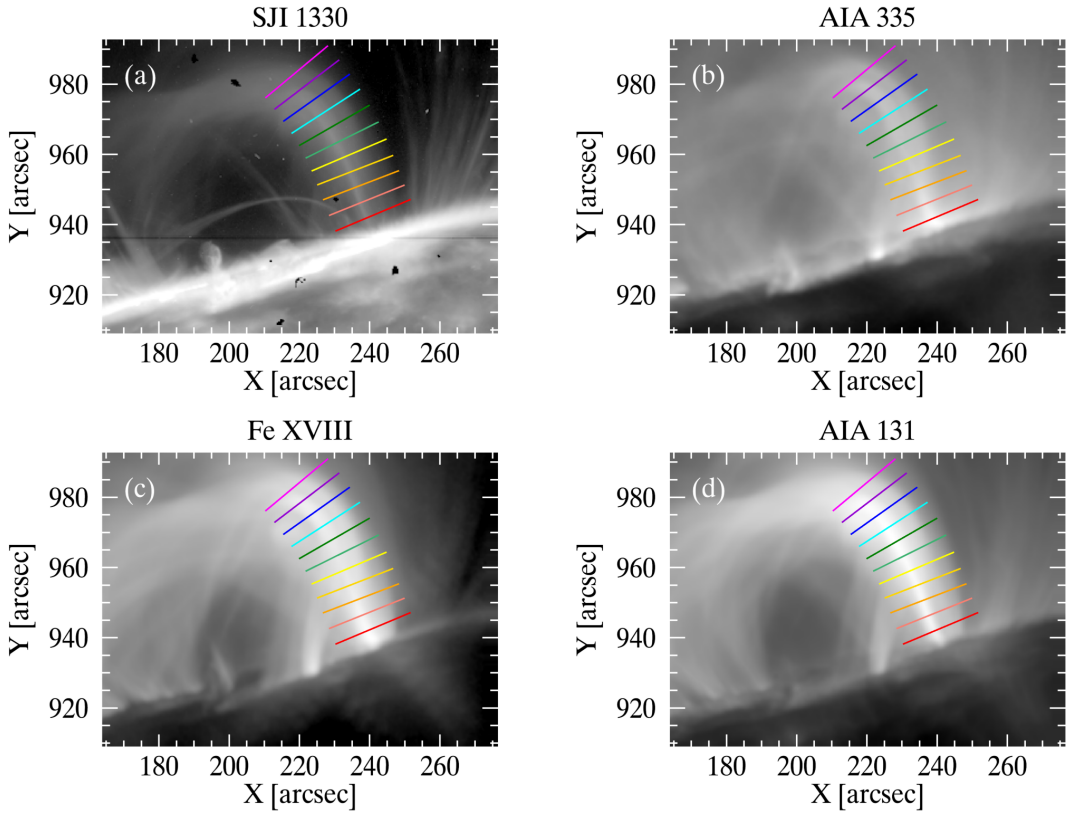

Figure A.3: The observed CE2 event shows a summed image over 19:32 and 19:56 time intervals during the impulsive phase. The rainbow colours indicate the perpendicular cuts to the loop trajectory.

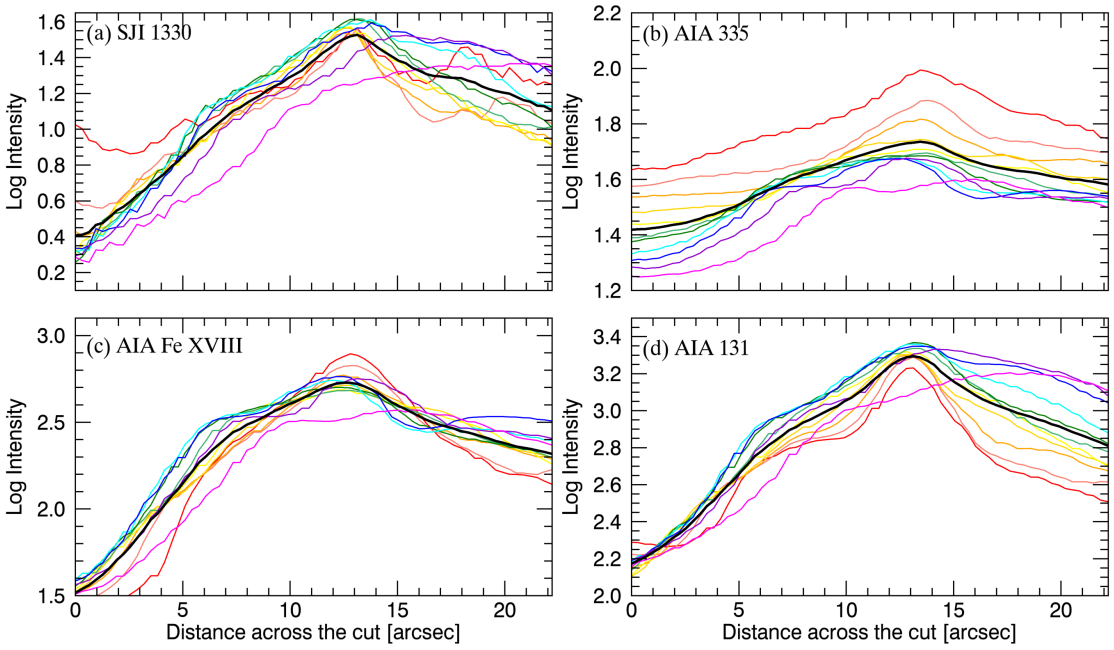

Figure A.4: The intensity variation over the distance of the perpendicular cuts shown in Figure A.3

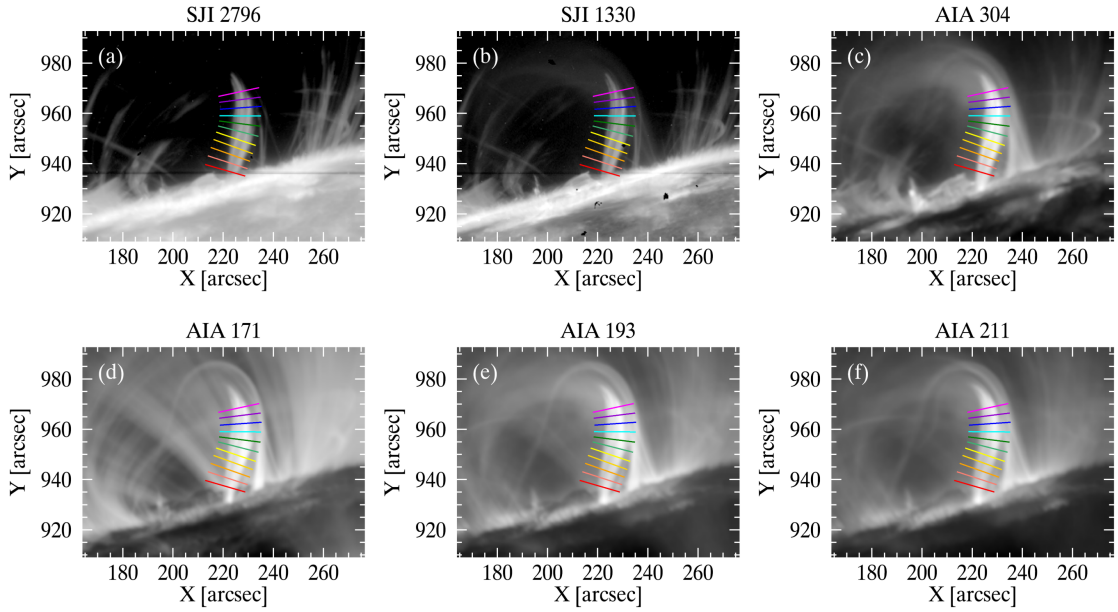

Figure A.5: A shower (SH1) event shows a summed image over 20:26 and 20:34 time intervals during the gradual phase. The rainbow colours indicate the perpendicular cuts to the loop trajectory.

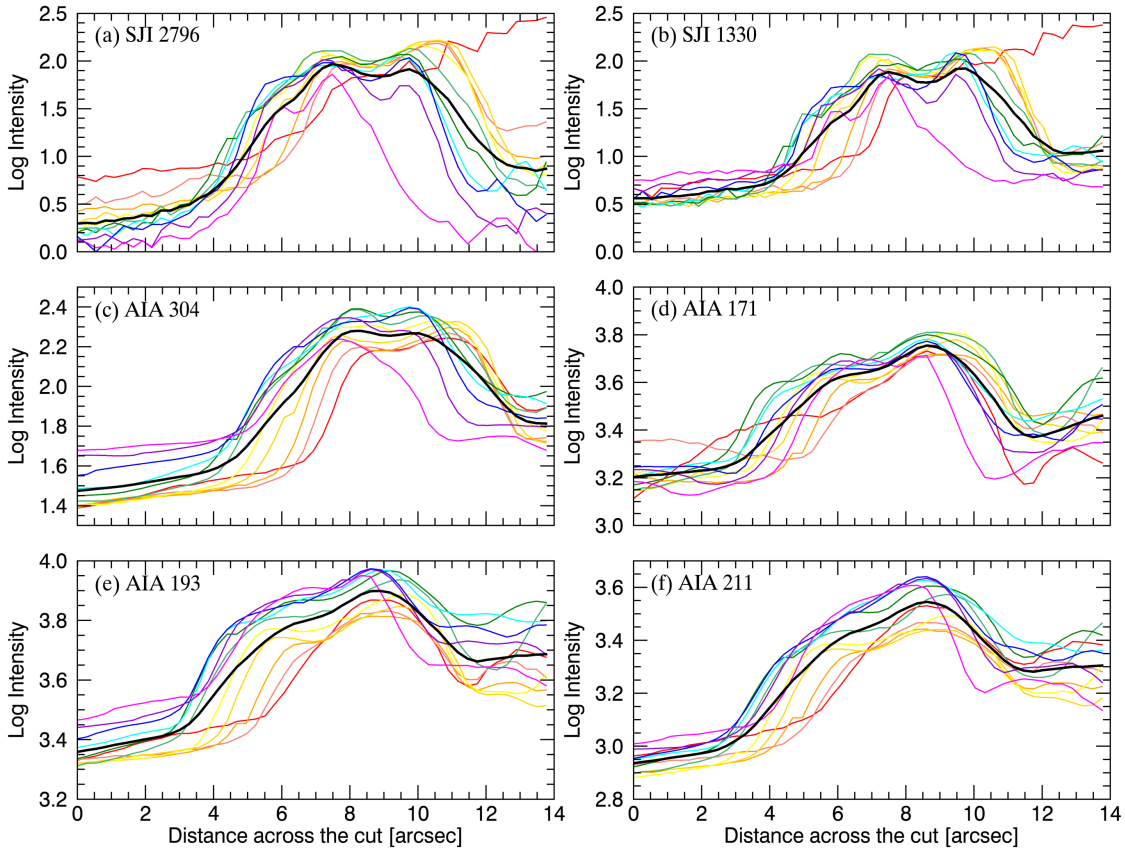

Figure A.6: The intensity variation over the distance of the perpendicular cuts shown in Figure A.5.

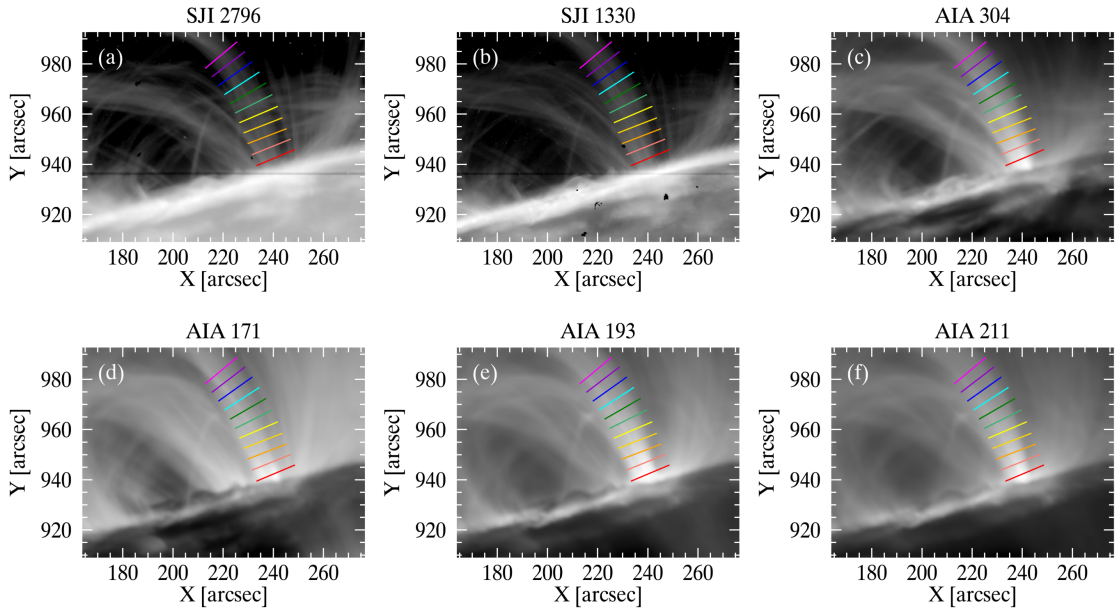

Figure A.7: A shower (SH2) event shows a summed image over 20:50 and 22:02 time intervals during the gradual phase. The rainbow colours indicate the perpendicular cuts to the loop trajectory.

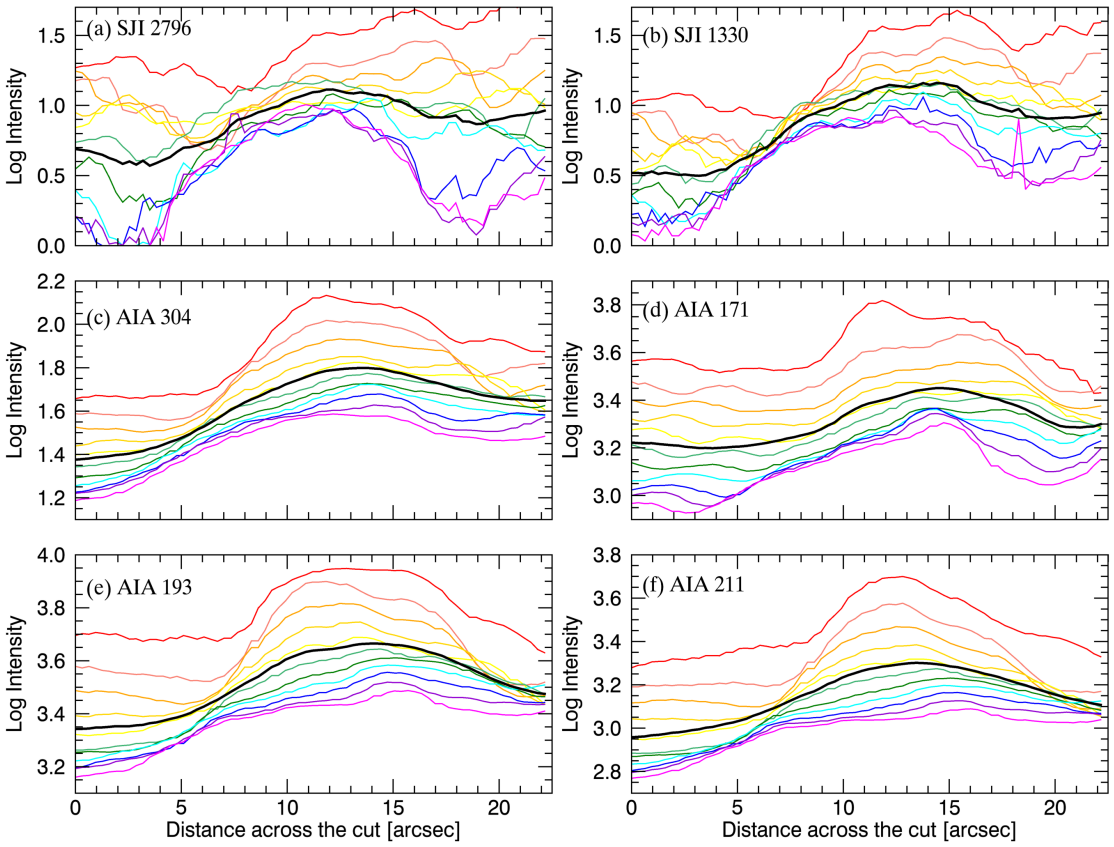

Figure A.8: The intensity variation over the distance of the perpendicular cuts shown in Figure A.7.

References

Adrover-González, A., Terradas, J., Oliver, R. and Carbonell, M. (2021), 'Gravitational instability of solar prominence threads. I. Curved magnetic fields without dips', *Astronomy and Astrophysics* **649**, A142.

Ahn, K., Chae, J., Cho, K.-S., Song, D., Yang, H., Goode, P. R., Cao, W., Park, H., Nah, J., Jang, B.-H. and Park, Y.-D. (2014), 'Active Region Coronal Rain Event Observed by the Fast Imaging Solar Spectrograph on the NST', *Solar Physics* **289**(11), 4117–4136.

Alfvén, H. (1947), 'Magneto hydrodynamic waves, and the heating of the solar corona', *Monthly Notices of the Royal Astronomical Society* **107**, 211.

Antiochos, S. K. (1980), 'A model of active prominences', *Astrophysical Journal* **236**, 270–279.

Antiochos, S. K. and Klimchuk, J. A. (1991), 'A Model for the Formation of Solar Prominences', *Astrophysical Journal* **378**, 372.

Antiochos, S. K., MacNeice, P. J., Spicer, D. S. and Klimchuk, J. A. (1999), 'The Dynamic Formation of Prominence Condensations', *Astrophysical Journal* **512**, 985–991.

Antiochos, S. K. and Sturrock, P. A. (1976), 'Influence of magnetic field structure on the conduction cooling of flare loops.', *Solar Physics* **49**(2), 359–367.

Antiochos, S. K. and Sturrock, P. A. (1978), 'Evaporative cooling of flare plasma.', *Astrophysical Journal* **220**, 1137–1143.

Antolin, P. (2020), 'Thermal instability and non-equilibrium in solar coronal loops: from coronal rain to long-period intensity pulsations', *Plasma Physics and Controlled Fusion* **62**(1), 014016.

Antolin, P., Dolliou, A., Auchère, F., Chitta, L. P., Parenti, S., Berghmans, D., Aznar Cuadrado, R., Barczynski, K., Gissot, S., Harra, L., Huang, Z., Janvier, M., Kraaikamp, E., Long, D. M., Mandal, S., Peter, H., Rodriguez, L., Schühle, U., Smith, P. J., Solanki, S. K., Stegen, K., Teriaca, L., Verbeeck, C., West, M. J., Zhukov, A. N., Appourchaux, T., Aulanier, G., Buchlin, E., Delmotte, F., Gilles, J. M., Haberreiter, M., Halain, J. P., Heerlein, K., Hochedez, J. F., Gyo, M., Poedts, S. and Rochus, P. (2023), 'Extreme-ultraviolet fine structure and variability associated with coronal rain revealed by Solar Orbiter/EUI HRI$_{EUV}$ and SPICE', *Astronomy and Astrophysics* **676**, A112.

Antolin, P. and Froment, C. (2022), 'Multi-Scale Variability of Coronal Loops Set by Thermal Non-Equilibrium and Instability as a Probe for Coronal Heating', *Frontiers in Astronomy and Space Sciences* **9**, 820116.

Antolin, P., Martínez-Sykora, J. and Şahin, S. (2022), 'Thermal Instability-Induced Fundamental Magnetic Field Strands in the Solar Corona', *Astrophysical Journal, Letters* **926**(2), L29.

Antolin, P., Pagano, P., Testa, P., Petralia, A. and Reale, F. (2021), 'Publisher Correction: Reconnection nanojets in the solar corona', *Nature Astronomy* **5**, 103–103.

Antolin, P. and Rouppe van der Voort, L. (2012), 'Observing the Fine Structure of Loops through High-resolution Spectroscopic Observations of Coronal Rain with the CRISP Instrument at the Swedish Solar Telescope', *Astrophysical Journal* **745**(2), 152.

Antolin, P., Shibata, K., Kudoh, T., Shiota, D. and Brooks, D. (2008), 'Predicting Observational Signatures of Coronal Heating by Alfvén Waves and Nanoflares', *Astrophysical Journal* **688**(1), 669–682.

Antolin, P., Shibata, K. and Vissers, G. (2010), 'Coronal Rain as a Marker for Coronal Heating Mechanisms', *Astrophysical Journal* **716**(1), 154–166.

Antolin, P. and Verwichte, E. (2011), 'Transverse Oscillations of Loops with Coronal Rain Observed by Hinode/Solar Optical Telescope', *Astrophysical Journal* **736**(2), 121.

Antolin, P., Vissers, G., Pereira, T. M. D., Rouppe van der Voort, L. and Scullion, E. (2015), 'The Multithermal and Multi-stranded Nature of Coronal Rain', *Astrophysical Journal* **806**(1), 81.

Arregui, I. (2015), 'Wave heating of the solar atmosphere', *Philosophical Transactions of the Royal Society of London Series A* **373**(2042), 20140261–20140261.

Arregui, I., Oliver, R. and Ballester, J. L. (2018), 'Prominence oscillations', *Living Reviews in Solar Physics* **15**(1), 3.

Aschwanden, M. J. (2001), 'Revisiting the Determination of the Coronal Heating Function from Yohkoh Data', *Astrophysical Journal, Letters* **559**(2), L171–L174.

Aschwanden, M. J. and Boerner, P. (2011), 'Solar Corona Loop Studies with the Atmospheric Imaging Assembly. I. Cross-sectional Temperature Structure', *Astrophysical Journal* **732**(2), 81.

Aschwanden, M. J. and Charbonneau, P. (2002), 'Effects of Temperature Bias on Nanoflare Statistics', *Astrophysical Journal, Letters* **566**(1), L59–L62.

Aschwanden, M. J., Fletcher, L., Schrijver, C. J. and Alexander, D. (1999), 'Coronal Loop Oscillations Observed with the Transition Region and Coronal Explorer', *Astrophysical Journal* **520**(2), 880–894.

Aschwanden, M. J. and Nightingale, R. W. (2005), 'Elementary Loop Structures in the Solar Corona Analyzed from TRACE Triple-Filter Images', *Astrophysical Journal* **633**(1), 499–517.

Aschwanden, M. J., Wuelser, J.-P., Nitta, N. V., Lemen, J. R. and Sandman, A. (2009), 'First Three-Dimensional Reconstructions of Coronal Loops with the STEREO A+B Spacecraft. III. Instant Stereoscopic Tomography of Active Regions', *Astrophysical Journal* **695**(1), 12–29.

Auchère, F., Bocchialini, K., Solomon, J. and Tison, E. (2014), 'Long-period intensity pulsations in the solar corona during activity cycle 23', *Astronomy and Astrophysics* **563**, A8.

Auchère, F., Froment, C., Bocchialini, K., Buchlin, E. and Solomon, J. (2016), 'On the Fourier and Wavelet Analysis of Coronal Time Series', *Astrophysical Journal* **825**(2), 110.

Auchère, F., Froment, C., Soubrié, E., Antolin, P., Oliver, R. and Pelouze, G. (2018*a*), 'The Coronal Monsoon: Thermal Nonequilibrium Revealed by Periodic Coronal Rain', *Astrophysical Journal* **853**(2), 176.

Auchère, F., Froment, C., Soubrié, E., Antolin, P., Oliver, R. and Pelouze, G. (2018*b*), 'The Coronal Monsoon: Thermal Nonequilibrium Revealed by Periodic Coronal Rain', *Astrophysical Journal* **853**(2), 176.

Babcock, H. W. and Babcock, H. D. (1955), 'The Sun's Magnetic Field, 1952-1954.', *Astrophysical Journal* **121**, 349.

Bahng, J. and Schwarzschild, M. (1961), 'Lifetime of Solar Granules.', *Astrophysical Journal* **134**, 312.

Beckers, J. M. (1968), 'Solar Spicules (Invited Review Paper)', *Solar Physics* **3**(3), 367–433.

Beckers, J. M. (1972), 'Solar Spicules', *Annual Review of Astronomy and Astrophysics* **10**, 73.

Benz, A. O. (2008), 'Flare Observations', *Living Reviews in Solar Physics* **5**(1), 1.

Berger, T. E., Slater, G., Hurlburt, N., Shine, R., Tarbell, T., Title, A., Lites, B. W., Okamoto, T. J., Ichimoto, K., Katsukawa, Y., Magara, T., Suematsu, Y. and Shimizu, T. (2010), 'Quiescent Prominence Dynamics Observed with the Hinode Solar Optical Telescope. I. Turbulent Upflow Plumes', *Astrophysical Journal* **716**(2), 1288–1307.

Berger, T., Hillier, A. and Liu, W. (2017), 'Quiescent Prominence Dynamics Observed with the Hinode Solar Optical Telescope. II. Prominence Bubble Boundary Layer Characteristics and the Onset of a Coupled Kelvin-Helmholtz Rayleigh-Taylor Instability', *Astrophysical Journal* **850**(1), 60.

Bocchialini, K., Baudin, F., Koutchmy, S., Pouget, G. and Solomon, J. (2011), 'Oscillatory motions observed in eruptive filaments', *Astronomy and Astrophysics* **533**, A96.

Borexino Collaboration, Agostini, M., Altenmüller, K., Appel, S., Atroshchenko, V., Bagdasarian, Z., Basilico, D., Bellini, G., Benziger, J., Bick, D., Bonfini, G., Bravo, D., Caccianiga, B., Calaprice, F., Caminata, A., Caprioli, S., Carlini, M., Cavalcante, P., Chepurnov, A., Choi, K., Collica, L., D'Angelo, D., Davini, S., Derbin, A., Ding, X. F., Di Ludovico, A., Di Noto, L., Drachnev, I., Fomenko, K., Formozov, A., Franco, D., Gabriele, F., Galbiati, C., Ghiano, C., Giammarchi, M., Goretti, A., Gromov, M., Guffanti, D., Hagner, C., Houdy, T., Hungerford, E., Ianni, A., Ianni, A., Jany, A., Jeschke, D., Kobychev, V., Korablev, D., Korga, G., Kryn, D.,

Laubenstein, M., Litvinovich, E., Lombardi, F., Lombardi, P., Ludhova, L., Lukyanchenko, G., Lukyanchenko, L., Machulin, I., Manuzio, G., Marcocci, S., Martyn, J., Meroni, E., Meyer, M., Miramonti, L., Misiaszek, M., Muratova, V., Neumair, B., Oberauer, L., Opitz, B., Orekhov, V., Ortica, F., Pallavicini, M., Papp, L., Penek, Ö., Pilipenko, N., Pocar, A., Porcelli, A., Raikov, G., Ranucci, G., Razeto, A., Re, A., Redchuk, M., Romani, A., Roncin, R., Rossi, N., Schönert, S., Semenov, D., Skorokhvatov, M., Smirnov, O., Sotnikov, A., Stokes, L. F. F., Suvorov, Y., Tartaglia, R., Testera, G., Thurn, J., Toropova, M., Unzhakov, E., Villante, F. L., Vishneva, A., Vogelaar, R. B., von Feilitzsch, F., ang, H., Weinz, S., Wojcik, M., Wurm, M., Yokley, Z., Zaimidoroga, O., Zavatarelli, S., Zuber, K. and Zuzel, G. (2018), 'Comprehensive measurement of pp-chain solar neutrinos', *Nature* **562**(7728), 505–510.

Brooks, D. H., Warren, H. P. and Ugarte-Urra, I. (2012), 'Solar Coronal Loops Resolved by Hinode and the Solar Dynamics Observatory', *Astrophysical Journal, Letters* **755**(2), L33.

Brooks, D. H., Warren, H. P., Ugarte-Urra, I. and Winebarger, A. R. (2013), 'High Spatial Resolution Observations of Loops in the Solar Corona', *Astrophysical Journal, Letters* **772**(2), L19.

Bruzek, A. (1964), 'On the Association Between Loop Prominences and Flares.', *Astrophysical Journal* **140**, 746.

Cargill, P. J. (1994), 'Some Implications of the Nanoflare Concept', *Astrophysical Journal* **422**, 381.

Cavagnolo, K. W., Donahue, M., Voit, G. M. and Sun, M. (2008), 'An Entropy Threshold for Strong Hα and Radio Emission in the Cores of Galaxy Clusters', *Astrophysical Journal, Letters* **683**(2), L107.

Charbonneau, P. (2020), 'Dynamo models of the solar cycle', *Living Reviews in Solar Physics* **17**(1), 4.

Chen, H., Tian, H., Li, L., Peter, H., Chitta, L. P. and Hou, Z. (2022), 'Coronal condensation as the source of transition-region supersonic downflows above a sunspot', *Astronomy and Astrophysics* **659**, A107.

Cheung, M. C. M., Boerner, P., Schrijver, C. J., Testa, P., Chen, F., Peter, H. and Malanushenko, A. (2015), 'Thermal Diagnostics with the Atmospheric Imaging Assembly on board the Solar

Dynamics Observatory: A Validated Method for Differential Emission Measure Inversions', *Astrophysical Journal* **807**(2), 143.

Cirtain, J. W., Golub, L., Winebarger, A. R., de Pontieu, B., Kobayashi, K., Moore, R. L., Walsh, R. W., Korreck, K. E., Weber, M., McCauley, P., Title, A., Kuzin, S. and Deforest, C. E. (2013), 'Energy release in the solar corona from spatially resolved magnetic braids', *Nature* **493**(7433), 501–503.

Claes, N. and Keppens, R. (2019), 'Thermal stability of magnetohydrodynamic modes in homogeneous plasmas', *Astronomy and Astrophysics* **624**, A96.

Clark, S. E., Peek, J. E. G. and Putman, M. E. (2014), 'Magnetically Aligned H I Fibers and the Rolling Hough Transform', *Astrophysical Journal* **789**(1), 82.

Colgan, J., Abdallah, J., J., Sherrill, M. E., Foster, M., Fontes, C. J. and Feldman, U. (2008), 'Radiative Losses of Solar Coronal Plasmas', *Astrophysical Journal* **689**(1), 585–592.

Cox, D. P. (2005), 'The Three-Phase Interstellar Medium Revisited', *Annual Review of Astronomy and Astrophysics* **43**(1), 337–385.

Şahin, S. and Antolin, P. (2022), 'Prevalence of Thermal Nonequilibrium over an Active Region', *Astrophysical Journal, Letters* **931**(2), L27.

Şahin, S., Antolin, P., Froment, C. and Schad, T. A. (2023), 'Spatial and Temporal Analysis of Quiescent Coronal Rain over an Active Region', *Astrophysical Journal* **950**(2), 171.

Şahin, S., Yurchyshyn, V., Kumar, P., Kilcik, A., Ahn, K. and Yang, X. (2019), 'Magnetic Field Dynamics and Varying Plasma Emission in Large-scale Coronal Loops', *Astrophysical Journal* **873**(1), 75.

Culhane, J. L., Vesecky, J. F. and Phillips, K. J. H. (1970), 'The Cooling of Flare Produced Plasmas in the Solar Corona', *Solar Physics* **15**(2), 394–413.

De Groof, A., Bastiaensen, C., Müller, D. A. N., Berghmans, D. and Poedts, S. (2005), 'Detailed comparison of downflows seen both in EIT 30.4 nm and Big Bear Hα movies', *Astronomy and Astrophysics* **443**(1), 319–328.

De Groof, A., Berghmans, D., van Driel-Gesztelyi, L. and Poedts, S. (2004), 'Intensity variations in EIT shutterless mode: Waves or flows?', *Astronomy and Astrophysics* **415**, 1141–1151.

De Pontieu, B., Erdélyi, R. and James, S. P. (2004), 'Solar chromospheric spicules from the leakage of photospheric oscillations and flows', *Nature* **430**(6999), 536–539.

de Pontieu, B., McIntosh, S., Hansteen, V. H., Carlsson, M., Schrijver, C. J., Tarbell, T. D., Title, A. M., Shine, R. A., Suematsu, Y., Tsuneta, S., Katsukawa, Y., Ichimoto, K., Shimizu, T. and Nagata, S. (2007), 'A Tale of Two Spicules: The Impact of Spicules on the Magnetic Chromosphere', *Publications of the ASJ* **59**, S655.

De Pontieu, B., Title, A. M., Lemen, J. R., Kushner, G. D., Akin, D. J., Allard, B., Berger, T., Boerner, P., Cheung, M., Chou, C., Drake, J. F., Duncan, D. W., Freeland, S., Heyman, G. F., Hoffman, C., Hurlburt, N. E., Lindgren, R. W., Mathur, D., Rehse, R., Sabolish, D., Seguin, R., Schrijver, C. J., Tarbell, T. D., Wülser, J. P., Wolfson, C. J., Yanari, C., Mudge, J., Nguyen-Phuc, N., Timmons, R., van Bezooijen, R., Weingrod, I., Brookner, R., Butcher, G., Dougherty, B., Eder, J., Knagenhjelm, V., Larsen, S., Mansir, D., Phan, L., Boyle, P., Cheimets, P. N., DeLuca, E. E., Golub, L., Gates, R., Hertz, E., McKillop, S., Park, S., Perry, T., Podgorski, W. A., Reeves, K., Saar, S., Testa, P., Tian, H., Weber, M., Dunn, C., Eccles, S., Jaeggli, S. A., Kankelborg, C. C., Mashburn, K., Pust, N., Springer, L., Carvalho, R., Kleint, L., Marmie, J., Mazmanian, E., Pereira, T. M. D., Sawyer, S., Strong, J., Worden, S. P., Carlsson, M., Hansteen, V. H., Leenaarts, J., Wiesmann, M., Aloise, J., Chu, K. C., Bush, R. I., Scherrer, P. H., Brekke, P., Martinez-Sykora, J., Lites, B. W., McIntosh, S. W., Uitenbroek, H., Okamoto, T. J., Gummin, M. A., Auker, G., Jerram, P., Pool, P. and Waltham, N. (2014), 'The Interface Region Imaging Spectrograph (IRIS)', *Solar Physics* **289**(7), 2733–2779.

DeForest, C. E. (2007), 'On the Size of Structures in the Solar Corona', *Astrophysical Journal* **661**(1), 532–542.

Del Zanna, G. (2003), 'Solar active regions: The footpoints of 1 MK loops', *Astronomy and Astrophysics* **406**, L5–L8.

Del Zanna, G. (2009), 'Benchmarking atomic data for astrophysics: Fe VII and other cool lines observed by Hinode EIS', *Astronomy and Astrophysics* **508**(1), 501–511.

Del Zanna, G. (2012), 'Benchmarking atomic data for the CHIANTI atomic database: coronal lines observed by Hinode EIS', *Astronomy and Astrophysics* **537**, A38.

Del Zanna, G. (2013), 'The multi-thermal emission in solar active regions', *Astronomy and Astrophysics* **558**, A73.

Delaboudinière, J. P., Artzner, G. E., Brunaud, J., Gabriel, A. H., Hochedez, J. F., Millier, F., Song, X. Y., Au, B., Dere, K. P., Howard, R. A., Kreplin, R., Michels, D. J., Moses, J. D., Defise, J. M., Jamar, C., Rochus, P., Chauvineau, J. P., Marioge, J. P., Catura, R. C., Lemen, J. R., Shing, L., Stern, R. A., Gurman, J. B., Neupert, W. M., Maucherat, A., Clette, F., Cugnon, P. and Van Dessel, E. L. (1995), 'EIT: Extreme-Ultraviolet Imaging Telescope for the SOHO Mission', *Solar Physics* **162**(1-2), 291–312.

Domingo, V., Fleck, B. and Poland, A. I. (1995), 'The SOHO Mission: an Overview', *Solar Physics* **162**(1-2), 1–37.

Doschek, G. A., Boris, J. P., Cheng, C. C., Mariska, J. T. and Oran, E. S. (1982), 'A Numerical Simulation of Cooling Coronal Flare Plasma', *Astrophysical Journal* **258**, 373.

Doschek, G. A., Mariska, J. T., Strong, K. T., Bentley, R. D., Brown, C. M., Culhane, J. L., Lang, J., Sterling, A. C. and Watanabe, T. (1994), 'The 1991 November 9 Flare at 03.2 UT: Observations from YOHKOH', *Astrophysical Journal* **431**, 888.

Doschek, G. A., Warren, H. P. and Young, P. R. (2013), 'Chromospheric Evaporation in an M1.8 Flare Observed by the Extreme-ultraviolet Imaging Spectrometer on Hinode', *Astrophysical Journal* **767**(1), 55.

Dudok de Wit, T., Moussaoui, S., Guennou, C., Auchère, F., Cessateur, G., Kretzschmar, M., Vieira, L. A. and Goryaev, F. F. (2013), 'Coronal temperature maps from solar euv images: A blind source separation approach', *Solar Physics* **283**(1), 31–47.

Fang, X., Xia, C. and Keppens, R. (2013), 'Multidimensional Modeling of Coronal Rain Dynamics', *Astrophysical Journal, Letters* **771**(2), L29.

Fang, X., Xia, C., Keppens, R. and Van Doorsselaere, T. (2015), 'Coronal Rain in Magnetic Arcades: Rebound Shocks, Limit Cycles, and Shear Flows', *Astrophysical Journal* **807**(2), 142.

Fang, X., Yuan, D., Xia, C., Van Doorsselaere, T. and Keppens, R. (2016), 'The Role of Kelvin-Helmholtz Instability for Producing Loop-top Hard X-Ray Sources in Solar Flares', *Astrophysical Journal* **833**(1), 36.

Feldman, U., Doschek, G. A., Kreplin, R. W. and Mariska, J. T. (1980), 'High-resolution X-ray spectra of solar flares. IV - General spectral properties of M type flares', *Astrophysical Journal* **241**, 1175–1185.

Field, G. B. (1965), 'Thermal Instability.', *Astrophysical Journal* **142**, 531.

Fisher, I. and Lewis, T. (1983), 'Estimating the common mean direction of several circular or spherical distributions with differing dispersions', *Biometrika* **70**(2), 333–341.

Fletcher, L., Dennis, B. R., Hudson, H. S., Krucker, S., Phillips, K., Veronig, A., Battaglia, M., Bone, L., Caspi, A., Chen, Q., Gallagher, P., Grigis, P. T., Ji, H., Liu, W., Milligan, R. O. and Temmer, M. (2011), 'An Observational Overview of Solar Flares', *Space Science Reviews* **159**(1-4), 19–106.

Foukal, P. (1978), 'Magnetic loop, downflows, and convection in the solar corona.', *Astrophysical Journal* **223**, 1046–1057.

Foukal, P. V. (1976), 'The pressure and energy balance of the cool corona over sunspots.', *Astrophysical Journal* **210**, 575–581.

Foullon, C., Verwichte, E. and Nakariakov, V. M. (2004), 'Detection of ultra-long-period oscillations in an EUV filament', *Astronomy and Astrophysics* **427**, L5–L8.

Freedman, R. A. and William III, J. (2008), 'Kaufmann iii. universe'.

Froment, C. (2016), Long-period intensity pulsations as the manifestation of heating stratification and timescale in solar coronal loops, PhD thesis, Institut d'Astrophysique Spatiale.

Froment, C., Antolin, P., Henriques, V. M. J., Kohutova, P. and Rouppe van der Voort, L. H. M. (2020), 'Multi-scale observations of thermal non-equilibrium cycles in coronal loops', *Astronomy and Astrophysics* **633**, A11.

Froment, C., Auchère, F., Aulanier, G., Mikić, Z., Bocchialini, K., Buchlin, E. and Solomon, J. (2017), 'Long-period Intensity Pulsations in Coronal Loops Explained by Thermal Non-equilibrium Cycles', *Astrophysical Journal* **835**(2), 272.

Froment, C., Auchère, F., Bocchialini, K., Buchlin, E., Guennou, C. and Solomon, J. (2015), 'Evidence for Evaporation-incomplete Condensation Cycles in Warm Solar Coronal Loops', *Astrophysical Journal* **807**, 158.

Froment, C., Auchère, F., Mikić, Z., Aulanier, G., Bocchialini, K., Buchlin, E., Solomon, J. and Soubrié, E. (2018), 'On the Occurrence of Thermal Nonequilibrium in Coronal Loops', *Astrophysical Journal* **855**(1), 52.

Galsgaard, K. and Nordlund, Å. (1996), 'Heating and activity of the solar corona 1. Boundary shearing of an initially homogeneous magnetic field', *Journal of Geophysics Research* **101**(A6), 13445–13460.

Gary, G. A. (2001), 'Plasma Beta above a Solar Active Region: Rethinking the Paradigm', *Solar Physics* **203**(1), 71–86.

Gibson, E. G. (1973), *The quiet sun*, Vol. 303, National Aeronautics and Space Administration, Scientific and Technical.

Golub, L., Bookbinder, J., Deluca, E., Karovska, M., Warren, H., Schrijver, C. J., Shine, R., Tarbell, T., Title, A., Wolfson, J., Handy, B. and Kankelborg, C. (1999), 'A new view of the solar corona from the transition region and coronal explorer (TRACE)', *Physics of Plasmas* **6**(5), 2205–2216.

Golub, L., Herant, M., Kalata, K., Lovas, I., Nystrom, G., Pardo, F., Spiller, E. and Wilczynski, J. (1990), 'Sub-arcsecond observations of the solar X-ray corona', *Nature* **344**(6269), 842–844.

Golub, L. and Pasachoff, J. M. (2009), *The Solar Corona*.

Grotrian, W. (1934), 'Über das Fraunhofersche Spektrum der Sonnenkorona. Mit 10 Abbildungen.', *Zeitschrift fuer Astrophysik* **8**, 124.

Gudiksen, B. V. and Nordlund, Å. (2005), 'An AB Initio Approach to Solar Coronal Loops', *Astrophysical Journal* **618**(2), 1031–1038.

Guennou, C., Auchère, F., Klimchuk, J. A., Bocchialini, K. and Parenti, S. (2013), 'Can the Differential Emission Measure Constrain the Timescale of Energy Deposition in the Corona?', *Astrophysical Journal* **774**(1), 31.

Guennou, C., Auchère, F., Soubrié, E., Bocchialini, K., Parenti, S. and Barbey, N. (2012), 'On the Accuracy of the Differential Emission Measure Diagnostics of Solar Plasmas. Application to SDO/AIA. I. Isothermal Plasmas', *Astrophysical Journal, Supplement* **203**(2), 25.

Gupta, G. R., Del Zanna, G. and Mason, H. E. (2019), 'Exploring the damping of Alfvén waves along a long off-limb coronal loop, up to 1.4 $R_{\odot}$', *Astronomy and Astrophysics* **627**, A62.

Hannah, I. G. and Kontar, E. P. (2012), 'Differential emission measures from the regularized inversion of Hinode and SDO data', *Astronomy and Astrophysics* **539**, A146.

Hansteen, V. H., De Pontieu, B., Rouppe van der Voort, L., van Noort, M. and Carlsson, M. (2006), 'Dynamic Fibrils Are Driven by Magnetoacoustic Shocks', *Astrophysical Journal, Letters* **647**(1), L73–L76.

Hara, H., Nishino, Y., Ichimoto, K. and Delaboudinière, J.-P. (2006), 'A Spectroscopic Observation of a Magnetic Reconnection Site in a Small Flaring Event', *Astrophysical Journal* **648**(1), 712–721.

Heinzel, P., Schmieder, B., Fárník, F., Schwartz, P., Labrosse, N., Kotrč, P., Anzer, U., Molodij, G., Berlicki, A., DeLuca, E. E., Golub, L., Watanabe, T. and Berger, T. (2008), 'Hinode, TRACE, SOHO, and Ground-based Observations of a Quiescent Prominence', *Astrophysical Journal* **686**(2), 1383–1396.

Holman, G. D. (2016), 'Scientific considerations for future spectroscopic measurements from space of activity on the Sun', *Journal of Geophysical Research (Space Physics)* **121**(12), 11,667–11,697.

Hough, P. (U.S. Patent 3 069 654, Dec. 18, 1962), 'Method and means for recognizing complex patterns'.

Huang, Z., Zhang, Q., Xia, L., Li, B., Wu, Z. and Fu, H. (2020), 'Heating at the Remote Footpoints as a Brake on Jet Flows along Loops in the Solar Atmosphere', *Astrophysical Journal* **897**(2), 113.

Hudson, H. S. and Warmuth, A. (2004), 'Coronal Loop Oscillations and Flare Shock Waves', *Astrophysical Journal, Letters* **614**(1), L85–L88.

Hyvarinen, A. (1999), 'Fast and robust fixed-point algorithms for independent component analysis', *IEEE Transactions on Neural Networks* **10**(3), 626–634.

Jejčič, S., Kleint, L. and Heinzel, P. (2018), 'High-density Off-limb Flare Loops Observed by SDO', *Astrophysical Journal* **867**(2), 134.

Jenkins, J. M. and Keppens, R. (2021), 'Prominence formation by levitation-condensation at extreme resolutions', *Astronomy and Astrophysics* **646**, A134.

Ji, S., Oh, S. P. and McCourt, M. (2018), 'The impact of magnetic fields on thermal instability', *Monthly Notices of the Royal Astronomical Society* **476**(1), 852–867.

Jing, J., Xu, Y., Cao, W., Liu, C., Gary, D. and Wang, H. (2016), 'Unprecedented Fine Structure of a Solar Flare Revealed by the 1.6 m New Solar Telescope', *Scientific Reports* **6**, 24319.

Johnston, C. D., Cargill, P. J., Antolin, P., Hood, A. W., De Moortel, I. and Bradshaw, S. J. (2019), 'The effects of numerical resolution, heating timescales and background heating on thermal non-equilibrium in coronal loops', *Astronomy and Astrophysics* **625**, A149.

Kane, S. R. (1974), Impulsive (flash) Phase of Solar Flares: Hard X-Ray Microwave, EUV and Optical Observations, *in* G. A. Newkirk, ed., 'Coronal Disturbances', Vol. 57, p. 105.

Karpen, J. T., Antiochos, S. K., Hohensee, M., Klimchuk, J. A. and MacNeice, P. J. (2001), 'Are Magnetic Dips Necessary for Prominence Formation?', *Astrophysical Journal, Letters* **553**(1), L85–L88.

Kawaguchi, I. (1970), 'Observed Interaction between Prominences', *Publications of the ASJ* **22**, 405.

Keppens, R., Xia, C. and Porth, O. (2015), 'Solar Prominences: "Double, Double... Boil and Bubble"', *Astrophysical Journal, Letters* **806**(1), L13.

Kleint, L., Antolin, P., Tian, H., Judge, P., Testa, P., De Pontieu, B., Martínez-Sykora, J., Reeves, K. K., Wuelser, J. P., McKillop, S., Saar, S., Carlsson, M., Boerner, P., Hurlburt, N., Lemen,

J., Tarbell, T. D., Title, A., Golub, L., Hansteen, V., Jaeggli, S. and Kankelborg, C. (2014), 'Detection of Supersonic Downflows and Associated Heating Events in the Transition Region above Sunspots', *Astrophysical Journal, Letters* **789**(2), L42.

Klimchuk, J. A. (2000), 'Cross-Sectional Properties of Coronal Loops', *Solar Physics* **193**, 53–75.

Klimchuk, J. A. (2006), 'On Solving the Coronal Heating Problem', *Solar Physics* **234**(1), 41–77.

Klimchuk, J. A. (2019), 'The Distinction Between Thermal Nonequilibrium and Thermal Instability', *Solar Physics* **294**(12), 173.

Klimchuk, J. A. and DeForest, C. E. (2020), 'Cross Sections of Coronal Loop Flux Tubes', *Astrophysical Journal* **900**(2), 167.

Klimchuk, J. A. and Luna, M. (2019), 'The Role of Asymmetries in Thermal Nonequilibrium', *Astrophysical Journal* **884**(1), 68.

Kohutova, P. and Verwichte, E. (2016), 'Analysis of Coronal Rain Observed by IRIS, HINODE/SOT, and SDO/AIA: Transverse Oscillations, Kinematics, and Thermal Evolution', *Astrophysical Journal* **827**(1), 39.

Kohutova, P. and Verwichte, E. (2017), 'Dynamics of plasma condensations in a gravitationally stratified coronal loop', *Astronomy and Astrophysics* **602**, A23.

Kontar, E. P., Hannah, I. G. and MacKinnon, A. L. (2008), 'Chromospheric magnetic field and density structure measurements using hard X-rays in a flaring coronal loop', *Astronomy and Astrophysics* **489**(3), L57–L60.

Koyama, H. and Inutsuka, S.-I. (2000), 'Molecular Cloud Formation in Shock-compressed Layers', *Astrophysical Journal* **532**(2), 980–993.

Koza, J., Kuridze, D., Heinzel, P., Jejčič, S., Morgan, H. and Zapiór, M. (2019), 'Spectral Diagnostics of Cool Flare Loops Observed by the SST. I. Inversion of the Ca II 8542 Å and Hβ Lines', *Astrophysical Journal* **885**(2), 154.

Kuin, N. P. M. and Martens, P. C. H. (1982), 'On the thermal stability of hot coronal loops - The coupling between chromosphere and corona', *Astronomy and Astrophysics* **108**(2), L1–L4.

Kuridze, D., Mathioudakis, M., Morgan, H., Oliver, R., Kleint, L., Zaqarashvili, T. V., Reid, A., Koza, J., Löfdahl, M. G., Hillberg, T., Kukhianidze, V. and Hanslmeier, A. (2019), 'Mapping the Magnetic Field of Flare Coronal Loops', *Astrophysical Journal* **874**(2), 126.

Labrosse, N., Heinzel, P., Vial, J. C., Kucera, T., Parenti, S., Gunár, S., Schmieder, B. and Kilper, G. (2010), 'Physics of Solar Prominences: I—Spectral Diagnostics and Non-LTE Modelling', *Space Science Reviews* **151**(4), 243–332.

Lacatus, D. A., Judge, P. G. and Donea, A. (2017), 'An Explanation of Remarkable Emission-line Profiles in Post-flare Coronal Rain', *Astrophysical Journal* **842**(1), 15.

Landi, E., Hutton, R., Brage, T. and Li, W. (2020), 'Hinode/EIS Measurements of Active-region Magnetic Fields', *Astrophysical Journal* **904**(2), 87.

Lemaire, P., Wilhelm, K., Curdt, W., SchÜle, U., Marsch, E., Poland, A. I., Jordan, S. D., Thomas, R. J., Hassler, D. M., Vial, J. C., KÜhne, M., Huber, M. C. E., Siegmund, O. H. W., Gabriel, A., Timothy, J. G. and Grewing, M. (1997), 'First Results of the SUMER Telescope and Spectrometer on SOHO - II. Imagery and Data Management', *Solar Physics* **170**(1), 105–122.

Lemen, J. R., Title, A. M., Akin, D. J., Boerner, P. F., Chou, C., Drake, J. F., Duncan, D. W., Edwards, C. G., Friedlaender, F. M., Heyman, G. F., Hurlburt, N. E., Katz, N. L., Kushner, G. D., Levay, M., Lindgren, R. W., Mathur, D. P., McFeaters, E. L., Mitchell, S., Rehse, R. A., Schrijver, C. J., Springer, L. A., Stern, R. A., Tarbell, T. D., Wuelser, J.-P., Wolfson, C. J., Yanari, C., Bookbinder, J. A., Cheimets, P. N., Caldwell, D., Deluca, E. E., Gates, R., Golub, L., Park, S., Podgorski, W. A., Bush, R. I., Scherrer, P. H., Gummin, M. A., Smith, P., Auker, G., Jerram, P., Pool, P., Soufli, R., Windt, D. L., Beardsley, S., Clapp, M., Lang, J. and Waltham, N. (2012), 'The Atmospheric Imaging Assembly (AIA) on the Solar Dynamics Observatory (SDO)', *Solar Physics* **275**(1-2), 17–40.

Leroy, J.-L. (1972), 'Emissions 'froides' dans la couronne solaire', *Solar Physics* **25**(2), 413–417.

Li, L. P. and Peter, H. (2019), 'Plasma injection into a solar coronal loop', *Astronomy and Astrophysics* **626**, A98.

Li, L., Zhang, J., Peter, H., Chitta, L. P., Su, J., Xia, C., Song, H. and Hou, Y. (2018), 'Coronal

Condensations Caused by Magnetic Reconnection between Solar Coronal Loops', *Astrophysical Journal, Letters* **864**(1), L4.

Li, X., Keppens, R. and Zhou, Y. (2022), 'Coronal Rain in Randomly Heated Arcades', *Astrophysical Journal* **926**(2), 216.

Liang, G. Y., Whiteford, A. D. and Badnell, N. R. (2009), 'R-matrix electron-impact excitation data for the Na-like iso-electronic sequence', *Astronomy and Astrophysics* **500**(3), 1263–1269.

Lionello, R., Winebarger, A. R., Mok, Y., Linker, J. A. and Mikić, Z. (2013), 'Thermal Non-equilibrium Revisited: A Heating Model for Coronal Loops', *Astrophysical Journal* **773**(2), 134.

Liu, W., Antolin, P. and Sun, X. (2016), IRIS Observations of a Novel, Hybrid Prominence-Coronal Rain Complex, *in* 'AAS/Solar Physics Division Abstracts #47', Vol. 47 of *AAS/Solar Physics Division Meeting*, p. 4.02.

Liu, W., Berger, T. E. and Low, B. C. (2012), 'First SDO/AIA Observation of Solar Prominence Formation Following an Eruption: Magnetic Dips and Sustained Condensation and Drainage', *Astrophysical Journal, Letters* **745**(2), L21.

Liu, W., Liu, S., Jiang, Y. W. and Petrosian, V. (2006), 'RHESSI Observation of Chromospheric Evaporation', *Astrophysical Journal* **649**(2), 1124–1139.

López Fuentes, M. C., Démoulin, P. and Klimchuk, J. A. (2008), 'Are Constant Loop Widths an Artifact of the Background and the Spatial Resolution?', *Astrophysical Journal* **673**(1), 586–597.

López Fuentes, M. C., Klimchuk, J. A. and Mandrini, C. H. (2007), 'The Temporal Evolution of Coronal Loops Observed by GOES SXI', *Astrophysical Journal* **657**(2), 1127–1136.

Luna, M., Karpen, J. T. and DeVore, C. R. (2012), 'Formation and Evolution of a Multi-threaded Solar Prominence', *Astrophysical Journal* **746**(1), 30.

Mackay, D. H. and Galsgaard, K. (2001), 'Evolution of a Density Enhancement in a Stratified Atmosphere With Uniform Vertical Magnetic Field', *Solar Physics* **198**(2), 289–312.

Mackay, D. H., Karpen, J. T., Ballester, J. L., Schmieder, B. and Aulanier, G. (2010), 'Physics of Solar Prominences: II—Magnetic Structure and Dynamics', *Space Science Reviews* **151**(4), 333–399.

Malanushenko, A., Cheung, M. C. M., DeForest, C. E., Klimchuk, J. A. and Rempel, M. (2022), 'The Coronal Veil', *Astrophysical Journal* **927**(1), 1.

Mardia, K. V. (1999), 'Directional statistics and shape analysis', *Journal of Applied Statistics* **26**(8), 949–957.

Martin, S. F. (1998), 'Conditions for the Formation and Maintenance of Filaments (Invited Review)', *Solar Physics* **182**(1), 107–137.

Martínez-Gómez, D., Oliver, R., Khomenko, E. and Collados, M. (2020), 'Two-dimensional simulations of coronal rain dynamics. I. Model consisting of a vertical magnetic field and an unbounded atmosphere', *Astronomy and Astrophysics* **634**, A36.

Martínez Oliveros, J.-C., Krucker, S., Hudson, H. S., Saint-Hilaire, P., Bain, H., Lindsey, C., Bogart, R., Couvidat, S., Scherrer, P. and Schou, J. (2014), 'Chromospheric and Coronal Observations of Solar Flares with the Helioseismic and Magnetic Imager', *Astrophysical Journal, Letters* **780**(2), L28.

Martínez-Sykora, J., De Pontieu, B., De Moortel, I., Hansteen, V. H. and Carlsson, M. (2018), 'Impact of Type II Spicules in the Corona: Simulations and Synthetic Observables', *Astrophysical Journal* **860**(2), 116.

Martínez-Sykora, J., De Pontieu, B., Hansteen, V. H., Rouppe van der Voort, L., Carlsson, M. and Pereira, T. M. D. (2017), 'On the generation of solar spicules and Alfvénic waves', *Science* **356**(6344), 1269–1272.

Mason, E. I., Antiochos, S. K. and Viall, N. M. (2019), 'Observations of Solar Coronal Rain in Null Point Topologies', *Astrophysical Journal, Letters* **874**(2), L33.

Mason, E. I. and Kniezewski, K. L. (2022), 'To Rain or Not to Rain: Correlating GOES Flare Class and Coronal Rain Statistics', *Astrophysical Journal* **939**(1), 21.

McIntosh, P. S. (1972), 'Solar magnetic fields derived from hydrogen alpha filtergrams.', *Reviews of Geophysics and Space Physics* **10**, 837–846.

McIntosh, S. W., Tian, H., Sechler, M. and De Pontieu, B. (2012), 'On the Doppler Velocity of Emission Line Profiles Formed in the "Coronal Contraflow" that Is the Chromosphere-Corona Mass Cycle', *Astrophysical Journal* **749**(1), 60.

Mendoza-Briceño, C. A., Sigalotti, L. D. G. and Erdélyi, R. (2005), 'Catastrophic Cooling of Impulsively Heated Coronal Loops', *Astrophysical Journal* **624**(2), 1080–1092.

Mikić, Z., Lionello, R., Mok, Y., Linker, J. A. and Winebarger, A. R. (2013), 'The Importance of Geometric Effects in Coronal Loop Models', *Astrophysical Journal* **773**(2), 94.

Milligan, R. O. and Dennis, B. R. (2009), 'Velocity Characteristics of Evaporated Plasma Using Hinode/EUV Imaging Spectrometer', *Astrophysical Journal* **699**(2), 968–975.

Morgan, H. and Druckmüller, M. (2014), 'Multi-Scale Gaussian Normalization for Solar Image Processing', *Solar Physics* **289**(8), 2945–2955.

Moriyasu, S., Kudoh, T., Yokoyama, T. and Shibata, K. (2004), 'The Nonlinear Alfvén Wave Model for Solar Coronal Heating and Nanoflares', *Astrophysical Journal, Letters* **601**(1), L107–L110.

Müller, D. A. N., De Groof, A., Hansteen, V. H. and Peter, H. (2005), 'High-speed coronal rain', *Astronomy and Astrophysics* **436**(3), 1067–1074.

Müller, D. A. N., Hansteen, V. H. and Peter, H. (2003), 'Dynamics of solar coronal loops. I. Condensation in cool loops and its effect on transition region lines', *Astronomy and Astrophysics* **411**, 605–613.

Müller, D. A. N., Peter, H. and Hansteen, V. H. (2004), 'Dynamics of solar coronal loops. II. Catastrophic cooling and high-speed downflows', *Astronomy and Astrophysics* **424**, 289–300.

Muller, R., Roudier, T., Vigneau, J. and Auffret, H. (1994), 'The proper motion of network bright points and the heating of the solar corona.', *Astronomy and Astrophysics* **283**, 232–240.

Mulu-Moore, F. M., Winebarger, A. R., Warren, H. P. and Aschwanden, M. J. (2011), 'Determining the Structure of Solar Coronal Loops Using Their Evolution', *Astrophysical Journal* **733**(1), 59.

Nagata, S., Hara, H., Kano, R., Kobayashi, K., Sakao, T., Shimizu, T., Tsuneta, S., Yoshida, T. and Gurman, J. B. (2003), 'Spatial and Temporal Properties of Hot and Cool Coronal Loops', *Astrophysical Journal* **590**(2), 1095–1110.

Nakariakov, V. M., Ofman, L., Deluca, E. E., Roberts, B. and Davila, J. M. (1999), 'TRACE observation of damped coronal loop oscillations: Implications for coronal heating', *Science* **285**, 862–864.

Nived, V. N., Scullion, E., Doyle, J. G., Susino, R., Antolin, P., Spadaro, D., Sasso, C., Sahin, S. and Mathioudakis, M. (2022), 'Implications of spicule activity on coronal loop heating and catastrophic cooling', *Monthly Notices of the Royal Astronomical Society* **509**(4), 5523–5537.

Nordlund, Å., Stein, R. F. and Asplund, M. (2009), 'Solar Surface Convection', *Living Reviews in Solar Physics* **6**(1), 2.

Oliver, R., Soler, R., Terradas, J. and Zaqarashvili, T. V. (2016), 'Dynamics of Coronal Rain and Descending Plasma Blobs in Solar Prominences. II. Partially Ionized Case', *Astrophysical Journal* **818**(2), 128.

Oliver, R., Soler, R., Terradas, J., Zaqarashvili, T. V. and Khodachenko, M. L. (2014), 'Dynamics of Coronal Rain and Descending Plasma Blobs in Solar Prominences. I. Fully Ionized Case', *Astrophysical Journal* **784**, 21.

Parker, E. N. (1953), 'Instability of Thermal Fields.', *Astrophysical Journal* **117**, 431.

Parker, E. N. (1972), 'Topological Dissipation and the Small-Scale Fields in Turbulent Gases', *Astrophysical Journal* **174**, 499.

Parker, E. N. (1988), 'Nanoflares and the Solar X-Ray Corona', *Astrophysical Journal* **330**, 474.

Parker, E. N. (1991), 'Heating Solar Coronal Holes', *Astrophysical Journal* **372**, 719.

Pelouze, G., Auchère, F., Bocchialini, K., Froment, C., Mikić, Z., Soubrié, E. and Voyeux, A. (2022), 'The role of asymmetries in coronal rain formation during thermal non-equilibrium cycles', *Astronomy and Astrophysics* **658**, A71.

Peng, C.-H. and Matsumoto, R. (2017), 'Formation of Galactic Prominence in the Galactic Central Region', *Astrophysical Journal* **836**(2), 149.

Peres, G., Orlando, S., Reale, F., Rosner, R. and Hudson, H. (2000), 'The Sun as an X-Ray Star. II. Using theYohkoh/Soft X-Ray Telescope-derived Solar Emission Measure versus Temperature to Interpret Stellar X-Ray Observations', *Astrophysical Journal* **528**(1), 537–551.

Pesnell, W. D., Thompson, B. J. and Chamberlin, P. C. (2012), 'The Solar Dynamics Observatory (SDO)', *Solar Physics* **275**(1-2), 3–15.

Peter, H. and Bingert, S. (2012), 'Constant cross section of loops in the solar corona', *Astronomy and Astrophysics* **548**, A1.

Peter, H., Bingert, S. and Kamio, S. (2012), 'Catastrophic cooling and cessation of heating in the solar corona', *Astronomy and Astrophysics* **537**, A152.

Peter, H., Bingert, S., Klimchuk, J. A., de Forest, C., Cirtain, J. W., Golub, L., Winebarger, A. R., Kobayashi, K. and Korreck, K. E. (2013), 'Structure of solar coronal loops: from miniature to large-scale', *Astronomy and Astrophysics* **556**, A104.

Peter, H., Gudiksen, B. V. and Nordlund, Å. (2004), 'Coronal Heating through Braiding of Magnetic Field Lines', *Astrophysical Journal, Letters* **617**(1), L85–L88.

Pitjeva, E. V. and Standish, E. M. (2009), 'Proposals for the masses of the three largest asteroids, the Moon-Earth mass ratio and the Astronomical Unit', *Celestial Mechanics and Dynamical Astronomy* **103**(4), 365–372.

Plowman, J. and Caspi, A. (2020), 'A Fast, Simple, Robust Algorithm for Coronal Temperature Reconstruction', *Astrophysical Journal* **905**(1), 17.

Pouget, G., Bocchialini, K. and Solomon, J. (2006), 'Oscillations in a solar filament: first observation of long periods in the HeI 584.33 Å line, modelling and diagnostic', *Astronomy and Astrophysics* **450**(3), 1189–1198.

Prasad, D., Sharma, P. and Babul, A. (2015), 'Cool Core Cycles: Cold Gas and AGN Jet Feedback in Cluster Cores', *Astrophysical Journal* **811**(2), 108.

Priest, E. (2014), *Magnetohydrodynamics of the Sun*.

Priest, E. R. and Forbes, T. G. (2002), 'The magnetic nature of solar flares', *Astronomy and Astrophysics Reviews* **10**(4), 313–377.

Rachmeler, L. A., Winebarger, A. R., Savage, S. L., Golub, L., Kobayashi, K., Vigil, G. D., Brooks, D. H., Cirtain, J. W., De Pontieu, B., McKenzie, D. E., Morton, R. J., Peter, H., Testa, P., Tiwari, S. K., Walsh, R. W., Warren, H. P., Alexander, C., Ansell, D., Beabout, B. L., Beabout, D. L., Bethge, C. W., Champey, P. R., Cheimets, P. N., Cooper, M. A., Creel, H. K., Gates, R., Gomez, C., Guillory, A., Haight, H., Hogue, W. D., Holloway, T., Hyde, D. W., Kenyon, R., Marshall, J. N., McCracken, J. E., McCracken, K., Mitchell, K. O., Ordway, M., Owen, T., Ranganathan, J., Robertson, B. A., Payne, M. J., Podgorski, W., Pryor, J., Samra, J., Sloan, M. D., Soohoo, H. A., Steele, D. B., Thompson, F. V., Thornton, G. S., Watkinson, B. and Windt, D. (2019), 'The High-Resolution Coronal Imager, Flight 2.1', *Solar Physics* **294**(12), 174.

Reale, F. (2014), 'Coronal Loops: Observations and Modeling of Confined Plasma', *Living Reviews in Solar Physics* **11**(1), 4.

Reep, J. W., Antolin, P. and Bradshaw, S. J. (2020), 'Electron Beams Cannot Directly Produce Coronal Rain', *Astrophysical Journal* **890**(2), 100.

Reep, J. W. and Toriumi, S. (2017), 'The Direct Relation between the Duration of Magnetic Reconnection and the Evolution of GOES Light Curves in Solar Flares', *Astrophysical Journal* **851**(1), 4.

Rosner, R., Tucker, W. H. and Vaiana, G. S. (1978), 'Dynamics of the quiescent solar corona.', *Astrophysical Journal* **220**, 643–645.

Ruan, W., Zhou, Y. and Keppens, R. (2021), 'When Hot Meets Cold: Post-flare Coronal Rain', *Astrophysical Journal, Letters* **920**(1), L15.

Schad, T. (2017), 'Automated Spatiotemporal Analysis of Fibrils and Coronal Rain Using the Rolling Hough Transform', *Solar Physics* **292**(9), 132.

Schad, T. A. (2018), 'Neutral Helium Triplet Spectroscopy of Quiescent Coronal Rain with Sensitivity Estimates for Spectropolarimetric Magnetic Field Diagnostics', *Astrophysical Journal* **865**(1), 31.

Schad, T. A., Dima, G. I. and Anan, T. (2021), 'He I Spectropolarimetry of a Supersonic Coronal Downflow Within a Sunspot Umbra', *Astrophysical Journal* **916**(1), 5.

Schad, T. A., Penn, M. J., Lin, H. and Judge, P. G. (2016), 'Vector Magnetic Field Measurements along a Cooled Stereo-imaged Coronal Loop', *Astrophysical Journal* **833**(1), 5.

Scharmer, G. B., Bjelksjo, K., Korhonen, T. K., Lindberg, B. and Petterson, B. (2003), The 1-meter Swedish solar telescope, *in* S. L. Keil and S. V. Avakyan, eds, 'Innovative Telescopes and Instrumentation for Solar Astrophysics', Vol. 4853 of *Society of Photo-Optical Instrumentation Engineers (SPIE) Conference Series*, pp. 341–350.

Scharmer, G. B., Narayan, G., Hillberg, T., de la Cruz Rodriguez, J., Löfdahl, M. G., Kiselman, D., Sütterlin, P., van Noort, M. and Lagg, A. (2008), 'CRISP Spectropolarimetric Imaging of Penumbral Fine Structure', *Astrophysical Journal, Letters* **689**(1), L69.

Scherrer, P. H., Schou, J., Bush, R. I., Kosovichev, A. G., Bogart, R. S., Hoeksema, J. T., Liu, Y., Duvall, T. L., Zhao, J., Title, A. M., Schrijver, C. J., Tarbell, T. D. and Tomczyk, S. (2012), 'The Helioseismic and Magnetic Imager (HMI) Investigation for the Solar Dynamics Observatory (SDO)', *Solar Physics* **275**(1-2), 207–227.

Schrijver, C. J. (2001), 'Catastrophic cooling and high-speed downflow in quiescent solar coronal loops observed with TRACE', *Solar Physics* **198**(2), 325–345.

Scullion, E., Rouppe van der Voort, L., Antolin, P., Wedemeyer, S., Vissers, G., Kontar, E. P. and Gallagher, P. T. (2016), 'Observing the Formation of Flare-driven Coronal Rain', *Astrophysical Journal* **833**(2), 184.

Scullion, E., Rouppe van der Voort, L., Wedemeyer, S. and Antolin, P. (2014), 'Unresolved Fine-scale Structure in Solar Coronal Loop-tops', *Astrophysical Journal* **797**(1), 36.

Secchi, A. (1875), *Le Soleil*.

Sharma, P., Parrish, I. J. and Quataert, E. (2010), 'Thermal Instability with Anisotropic Thermal Conduction and Adiabatic Cosmic Rays: Implications for Cold Filaments in Galaxy Clusters', *Astrophysical Journal* **720**(1), 652–665.

Shibata, K. and Magara, T. (2011), 'Solar Flares: Magnetohydrodynamic Processes', *Living Reviews in Solar Physics* **8**(1), 6.

Shibata, K., Masuda, S., Shimojo, M., Hara, H., Yokoyama, T., Tsuneta, S., Kosugi, T. and Ogawara, Y. (1995), 'Hot-Plasma Ejections Associated with Compact-Loop Solar Flares', *Astrophysical Journal, Letters* **451**, L83.

Shibata, K., Tajima, T., Matsumoto, R., Horiuchi, T., Hanawa, T., Rosner, R. and Uchida, Y. (1989), 'Nonlinear Parker Instability of Isolated Magnetic Flux in a Plasma', *Astrophysical Journal* **338**, 471.

Song, Q., Wang, J.-S., Feng, X. and Zhang, X. (2016), 'Dark Post-flare Loops Observed by the Solar Dynamics Observatory', *Astrophysical Journal* **821**(2), 83.

Spiegel, E. A. and Zahn, J. P. (1992), 'The solar tachocline.', *Astronomy and Astrophysics* **265**, 106–114.

Srivastava, A. K., Mishra, S. K., Jelínek, P., Samanta, T., Tian, H., Pant, V., Kayshap, P., Banerjee, D., Doyle, J. G. and Dwivedi, B. N. (2019), 'On the Observations of Rapid Forced Reconnection in the Solar Corona', *Astrophysical Journal* **887**(2), 137.

Stix, M. (2002), *The sun: an introduction*.

Sturrock, P. A. and Uchida, Y. (1981), 'Coronal heating by stochastic magnetic pumping', *Astrophysical Journal* **246**, 331–336.

Sweet, P. A. (1958), The Neutral Point Theory of Solar Flares, *in* B. Lehnert, ed., 'Electromagnetic Phenomena in Cosmical Physics', Vol. 6, p. 123.

Takasao, S. and Shibata, K. (2016), 'Above-the-loop-top Oscillation and Quasi-periodic Coronal Wave Generation in Solar Flares', *Astrophysical Journal* **823**(2), 150.

Takeuchi, A. and Shibata, K. (2001), 'Magnetic Reconnection Induced by Convective Intensification of Solar Photospheric Magnetic Fields', *Astrophysical Journal, Letters* **546**(1), L73–L76.

Tandberg-Hanssen, E. (1995), 'Books-Received - the Nature of Solar Prominences', *Science* **269**, 111.

Tang, F. (1987), 'Quiescent prominences - where are they formed?', *Solar Physics* **107**(2), 233–237.

Testa, P. and Reale, F. (2012), 'Hinode/EIS Spectroscopic Validation of Very Hot Plasma Imaged with the Solar Dynamics Observatory in Non-flaring Active Region Cores', *Astrophysical Journal, Letters* **750**(1), L10.

Thompson, W. T. (2006), 'Coordinate systems for solar image data', *Astronomy and Astrophysics* **449**(2), 791–803.

Tian, H. and Chen, N. H. (2018), 'Multi-episode Chromospheric Evaporation Observed in a Solar Flare', *Astrophysical Journal* **856**(1), 34.

Tian, H., Xia, L. D. and Li, S. (2008), 'Long-period oscillations in solar coronal bright points', *Astronomy and Astrophysics* **489**(2), 741–745.

Tomczak, M. (1997), 'The impulsive phase of the arcade flare of 28 June 1992, 14:24 UT.', *Astronomy and Astrophysics* **317**, 223–231.

Tomczyk, S., Card, G. L., Darnell, T., Elmore, D. F., Lull, R., Nelson, P. G., Streander, K. V., Burkepile, J., Casini, R. and Judge, P. G. (2008), 'An Instrument to Measure Coronal Emission Line Polarization', *Solar Physics* **247**(2), 411–428.

Torrence, C. and Compo, G. P. (1998), 'A Practical Guide to Wavelet Analysis.', *Bulletin of the American Meteorological Society* **79**(1), 61–78.

Tsiropoula, G. and Tziotziou, K. (2004), 'The role of chromospheric mottles in the mass balance and heating of the solar atmosphere', *Astronomy and Astrophysics* **424**, 279–288.

Ugarte-Urra, I., Doyle, J. G., Madjarska, M. S. and O'Shea, E. (2004), 'Signature of oscillations in coronal bright points', *Astronomy and Astrophysics* **418**, 313–324.

Ugarte-Urra, I. and Warren, H. P. (2014), 'Determining Heating Timescales in Solar Active Region Cores from AIA/SDO Fe XVIII Images', *Astrophysical Journal* **783**(1), 12.

Ugarte-Urra, I., Warren, H. P. and Brooks, D. H. (2009), 'Active Region Transition Region Loop Populations and Their Relationship to the Corona', *Astrophysical Journal* **695**(1), 642–651.

van Ballegooijen, A. A. (1986), 'Cascade of Magnetic Energy as a Mechanism of Coronal Heating', *Astrophysical Journal* **311**, 1001.

van der Linden, R. A. M. and Goossens, M. (1991), 'The thermal continuum in coronal loops - Instability criteria and the influence of perpendicular thermal conduction', *Solar Physics* **134**, 247–273.

Van Doorsselaere, T., Srivastava, A. K., Antolin, P., Magyar, N., Vasheghani Farahani, S., Tian, H., Kolotkov, D., Ofman, L., Guo, M., Arregui, I., De Moortel, I. and Pascoe, D. (2020), 'Coronal Heating by MHD Waves', *Space Science Reviews* **216**(8), 140.

van Driel-Gesztelyi, L. and Green, L. M. (2015), 'Evolution of Active Regions', *Living Reviews in Solar Physics* **12**(1), 1.

Vashalomidze, Z., Kukhianidze, V., Zaqarashvili, T. V., Oliver, R., Shergelashvili, B., Ramishvili, G., Poedts, S. and De Causmaecker, P. (2015), 'Formation and evolution of coronal rain observed by SDO/AIA on February 22, 2012', *Astronomy and Astrophysics* **577**, A136.

Venkatakrishnan, P., Hagyard, M. J. and Hathaway, D. H. (1989), 'Evaluation of Magnetic Shear in Off-Disk Center Active Regions', *Solar Physics* **122**(2), 215–226.

Veronig, A. M., Rybák, J., Gömöry, P., Berkebile-Stoiser, S., Temmer, M., Otruba, W., Vršnak, B., Pötzi, W. and Baumgartner, D. (2010), 'Multiwavelength Imaging and Spectroscopy of Chromospheric Evaporation in an M-class Solar Flare', *Astrophysical Journal* **719**(1), 655–670.

Verwichte, E., Antolin, P., Rowlands, G., Kohutova, P. and Neukirch, T. (2017), 'Kinematics of coronal rain in a transversely oscillating loop: Ponderomotive force and rain-excited oscillations', *Astronomy and Astrophysics* **598**, A57.

Vial, J.-C. and Engvold, O. (2015), *Solar prominences*, Springer.

Viall, N. M. and Klimchuk, J. A. (2012), 'Evidence for Widespread Cooling in an Active Region Observed with the SDO Atmospheric Imaging Assembly', *Astrophysical Journal* **753**(1), 35.

Vissers, G. and Rouppe van der Voort, L. (2012), 'Flocculent Flows in the Chromospheric Canopy of a Sunspot', *Astrophysical Journal* **750**, 22.

Wang, H., Chae, J., Gurman, J. B. and Kucera, T. A. (1998), 'Comparison of Prominences in Hα and He II 304 Å', *Solar Physics* **183**(1), 91–96.

Warren, H. P., Ugarte-Urra, I., Doschek, G. A., Brooks, D. H. and Williams, D. R. (2008), 'Observations of Active Region Loops with the EUV Imaging Spectrometer on Hinode', *Astrophysical Journal, Letters* **686**(2), L131.

Waters, T. and Proga, D. (2019), 'Non-isobaric thermal instability', *The Astrophysical Journal* **875**(2), 158.

Watko, J. A. and Klimchuk, J. A. (2000), 'Width Variations along Coronal Loops Observed by TRACE', *Solar Physics* **193**, 77–92.

White, S. D. M. and Rees, M. J. (1978), 'Core condensation in heavy halos: a two-stage theory for galaxy formation and clustering.', *Monthly Notices of the Royal Astronomical Society* **183**, 341–358.

Wilhelm, K., Curdt, W., Marsch, E., Schühle, U., Lemaire, P., Gabriel, A., Vial, J. C., Grewing, M., Huber, M. C. E., Jordan, S. D., Poland, A. I., Thomas, R. J., Kühne, M., Timothy, J. G., Hassler, D. M. and Siegmund, O. H. W. (1995), 'SUMER - Solar Ultraviolet Measurements of Emitted Radiation', *Solar Physics* **162**(1-2), 189–231.

Williams, T., Walsh, R. W., Regnier, S. and Johnston, C. D. (2021), 'Multi-Stranded Coronal Loops: Quantifying Strand Number and Heating Frequency from Simulated Solar Dynamics Observatory (SDO) Atmospheric Imaging Assembly (AIA) Observations', *Solar Physics* **296**(6), 102.

Williams, T., Walsh, R. W., Winebarger, A. R., Brooks, D. H., Cirtain, J. W., De Pontieu, B., Golub, L., Kobayashi, K., McKenzie, D. E., Morton, R. J., Peter, H., Rachmeler, L. A., Savage, S. L., Testa, P., Tiwari, S. K., Warren, H. P. and Watkinson, B. J. (2020), 'Is the High-Resolution Coronal Imager Resolving Coronal Strands? Results from AR 12712', *Astrophysical Journal* **892**(2), 134.

Woods, T. N., Eparvier, F. G., Hock, R., Jones, A. R., Woodraska, D., Judge, D., Didkovsky, L., Lean, J., Mariska, J., Warren, H., McMullin, D., Chamberlin, P., Berthiaume, G., Bailey, S., Fuller-Rowell, T., Sojka, J., Tobiska, W. K. and Viereck, R. (2012), 'Extreme Ultraviolet Variability Experiment (EVE) on the Solar Dynamics Observatory (SDO): Overview of Science Objectives, Instrument Design, Data Products, and Model Developments', *Solar Physics* **275**(1-2), 115–143.

Wuelser, J.-P., Canfield, R. C., Acton, L. W., Culhane, J. L., Phillips, A., Fludra, A., Sakao, T., Masuda, S., Kosugi, T. and Tsuneta, S. (1994), 'Multispectral Observations of Chromospheric Evaporation in the 1991 November 15 X-Class Solar Flare', *Astrophysical Journal* **424**, 459.

Wülser, J. P., Jaeggli, S., De Pontieu, B., Tarbell, T., Boerner, P., Freeland, S., Liu, W., Timmons, R., Brannon, S., Kankelborg, C., Madsen, C., McKillop, S., Prchlik, J., Saar, S., Schanche, N., Testa, P., Bryans, P. and Wiesmann, M. (2018), 'Instrument Calibration of the Interface Region Imaging Spectrograph (IRIS) Mission', *Solar Physics* **293**(11), 149.

Xia, C., Chen, P. F., Keppens, R. and van Marle, A. J. (2011), 'Formation of Solar Filaments by Steady and Nonsteady Chromospheric Heating', *Astrophysical Journal* **737**(1), 27.

Zhang, Q. M., Li, D., Ning, Z. J., Su, Y. N., Ji, H. S. and Guo, Y. (2016), 'Explosive Chromospheric Evaporation in a Circular-ribbon Flare', *Astrophysical Journal* **827**(1), 27.

Zirin, H. (1988), *Astrophysics of the sun*.

Zirker, J. B. (1993), 'Coronal Heating', *Solar Physics* **148**(1), 43–60.